Springer Theses
Recognizing Outstanding Ph.D. Research

Kaitlin Jennifer Cook

Zeptosecond Dynamics of Transfer-Triggered Breakup

Mechanisms, Timescales, and Consequences for Fusion

Springer

Springer Theses

Recognizing Outstanding Ph.D. Research

Aims and Scope

The series "Springer Theses" brings together a selection of the very best Ph.D. theses from around the world and across the physical sciences. Nominated and endorsed by two recognized specialists, each published volume has been selected for its scientific excellence and the high impact of its contents for the pertinent field of research. For greater accessibility to non-specialists, the published versions include an extended introduction, as well as a foreword by the student's supervisor explaining the special relevance of the work for the field. As a whole, the series will provide a valuable resource both for newcomers to the research fields described, and for other scientists seeking detailed background information on special questions. Finally, it provides an accredited documentation of the valuable contributions made by today's younger generation of scientists.

Theses are accepted into the series by invited nomination only and must fulfill all of the following criteria

- They must be written in good English.
- The topic should fall within the confines of Chemistry, Physics, Earth Sciences, Engineering and related interdisciplinary fields such as Materials, Nanoscience, Chemical Engineering, Complex Systems and Biophysics.
- The work reported in the thesis must represent a significant scientific advance.
- If the thesis includes previously published material, permission to reproduce this must be gained from the respective copyright holder.
- They must have been examined and passed during the 12 months prior to nomination.
- Each thesis should include a foreword by the supervisor outlining the significance of its content.
- The theses should have a clearly defined structure including an introduction accessible to scientists not expert in that particular field.

More information about this series at http://www.springer.com/series/8790

Kaitlin Jennifer Cook

Zeptosecond Dynamics of Transfer-Triggered Breakup

Mechanisms, Timescales, and Consequences for Fusion

Doctoral Thesis accepted by
the Australian National University, Canberra, Australia

Springer

Author
Dr. Kaitlin Jennifer Cook
Department of Nuclear Physics, Research School of Physics and Engineering
Australian National University
Canberra, ACT, Australia

Supervisor
Prof. Mahananda Dasgupta
Australian National University
Canberra, ACT, Australia

ISSN 2190-5053 ISSN 2190-5061 (electronic)
Springer Theses
ISBN 978-3-319-96016-6 ISBN 978-3-319-96017-3 (eBook)
https://doi.org/10.1007/978-3-319-96017-3

Library of Congress Control Number: 2018948585

Printed on acid-free paper

This Springer imprint is published by the registered company Springer Nature Switzerland AG
The registered company address is: Gewerbestrasse 11, 6330 Cham, Switzerland

By convention sweet is sweet,
bitter is bitter,
hot is hot,
cold is cold,
colour is colour;
but in truth there are only atoms and the void.

Democritus (460–370 BCE)

To my parents.

Supervisor's Foreword

The elements that make us, our planet, and the Universe result from nuclear reactions in the cosmos. Synthesis of elements occurs through fusion of atomic nuclei, reactions involving neutron-rich nuclei, and nuclear fission. Atomic nuclei, made of protons and neutrons, are quantum objects and their interactions are largely determined by the strong and electromagnetic forces. The outcomes of nuclear reactions are thus fundamentally determined by many-body quantum dynamics of strongly interacting systems. This results in striking consequences, as exemplified by the many-fold increase in fusion at energies below the Coulomb barrier due to couplings to low-energy quantum states of the two interacting nuclei. Accurate prediction, particularly at energies near the barrier where quantum structure and dynamics are clearly intertwined, is a formidable challenge to our understanding of many-body physics.

We are entering an era that promises a vastly improved understanding through a happy coincidence of new experimental techniques, new accelerators of intense beams of both stable and unstable (rare) isotopes, and increased computational power that allows microscopic many-body calculations. This thesis presents an incisive new method that demonstrates how the subtleties of quantum structure of light weakly bound nuclei affect reaction outcomes. This is of immediate interest due to the worldwide availability of accelerated beams of rare short-lived nuclei. Currently, there is no theoretical model that describes the (experimentally observed) routes that cause breakup of weakly bound fragile nuclei. The excited quantum states of such nuclei are typically particle-unbound resonances and the effect of couplings to these resonant states on fusion continues to generate controversy. For these reasons, a realistic understanding of the processes influencing near-barrier fusion of weakly bound nuclei remains elusive.

This thesis highlights the role of resonance lifetimes in determining reaction outcomes through selecting experimental observables that are sensitive to the location of breakup, and combined with stochastic model simulations. Lifetimes as short as 10^{-21}s must not be assumed to lead to "instantaneous" breakup, but must be treated explicitly to reproduce experimental results.

Breakup that occurs as the weakly bound projectile nucleus approaches the target nucleus could be separated from that occurring when the projectile recedes from the target. This separation led to another physics insight: breakup prior to reaching the barrier is insufficient to explain the experimentally observed suppression of complete fusion. This result means that efforts must now be directed towards finding a different mechanism that can cause the suppression of complete fusion.

The results described in this thesis make a compelling case for the practitioners in the field to design new experiments and develop theories to include the latest findings. The pedagogical treatment of nuclear reactions at energies near the fusion barrier, and the analysis methods presented for the large-coverage and high-granularity detector array will be helpful for graduate students entering the field. The ideas presented in this thesis, I hope, will open up innovations in experimental and theoretical methods that will ultimately allow prediction of the products of nuclear collisions, urgently needed for research with next-generation radioactive beams.

Canberra, Australia
June 2018

Prof. Mahananda Dasgupta

Abstract

Above-barrier complete fusion cross sections for reactions with light, weakly bound nuclei such as ^{6,7}Li and ^{9}Be are suppressed relative to expectations from theory and experiment. This has been interpreted to be a result of the weakly bound nucleus breaking up into its cluster constituents, reducing the probability of complete charge capture. However, experiments to probe mechanisms of breakup in below-barrier reactions of ^{9}Be and ^{6,7}Li with high atomic number targets have shown that breakup of unbound states formed following nucleon transfer dominates over direct breakup of the projectile into its cluster constituents. This thesis extends the study of breakup following transfer in interactions of ^{9}Be and ^{7}Li with light targets of $6 \leq Z \leq 28$. Below-barrier coincidence measurements of breakup fragments produced in these reactions show a vanishing amount of direct breakup, and the dominance of transfer-triggered breakup.

Since breakup can only suppress complete fusion if it occurs prior to the collision partners reaching the fusion barrier, the location of breakup is crucial. In turn, the location of breakup is intimately related to the lifetime of the unbound state that is populated. Nuclei produced in long-lived states cannot suppress complete fusion, since they will pass the barrier before breakup can occur. Conversely, nuclei produced in states with lifetimes comparable to the zeptosecond (10^{-21}s) timescale of the collision may break up before reaching the fusion barrier. Through the use of experimental observables that are sensitive to the location of breakup, the importance of a realistic treatment of resonance lifetimes to correctly reproduce experimental results with theoretical modelling will be established.

Below-barrier measurements of transfer-triggered breakup, where capture is minimised, are used to determine the breakup probability as a function of distance of closest approach for reactions of ^{7}Li and ^{9}Be with light targets of $13 \leq Z \leq 28$, as well for reactions of ^{9}Be with heavy targets of $62 \leq Z \leq 83$. These probability functions are used as input into classical dynamical trajectory models to predict above-barrier complete and incomplete fusion cross sections. These fusion cross sections are found to be sensitive to the lifetime of the weakly bound nucleus produced after transfer. When realistically modelled, the inclusion of lifetime leads

to the conclusion that breakup alone cannot account for the observed suppression of complete fusion in reactions ^{9}Be with ^{144}Sm to ^{209}Bi.

Experimental groundwork is laid for measurement of the ^{7}Be(d,p)^{8}Be reaction at the Australian National University, relevant to Big Bang nucleosynthesis. The efficacy of using a large solid angle array and kinematic reconstruction techniques for such studies is demonstrated through a measurement of αparticles produced in the mirror reaction ^{7}Li(d,n)^{8}Be. In this reaction, a high population of the broad 4^{+}resonance in ^{8}Be is observed, totalling 69% of the coincidence yield after efficiency correction. It is therefore crucial to investigate the excitation of ^{8}Be in the ^{7}Be(d,p)^{8}Be reaction. Test measurements of ^{7}Be production via the ^{10}B(^{6}Li, ^{7}Be)^{9}Be reaction are made using the SOLEROO RIB facility. Normalised secondary beam intensities above 10^{4}cts/s/mg/cm^{-2}/μeA are achieved with beam purity of $\sim$96%.

Preface

This thesis is an account of research undertaken between February 2013 and December 2016 at the Department of Nuclear Physics, Research School of Physics and Engineering, College of Physical and Mathematical Sciences, the Australian National University, Canberra, Australia. This thesis presents a study of breakup triggered by transfer in below-barrier reactions of ^{7}Li and ^{9}Be with targets of mass ranging across the nuclear chart, $6 \leq Z \leq 28$, in a series of four experimental runs. In addition, previously measured reactions of ^{9}Be with targets of $62 \leq Z \leq 83$, measured by Dr. R. Rafiei and colleagues, are reanalysed.

The project was originally proposed by Prof. M. Dasgupta and Prof. D. J. Hinde. Beams of accelerated ^{7}Li and ^{9}Be were provided by the 14UD tandem accelerator of the Heavy Ion Accelerator Facility at the Australian National University in Canberra, Australia. All measurements were carried out with the assistance of the nuclear reaction dynamics group and the technical staff of the Department of Nuclear Physics. Measurements were made with the Breakup Array for Light Nuclei (BALiN), a large, position sensitive array, originally commissioned by Dr. D. H. Luong and Dr. R. Rafiei. The array and associated electronics was set up by the author, with assistance from Dr. D. H. Luong, Prof. M. Dasgupta, Prof. D. J. Hinde, and Dr. E. Williams.

All data analysis was done by the author. Analysis was performed using the CERN ROOT analysis framework, using scripts originally written by Dr. D. H. Luong, extensively modified by the author. The author collaborated with Dr. D. H. Luong and Dr. Sunil Kalkal closely in the extraction, analysis, and interpretation of breakup events. Two classical dynamical trajectory models of breakup were utilised to establish the coincidence efficiency of BALiN for each measurement. The models were also used to predict the effect of breakup on incomplete and complete fusion cross sections at above-barrier energies from experimentally determined below-breakup probabilities. The first model was M-PLATYPUS, a modified version of PLATYPUS written by Dr. A. Diaz-Torres, and modified by Dr. E. C. Simpson. The second was KOOKABURRA, written by Dr. E. C. Simpson. Both models were tested by the author and Dr. Sunil Kalkal.

Developmental work was undertaken to measure the astrophysically relevant ^{7}Be(d,p)^{8}Be reaction at the Australian National University. The mirror reaction ^{7}Li(d,n)^{8}Be was measured using the BALiN array to establish the efficacy of the array and analysis techniques for such reactions. Targets of deuterated polyethylene were produced by the author with the assistance of Mr. S. McNeil. In addition to this measurement, this thesis describes the development of a ^{7}Be radioactive ion beam, using the SOLEROO RIB facility at the Australian National University. The commissioning of the facility was completed over the course of this thesis by Mr. I. P. Carter. Measurements were made by the author in collaboration with Mr. I. P. Carter and Dr. E. C. Simpson and with assistance from the nuclear reaction dynamics group.

The following publications and conference proceedings, to which the author contributed to, are directly related to the work in this thesis:

1. **K.J. Cook**, E.C. Simpson, D.H. Luong, Sunil Kalkal, M. Dasgupta and D.J. Hinde, "Importance of lifetime effects in breakup and suppression of complete fusion in reactions of weakly bound nuclei", *Physical Review C* **93**, 064604 (2016)
2. E.C. Simpson, **K.J. Cook**, D.H. Luong, Sunil Kalkal, I.P. Carter, M. Dasgupta, D.J. Hinde, and E. Williams, "Disintegration locations in ^{7}Li→^{8}Be transfer-triggered breakup at near-barrier energies", *Physical Review C* **93**, 024605 (2016)
3. Sunil Kalkal, E.C. Simpson, D.H. Luong, **K.J. Cook**, M. Dasgupta, D.J. Hinde, I.P. Carter, D.Y. Jeung, G. Mohanto, C.S. Palshetkar, E. Prasad, D.C. Rafferty, C. Simenel, K. Vo-Phuoc, E. Williams, L.R. Gasques, P.R.S. Gomes and Linares, R. "Asymptotic and near-target direct breakup of ^{6}Li and ^{7}Li", *Physical Review C* **93**, 044605 (2016)
4. M. Dasgupta, E.C. Simpson, D.H. Luong, Sunil Kalkal, **K.J. Cook**, I.P. Carter, D.J. Hinde and E. Williams, "Breakup locations: Intertwining effects of nuclear structure and reaction dynamics", *EPJ Web of Conferences* **117**, 08005 (2016)
5. **K.J. Cook**, D.H. Luong, I.P. Carter, M. Dasgupta, D.J. Hinde, S. McNeil, D. Rafferty, K. Ramachandran, C. Simenel and E. Williams, "Breakup following interactions with light targets: Investigating new methods to probe nuclear physics input to the cosmological lithium problem", *EPJ Web of Conferences* **91**, 00002 (2015)
6. I.P. Carter, M. Dasgupta, D.J. Hinde, D.H. Luong, E. Williams, K. Ramachandran, **K.J. Cook**, A.G. Muirhead, S. Marshall and T. Tunningley, "Recent developments of SOLEROO: Australia's first high energy radioactive ion beam capability", *EPJ Web of Conferences* **91**, 00001 (2015)
7. I.P. Carter, K. Ramachandran, M. Dasgupta, D.J. Hinde, R.Rafiei, D.H. Luong, E. Williams, **K.J. Cook**, S. McNeil, D.C. Rafferty, A.B. Harding, A.G. Muirhead and T. Tunningley, "An ion beam tracking system based on a parallel plate avalanche counter", *EPJ Web of Conferences* **63**, 02022 (2013)

8. **K.J. Cook**, D.H. Luong, E. Williams, I.P. Carter, M. Dasgupta, D.J. Hinde and K. Ramachandran, "Developing new methods to investigate nuclear physics input into the cosmological lithium problem", *EPJ Web of Conferences* **63**, 03011 (2013)
9. **K.J. Cook**, D.H. Luong, E. Williams, "Nuclear physics solutions to the primordial lithium problem", *EPJ Web of Conferences* **35**, 05004 (2012)
10. D.H. Luong, **K.J. Cook**, E. Williams, M. Dasgupta, D.J. Hinde, R. duRietz, R. Rafiei and M. Evers, "Break-up Array for Light Nuclei: A new tool for exploring nuclear reactions of relevance to the cosmological ^{7}Li problem", *Proceedings of Science (NIC XII)*, 185 (2012)

The author also contributed to the following publications and conference proceedings published during her Ph.D. work:

11. D.C. Rafferty, M. Dasgupta, D.J. Hinde, C. Simenel, E.C. Simpson, E. Williams, I.P. Carter, **K.J. Cook**, D.H. Luong, S.D. McNeil, K. Ramachandran, K. Vo-Phuoc and A. Wakhle, "Multinucleon transfer in ^{16,18}O, ^{19}F + ^{208}Pb reactions at energies near the fusion barrier", *Physical Review C* **94**, 024607 (2016)
12. E. Prasad, D.J. Hinde, K. Ramachandran, E. Williams, M. Dasgupta, I.P. Carter, **K.J. Cook**, D.Y. Jeung, D.H. Luong, S. McNeil, C.S. Palshetkar, D.C. Rafferty, C. Simenel and A. Wakhle, "Observation of mass-asymmetric fission of mercury nuclei in heavy ion fusion", *Physical Review C* **91**, 064605 (2015)
13. K. Hammerton, Z. Kohley, D.J. Hinde, M. Dasgupta, A. Wakhle, E. Williams, V.E. Oberacker, A.S. Umar, I.P. Carter, **K.J. Cook**, J. Greene, D.Y. Jeung, D.H. Luong, S.D. McNeil, C.S. Palshetkar, D.C. Rafferty, C. Simenel and K. Stiefel, "Reduced quasifission competition in fusion reactions forming neutron-rich heavy elements", *Physical Review C* **91**, 041602(R) (2015)
14. D.J. Hinde, E. Williams, G. Mohanto, C. Simenel, M. Dasgupta, A. Wakhle, I.P. Cater, **K.J. Cook**, D.Y. Jeung, D.H. Luong, C.S. Palshetkar, E. Prasad, D.C. Rafferty, R. du Rietz and E.C. Simpson, "Systematic study of quasifission characteristics and timescales in heavy element formation reactions", *EPJ Web of Conferences* **117**, 08006 (2016)
15. E. Williams, D.J. Hinde, M. Dasgupta, I.P. Carter, **K.J. Cook**, D.Y. Jeung, D.H. Luong, S.D. McNeil, C.S. Palshetkar, D.C. Rafferty, K. Ramachandran, C. Simenel, E.C. Simpson and A. Wakhle, "Exploring dissipative processes at high angular momentum in ^{58}Ni+^{60}Ni reactions", *EPJ Web of Conferences* **117**, 08021 (2016)
16. D.C. Rafferty, M. Dasgupta, D.J. Hinde, C. Simenel, **K.J. Cook**, I.P. Carter, D.H. Luong, S.D. McNeil, K. Ramachandran, A. Wakhle and E. Williams, "Investigating energy dissipation through nucleon transfer reactions", *EPJ Web of Conferences* **91**, 00010 (2015)

17. D.J. Hinde, E. Williams, R. du Rietz, M. Dasgupta, A. Wakhle, C. Simenel, D.H. Luong, and **K.J. Cook**, "Mapping quasifission characteristics in heavy element formation reactions", *EPJ Web of Conferences* **86**, 00015 (2015)
18. D.J. Hinde, R. du Rietz, E. Williams, C. Simenel, C.J. Lin, A. Wakhle, **K.J. Cook**, M. Dasgupta, M. Evers, and D.H. Luong, "Mass-angle distributions: Insights into the dynamics of heavy element formation", *EPJ Web of Conferences* **66**, 03037 (2014)
19. D.J. Hinde, M. Dasgupta, I.P. Carter, **K.J. Cook**, M. Evers, D.H. Luong, K. Ramachandran, D. Rafferty, C. Simenel, A. Wakhle, and E. Williams, "Nuclear reaction dynamics research at the Australian National University", *EPJ Web of Conferences* **63**, 02005 (2013)

Canberra, Australia Kaitlin Jennifer Cook

Acknowledgements

There are certain calculations I should like to make with you,
To be sure that your deductions will be logical and true;
And remember, "Patience, Patience," is the watchword of a sage,
Not to-day nor yet to-morrow can complete a perfect age
Sarah Williams 1837–1868

First and foremost, I thank my supervisors, Nanda Dasgupta and David Hinde. It is hard to imagine a better pair of supervisors. Thank you for your mentorship, good humour, and ability to shed light on the most stubborn of problems. Your constant endeavour towards excellence has been a source of personal inspiration.

Immense thanks go to my supervisor Ed Simpson, whose theoretical insights changed the direction of my project. Thank you for your calm humour and patience. Thanks also go to Huy Luong whose Ph.D. work has been the foundation of the intricate analysis of this thesis. I would like to thank Sunil Kalkal, who more than anyone else, will understand why this thesis had to be quite as long and complex as it is. Collaborating (and arguing) with you was a joy. Thanks to Ian Carter, for his expertise in all things RIB.

In collecting the data, I thank Liz Williams and Ramachandran, whose knowledge of detector electronics was of immense help during set-up. Other members of the reaction dynamics group made this thesis possible by their hard work during weeks of beamtime: Prasad Edayillam, Dongyun Jeung, Steven McNeil, Gayatri Mohanto, Chandani Palshetkar, Dominic Rafferty, Cédric Simenel, and Kirsten Vo-Phuoc.

Nothing could happen without the work of the technical officers of the Department of Nuclear Physics. Particular thanks go to Alistair Muirhead, for always teaching me the right way to do something, to Dimitrios Tsifakis for his knowledge of RF noise, and to Nikolai Lobanov, our Accelerator Manager, whose work made generating intense ^{7}Li beams routine.

Thanks also must go to Joe Walshe and Bonnie Zhang, who read chapters and listened to me complain about writing, and to Lindon Roberts and Erin Stewart, for never letting me take myself too seriously.

To my Mum and Dad. Thank you for raising me to know the pleasure of finding things out, and the value of building something with my own hands. You have given me every opportunity, and it is because of you that I have achieved all I have.

Finally, my deepest gratitude goes to Kira for her love, laughter, and unflagging belief in me. I'm not sure I have the right words to thank you.

Contents

Chapter 1
Introduction

Let's think the unthinkable, let's do the undoable. Let us prepare to grapple with the ineffable itself, and see if we may not eff it after all

Douglas Adams 1952–2001

Every nucleus heavier than ^{1}H is the product of a nuclear reaction. We are, in a very real way, the result of billions of years of nuclear physics. Therefore, to study nuclear reactions is to study our origins. Nuclear reactions involve fleeting collisions of finite quantum systems which occur on timescales of 10^{-21} s and on distances of 10^{-15} m. These collisions, which are governed by the electromagnetic and strong interactions, have many possible outcomes, ranging from elastic scattering, where the colliding remain in their ground states, through to complete fusion, where the two nuclei combine to produce a single compound nucleus. As a field, nuclear reaction dynamics is concerned with understanding the physical mechanisms that dictate the outcomes of nuclear collisions.

Arguably, the modern approach to nuclear physics, where accelerated beams of nuclei are collided with a stationary target, began with the work of Cockcroft and Walton in 1932 [1, 2]. Cockcroft and Walton produced an accelerated beam of protons and used them to bombard a target of lithium. The resulting $p + {}^{7}\mathrm{Li} \rightarrow \alpha + \alpha$ reaction was the first entirely artificial nuclear reaction. More than eighty years later, the processes through which light weakly-bound nuclides such as ^{7}Li disintegrate are still not fully understood. This thesis is a continuation of the work towards understanding the interactions of light weakly-bound nuclei.

The central theme of this thesis is to understand the mechanisms through which the weakly-bound ^{7}Li and ^{9}Be nuclides break up in reactions with targets of atomic number Z varying from 1 to 83, and to understand the way in which these processes affect complete and incomplete fusion. This work lies in the broader context of the continuing work in nuclear reactions towards forming a consistent framework for relating the nuclear structure of light weakly-bound nuclei to reaction outcomes. Understanding the reaction dynamics of these nuclides is a pressing need in light of

K. J. Cook, *Zeptosecond Dynamics of Transfer-Triggered Breakup*,
Springer Theses, https://doi.org/10.1007/978-3-319-96017-3_1

the increasing availability of Radioactive Ion Beams (RIBs) that probe the limits of nuclear existence. Of key interest is the effect of weak binding on complete fusion.

1.1 Complete Fusion Suppression

Fusion measurements of ^{9}Be + ^{208}Pb, ^{209}Bi [3–6] and ^{6,7}Li + ^{209}Bi [3, 7] were amongst the first to show that above-barrier complete fusion cross-sections (experimentally defined as capture of the full charge of the projectile) are reduced by ∼30%, both in comparison with those predicted by standard fusion models and with measurements for well-bound nuclei forming the same compound nucleus [3, 8]. An example of the suppression of complete fusion is shown in Fig. 1.1 for complete fusion of ^{7}Li + ^{209}Bi compared to ^{18}O + ^{198}Pt, where cross-sections have been normalised to the fusion barrier radius, and energies normalised to the fusion barrier energy (both of these concepts are defined in the following chapter). It is readily apparent that the normalised complete fusion cross-sections are suppressed relative to both ^{18}O + ^{198}Pt and expectations from single barrier penetration model calculations [3]. This suppression has been observed to varying extents for reactions of stable light weakly-bound nuclides ^{6,7}Li, ^{9}Be with targets in the range $28 \leq Z \leq 83$

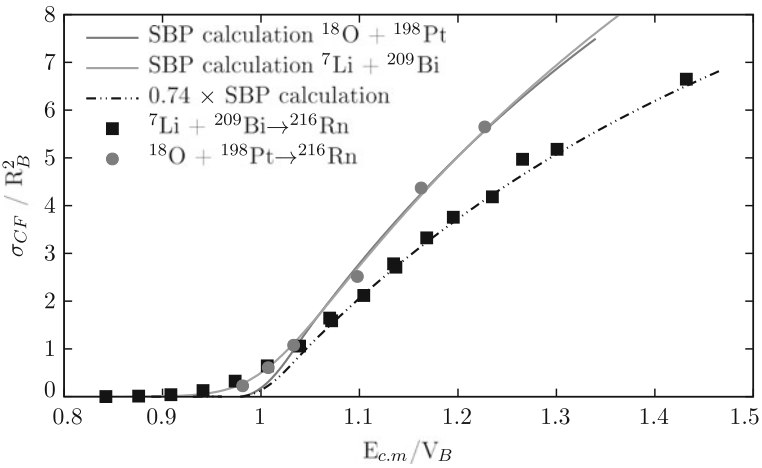

Fig. 1.1 Complete fusion cross-sections σ_{CF} for ^{7}Li + ^{209}Bi and ^{18}O + ^{198}Pt, forming the same compound nucleus, normalised to the average barrier radius (R_B), as a function of centre-of-mass energy normalised to the average barrier energy (V_B). Fusion reactions with weakly-bound ^{7}Li are suppressed relative to the fusion with the well bound ^{18}O nucleus. Single Barrier Penetration (SBP) model calculations are shown for ^{7}Li + ^{209}Bi and ^{18}O + ^{198}Pt, showing the validity of normalising cross-sections in this manner. The SBP calculation needs to be scaled by 0.74 to correspond to the ^{7}Li + ^{209}Bi experimental data, demonstrating the suppression of complete fusion relative to model calculations. Adapted from [3]

[3–19]. Smaller suppressions have been observed for reactions of the less weakly-bound ^{11}B and ^{10}B nuclides [20, 21]. Detailed reviews on the fusion of light weakly-bound nuclei may be found in Refs. [22, 23].

Although complete fusion suppression has been observed in reactions with heavy targets, the status of complete fusion suppression is not clear in reactions with light targets, since the separation of complete and incomplete fusion (experimentally defined as partial charge capture) is very difficult. This is due to the significant charged particle evaporation that will occur for compound nuclei with lower Z. As a result, the same reaction product can be formed via complete fusion following particle evaporation and by incomplete fusion. This has precluded a systematic understanding of the trends of complete fusion suppression.

While the phenomenon of above-barrier complete fusion suppression for weakly-bound nuclei is by now well established in reactions with heavy targets, the mechanism responsible is not. It was originally suggested that complete fusion suppression should result from direct breakup of the weakly-bound nucleus [e.g. ^{9}Be($\rightarrow \alpha + \alpha + n$), ^{7}Li($\rightarrow \alpha + t$), ^{6}Li($\rightarrow \alpha + d$)] prior to reaching the fusion barrier [4]. It was conjectured that breakup reduces the probability of the full charge of the projectile-like nucleus being captured, thus suppressing complete fusion (CF), and increasing the incomplete fusion (ICF) cross-sections, shown schematically in Fig. 1.2.

Experiments were undertaken to probe the extent of the role of breakup in complete fusion suppression. Coincidence measurements of breakup fragments were made at below-barrier energies with a large position sensitive array, and key kinematic quantities were reconstructed. These experiments were performed at below-barrier energies to allow clearer investigation of breakup mechanisms, as there is essentially no absorption of the charged fragments [24]. These investigations found that transfer to particle unbound states of neighbouring nuclei followed by breakup contributes much more than direct breakup to the total breakup probability [25–28]. In the case of ^{9}Be, breakup in interactions with targets ranging from ^{144}Sm to ^{209}Bi is dominated by neutron stripping forming ^{8}Be which subsequently breaks up into $\alpha + \alpha$, rather than ^{9}Be undergoing direct breakup into $\alpha + \alpha + n$ or ^{8}Be+n [25]. In reactions of ^{7}Li with ^{144}Sm, ^{207,208}Pb and ^{209}Bi, below-barrier breakup yields are dominated by proton pickup forming ^{8}Be($\rightarrow \alpha + \alpha$), neutron stripping forming ^{6}Li($\rightarrow \alpha + d$) and two neutron stripping forming ^{5}Li($\rightarrow \alpha + p$) [26–28]. In reactions of ^{6}Li with ^{207,208}Pb and ^{209}Bi, one neutron stripping forming ^{5}Li and deuteron pickup forming ^{8}Be dominate over direct ^{6}Li$\rightarrow \alpha + d$ breakup [26–28]. These results explained earlier work that showed unexpectedly high α singles production cross-sections relative to t in reactions of ^{7}Li with ^{208}Pb [29] as well as unexpected proton production in ^{6}Li + ^{208}Pb reactions [30]. It is only through coincidence measurements of fragments that clear pictures of these reactions emerge [31, 32].

It is now very clear that it is not only direct breakup that should be considered as a candidate for above-barrier complete fusion suppression, but also transfer populating particle unbound states of neighbouring nuclei that subsequently break up. The breakup of neighbouring nuclei populated following transfer is termed “transfer-triggered breakup”. Following transfer, the projectile-like nucleus may break up

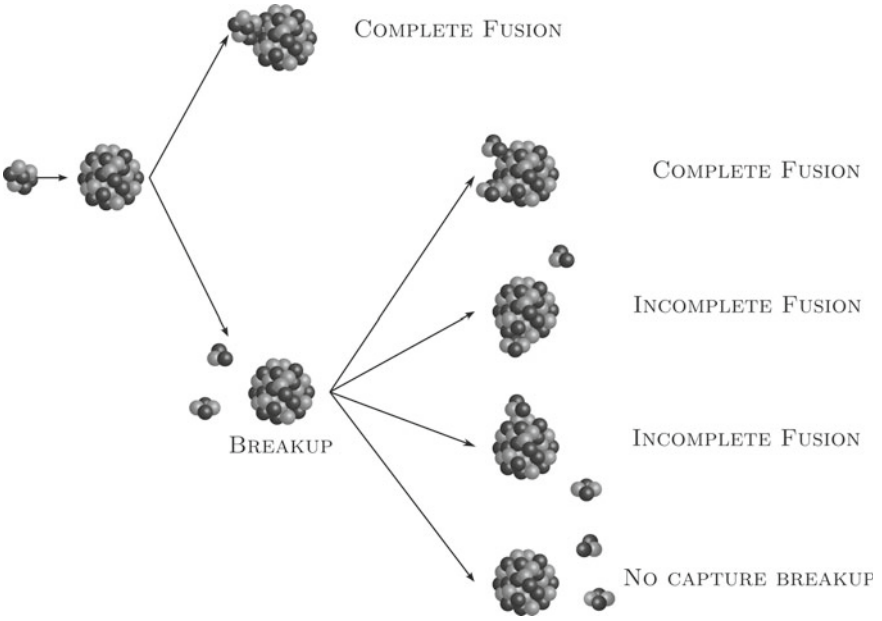

Fig. 1.2 Reaction pathways affecting complete fusion. If a weakly-bound nucleus breaks up as it approaches another nucleus, the resulting fragments may both be captured, and so undergo sequential complete fusion. On the other hand, one of the fragments may be captured, resulting in incomplete fusion. When neither fragment is captured, this is no capture breakup. These processes reduce the probability of complete fusion. Note that transfer and incomplete fusion can lead to the same final product. However, within the coupled channels framework, transfer is not thought to suppress complete fusion significantly

before it can be captured. As a result, there will be a decreased probability of complete fusion, and a corresponding increase of incomplete fusion and no capture breakup.

The capability of any breakup process to suppress above-barrier complete fusion depends on its location. It was recognised early on [24] that the population of long-lived states, such as the 0^+ ground-state of ^{8}Be, which has a mean life of $\sim 10^{-16}$ s [33], results in breakup far from the target-like nucleus at energies below the barrier. At above-barrier energies, the ^{8}Be nucleus in its ground-state will pass inside the fusion barrier and be absorbed long before decay can occur. It therefore cannot contribute to complete fusion suppression. Similarly, population of ^{6}Li in its long-lived 3^+ state (mean life $= 2.74 \times 10^{-20}$ s) located 711 keV above the $\alpha + d$ breakup threshold [34] cannot suppress complete fusion. However, population of broad resonances with much shorter mean lives will result in breakup close to the target-like nucleus. It is this type of breakup that may suppress complete fusion.

As an example, measurements of transfer reactions populating ^{8}Be show the population of ^{8}Be in its 0^+, 2^+, and at higher excitations, 4^+ states [35, 36]. The 3.03 MeV 2^+ state of ^{8}Be has an on-resonance width of $\Gamma(E_R) = 1513 \pm 15$ keV, and thus a mean life of $\tau = \hbar/\Gamma(E_R) = 0.44 \times 10^{-21}$ s [33]. Breakup from this state

will occur very close to the target-like nucleus. To determine the effect on complete fusion, it is then necessary to quantitatively understand whether such short mean lives carry a significant fraction of excited projectile-like nuclei inside the fusion barrier before breakup occurs, thus reducing the suppression of complete fusion due to breakup.

The question then is: what is the quantitative contribution of near-target transfer-triggered breakup to the suppression of complete fusion? This was previously addressed by first obtaining breakup probabilities as a function of distance of closest approach ("breakup functions") [25] at below-barrier energies. These breakup functions were then used as input to the classical dynamical model code PLATYPUS [37, 38], to predict complete and incomplete fusion cross-sections at above-barrier energies [25, 37] that agreed satisfactorily with experimental results [3, 6, 12, 15].

In PLATYPUS, the lifetimes of the intermediate states populated are not explicitly taken into account. However, locations of breakup and the lifetimes of states are intimately related: finite but small mean lives will change the positions at which breakup occurs along the trajectory of the nuclei. Therefore, accurate simulation of excitation and lifetime of states is essential to reliably predict the effect of breakup on fusion suppression. Indeed, recent work [39] has highlighted that the precise location of breakup relative to the target-like nucleus is critical to reaction outcomes, and further, that there exist experimental observables that can probe these effects. This thesis makes use of coincidence measurements of breakup fragments to investigate the role of zeptosecond lifetimes in breakup and fusion suppression. Further, this thesis presents a re-analysis of the extensive sub-barrier breakup measurements of Rafiei et al. [25], using a modified version of PLATYPUS which incorporates resonance lifetimes. After taking into account these lifetimes, new predictions of the contribution of breakup to fusion suppression will be presented. Finally, the magnitude of complete fusion suppression in reactions of ^{7}Li and ^{9}Be with light targets will be predicted using a new classical trajectory model code KOOKABURRA.

1.2 Cosmological Lithium Problem

An additional focus of this thesis lies in the use of the coincidence measurement and kinematic reconstruction techniques developed for the study of breakup for the study of reactions of astrophysical interest. Specifically, the interest lies in the ^{7}Be(d,p)^{8}Be reaction, which destroys ^{7}Be during Big Bang Nucleosynthesis (BBN), and is therefore a candidate for a nuclear physics solution to the cosmological lithium problem.

The cosmological lithium problem is a long-standing problem in concordance models of the Big Bang, wherein the abundances of ^{7}Li predicted in models of BBN are a factor of 2.4–3.2 times larger than those inferred from spectroscopic observations of metal-poor halo stars [40, 41]. These stars have very small convection zones, and thus cannot modify the composition of their surface layers by nuclear reactions. As a result, it is thought that the ^{7}Li abundances in these stars represent the abundance of ^{7}Li arising from BBN (i.e. the abundance is "primordial"). The

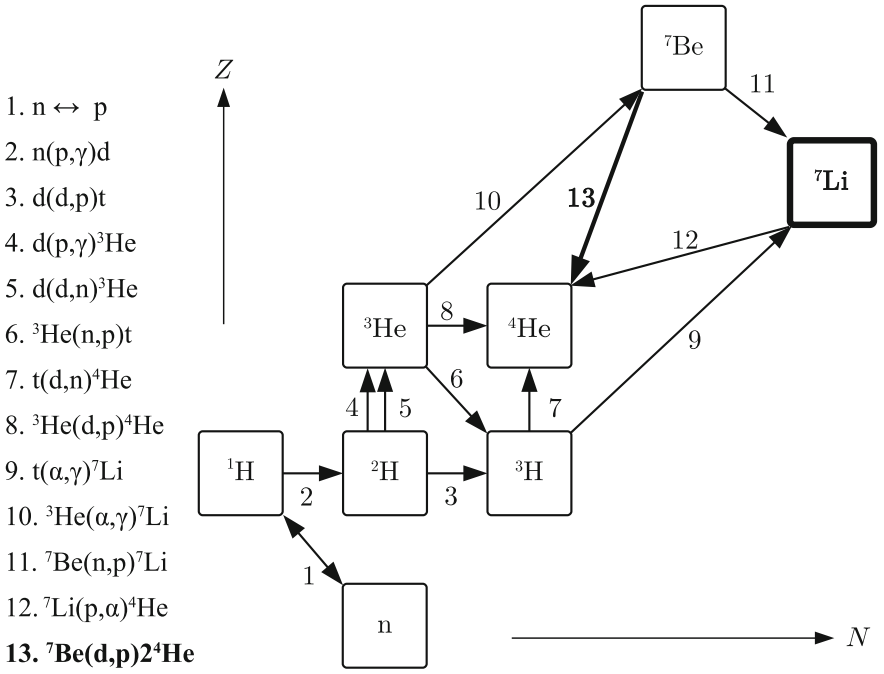

Fig. 1.3 Simplified nuclear reaction network showing the important reactions forming ^{7}Li during BBN, plus ^{7}Be(d,p)^{8}Be. Adapted from [41, 54]

discrepancy, which has been well established since 1982 [42], has a significance of $4-5\sigma$ and is yet to find satisfactory conclusion, although there has been significant effort to achieve one.

Proposed solutions to the cosmological lithium problem can be found in many areas of nuclear astrophysics, and include (but are by no means limited to): stellar models with increased turbulence and diffusion between surface and burning layers [43]; inferring primordial abundances from low metalicity gases in the Small Magellanic Cloud [44]; non-standard cosmologies [45, 46]; particle physics beyond the standard model [47–49]; and improved understandings of relevant nuclear reaction rates [50–53].

Nuclear physics solutions centre around the determination of the most relevant reactions that contribute to the abundance of ^{7}Li produced during BBN and the subsequent measurement of these cross-sections. Shown in Fig. 1.3 is a simplified nuclear reaction network, showing the dominant reactions that contribute to ^{7}Li abundances. Importantly, the main reaction forming ^{7}Li during BBN isn't the direct $^{3}\mathrm{H}(\alpha,\gamma)^{7}\mathrm{Li}$ fusion reaction, but instead the production of ^{7}Be and its subsequent decay into ^{7}Li via electron capture ($t_{1/2} = 52.3$ days). The production rate of ^{7}Be is strongly constrained by observations of solar neutrino production [55, 56]. Therefore, the search for nuclear physics solutions to the cosmological lithium problem focus on reactions that destroy ^{7}Be without producing ^{7}Li.

One such candidate is the ^{7}Be(d,p)^{8}Be($\rightarrow \alpha + \alpha$) reaction. A sensitivity study [54] has shown that this reaction is able to resolve the ^{7}Li problem if the reaction rate is one hundred times larger than the adopted estimate [57]. A measurement of this reaction swiftly followed, which found a value ten times *smaller* than the previously adopted value [58]. This measurement was performed by measurement of the recoiling protons. This means that the measurement of low energy protons was precluded, such as those that will be produced when ^{8}Be is excited to its broad 4^{+} resonance at 11.35 MeV, which may be expected to be populated with high probability. Instead, the population of the 4^{+} state had to be estimated. To fully determine the contribution of the ^{7}Be(d,p)^{8}Be reaction to ^{7}Li abundances in BBN, it is imperative that this reaction be remeasured through the coincidence measurement of α particles in coincidence, which will have high energy when ^{8}Be is produced in highly excited states.

1.3 Aims

In light of the above discussion, this thesis has several key goals.

1. To identify the modes of breakup in interactions of ^{7}Li and ^{9}Be with light targets of $6 \leq Z \leq 28$ using coincidence measurement techniques, and to extract breakup probabilities as a function of the distance of closest approach.
2. To investigate *qualitatively* the kinematic signatures of breakup through short-lived resonant states, and so provide experimental guidance into the essential physics input in classical models of breakup.
3. To *quantitatively* predict the effect of the lifetime of short-lived resonant states on breakup processes and the resultant incomplete fusion, and thus the suppression of complete fusion for targets of $13 \leq Z \leq 83$.
4. To explore the use of coincidence measurement and kinematic reconstruction techniques developed for the study of breakup in measurements of the astrophysically relevant ^{7}Be(d,p)^{8}Be reaction. In addition, to test the production of ^{7}Be beams using the radioactive ion beam facility SOLEROO [59–61] at the Australian National University.

1.4 Thesis Outline

Chapter 2 contains an overview of the key nuclear physics concepts required in this thesis. The role of the resonant structure of light weakly-bound nuclei in reaction outcomes will be introduced, as well as key kinematic observables that provide insight into the mechanisms of breakup. The classical models of breakup that are used extensively throughout this thesis are introduced.

Chapter 3 describes the experimental measurement and analysis techniques used to measure breakup fragments in coincidence at below-barrier energies with the Breakup Array for Light Nuclei (BALiN), a large position sensitive silicon detector array. There will be a focus on the advances made for measurements of breakup in reactions with light to medium mass targets.

Chapter 4 concerns the identification of all the major breakup modes seen in interactions of ^{7}Li and ^{9}Be with ^{12}C, ^{16}O, ^{27}Al, ^{28}Si, ^{58}Ni, ^{144}Sm, ^{168}Er, ^{186}W, ^{196}Pt, ^{208}Pb and ^{209}Bi.

Chapter 5 explores the signatures of asymptotic and near-target breakup on key kinematic quantities. Experimental distributions of breakup fragments will be compared to classical trajectory calculations and model sensitivities to the lifetime of short-lived resonant states will be established. Sensitivities of experimental distributions to sub-zeptosecond lifetimes will be shown.

Chapter 6 describes the extraction of breakup probability functions for the breakup modes identified in previous chapters. Improved coincidence efficiency correction techniques will be presented, as well as inventive beam normalisation methods.

Chapter 7 presents the resulting breakup functions, which are critically examined before being used as input into classical trajectory calculations to predict the contribution of breakup to above-barrier complete fusion suppression in reactions of ^{7}Li with ^{27}Al, ^{28}Si and ^{58}Ni as well as ^{9}Be with ^{27}Al, ^{28}Si, ^{144}Sm, ^{168}Er, ^{186}W, ^{196}Pt, ^{208}Pb and ^{209}Bi.

Chapter 8 assesses the feasibility of leveraging the measurement and kinematic reconstruction techniques developed in the course of this thesis to measuring the astrophysically relevant ^{7}Be(d,p)^{8}Be reaction. Pilot measurements with the mirror reaction ^{7}Li(d,n)^{8}Be will be presented. In addition, the results of ^{7}Be beam production experiments will be shown.

Chapter 9 summarises the work of this thesis, with a focus on future directions.

References

1. Cockcroft, J.D., Walton, E.T.S.: Disintegration of lithium by swift protons. Nature **129**(3261), 649 (1932)
2. Cockcroft, J.D., Walton, E.T.S.: Artificial production of fast protons. Nature **129**(3250), 242 (1932)
3. Dasgupta, M., Gomes, P.R.S., Hinde, D.J., Moraes, S.B., Anjos, R.M., Berriman, A.C., Butt, R.D., Carlin, N., Lubian, J., Morton, C.R., Szanto de Toledo, A.: Effect of breakup on the fusion of ^{6}Li,^{7}Li, and ^{9}Be with heavy nuclei. Phys. Rev. C **70**(2), 024606 (2004)

4. Dasgupta, M., Hinde, D.J., Butt, R.D., Anjos, R.M., Berriman, A., Carlin, N., Gomes, P.R.S., Morton, C.R., Newton, J.O., Szanto de Toledo, A., Hagino, K.: Fusion versus breakup: observation of large fusion suppression for ^{9}Be+ ^{208}Pb. Phys. Rev. Lett. **82**(7), 1395 (1999)
5. Signorini, C., Glodariu, T., Liu, Z.H., Mazzocco, M., Ruan, M., Soramel, F.: Breakup processes in the systems ^{9}Be+^{208}Pb,^{209}Bi and ^{6}Li + ^{208}Pb around the Coulomb barrier. Prog. Theor. Phys. Suppl. **154**, 272 (2004)
6. Dasgupta, M., Hinde, D.J., Sheehy, S.L., Bouriquet, B.: Suppression of fusion by breakup: resolving the discrepancy between the reactions of ^{9}Be with ^{208}Pb and ^{209}Bi. Phys. Rev. C **81**(2), 024608 (2010)
7. Dasgupta, M., Hinde, D., Hagino, K., Moraes, S.B., Gomes, P.R.S., Anjos, R.M., Butt, R.D., Berriman, A.C., Carlin, N., Morton, C.R., Newton, J.O., Szanto de Toledo, A.: Fusion and breakup in the reactions of ^{6}Li and ^{7}Li nuclei with ^{209}Bi. Phys. Rev. C **66**(4), 041602(R) (2002)
8. Rath, P.K., Santra, S., Singh, N.L., Tripathi, R., Parkar, V.V., Nayak, B.K., Mahata, K., Palit, R., Kumar, S., Mukherjee, S., Appannababu, S., Choudhury, R.K.: Suppression of complete fusion in the ^{6}Li + ^{144}Sm reaction. Phys. Rev. C **79**(5), 051601 (2009)
9. Signorini, C., Liu, Z., Li, Z., Löbner, K., Müller, L., Ruan, M., Rudolph, K., Soramel, F., Zotti, C., Andrighetto, A., Stroe, L., Vitturi, A., Zhang, H.: Does break-up affect ^{9}Be + ^{209}Bi fusion at the barrier? Eur. Phys. J. A **5**, 7 (1999)
10. Tripathi, V., Navin, A., Mahata, K., Ramachandran, K., Chatterjee, A., Kailas, S.: Angular momentum and cross sections for fusion with weakly bound nuclei: breakup, a coherent effect. Phys. Rev. Lett. **88**(17), 172701 (2002)
11. Wu, Y.W., Liu, Z.H., Lin, C.J., Zhang, H.Q., Ruan, M., Yang, F., Li, Z.C., Trotta, M., Hagino, K.: Near barrier fusion excitation function of ^{6}Li + ^{208}Pb. Phys. Rev. C **68**(4), 044605 (2003)
12. Gomes, P.R.S., Padron, I., Crema, E., Capurro, O.A., Fernández Niello, J.O., Arazi, A., Martí, G.V., Lubian, J., Trotta, M., Pacheco, A.J., Testoni, J.E., Rodríguez, M.D., Ortega, M.E., Chamon, L.C., Anjos, R.M., Veiga, R., Dasgupta, M., Hinde, D.J., Hagino, K.: Comprehensive study of reaction mechanisms for the ^{9}Be+^{144}Sm system at near- and sub-barrier energies. Phys. Rev. C **73**(6), 064606 (2006)
13. Palshetkar, C.S., Santra, S., Chatterjee, A., Ramachandran, K., Thakur, S., Pandit, S.K., Mahata, K., Shrivastava, A., Parkar, V.V., Nanal, V.: Fusion of the weakly bound projectile ^{9}Be with ^{89}Y. Phys. Rev. C **82**(4), 044608 (2010)
14. Parkar, V.V., Palit, R., Sharma, S.K., Naidu, B.S., Santra, S., Joshi, P.K., Rath, P.K., Mahata, K., Ramachandran, K., Trivedi, T., Raghav, A.: Fusion cross sections for the ^{9}Be+^{124}Sn reaction at energies near the Coulomb barrier. Phys. Rev. C **82**(5), 054601 (2010)
15. Fang, Y.D., Gomes, P.R.S., Lubian, J., Zhou, X.H., Zhang, Y.H., Han, J.L., Liu, M.L., Zheng, Y., Guo, S., Wang, J.G., Qiang, Y.H., Wang, Z.G., Wu, X.G., He, C.Y., Li, C.B., Hu, S.P., Yao, S.H.: Fusion and one-neutron stripping reactions in the ^{9}Be+^{186}W system above the Coulomb barrier. Phys. Rev. C **87**(2), 024604 (2013)
16. Shaikh, M.M., Roy, S., Rajbanshi, S., Pradhan, M.K., Mukherjee, A., Basu, P., Pal, S., Nanal, V., Pillay, R.G., Shrivastava, A.: Investigation of ^{6}Li + ^{64}Ni fusion at near-barrier energies. Phys. Rev. C **90**(2), 024615 (2014)
17. Zhang, N.T., Fang, Y.D., Gomes, P.R.S., Lubian, J., Liu, M.L., Zhou, X.H., Li, G.S., Wang, J.G., Guo, S., Qiang, Y.H., Zhang, Y.H., Mendes Junior, D.R., Zheng, Y., Lei, X.G., Gao, B.S., Wang, Z.G., Wang, K.L., He, X.F.: Complete and incomplete fusion in the ^{9}Be + ^{181}Ta reaction. Phys. Rev. C **90**(2), 024621 (2014)
18. Hu, S.P., Zhang, G.L., Yang, J.C., Zhang, H.Q., Gomes, P.R.S., Lubian, J., Wu, X.G., Zhong, J., He, C.Y., Zheng, Y., Li, C.B., Li, G.S., Qu, W.W., Wang, F., Zheng, L., Yu, L., Chen, Q.M., Luo, P.W., Li, H.W., Wu, Y.H., Zhou, W.K., Zhu, B.J., Sun, H.B.: Small suppression of the complete fusion of the ^{6}Li + ^{96}Zr system at near-barrier energies. Phys. Rev. C - Nucl. Phys. **91**(4), 044619 (2015)
19. Fang, Y.D., Gomes, P.R.S., Lubian, J., Liu, M.L., Zhou, X.H., Mendes Junior, D.R., Zhang, N.T., Zhang, Y.H., Li, G.S., Wang, J.G., Guo, S., Qiang, Y.H., Gao, B.S., Zheng, Y., Lei, X.G., Wang, Z.G.: Complete and incomplete fusion of ^{9}Be + ^{169}Tm, ^{187}Re at near-barrier energies. Phys. Rev. C **91**(1), 014608 (2015)

20. Mukherjee, A., Subinit, R., Pradhan, M., Saha Sarkar, M., Basu, P., Dasmahapatra, B., Bhattacharya, T., Bhattacharya, S., Basu, S., Chatterjee, A., Tripathi, V., Kailas, S.: Influence of projectile α-breakup threshold on complete fusion. Phys. Lett. B **636**(2), 91 (2006)
21. Gasques, L.R., Hinde, D.J., Dasgupta, M., Mukherjee, A., Thomas, R.G.: Suppression of complete fusion due to breakup in the reactions ^{10,11}B+^{209}Bi. Phys. Rev. C **79**(3), 034605 (2009)
22. Canto, L., Gomes, P.R.S., Donangelo, R., Hussein, M.: Fusion and breakup of weakly bound nuclei. Phys. Rep. **424**, 1 (2006)
23. Canto, L., Gomes, P.R.S., Donangelo, R., Lubian, J., Hussein, M.: Recent developments in fusion and direct reactions with weakly bound nuclei. Phys. Rep. **596**, 1 (2015)
24. Hinde, D.J., Dasgupta, M., Fulton, B., Morton, C., Wooliscroft, R., Berriman, A., Hagino, K.: Fusion suppression and sub-barrier breakup of weakly bound nuclei. Phys. Rev. Lett. **89**(27), 7 (2002)
25. Rafiei, R., du Rietz, R., Luong, D.H., Hinde, D.J., Dasgupta, M., Evers, M., Diaz-torres, A.: Mechanisms and systematics of breakup in reactions of ^{9}Be at near-barrier energies. Phys. Rev. C **81**(2), 024601 (2010)
26. Luong, D.H., Dasgupta, M., Hinde, D.J., Du Rietz, R., Rafiei, R., Lin, C.J., Evers, M., Diaz-torres, A.: Insights into the mechanisms and time-scales of breakup of ^{6,7}Li. Phys. Lett. B **695**, 105 (2011)
27. Luong, D.H.: Mechanisms and time-scales in breakup of ^{6,7} Li. Ph.D. thesis, Australian National University (2012)
28. Luong, D.H., Dasgupta, M., Hinde, D.J., du Rietz, R., Rafiei, R., Lin, C.J., Evers, M., Diaz-Torres, A.: Predominance of transfer in triggering breakup in sub-barrier reactions of ^{6,7}Li. Phys. Rev. C **88**(3), 34609 (2013)
29. Häusser, O., McDonald, A.B., Alexander, T.K., Ferguson, A.J., Warner, R.E.: Nuclear polarizability of ^{7}Li from Coulomb excitation. Phys. Lett. B **38**(2), 75 (1972)
30. Ost, R., Speth, E., Pfeiffer, K.O., Bethge, K.: Coulomb breakup of ^{6}Li. Phys. Rev. C **5**(6), 1835 (1972)
31. Ost, R., Bethge, K., Gemmeke, H., Lassen, L., Scholz, D.: Three-particle correlations from ^{208}Pb + ^{6}Li. Z. Phys. **266**, 369 (1974)
32. Québert, J.L., Frois, B., Marquez, L., Sousbie, G., Ost, R., Bethge, K., Gruber, G.: Search for ^{7}Li breakup in ^{7}Li + ^{197}Au near grazing incidence. Phys. Rev. Lett. **32**(20), 1136 (1974)
33. Tilley, D.R., Kelley, J.H., Godwin, J.L., Millener, D.J., Purcell, J.E., Sheu, C.G., Weller, H.R.: Energy levels of light nuclei A = 8,9,10. Nucl. Phys. A **745**, 155 (2004)
34. Tilley, D., Cheves, C., Godwin, J., Hale, G., Hofmann, H., Kelley, J., Sheu, C., Weller, H.: Energy levels of light nuclei A = 5,6,7. Nucl. Phys. A **708**, 3 (2002)
35. Barker, F.C., Treacy, P.B.: Nuclear levels near thresholds. Nucl. Phys. **38**, 33 (1962)
36. Barker, F.C.: Consistent description of unbound states observed in scattering and reactions. Aust. J. Phys. **41**, 743 (1988)
37. Diaz-Torres, A., Hinde, D.J., Tostevin, J.A., Dasgupta, M., Gasques, L.R.: Relating breakup and incomplete fusion of weakly bound nuclei through a classical trajectory model with stochastic breakup. Phys. Rev. Lett. **98**(15), 152701 (2007)
38. Diaz-Torres, A.: PLATYPUS: a code for reaction dynamics of weakly-bound nuclei at near-barrier energies within a classical dynamical model. Comput. Phys. Commun. **182**(4), 1100 (2011)
39. Simpson, E.C., Cook, K.J., Luong, D.H., Kalkal, S., Carter, I.P., Dasgupta, M., Hinde, D.J., Williams, E.: Disintegration locations in ^{7}Li$\rightarrow$ ^{8}Be transfer-triggered breakup at near-barrier energies. Phys. Rev. C **93**(2), 024605 (2016)
40. Asplund, M., Lambert, D.L., Nissen, P.E., Primas, F., Smith, V.V.: Lithium isotopic abundances in metal-poor halo stars. Astrophys. J. **644**, 229 (2006)
41. Fields, B.: The primordial lithium problem. Annu. Rev. Nucl. Part. Sci. **61**, 47 (2011)
42. Spite, F., Spite, M.: Abundance of lithium in unevolved halo stars and old disk stars: interpretation and consequences. Astron. Astrophys. **115**, 357 (1982)
43. Korn, A.J., Grundahl, F., Richard, O., Barklem, P.S., Mashonkina, L., Collet, R., Piskunov, N., Gustafsson, B.: A probable stellar solution to the cosmological lithium discrepancy. Nature **442**, 657 (2006)

44. Howk, J.C., Lehner, N., Fields, B., Mathews, G.J.: Observation of interstellar lithium in the low-metallicity Small Magellanic Cloud. Nature **489**, 121 (2012)
45. Regis, M., Clarkson, C.: Do primordial lithium abundances imply there's no dark energy? Gen. Relativ. Gravit. **44**(3), 567 (2012)
46. Coc, A., Goriely, S., Xu, Y., Saimpert, M., Vangioni, E.: Standard Big Bang Nucleosynthesis up to CNO with an improved nuclear network. Astrophys. J. **744**(2), 158 (2012)
47. Coc, A., Uzan, J., Vangioni, E.: Mirror matter can alleviate the cosmological lithium problem. Phys. Rev. D **87**(12), 123530 (2013)
48. Salvati, L., Pagano, L., Lattanzi, M., Gerbino, M., Melchiorri, A.: Breaking Be: a sterile neutrino solution to the cosmological lithium problem. J. Cosmol. Astropart. Phys. **08**, 022 (2016)
49. Vasquez, D.A., Belikov, A., Coc, A., Silk, J., Vangioni, E.: Neutron injection during primordial nucleosynthesis alleviates the primoridal ^{7}Li Problem. Phys. Rev. D **86**(6), 063501 (2012)
50. Broggini, C., Canton, L., Fiorentini, G., Villante, F.L.: The cosmological ^{7}Li problem from a nuclear physics perspective. J. Cosmol. Astropart. Phys. **06**, 030 (2012)
51. Cyburt, R.H., Pospelov, M.: Resonant enhancement of nuclear reactions as a possible solution to the cosmological lithium problem. Int. J. Mod. Phys. E **21**(01), 1250004 (2012)
52. Kirsebom, O., Davids, B.: One fewer solution to the cosmological lithium problem. Phys. Rev. C **84**(5), 058801 (2011)
53. Barbagallo, M., Musumarra, A., Cosentino, L., Maugeri, E., Heinitz, S., Mengoni, A., Dressler, R., Schumann, D., Käppeler, F., Colonna, N., Finocchiaro, P., Ayranov, M., Damone, L., Kivel, N., Aberle, O., Altstadt, S., Andrzejewski, J., Audouin, L., Bacak, M., Balibrea-Correa, J., Barros, S., Bécares, V., Bečvář, F., Beinrucker, C., Berthoumieux, E., Billowes, J., Bosnar, D., Brugger, M., Caamaño, M., Calviani, M., Calviño, F., Cano-Ott, D., Cardella, R., Casanovas, A., Castelluccio, D.M., Cerutti, F., Chen, Y.H., Chiaveri, E., Cortés, G., Cortés-Giraldo, M.A., Cristallo, S., Diakaki, M., Domingo-Pardo, C., Dupont, E., Duran, I., Fernandez-Dominguez, B., Ferrari, A., Ferreira, P., Furman, W., Ganesan, S., García-Rios, A., Gawlik, A., Glodariu, T., Göbel, K., Gonçalves, I.F., González-Romero, E., Griesmayer, E., Guerrero, C., Gunsing, F., Harada, H., Heftrich, T., Heyse, J., Jenkins, D.G., Jericha, E., Katabuchi, T., Kavrigin, P., Kimura, A., Kokkoris, M., Krtička, M., Leal-Cidoncha, E., Lerendegui, J., Lederer, C., Leeb, H.: Lo, Meo S., Lonsdale, S.J., Losito, R., Macina, D., Marganiec, J., Martínez, T., Massimi, C., Mastinu, P., Mastromarco, M., Mazzone, A., Mendoza, E., Milazzo, P.M., Mingrone, F., Mirea, M., Montesano, S., Nolte, R., Oprea, A., Pappalardo, A., Patronis, N., Pavlik, A., Perkowski, J., Piscopo, M., Plompen, A., Porras, I., Praena, J., Quesada, J., Rajeev, K., Rauscher, T., Reifarth, R., Riego-Perez, A., Rout, P., Rubbia, C., Ryan, J., Sabate-Gilarte, M., Saxena, A., Schillebeeckx, P., Schmidt, S., Sedyshev, P., Smith, A.G., Stamatopoulos, A., Tagliente, G., Tain, J.L., Tarifeño-Saldivia, A., Tassan-Got, L., Tsinganis, A., Valenta, S., Vannini, G., Variale, V., Vaz, P., Ventura, A., Vlachoudis, V., Vlastou, R., Vollaire, J., Wallner, A., Warren, S., Weigand, M., Weiß, C., Wolf, C., Woods, P.J., Wright, T., Žugec, P.: ^{7}Be$(n,\alpha)^4$He reaction and the cosmological lithium problem: measurement of the cross section in a wide energy range at n_TOF at CERN. Phys. Rev. Lett. **117**(15), 152701 (2016)
54. Coc, A., Vangioni-Flam, E., Descouvemont, P., Adahchour, A., Angulo, C.: Updated big bang nucleosynthesis compared with known Wilkinson microwave anisotropy probe observations and the abundance of light elements. Astrophys. J. **600**, 544 (2004)
55. Cyburt, R.H., Fields, B., Olive, K.A.: Solar neutrino constraints on the BBN production of Li. Phys. Rev. D **69**(12), 123519 (2004)
56. Gyurky, G., Confortola, F., Costantini, H., Formicola, A., Bemmerer, D., Bonetti, R., Broggini, C., Corvisiero, P., Elekes, Z., Zs, F., Laubenstein, M., Lemut, A., Limata, B., Lozza, V., Marta, M., Menegazzo, R., Prati, P., Roca, V., Rolfs, C., Alvarez, C.R., Somorjai, E., Straniero, O., Strieder, F., Terrasi, F., Trautvetter, H.P.: ^{3}He$(\alpha,\gamma)^7$Be cross section at low energies. Phys. Rev. C **75**(3), 035805 (2007)
57. Parker, P.D.: Comments on the destruction of ^{7}Be in the solar interior. Astrophys. J. **175**, 261 (1972)
58. Angulo, C., Casarejos, E., Couder, M., Demaret, P., Leleux, P., Vanderbist, F., Coc, A., Kiener, J., Tatischeff, V., Davinson, T., Murphy, A., Achouri, N., Orr, N., Cortina-Gil, D., Figuerra, P.,

Fulton, B., Mukha, I., Vangioni, E.: The ^{7}Be(d, p)2α cross section at Big Bang energies and the primordial ^{7}Li abundance. Astrophys. J. Lett. **630**(2), 105 (2005)
59. Rafiei, R., Hinde, D.J., Dasgupta, M., Weisser, D.C., Muirhead, A.G., Harding, A.B., Cooper, A.K., Wallace, H.J., Lobanov, N.R., Wakhle, A., Brown, M.L., Lin, C.J., Horsley, A.J., Du Rietz, R., Luong, D.H., Evers, M.: SOLEROO: A solenoidal exotic rare isotope separator at the Australian National University. Nucl. Instrum. Methods Phys. Res. A **631**(1), 12 (2011)
60. Carter, I.P., Ramachandran, K., Dasgupta, M., Hinde, D.J., Rafiei, R., Luong, D.H., Williams, E., Cook, K.J., McNeil, S., Rafferty, D.C., Harding, A.B., Muirhead, A.G., Tunningley, T.: An ion beam tracking system based on a parallel plate avalanche counter. EPJ Web Conf. **63**, 02022 (2013)
61. Carter, I.P., Dasgupta, M., Hinde, D.J., Luong, D.H., Williams, E., Ramachandran, K., Cook, K.J., Muirhead, A.G., Marshall, S., Tunningley, T.: Recent developments of SOLEROO: Australia's first high energy radioactive Ion Beam capability. EPJ Web Conf. **91**, 00001 (2015)

Chapter 2
Background Concepts

To me, what makes physics physics is that experiment is intimately connected to theory. It's one whole

Lene Hau 1959

The fact that complete fusion cross-sections of light, weakly-bound nuclei are suppressed relative to well bound nuclei forming the same compound system demonstrates that, while nuclear reactions and nuclear structure are typically considered distinct fields of study, the two cannot be readily separated. If nuclear structure had no influence on the outcome of nuclear reactions, then renormalised complete fusion cross-sections forming the same compound nucleus would not change whether or not weakly-bound nuclei were involved. Therefore, in this chapter, the key concepts in nuclear structure and reactions required for this thesis will be outlined.

Fundamentally, nuclear structure is the study of quantum states that arise from finite collections of quarks and gluons while nuclear reactions is the study of the dynamics of colliding collections of quarks and gluons. It is not yet possible to consider nuclei at the level of quarks and gluons for either structure or reactions. Instead, microscopic models treat nucleons as structureless particles. To look at the broad features of nuclear reactions, it is even possible to take a step further back, and consider nuclei as single entities. At this level, to first order, nuclear reactions can be understood through their mutual (nucleus-nucleus) potential.

2.1 Nucleus-Nucleus Potentials

Only two fundamental forces[1] are relevant for nucleus-nucleus interactions – the electromagnetic and strong nuclear interactions. Therefore, the total nucleus-nucleus potential is the sum of the electromagnetic (Coulomb) and nuclear potentials, V_C and

[1] With rare exception.

K. J. Cook, *Zeptosecond Dynamics of Transfer-Triggered Breakup*,
Springer Theses, https://doi.org/10.1007/978-3-319-96017-3_2

V_N, respectively. The Coulomb potential is typically modelled using the repulsive potential between a positively charged finite sphere of radius $R_c = 1.2(A_P^{1/3} + A_T^{1/3})$ and a positive point charge:

$$V_C(r) = \begin{cases} \frac{Z_P Z_T e^2}{4\pi\epsilon_0 r} & r \leq R_c \\ \frac{Z_P Z_T e^2}{4\pi\epsilon_0} \frac{3R_c^2 - r^2}{2R_c^3} & r > R_c \end{cases} \tag{2.1}$$

where Z_P, Z_T and A_P, A_T are the charges and mass numbers of each nucleus, respectively. The Coulomb potential for ^{9}Be + ^{208}Pb is shown by the green line in Fig. 2.1a.

The short range attractive internuclear potential V_N is due to the nuclear force between the protons and neutrons inside the nucleus. As these forces arise from quantum chromodynamics (QCD), it is not possible to calculate the internuclear potential exactly. Instead, phenomenological methods are often used, where parameters are fit to experimental data. The phenomenological potential used throughout this work is the São Paulo Potential (SPP) [1], a density dependent double-folding potential, which depends on the densities of the nuclei, with an energy dependent correction arising from Pauli non-locality. It is given by:

$$V_N(\mathcal{R}, E) = e^{\frac{-4v^2}{c^2}} \int \rho_1(\vec{r}_1)\rho_2(\vec{r}_2)v_{nn}(\vec{\mathcal{R}} - \vec{r}_1 + \vec{r}_2)d\vec{r}_1 d\vec{r}_2, \tag{2.2}$$

where v the local relative velocity between the two nuclei, $\rho_i(\vec{r}_i)$ are the density distributions of each nucleus, $\mathcal{R}$ the distance between their centres, and v_{nn} the effective nucleon-nucleon interaction. The nuclear densities were found by a systematic study of theoretical distributions from microscopic nuclear models, as well as a large set

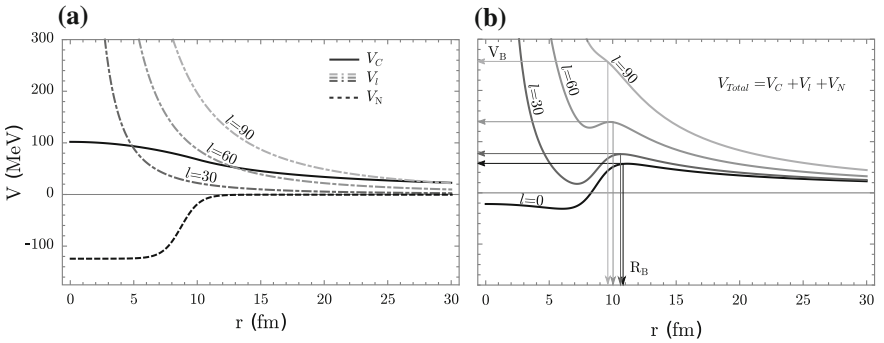

Fig. 2.1 The potential between two colliding nuclei arises from the sum of three components (**a**) a Coulomb interaction V_C (solid line), a nuclear term V_N (dashed line) and a centrifugal term V_l (dot-dashed lines) that arises due to the angular momenta of the colliding nuclei. Summed, these potentials form a potential barrier with energy V_B at radius R_B (**b**). As the angular momentum l increases, the barrier energy increases and the radius decreases (indicated by the arrows) as does the size of the potential pocket

of experimental distributions from elastic scattering measurements [1]. The effective nucleon-nucleon interaction is determined from the zero-range approach to the folding potential, which assumes that the range of ν_{nn} is negligible with respect to the diffuseness of the nuclear densities, and is then dependent only on the nuclear densities [1]. This potential has no free parameters, and is valid over a large energy range.

For convenience of later calculation and visualisation, in this thesis, the SPP potentials are fit with a Woods–Saxon form [2]:

$$V_N(r) = \frac{-V_0}{1 + e^{\frac{r-R_0}{a_0}}}. \tag{2.3}$$

Here, V_0 is the depth of the potential, R_0 a radius parameter and a_0 a diffuseness parameter. The fitting is performed over a range of ± 2 fm around the radius of the local maximum of the total internuclear potential R_B (which will be discussed in more detail shortly). A Woods–Saxon fit to a SPP calculation for ^{9}Be + ^{208}Pb is shown by the red curve in Fig. 2.1a, with $R_0 = 1.087 * (A_T^{1/3} + A_P^{1/3}) = 8.70$ fm and $a_0 = 0.726$ fm. Unlike the Coulomb potential, the nuclear potential is short-ranged, and only has an effect when the nuclei are close to touching.

Since both potentials are spherically symmetric, $V(r) = V_N(r) + V_C(r)$ only depends on r. It is therefore desirable to reduce the problem to one dimension. Consider the Hamiltonian

$$\hat{H} = \frac{-\hbar^2}{2\mu}\nabla^2 + V(r) \tag{2.4}$$

where $\mu = \frac{m_1 m_2}{m_1 + m_2}$ is the reduced mass of the system. Since $\hat{H}$ is spherically symmetric, it commutes with $\hat{\mathbf{l}}^2$ and $\hat{l}_z$, so the eigenfunctions ψ of $\hat{H}$ can be written as

$$\psi(r) = R(r)Y_{lm}(\theta, \phi), \tag{2.5}$$

where $Y_{lm}(\theta, \phi)$ are the usual spherical harmonics, and $R(r)$ is a function that depends only on r. To solve for $R(r)$, consider the Schrödinger equation

$$\hat{H}\psi(r) = E\psi(r) \tag{2.6}$$

The Laplacian in spherical coordinates is given by

$$\nabla^2 = \frac{1}{r^2}\frac{\partial}{\partial r}\left(r^2\frac{\partial}{\partial r}\right) - \frac{\hat{\mathbf{l}}^2}{r^2}. \tag{2.7}$$

Recalling that eigenstates of $\hat{\mathbf{l}}^2$ are also eigenstates of $\hat{H}$, one obtains

$$\left(\frac{-\hbar^2}{2\mu}\left(\frac{1}{r^2}\frac{\partial}{\partial r}\left(r^2\frac{\partial}{\partial r}\right) - \frac{l(l+1)}{r^2}\right) + V(r) - E\right)R(r) = 0. \tag{2.8}$$

Introducing the substitution $R(r) = \frac{\epsilon(r)}{r}$, this expression becomes

$$-\frac{\hbar^2}{2\mu}\frac{\partial}{\partial r}\epsilon(r) + \left(\frac{\hbar^2 l(l+1)}{2\mu r^2} + V(r) - E\right)\epsilon(r) = 0, \tag{2.9}$$

which is identical to the one dimensional Schrödinger equation, with $V_T(r) = V(r) + \frac{\hbar^2 l(l+1)}{2\mu r^2}$. Thus, this l dependent term, known as the "centrifugal potential", acts as an additional effective repulsive potential that is dependent on the angular momentum of the colliding nuclei. Compared to low-energy nuclear structure, the angular momenta in heavy ion collisions can be rather large.

The centrifugal potential for ^{9}Be + ^{208}Pb $l = 30, 60, 90$ is shown by the dashed curves in Fig. 2.1a. The total one dimensional internuclear potential is the sum of the repulsive Coulomb and centrifugal potentials as well as the attractive nuclear potential, and can be written as

$$V_T(r) = V_C(r) + V_N(r) + V_l(r). \tag{2.10}$$

The total internuclear potential is shown for ^{9}Be + ^{208}Pb with $l = 0, 30, 60, 90$ in Fig. 2.1b. The sum of the nuclear and Coulomb potentials create a local maximum of V_B at $R_B \sim 10$ fm. This is called the "fusion barrier". At energies below V_B, nuclei must tunnel through this barrier before entering the pocket in the potential and fusing. As nuclei collide with increasing angular momentum, the energy of the barrier increases, and the radius at which it occurs moves inwards. Due to this, the nuclear processes that can occur depend on the energies and angular momenta of the colliding nuclei.

2.2 Reaction Outcomes

As nuclei collide, they interact through their mutual internuclear potential, and the potential encountered depends on the energy and angular momentum with which they collide. A useful way of parameterising this is through the "impact parameter" $b = \frac{l}{\sqrt{2\mu E}}$ (with units of length), defined as the perpendicular distance (shown in Fig. 2.2) between the centres of the colliding nuclei at infinity. Nuclei colliding with smaller b (due to larger E or smaller l) will approach closer to each other than a collision with larger b (with smaller E or larger l). A nuclear interaction with a given b will experience different regions of the internuclear potential shown in Fig. 2.1 as the nuclei approach and recede. Therefore different reaction outcomes can occur, depending on b, illustrated in Fig. 2.2, and will be described briefly next.

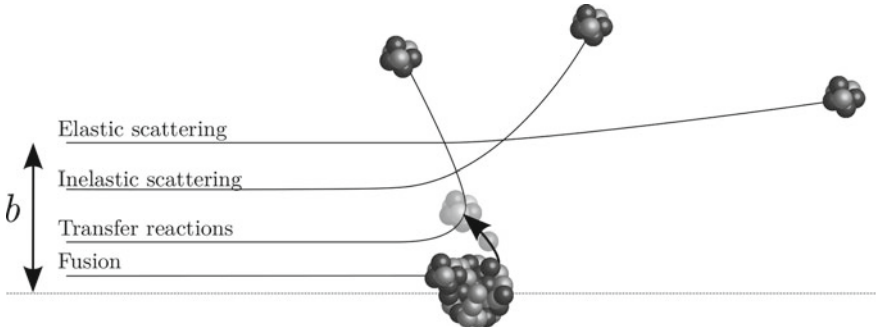

Fig. 2.2 Nuclei that collide with different impact parameters b result in different reaction outcomes. Nuclei that approach at large distances will only interact with the Coulomb part of the potential, and elastically scatter. Nuclei with slightly smaller b may excite an internal state, leading to inelastic scattering. Nuclei that approach close enough to interact through the nuclear potential may undergo a reaction such as transfer. At even smaller impact parameters, the nuclei may experience processes such as fusion

2.2.1 Elastic Scattering

At the largest b, the distance of closest approach of the nuclei, R_{min}, is large, and the nuclei will only interact via the long-range Coulomb potential. In reactions such as these, only elastic scattering can occur, wherein the nuclei change their direction of propagation, but the total kinetic energy of the system remains unchanged.

2.2.2 Inelastic Scattering

At a smaller b the gradient of the interaction potential may be sufficiently large so as to enable either nucleus to excite one of their low-lying internal states. This changes the total kinetic energy of the system, as some kinetic energy is converted into internal excitation. This is known as "inelastic scattering". In this process, weakly-bound nuclei, such as ^{7}Li, ^{9}Be may be excited above their breakup thresholds–the energy required to break the nuclei into their cluster constituents $^{7}\text{Li} \rightarrow \alpha + t$, $^{9}\text{Be} \rightarrow \alpha + \alpha + n$ – in a process known as "direct breakup". Inelastic processes can occur via Coulomb and nuclear interactions.

2.2.3 Transfer and Breakup

Transfer and breakup reactions are a class of direct (or peripheral) reactions and begin to occur at smaller b than that of elastic or inelastic scattering. In these collisions, the

nuclei interact through the nuclear force and may exchange one or more nucleons. These reactions, where few nucleons participate, occur on very short timescales of $\sim 10^{-22}$ s, the typical time taken for a nucleon to travel across the nucleus. In these collisions, one or more nucleons may be transferred from the projectile to the target in a stripping reaction. The reverse, where one or more nucleons are transferred from the target to the projectile, is known as a pickup reaction. In reactions with light, weakly-bound nuclei, such as ^{7}Li and ^{9}Be, transfer reactions may populate neighbouring nuclei in states above their threshold for breakup into their cluster constituents. For instance, proton pickup in reactions with ^{7}Li will form ^{8}Be which is unbound and decays into alpha clusters, $^{8}\text{Be} \rightarrow \alpha + \alpha$. In this thesis, this process will be referred to as "transfer-triggered breakup". Transfer-triggered breakup is a two-step process–a peripheral collision results in nucleon transfer with the resulting nucleus being in an unbound state, which then decays (breaks up). It is this process that is the focus of this work.

2.2.4 Incomplete Fusion

Breakup can be followed by incomplete fusion (ICF), the partial capture of the charge of the projectile. In this thesis, no distinction is made between the capture of a breakup fragment and a reaction where, in one step, the projectile transfers the same charge to the target (massive transfer). Indeed, it is not clear if a clean distinction can be made.

If breakup occurs as the nuclei approach each other (on the incoming trajectory), with enough energy and small enough l, there is a chance that one of the breakup fragments can pass the fusion barrier and be captured, forming a combined nucleus. Transfer triggered breakup followed by capture is thus a three-step process. Breakup followed by capture is essentially indistinguishable from transfer forming the same compound nucleus. Nevertheless, ICF is defined in experiments as capture of part of the charge of the projectile (e.g. [3]).

2.2.5 Complete Fusion

At the smaller b, complete fusion (CF) can occur. The nuclei can pass inside their mutual barrier, be captured within the potential pocket forming an equilibrated, new nucleus, called the compound nucleus (CN), which is highly excited (or hot). The nucleus can de-excite by fission, forming two fission fragments, or it may de-excite via emission of particles leaving an evaporation residue. Heavy compound nuclei will emit neutrons, and light compound nuclei will emit neutrons as well as charged particles. Breakup (transfer-triggered or otherwise) followed by capture of *both* fragments is indistinguishable from complete fusion of the unbroken projectile.

CF is defined experimentally as the capture of the total charge of the projectile. In light systems, where charged particles are evaporated, it is extremely challenging to distinguish CF from ICF and transfer, though there are models [4] that attempt to quantify the probability of charged particle evaporation. Another related quantity is often introduced: Total Fusion (TF), the sum of complete and incomplete fusion, which is more readily measured in experiments performed with light systems.

It is important to note that as new reaction outcomes emerge with decreasing b, the reactions that could occur at larger b do not cease. For instance, elastic scattering will occur for all b. As a result, different reaction outcomes influence each other. For example, fusion reduces the flux in elastic scattering channels. This fact is a crucial concept in this thesis. Breakup that occurs as the nuclei approach each other will reduce the probability of complete charge capture, and increase the probability of incomplete charge capture. Understanding the contribution of breakup to incomplete fusion is a key goal of this thesis and can be quantified by use of the cross-section.

2.3 Cross-Sections

The cross-section characterises the probability of a given reaction to occur. When a beam of intensity I_{beam} particles per unit time is incident on a target with N_{target} nuclei per unit area, the number of reactions that occur each unit time Y_{reaction} and the cross-section σ is related through the expression:

$$\sigma = \frac{Y_{\text{reaction}}}{I_{\text{beam}} N_{\text{target}}}, \tag{2.11}$$

which has units of area. The cross-section for scattering into a particular solid angle $\Delta\Omega = \sin\theta d\theta d\phi$ is called the differential cross-section, and is defined as

$$\frac{d\sigma}{d\Omega} = \frac{Y_{\text{reaction}}(\theta, \phi)}{I_{\text{beam}} N_{\text{target}} \Delta\Omega}. \tag{2.12}$$

2.3.1 Rutherford Scattering Cross-Sections

If colliding nuclei are not subject to the nuclear force, and if they do not experience Coulomb excitation, then the only possible reaction outcome is elastic scattering, or Rutherford scattering. In this case, the probability of a scattering with a particular scattering angle can be known exactly. The differential cross-section in the centre of mass frame is given by:

$$\frac{d\sigma_{\text{Rutherford}}}{d\Omega} = \left(\frac{Z_P Z_T e^2}{4\pi\epsilon_0}\right)^2 \frac{1}{E_{\text{CM}}^2} \frac{1}{16\sin^4\frac{\theta_{\text{CM}}}{2}} \tag{2.13}$$

where Z_i is the atomic number of each nucleus, E_{CM} their kinetic energy in the centre of mass frame, and θ_{CM} is the scattering angle in the centre of mass frame.

When the colliding nuclei have sufficient energy and small enough impact parameter (b) to experience the nuclear potential, the elastic scattering yield will deviate from Rutherford expectations. Therefore, $\frac{d\sigma_{\mathrm{elastic}}}{d\Omega}$ does not equal $\frac{d\sigma_{\mathrm{Rutherford}}}{d\Omega}$ in general. In Rutherford scattering, b and θ_{CM} are related by $b = \frac{D}{2}\cot\frac{\theta_{\mathrm{CM}}}{2}$, where $D = \frac{Z_P Z_T e^2}{4\pi\epsilon_0 E_{\mathrm{CM}}}$. So, the deviation between elastic and Rutherford cross-sections depends on θ_{CM}; at below-barrier energies and at the most forward angles, $\frac{d\sigma_{\mathrm{elastic}}}{d\Omega} = \frac{d\sigma_{\mathrm{Rutherford}}}{d\Omega}$. This fact can be exploited for normalisation of cross-sections for other reaction outcomes, as will be discussed in Chap. 6.

2.4 Importance of the Nuclear Structure of Light Weakly-Bound Nuclei

Rutherford scattering cross-sections do not depend on the internal structure of the colliding nuclei, but the same cannot be said for other reaction outcomes. As alluded to earlier, transfer-triggered breakup can suppress complete fusion cross-sections provided breakup occurs as the nuclei are approaching each other. Therefore, the probability of this process occurring depends on several properties of the colliding nuclei:

1. The projectile must transfer a nucleon to or from the target, leaving the target in a particular state. The probability of transfer into a given state depends on the structure of the colliding nuclei.
2. The transfer must leave the transfer product in an unbound state.
3. The unbound state must be short lived, otherwise at above-barrier energies, the transfer product will pass inside the fusion barrier before breakup can occur.

Due to these facts, the structure of light weakly-bound nuclei, as well as neighbouring nuclei populated during transfer, is crucial to the ability of breakup to suppress complete fusion. Some key features of light, weakly-bound nuclei will be briefly presented before addressing nuclear reaction dynamics in more detail.

2.5 Nuclear Structure of Light Weakly-Bound Nuclei

The structure of light nuclei show a remarkable amount of variation between neighbouring isotopes – more so than is seen in heavy nuclei. This can be seen in properties such as the half-life of each isotope. A portion of the nuclear chart for $0 \leq Z \leq 7$, coloured by the half-life of each isotope is shown in Fig. 2.3. Two features are readily apparent. Firstly, the half-lives of neighbouring nuclei change rapidly. The isotopes of Be provide a good example: ^{7}Be has a half-life of 53.2 days, ^{8}Be has a half-life of

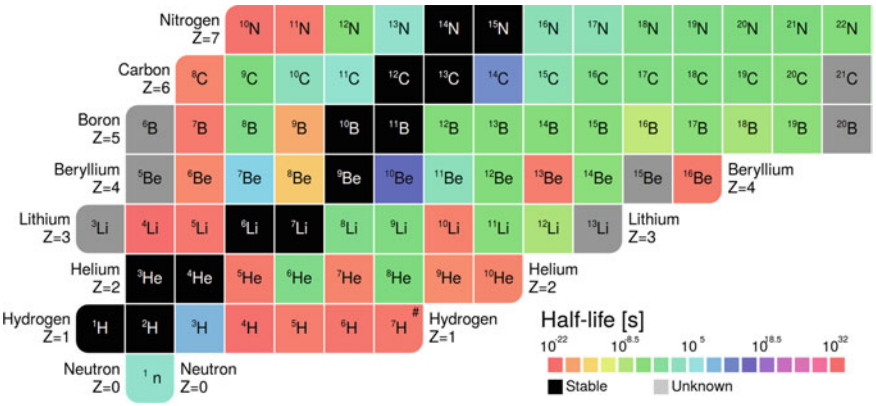

Fig. 2.3 Portion of the nuclear chart for $0 \leq Z \leq 7$, coloured by the half life of each isotope, an example of the large variance in nuclear properties for light nuclei. Figure created using the *Colourful Nuclear Chart* by E.C. Simpson [5]

$\sim 10^{-16}$ s, while ^{9}Be is stable. Secondly, some of these nuclei have an extremely short half life-on the order of $\sim 10^{-22}$ s, the same timescale as direct nuclear reactions.

The light nuclei of interest in this work are the beams, ^{7}Li and ^{9}Be, and the transfer products ^{5}Li, ^{6}Li and ^{8}Be. In particular, when the transfer products ^{5}Li, ^{6}Li and ^{8}Be are populated above their breakup threshold, these nuclei show a variety of different resonant structures.

2.5.1 Resonances

It is useful here to emphasise the difference between nuclear states and nuclear resonances. In stable nuclei, below any particle decay threshold, solutions to the Schrödinger equation are discrete, with specific spin, parity and energy–these are bound states. In contrast, above particle decay thresholds, the Schrödinger equation permits solutions at every energy. As a result, scattering processes (such as transfer) that populate nuclei above their particle decay thresholds should be expected to populate every excitation energy with some probability. Very briefly, the asymptotic solution to the Schrödinger equation

$$\frac{-\hbar^2}{2\mu}\nabla^2\psi + V(r)\psi = \frac{\hbar^2 k^2}{2\mu}\psi \tag{2.14}$$

for elastic scattering of a plane wave with wavenumber k and reduced mass μ from a central potential, $V(r)$, has the form

$$\psi(r,k) \cong N\left(e^{ikr\cos\theta} + f_k(\theta)\frac{e^{ikr}}{r}\right). \tag{2.15}$$

Which differs from the incoming plane wave by an outgoing spherical wave. f_k is known as the *scattering amplitude*, and the cross-section associated with this process is

$$\frac{d\sigma}{d\Omega} = |f_k(\theta)|^2. \tag{2.16}$$

Since the potential is central, as discussed in Sect. 2.1, it is possible to separate the wavefunction into radial and angular parts, and, after some work (for a more detailed discussion, see [6]) obtain an expression for the asymptotic wavefunction that is the sum of each angular momentum l

$$\psi(r,k) \cong N\sum_{l=0}^{\infty}(2l+1)i^l e^{i\delta_l(k)}\frac{\sin[kr - l\pi/2 + \delta_l(k)]}{kr}P_l(\cos\theta)$$

with scattering amplitude

$$f_k(\theta) = \frac{1}{k}\sum_{l=0}^{\infty}(2l+1)e^{i\delta_l(k)}\sin\delta_l(k)P_l\cos(\theta)$$

and total cross-section

$$\sigma = \frac{4\pi}{k^2}\sum_{l=0}^{\infty}(2l+1)\sin^2\delta_l(k).$$

Where $P_l(\cos\theta)$ are the usual Legendre polynomials, and $\delta_l(k)$ is the "scattering phase shift" for each l. The phase shift is a measure of the amount by which the phase of the radial part of the wave function for each l differs from the no scattering case, where $\delta_l(k) = 0$, and so is a measure of the strength of the scattering potential. Each ψ for a given l is known as a "partial wave", and the cross-section for populating an unbound nucleus to an excitation energy E can be expressed as the sum of partial waves for each l at E. In scattering measurements, peaks are observed in the scattering cross-section at certain energies E_{res}. These are called resonances, and correspond to rapid shifts in $\delta_l(E)$ of the form

$$\delta_l(E) = \delta_{bg}(E) + \arctan\left(\frac{\Gamma/2}{E_{res} - E}\right), \tag{2.17}$$

where $\delta_{bg}(E)$ is a background term that slowly varies with E [7], E_{res} is the resonance energy and Γ the width of the resonance. The propagation of the wavefunction at

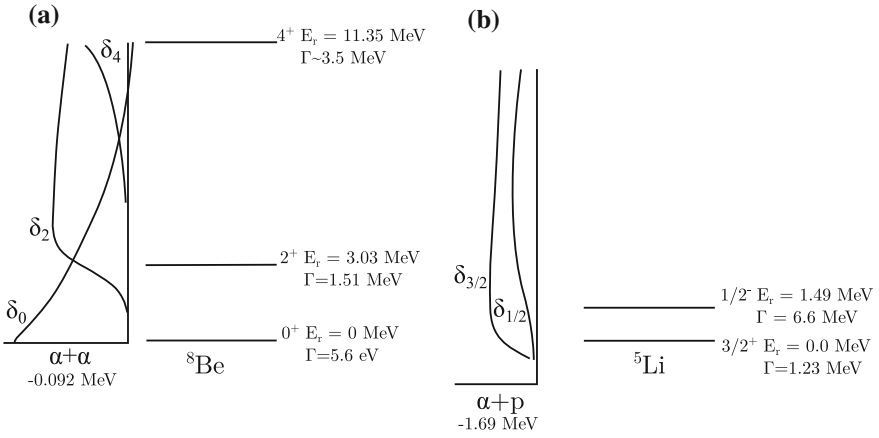

Fig. 2.4 Low excitation energy resonant structure of ^{8}Be and ^{5}Li along with the associated phase shifts. It should be noted that as an even-even nucleus, only even partial waves contribute to ^{8}Be, so the set of partial waves shown here is complete. The same cannot be said for ^{5}Li, and there remains the possibility of higher partial waves contributing in this region. Adapted from [8]

a resonant energy experiences a time delay of the order $\tau \sim \hbar/\Gamma$, leading to each resonant state having a lifetime τ at the resonant energy.

Shown in Fig. 2.4 are the phase shifts for $\alpha + \alpha$ scattering, with the corresponding low excitation energy resonant structure of ^{8}Be [8]. There are three resonances present: a narrow 0^+ resonance at 92 keV, a broad 2^+ (and so short-lived) resonance at 3.03 MeV, and a very broad 4^+ resonance at 11.35 MeV, and the corresponding phase shifts, δ_0, δ_2 and δ_4 show corresponding rapid changes at each energy.

It is tempting to think of these resonances as being isolated, analogous to bound nuclear states, especially as the resonant structure of unbound nuclei is usually shown diagrammatically in a similar way to that of the states of bound nuclei. However, the result of Eq. 2.17 obtained from scattering theory shows that *every* partial wave may contribute at *every* excitation energy. This is especially relevant in the case of broad resonances.

2.5.2 Excitation Energy Probability Distributions

In this thesis, classical models of breakup are used extensively, and will be introduced in detail in Sect. 2.9. These models take the excitation energy of the projectile-like nucleus as input. As has been discussed, modelling the excitation energy as a single on-resonance energy is inappropriate as excitation can occur at any energy above the particle decay threshold. Resonances are a peak in the probability of this excitation due to some structural feature of the nucleus, but where resonances are particularly

broad, as are seen in ^{5}Li and ^{8}Be, the peaks in probability are similarly smooth and broad.

In order to model breakup classically in a reasonably realistic way, it is useful to estimate the relative probability of populating a given excitation energy with a given partial wave. The excitation energy probability distributions $\rho_\ell(E)$ are estimated in the in the one-state, one-decay-channel limit of R-matrix theory[2] [9–11]. In this limit, the density of states function $\rho_\ell(E)$ is given by

$$\rho_\ell(E) \propto \frac{\Gamma_\ell(E)}{[E_{res} + \Delta_\ell(E) - E]^2 + [\frac{1}{2}\Gamma_\ell(E)]^2}. \tag{2.18}$$

ℓ is the angular momentum of the partial wave, $\Gamma_\ell(E)$ is the energy-dependent resonance width, and the level shift function is $\Delta_\ell(E) = S(E) - B$, where $S(E)$ is the shift factor [9], and B a constant set such that $\Delta_\ell(E)$ is zero at the resonance energy $E = E_{res}$.

The energy-dependent resonance width $\Gamma_\ell(E)$ can be determined from the reduced-width amplitude γ_ℓ^2 and the penetrability $P_\ell(E)$,

$$\Gamma_\ell(E) = 2P_\ell(E)\gamma_\ell^2. \tag{2.19}$$

In R-matrix models, γ_ℓ is related to the overlap integral of the internal compound nucleus state with the external outgoing wave functions over the dividing surface defined by the radius parameter R_n. R_n defines the division between the internal (pure nuclear) and external (pure Coulomb) regions, and depends on ℓ. Here, γ_ℓ was chosen as a parameter to match the experimentally observed on-resonance width, $\Gamma_\ell(E_{res})$, shown for ^{5}Li and ^{8}Be in Fig. 2.4, from the evaluation of Tilley et al. The penetrability was calculated from regular and irregular Coulomb wave functions at $R_n = 5$ fm for ^{8}Be and ^{6}Li, and $R_n = 2.9$ fm for ^{5}Li [8, 12]. Using γ_ℓ and $P_\ell(E)$, $\rho_\ell(E)$ was then calculated for all excitation energies, and the corresponding mean life estimated with

$$\tau(E) = \hbar/\,\Gamma_\ell(E). \tag{2.20}$$

Shown in Fig. 2.5 are the resulting excitation energy probability distributions (a), (b), (c) and excitation energy dependent mean lives (d), (e), (f) for the ^{8}Be 0^+, 2^+ and 4^+ states, the narrow ^{6}Li 3^+ resonance, and the ^{5}Li $\frac{3}{2}^-$ and $\frac{1}{2}^-$ states. For the case of ^{6}Li, the experimental data suggest (see Chap. 5) that some non-resonant breakup component is also present. The origin of this is not clear – it may be from population of non-resonant partial waves, or from breakup due to differential Coulomb forces ("tidal breakup") experienced by the α and d clusters that make up ^{6}Li in otherwise long-lived resonant states. A uniform probability for exciting ^{6}Li between 0.5 and 2.5 MeV above the threshold is assumed since the mechanism for populating this state is not clear. The reduced-width amplitude γ_ℓ is assumed to be equal to the Wigner

[2] A description of R-matrix theory in general is outside the scope of this work – a more detailed discussion can be found in [9].

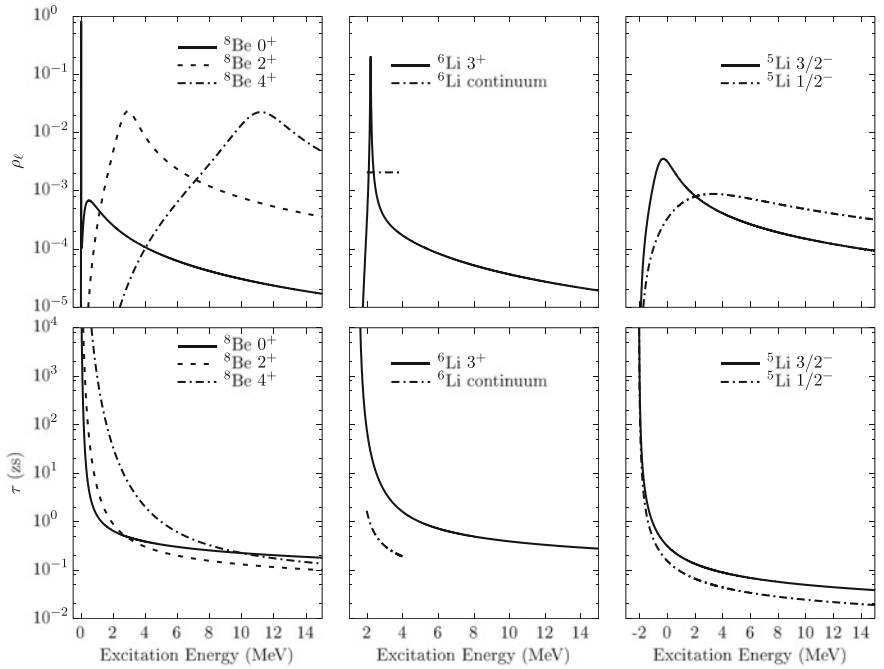

Fig. 2.5 Calculated excitation energy probability distributions for 0^+ (solid line), 2^+ (dashed line) and 4^+ (dot-dashed line) states in ^{8}Be (**a**), the 3^+ first excited state of ^{6}Li and the continuum (**b**), and the $\frac{3}{2}^-$ and $\frac{1}{2}^-$ ground and first resonances of ^{5}Li (**c**). The associated excitation energy dependent mean lives τ for each state are shown for ^{8}Be (**d**), ^{6}Li (**e**) and ^{5}Li (**f**). The zero of the excitation energy distributions correspond to the centroid of the ground-state of each nuclide. Negative excitation energies in the ^{5}Li distributions therefore result from the large width of these resonances

limit (i.e. be a pure single particle state) [9, 13, 14], giving

$$\Gamma_\ell(E) = 2P_l(E)\frac{\hbar^2}{\mu R_n^2}. \tag{2.21}$$

It is also assumed that the decay occurs quickly, and so choose $l = 0$, giving the maximum value for $\Gamma_\ell(E)$ and a corresponding lower limit for the lifetime, $\tau(E) = \hbar/\Gamma_\ell(E)$, which is shown in Fig. 2.5e, f).

2.5.2.1 Resonances Near Thresholds: "Ghost States"

An interesting feature arises in the probability distribution of excitation energies for the 0^+ state of ^{8}Be; as seen in Fig. 2.5a there is an additional maximum of probability at approximately 1 MeV, above the expected narrow resonance located 92 keV. This

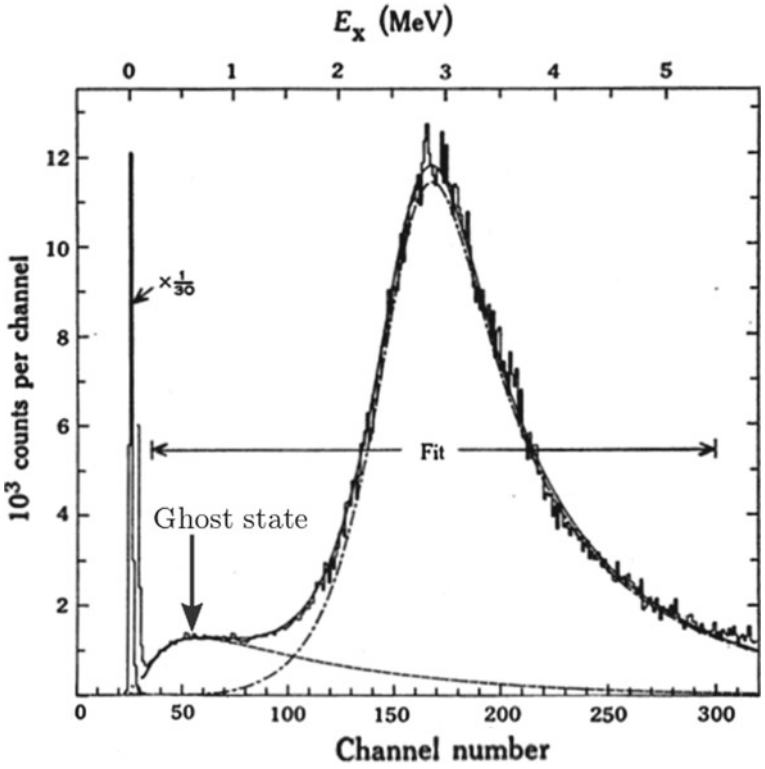

Fig. 2.6 Measured and calculated (with many-level R-matrix formalism for $l = 0$ and $l = 2$) spectrum of deuterons produced in the reaction ^{9}Be(p, d)^{8}Be, measured at a scattering angle of 10° with a proton beam energy of 39.91 MeV. The peak at $E \sim 0$ MeV corresponds to the ground state of ^{8}Be and the peak at $E \sim 3$ MeV corresponds to the first 2^+ resonance. There is an increase of events at $E \sim 0.6$ MeV, due to the proximity of the 0^+ resonance to the $\alpha + \alpha$ breakup threshold. This is a "ghost state". Reproduced from [15]

increase has been observed experimentally. A measured spectrum of deuterons from the reaction ^{9}Be(p, d)^{8}Be performed with a proton beam of energy 39.91 MeV [15] is shown in Fig. 2.6. There is an increase in the number of counts at about 0.6 MeV above the 92 keV ground state peak (marked by the red arrow) with an intensity of approximately 10% per MeV compared to the ground-state peak. This feature has been observed in a number of reactions, and is relatively independent of energy and angle [16, 17]. This "state" is not an independent resonance, but a result of the proximity of the 0^+ state to the breakup threshold, and is known as a *ghost state* [10, 11, 15]. The reason for the appearance of this ghost state can be seen from Eq. 2.18: near threshold, the numerator in Eq. 2.18 increases more rapidly than the denominator, as the penetrability factor $P_\ell(E)$ changes rapidly near threshold. As a result, there is an increase in $\rho_\ell(E)$ above the 0^+ resonance.

2.5.3 Clustering

^{7}Li and ^{9}Be are described as "weakly-bound nuclei" as they have a low energy threshold E_{thr} to breakup into their *cluster constituents*:

$$^{9}\text{Be} \rightarrow \alpha + \alpha + n \qquad E_{\text{thr}} = 1.572\,\text{MeV}$$
$$^{7}\text{Li} \rightarrow \alpha + t \qquad E_{\text{thr}} = 2.47\,\text{MeV}$$

Rather than treat these nuclei using the shell model of nuclear structure, it has proven fruitful in terms of both structure (e.g. [18–23]) and reactions (e.g. [24]) to describe these nuclei (and others, e.g. ^{6}Li, ^{8}Be, ^{12}C, ^{16}O) as having an internal cluster structure composed of α particles and valence nucleons. This idea was pioneered early in the history of nuclear physics by Hafstad and Teller [25], and is driven by the fact that α particles are extremely well bound. Indeed, quantum Monte-Carlo simulations of ^{8}Be indicate that its ground and first two excited states can be well described by two α particles [23]. Similarly, calculations of ^{9}Be indicate that it has a molecular $\alpha + n + \alpha$ structure, with the neutron acting in analogy with a covalent bond. The neutron is exchanged between the two α particles, providing extra binding energy, making ^{9}Be stable, where ^{8}Be is not [20–22]. Similarly, the first few excited states of ^{6}Li and ^{7}Li can be described by $\alpha + d$ and $\alpha + t$ structures, respectively [18, 24].

While clustering in light, weakly-bound nuclei is not a focus of this work, this concept provides important context. The fact that ^{7}Li and ^{9}Be are weakly bound to direct breakup is explained by their cluster structure. However, these light nuclei are weakly bound precisely because α particles are so well bound; reactions such $^{7}\text{Li} + {}^{A}_{Z}X \rightarrow {}^{8}\text{Be}(\rightarrow \alpha + \alpha) + {}^{A-1}_{Z-1}Y$ may be strongly favoured. Further, cluster transfer may be enhanced in reactions where the projectile or target has significant cluster structures [19, 26].

2.6 Structure of Target-Like Nuclei

It should be clear from the above discussion that the structure of light weakly-bound nuclei is crucial to the observed reaction outcomes in transfer-triggered breakup. But what of the target-like nuclei? The structure of the target nucleus comes into play during the transfer process.

The role of nuclear structure in transfer can be understood by separating the transfer cross-section into the product of a reaction dependent factor, typically calculated using the Distorted Wave Born Approximation (DWBA), $\frac{d\sigma}{d\Omega}_{\text{DWBA}}$, and structure dependent spectroscopic factors[3] S, such that

[3]Often denoted C^2S, where C^2 is the isospin Clebsch–Gordan coefficient and S is calculated using isospin formalism (i.e. protons and neutrons are indistinguishable) [27].

$$\frac{d\sigma}{d\Omega}_{exp} = S_1 S_2 \frac{d\sigma}{d\Omega}_{\text{DWBA}} \tag{2.22}$$

S_i are the overlaps between the initial state of the target and recoiling particle and projectile and ejectile [28]. For example, in a stripping reaction removing a nucleon j, from a nucleus $(A = N) \rightarrow (A = N - 1)$

$$S \propto |\langle \psi_{N-1} \otimes j | \psi_N \rangle|^2. \tag{2.23}$$

This is a measure of the single-particle nature in a particular state, and may be interpreted as the probability of finding the nucleus with A = N-1 as a core within the A = N nucleus [7]. As seen in Eq. 2.22, the larger S_i is, the larger the cross-section for transfer into a particular state.

2.7 Q-Values

2.7.1 Endothermic and Exothermic Reactions

Another important quantity that influences the probability of a reaction occurring is the reaction Q-value. When the nuclei are in their ground state, the reaction Q-value is defined as the difference between the masses of the nuclei in the initial i and final f reaction products in their ground state

$$Q_{\text{gg}} = \left(\sum_i m_i - \sum_f m_f \right) c^2. \tag{2.24}$$

If Q_{gg} is positive the reaction is said to be exothermic. That is, binding energy is converted into kinetic energy of the final reaction products. On the other hand, negative Q_{gg} indicate a reaction is endothermic, and kinetic energy of the incoming channel is converted into binding energy. In endothermic reactions, particles in the entrance (initial) channel must have a minimum kinetic energy E_{thr} such that $E_{\text{thr}} + Q_{\text{gg}} = 0$ in the centre of mass frame, before reactions with negative Q_{gg} can occur.

When a reaction populates an excited state E_x of the outgoing reaction products, then the measured Q-value, Q, becomes

$$Q = Q_{\text{gg}} - E_x, \tag{2.25}$$

where Q_{gg} is the ground-state to ground-state Q-value, as defined above.

2.7.2 Optimum Q-Values

It is clear from Eq. 2.25 that the measured Q of a reaction changes with the excitation of the outgoing reaction products. It has also been shown that different states of the target-like nucleus are populated to different strengths depending on their single-particle structure, given by the spectroscopic factor (defined in Eq. 2.23). Another reaction property that changes the population of states in the target-like nucleus (and hence Q) during a reaction is the *optimum Q-value*, Q_{opt}. The quantity Q_{opt} is the Q at which there is a smooth transition between the classical trajectories on the incoming and outgoing trajectories of the projectile-like nucleus.

Classically, Q_{opt} may be estimated by requiring that the (zero angular momentum) classical trajectory that the particles follow is continuous at the point of transfer, and by assuming that transfer will occur at the distance of closest approach of the nuclei, R. At this point, the centre of mass energy, E_{CM} is equal to the value of the Coulomb potential V_C. Before transfer,

$$E_{\text{CM}} = V_C = \frac{Z_P Z_T e^2}{4\pi\epsilon_0 R} \tag{2.26}$$

And, after transfer

$$E'_{\text{CM}} = V'_C = \frac{Z'_P Z'_T e^2}{4\pi\epsilon_0 R'}, \tag{2.27}$$

where the primed quantities indicate the new distance of closest approach, centre of mass energy and charges. When Q is optimal, R = R' and $Q = E_{\text{CM}} - E'_{\text{CM}}$, giving

$$Q_{\text{opt}} = E_{\text{CM}} \left(\frac{Z'_P Z'_T}{Z_P Z_T} - 1 \right). \tag{2.28}$$

There are a number of more sophisticated estimates of Q_{opt} e.g. [29–32]. The formulation of Eq. 2.28, which is the same of Ref. [33], is fairly simplistic and does not include recoil effects considered in Ref. [30], for example. While more sophisticated estimates are required for quantitative conclusions, this formulation is sufficient to see the broad effects of Q_{opt} [34].

In a neutron transfer reaction, the charge product of the initial and final states is unchanged, giving $Q_{\text{opt}} = 0$. Therefore, the neutron transfer cross-section should be expected to be maximum at target-like excitations such that $Q = 0$ [7]. This effect is modulated by the structure of the target-like nucleus: the effect of Q_{opt} coexists with the effect of the spectroscopic factors, and depends on the level density at Q_{opt}.

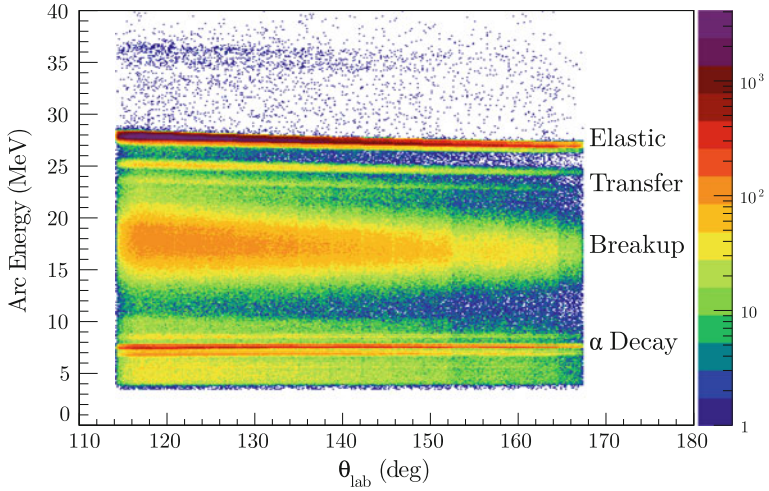

Fig. 2.7 (θ, Arc Energy) correlation for reactions of ^{7}Li and ^{209}Bi performed with a beam energy of 31.5 MeV, for the work reported in Refs. [35, 37, 38]. The correlation between scattered energy and angle yields insight into the different reaction outcomes present in nuclear collisions, as described in the text

2.8 Reaction Observables

So far, the nuclear structure and nuclear reaction effects that influence the outcome of nuclear collisions have been described. These effects manifest in reaction observables. In particular, we are interested in the quantities that give insight into the mechanisms and timescales of breakup. In this section some observables that are well established in investigating breakup [35–38] will be discussed. Further reconstructed observables useful for understanding breakup that were developed in the course of this work will be introduced in Chap. 4.

2.8.1 Scattering Angle versus Fragment Energy (θ, E)

Due to energy and momentum conservation, the relationship between the energy of a scattered particle and its scattering angle θ is dependent on the masses of the participating nuclei, the beam energy, and the Q of the reaction. For reactions in normal kinematics that produce two nuclei in the final state, such as elastic scattering or transfer, the energy of the projectile-like nucleus decreases monotonically with θ so that there is a single E for each θ. If the reaction produces three or more nuclei in the final state (e.g. direct or transfer-triggered breakup), a measurement of fragment energy as a function of θ will yield a smooth, broad distribution of energy for every θ. In fusion reactions, producing high mass evaporation residues

that decay via α emission, the energy of the measured α particles will have no θ dependence. Therefore, a measurement of (θ, E) can give insights into the different reaction mechanisms at play in a particular collision.

A particularly vivid example can be seen in Fig. 2.7, which shows (θ, E) for reactions of ^{7}Li with ^{209}Bi at a beam energy of 31.5 MeV [35, 37, 38]. In this spectrum, many reaction processes appear. The most intense band, located at ∼28 MeV corresponds to elastic scattering, and the less intense, narrow bands at ∼37, 26, 24 and 23 MeV correspond to different transfer modes. The very narrow lines seen at ∼7 MeV are due to α decay from decaying heavy compound nuclei. Finally, there is a very broad region of events from ∼15 to 27 MeV. These events are due to breakup processes, and it is this class of events that are of key interest in this thesis. Unfortunately, these events are also the least sharply delineated in (θ, E). So, while (θ, E) is useful to demonstrate the reaction processes that are occurring, and to identify that breakup is present (although this becomes more challenging with lighter targets, as will be shown), it is not sufficient to tell us the mechanism of breakup or its influence on complete fusion.

While (θ, E) has the distinct advantage of not requiring coincidence measurements to be made in order to access this observable, making coincidence measurements of breakup fragments enables the extraction of a great deal more information about breakup processes. When looking at particles in coincidence, the next most accessible observable is the correlation seen between the energies of breakup fragments (E_1, E_2).

2.8.2 *Energies of Coincident Breakup Fragments* (E_1, E_2)

Applying energy conservation to a breakup reaction resulting in two fragments with energies E_1 and E_2 (corrected for energy losses) the following expression is obtained:

$$E_{\text{lab}} + Q = E_r + E_1 + E_2. \tag{2.29}$$

Here, E_r is the energy of the recoiling nucleus and E_{lab} is the energy of the projectile, corrected for energy loss through half the target thickness. If the mass of the recoiling nucleus is heavy compared to that of the transfer product, then E_r is small and $E_1 + E_2 \approx E_{\text{lab}} + Q$. Therefore, for reactions with heavy targets, E_1 and E_2 will be strongly correlated, and appear as diagonal lines in a scatterplot of E_1 against E_2 characteristic of the beam energy and Q. This is indeed seen for the neutron stripping triggered breakup of ^{8}Be after interactions of ^{9}Be with ^{209}Bi at a beam energy of E_{beam} of 37.0 MeV, shown in Fig. 2.8. This reaction produces ^{8}Be, which then decays into two α particles. The distribution of E_1 and E_2 is not constant in intensity along the diagonal bands: there is a central region of increased intensity. As will be shown in Sect. 2.8.4 these events correspond to breakup from the long lived 0^+ state of ^{8}Be located 92 keV above the breakup threshold.

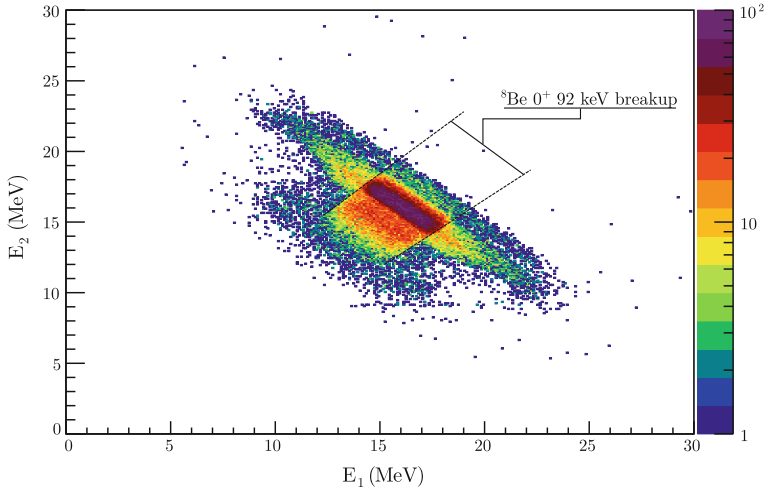

Fig. 2.8 The energy of one breakup fragment is correlated with the energy of the other due to energy conservation. When breakup occurs after interactions with a heavy target, the energy of the recoiling nucleus is small, and E_1 and E_2 appear as diagonal bands, with their sum of energies characteristic of the Q of the breakup process. This is shown for the neutron pickup triggered breakup in interactions of ^{9}Be with ^{209}Bi at $E_{\text{beam}} = 37.0$ MeV, producing two α particles, with energy E_1 and E_2

During breakup, conservation of momentum dictates that the total momentum of the breakup fragments should remain zero in the centre of mass frame of the projectile-like nucleus. Therefore the fragments must travel in opposite directions in the centre of mass frame, but may be emitted in any direction. As a result, there is a continuous distribution of energies with maximum and minimum energy given by

$$E_1^{\frac{\max}{\min}} = \frac{m_1}{m_1 + m_2}\left(E_p + \frac{m_2}{m_1}Q_{\text{BU}} \pm 2\sqrt{\frac{m_2}{m_1}Q_{\text{BU}}E_p}\right) \tag{2.30}$$

where E_p is the energy of the projectile-like nucleus prior to breakup, m_i the masses of the breakup fragments and Q_{BU} the Q-value for the breakup process (i.e. $Q_{\text{BU}} =$ 92 keV for breakup of ^{8}Be from its 92 keV 0^+ resonance). This relationship only holds for breakup that occurs asymptotically far from the target-like nucleus (from a narrow resonance). The energy of breakup fragments that are produced close to the target-like nucleus (from broad resonances) will be perturbed due to interactions with the Coulomb field of the target. In this way, correlations between E_1 and E_2 contain information about the state of the projectile-like and target-like nuclei, but it is difficult to obtain quantitative information. In addition, when the mass of target nucleus decreases, the energy of the recoiling target-like nucleus increases, "smearing out" the (E_1, E_2) correlations, so that they no longer appear as sharp diagonal lines. Much more useful information can be gained by taking the energy and angles of

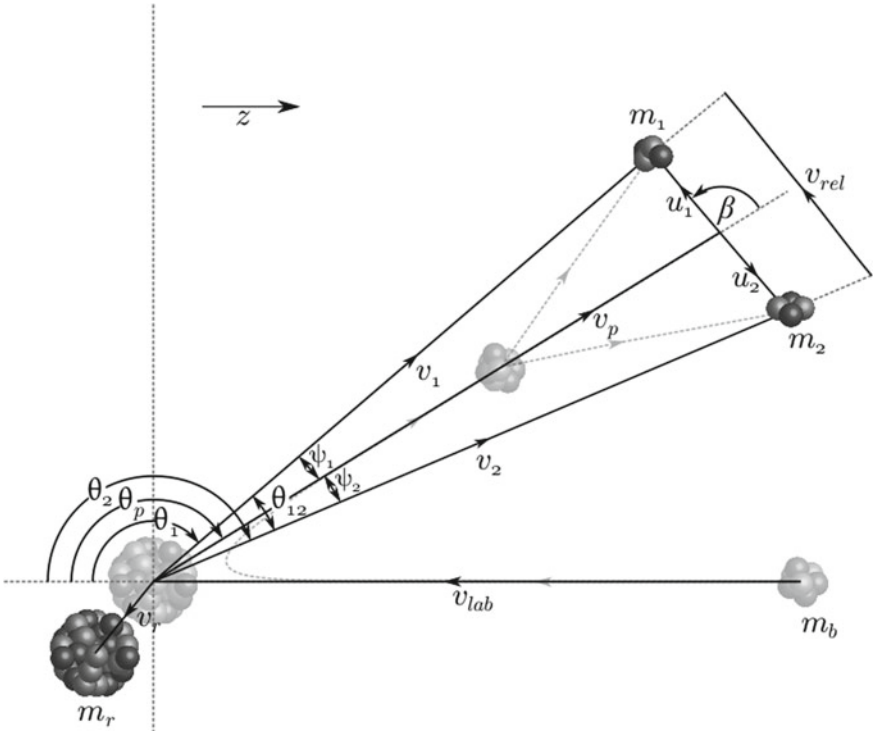

Fig. 2.9 Schematic demonstrating the velocity vectors used to determine Q, opening angle θ_{12}, and relative energy and β angle. v_{lab}, v_p, v_r, v_1 and v_2 are the laboratory velocities of the beam, projectile-like nucleus, recoiling nucleus and breakup fragments, respectively. The masses of the beam, recoiling nucleus and breakup fragments are given by m_b, m_r, m_1 and m_2. The velocities of the breakup fragments in their centre of mass is given by u_1 and u_2 and their relative velocity is v_{rel}. The scattering angles of the projectile and breakup fragments are given by θ_p, θ_1 and θ_2

each particle detected in coincidence (E_i, θ_i, ϕ_i) and reconstructing two key reaction quantities, namely Q-value and relative energy of the fragments.

2.8.3 *Reconstructed Q-Value (*Q*)*

In a coincidence measurement of the energies and positions of the two breakup fragments, it is possible to determine the Q of the reaction, defined by Eq. 2.25, via the initial and final rest masses of the nuclei involved in the reaction, as well as the excitation energy of the nuclei. Experimentally, Q can be determined from the equivalent expression,

$$Q = \sum E_f - \sum E_i, \tag{2.31}$$

where E_f and E_i are the initial and final kinetic energies of the participating nuclei. For a breakup reaction producing three nuclei in the final state, in the laboratory frame this expression becomes

$$Q = (E_1 + E_2 + E_r) - E_{\text{lab}}, \tag{2.32}$$

where E_i are the measured energies of each fragment. For thin targets, E_{lab} can be determined by correcting the beam energy E_{beam} for energy loss of the projectile after traversing half the target thickness. E_r, the energy of the recoiling target-like nucleus, is not measured, so it must be reconstructed using energy and momentum conservation:

$$m_b\vec{v}_{lab} + m_t\vec{v}_t = m_1\vec{v}_1 + m_2\vec{v}_2 + m_r\vec{v}_r, \tag{2.33}$$

where m_b, m_t, m_r and $m_{1,2}$ are the masses of the beam, target, recoil and breakup fragments, respectively, and v_i their associated velocities, shown in Fig. 2.9. As the target is at rest in the laboratory frame, $|\vec{v}_t| = 0$, simplifying the expression.

Given a measurement of two fragments with mass m_i, energies E_i (corrected for energy losses) and scattering angles (θ_i, ϕ_i), the position vectors of each nuclide are given by:

$$\vec{r}_i = \{\sin\theta_i \cos(270 - \phi_i), \sin\theta_i \sin(270 - \phi_i), -\cos\theta_i\}, \tag{2.34}$$

and the magnitude of the velocity of each fragment in the non-relativistic limit[4] is given by

$$|\vec{v}_i| = \sqrt{\frac{2E_i}{m_i}}. \tag{2.35}$$

The velocity of the projectile-like nucleus prior to breakup is then given by momentum conservation

$$\vec{v}_p = \frac{m_1\vec{v}_1 + m_2\vec{v}_2}{m_1 + m_2}. \tag{2.36}$$

The velocity of the beam is

$$\vec{v}_{lab} = \{x, y, z\} = \left\{0, 0, -\sqrt{\frac{2E_{\text{lab}}}{m_b}}\right\}, \tag{2.37}$$

and so by momentum conservation, the velocity of the recoiling target-like nucleus is

$$\vec{v}_r = \frac{m_p\vec{v}_p + m_b\vec{v}_{lab}}{m_r}. \tag{2.38}$$

This expression can be then used to determine the energy of the recoiling nucleus using $E_r = \frac{1}{2}m_r\vec{v}_r^{\,2}$, which allows Q to be determined from Eq. 2.32.

[4] A non-relativistic treatment applies at the energy regime of this thesis.

As shown in Sect. 2.7, when a reaction leaves the target-like nucleus in an excited state, the energy available to the breakup fragments decreases, and thus the reconstructed Q also decreases. Since

$$Q = Q_{\mathrm{gg}} - E_r^*. \tag{2.39}$$

E_r^* is the excitation of the recoiling target-like nucleus, and Q_{gg} is the Q of the reaction had the target-like nucleus remained in its ground state. The distribution of Q thus reflects the excitation of the target-like nucleus, and provides a key insight into breakup mechanisms.

2.8.4 Relative Energy (E_{rel})

While the Q provides insight into the excitation of the target-like nucleus, it does not provide any information regarding the excitation of the projectile-like nucleus since this energy is converted into the kinetic energy of the breakup fragments. To gain insight into the state of the projectile-like nucleus, another useful quantity must be examined, the relative energy E_{rel} of the fragments. Conceptually, E_{rel} is comprised of three terms:

$$E_{\mathrm{rel}} = Q_{\mathrm{BU}} + E_p^* + \Delta E_{\mathrm{acc}}. \tag{2.40}$$

Q_{BU} is the breakup Q, and E_p^* is the excitation energy of the projectile-like nucleus. ΔE_{acc} is a modification to E_{rel} due to the interaction of the fragments with the target-like nucleus following breakup. As such, the magnitude and sign of ΔE_{acc} depends on where breakup occurs with respect to the target nucleus, as well as the orientation of the breakup fragments relative to the Coulomb target. When breakup occurs far from the target-like nucleus, the gradient of the Coulomb field accelerates the fragments in essentially the same direction regardless of their orientation, and $\Delta E_{\mathrm{acc}} = 0$. This is seen for the case for long-lived narrow resonances, such as the ground-state of ^{8}Be. There, E_{rel} is sharply peaked at $E_{\mathrm{rel}} = Q_{\mathrm{BU}} + E_p^*$. This is termed *asymptotic breakup*, and is shown in Fig. 2.10a. Alternatively, breakup can occur close to the target-like nucleus, termed *near-target breakup*. Here, the initial orientation of the fragments will change ΔE_{acc}, due to a differential acceleration of the fragments. If the fragments are aligned perpendicularly to the field of the target-like nucleus, as shown schematically in Fig. 2.10b, ΔE_{acc} will be positive, and increase E_{rel}. Conversely, alignment in the direction of the field, shown in Fig. 2.10c will decrease E_{rel}. As a result, breakup close to the target, via the short-lived ^{8}Be 2^+ state for example, will result in a broad, relatively featureless E_{rel} distribution.

The discussion above shows us that the E_{rel} distribution provides useful insight into the proximity of breakup to the target-like nucleus and the state of the projectile-like nucleus prior to breakup. The E_{rel} of a pair of breakup fragments can be obtained from the observed energy and angles of the fragments by the reconstruction of their relative velocity $\vec{v}_{\mathrm{rel}}$, with

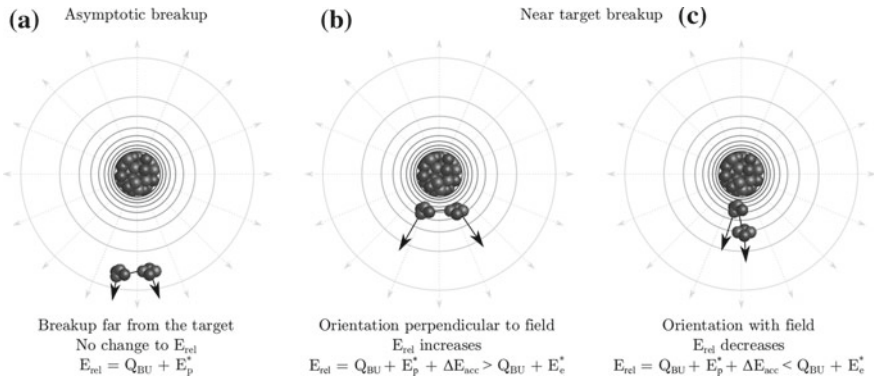

Fig. 2.10 The relative energy E_{rel} of breakup fragments depends on the proximity of breakup to the target-like nucleus as well as the initial orientation of breakup fragments. When breakup occurs asymptotically far from the target-like nucleus (**a**), both breakup fragments receive essentially the same acceleration in the Coulomb field of the target-like nucleus. However, if breakup occurs close to the target-like nucleus, the direction of the vector joining the breakup fragments will result in a differential acceleration between the two fragments, perturbing E_{rel}. When the fragments are oriented perpendicular to the Coulomb field (**b**), the relative velocity of the fragments increases, increasing E_{rel}. On the other hand, when the fragments are oriented in the same direction as the field (**c**), their E_{rel} decreases

$$E_{\text{rel}} = \frac{1}{2}\mu\vec{v}_{\text{rel}}^2. \tag{2.41}$$

Here, μ is the reduced mass of the fragments $\mu = \frac{m_1 m_2}{m_1+m_2}$. From geometry, shown in Fig. 2.9, $\vec{v}_{\text{rel}}$ can be determined from $\vec{v}_1$, $\vec{v}_2$ and the opening angle between the fragments θ_{12},

$$\cos\theta_{12} = \cos\theta_1\cos\theta_2 + \sin\theta_1\sin\theta_2\cos(\phi_1 - \phi_2). \tag{2.42}$$

Using the cosine rule,

$$\vec{v}_{\text{rel}}^2 = \vec{v}_1^2 + \vec{v}_2^2 - 2\vec{v}_1\vec{v}_2\cos\theta_{12}. \tag{2.43}$$

Substitution of this expression into Eq. 2.41 and re-arrangement gives

$$E_{\text{rel}} = \frac{m_2E_1 + m_1E_2 - 2\sqrt{m_1E_1m_2E_2}\cos\theta_{12}}{m_1+m_2}. \tag{2.44}$$

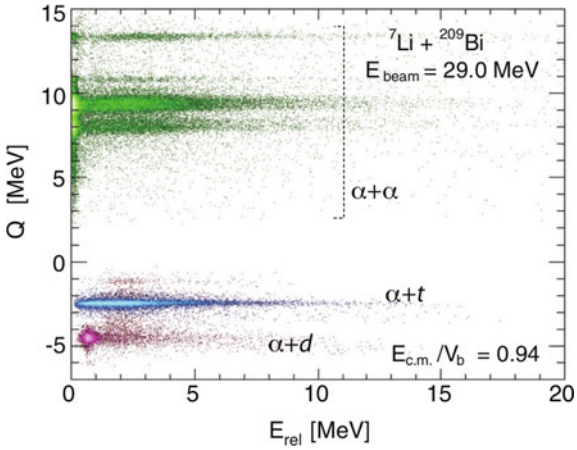

Fig. 2.11 Q against $E_{\rm rel}$ spectrum for the breakup after interactions of ^{7}Li with ^{209}Bi at $E_b = 29.0$ MeV, adapted from Ref. [38]. Breakup following proton pickup $^{7}\text{Li} + {}^{209}\text{Bi} \rightarrow {}^{8}\text{Be}(\rightarrow \alpha + \alpha) + {}^{208}\text{Pb}$ is indicated by the green points. Breakup following neutron stripping $^{7}\text{Li} + {}^{209}\text{Bi} \rightarrow {}^{6}\text{Li}(\rightarrow \alpha + d) + {}^{210}\text{Bi}$ is indicated with the magenta points. Direct breakup $^{7}\text{Li} + {}^{209}\text{Bi} \rightarrow {}^{7}\text{Li}(\rightarrow \alpha + t) + {}^{209}\text{Bi}$ is indicated with the blue points. The features of this plot are discussed in more detail in the text

2.8.5 $E_{\rm rel}$ versus Q

The reconstructed Q gives information on the state of the target-like nucleus, while $E_{\rm rel}$ provides information on the state of the projectile-like prior to breakup. Together these quantities provide a detailed picture of breakup mechanisms. Shown in Fig. 2.11 is the reconstructed Q and $E_{\rm rel}$ for breakup after interactions of ^{7}Li with ^{209}Bi from Ref. [38]. Different breakup modes have been indicated with different coloured points. Breakup following proton pickup $^{7}\text{Li} + {}^{209}\text{Bi} \rightarrow {}^{8}\text{Be}(\rightarrow \alpha + \alpha) + {}^{208}\text{Pb}$ is indicated by green points. Breakup following neutron stripping $^{7}\text{Li} + {}^{209}\text{Bi} \rightarrow {}^{6}\text{Li}(\rightarrow \alpha + d) + {}^{210}\text{Bi}$ is indicated with magenta points. Direct breakup $^{7}\text{Li} + {}^{209}\text{Bi} \rightarrow {}^{7}\text{Li}(\rightarrow \alpha + t) + {}^{209}\text{Bi}$ is indicated with blue points.

This plot tells us several pieces of information. On a broad level, it is seen that there are several breakup modes present for breakup after reactions of ^{7}Li. Contrary to expectations prior to the work of Refs. [36, 37], direct breakup into $\alpha + t$ is not the dominant breakup mode. Further, in the case of breakup following proton pickup producing two α particles ($\alpha + \alpha$ breakup), many states of ^{208}Pb are populated, with excitations up to $\sim$10 MeV, shown by the range of the measured Q. The relative populations of different states of ^{208}Pb reflect the spectroscopic factors for transfer into each state as well as $Q_{\rm opt}$.

The relative energy distribution of each mode is also illustrative. For $\alpha + \alpha$ breakup, there is a peak at small $E_{\rm rel}$, demonstrating that breakup is occurring far from the target ($\Delta E_{\rm acc} = 0$ in Eq. 2.40) through the long-lived 0^+ resonance of ^{8}Be. There is also a broad tail of events extending to large $E_{\rm rel}$, indicative of breakup close to the

target-like nucleus ($\Delta E_{\rm acc} \neq 0$ in Eq. 2.40). Similarly, much of the $\alpha + d$ breakup has a relative energy of ~0.71 MeV. This is breakup from the long-lived 3^+ state of ^{6}Li, which lies 0.71 MeV above the $\alpha + d$ breakup threshold of ^{6}Li. There is also a small tail of events extending to large $E_{\rm rel}$. On the other hand, direct breakup of ^{7}Li extends to large $E_{\rm rel}$ and has no strong features, indicating that no long-lived resonances have been populated.

Plots of Q and $E_{\rm rel}$ will be used repeatedly throughout this work to enable both identification and characterisation of different breakup modes and their possible effects on complete fusion. Other reconstructed quantities that complement Q and $E_{\rm rel}$ and enable more detailed examination of near-target breakup will also be shown. These will be introduced in Chap. 5.

2.8.6 *Reconstructed Scattering Pseudo-Angle of the Transfer Product (θ_p)*

At this juncture, it is useful to introduce the notion of the "breakup pseudo-angle" θ_p – the reconstructed ejectile angle of the transfer product prior to breakup. The breakup pseudo-angle is used to remove breakup events arising from interactions with light impurities in Chap. 4, to define the reaction plane in Chap. 5, and to extract breakup functions from coincidence data in Chap. 6.

When a reaction produces only one nucleus in the outgoing trajectory, the angular distribution and distance of closest approach of the projectile and target nuclei may be determined from the measured ejectile angle in a straightforward manner. In a breakup reaction producing pairs of particles which will have different angles θ and ϕ, a sensible way to extract the breakup probabilities is by use of θ_p, which can be interpreted as the reconstructed angle of the ^{8}Be had it not broken up.

In Sect. 2.8.3, the reconstructed velocity of the transfer product prior to breakup $\vec{v}_p$ was derived in Eq. 2.36 to determine the recoil velocity, and so the recoil energy, to find Q. The ejectile angle of the transfer product is the angle between the reconstructed velocity and the velocity of the beam $\vec{v}_{\rm lab}$, defined in Eq. 2.37, giving:

$$\cos\theta_p = \frac{\vec{v}_p.\vec{v}_{\rm lab}}{|\vec{v}_p||\vec{v}_{\rm lab}|}. \tag{2.45}$$

It will be convenient for determining breakup functions to have this angle in the centre of mass frame. In this case, the beam velocity becomes $\vec{v}_{\rm CM} = \left\{0, 0, -\sqrt{\frac{2E_{\rm CM}}{m_b+m_t}}\right\}$, and the velocity of the transfer product is $\vec{v}_p = \frac{m_1\vec{v}_1+m_2\vec{v}_2}{m_1+m_2} - \vec{v}_{\rm CM}$.

The corresponding reconstructed azimuthal angle ϕ_p is given by

$$\phi_p = \tan^{-1}\left(\frac{v_p^y}{v_p^x}\right) \tag{2.46}$$

where v_p^x and v_p^y are the x and y components of the reconstructed velocity of the transfer product.

2.9 Modelling Breakup

In this thesis, models of transfer-triggered breakup that predict the energy and angular distributions of breakup fragments will be used extensively. This is for four reasons:

1. To guide experimental setup. Knowledge of the broad features of breakup distributions aids in deciding where to place the BALiN detectors to be sensitive to as wide a range of breakup modes as possible. Further, when the target mass decreases, and the energy of the recoiling nucleus increases, the distribution of breakup fragments becomes less intuitive, making a model of breakup essential.
2. To aid in the interpretation of experimental results. By simulating breakup, the effect of projectile-target interactions on breakup observables can be assessed in detail.
3. To determine the coincidence efficiency of BALiN so as to extract below-barrier breakup cross-sections and probabilities.
4. To relate the experimentally determined below-barrier breakup functions to above-barrier CF (Sect. 2.2.5) and ICF (Sect. 2.2.4) cross-sections, so to determine the contribution of breakup to the suppression of above-barrier CF.

To guide the experimental setup – point (1) above – it is desirable that the model be simple and fast, and it needs to reproduce only the broad features of breakup, namely the energy and angular distribution of the breakup fragments. However, to address the last three points, a detailed model of breakup is required that reliably simulates post-breakup trajectories of breakup fragments as well as the cross-sections of the different reaction outcomes. Two classes of model will be used in this work. The first class are purely kinematic models, that use three body kinematics to predict the energy and angular distribution of breakup fragments, used to guide the experimental setup. The second class are that of classical dynamical models which simulate the trajectories of nuclei in their internuclear potential, the breakup process and the subsequent propagation (and possible capture) of particles to infinity. This class of models will be used to relate angular distributions of measured events to their location of breakup and the excitation of the projectile-like nucleus in Chaps. 5 and 8. They will also be used to determine the coincidence efficiency of BALiN and, with experimentally determined breakup functions as input, predict above-barrier ICF and CF cross-sections in Chap. 7.

2.9.1 Kinematical Model: KaitKin

To guide the experimental configuration of BALiN and to assess the feasibility of measuring ^{7}Be(d, p)^{8}Be reactions, a classical 3-body kinematical model of breakup "KaitKin"[5] was developed in the course of this thesis. In two-body kinematic models such as Catkin [39], the energy and angular distributions of fragments can be calculated analytically. In breakup, as shown in Fig. 2.7, the breakup fragments have a broad range of energies and angles due to the fact that the breakup fragments share the original energy of the projectile-like nucleus according to their masses, in the centre of mass frame. In the laboratory frame, this results in a broad spread in energies at a particular angle. To simulate this, KaitKin is a Monte-Carlo model that simulates breakup in a two-step process: transfer, followed by breakup of either the projectile- or target-like nucleus. First, a set of N ejectile and azimuthal angles (θ_p, ϕ_p), evenly distributed on a sphere, are generated.[6] In two body scattering, the relationship between the energy of a scattered projectile-like particle E_p and its ejectile angle θ_p is given by

$$E_p = (E_{\text{lab}} + Q)B(\cos\theta_p \pm (D/B - \sin^2\theta_p)^{1/2})^2. \tag{2.47}$$

where

$$B = \frac{m_b m_p (E_{\text{lab}}/(E_{\text{lab}} + Q))}{(m_b + m_t)(m_p + m_r)} \tag{2.48}$$

$$D = \frac{m_t m_r}{(m_b + m_t)(m_p + m_r)} \left(1 + \frac{m_b Q}{m_t (E_{\text{lab}} + Q)}\right) \tag{2.49}$$

and where the plus sign in Eq. 2.47 is used, unless $B > D$ [40]. Here, m_b, m_t, m_p and m_r are the masses of the beam, target, ejectile and recoil nuclei, and E_i their corresponding energies. These quantities are shown schematically in Fig. 2.12a. Q is the Q-value taking into account any internal excitation of the nuclei after transfer. By considering conservation of energy, $E_r = E_{\text{lab}} + Q - E_p$, and the ejectile angle of the recoiling fragment is given by

$$\sin\theta_r = \left(\frac{m_p E_p}{m_r E_r}\right)^{1/2} \sin\theta_p. \tag{2.50}$$

In the second step of the calculation, either the ejectile or projectile-like nucleus breaks up. This is shown schematically in Fig. 2.12b. In the rest frame of the projectile-like particle, the breakup fragments are distributed isotropically, and 180° apart. The first fragment is given a random orientation of its velocity (θ_1', ϕ_1') on a sphere (such that the total distribution is evenly distributed), and the second fragment

[5] Named in the manner of Catkin [39].

[6] The intensity distribution in (θ_p, ϕ_p) is not crucial.

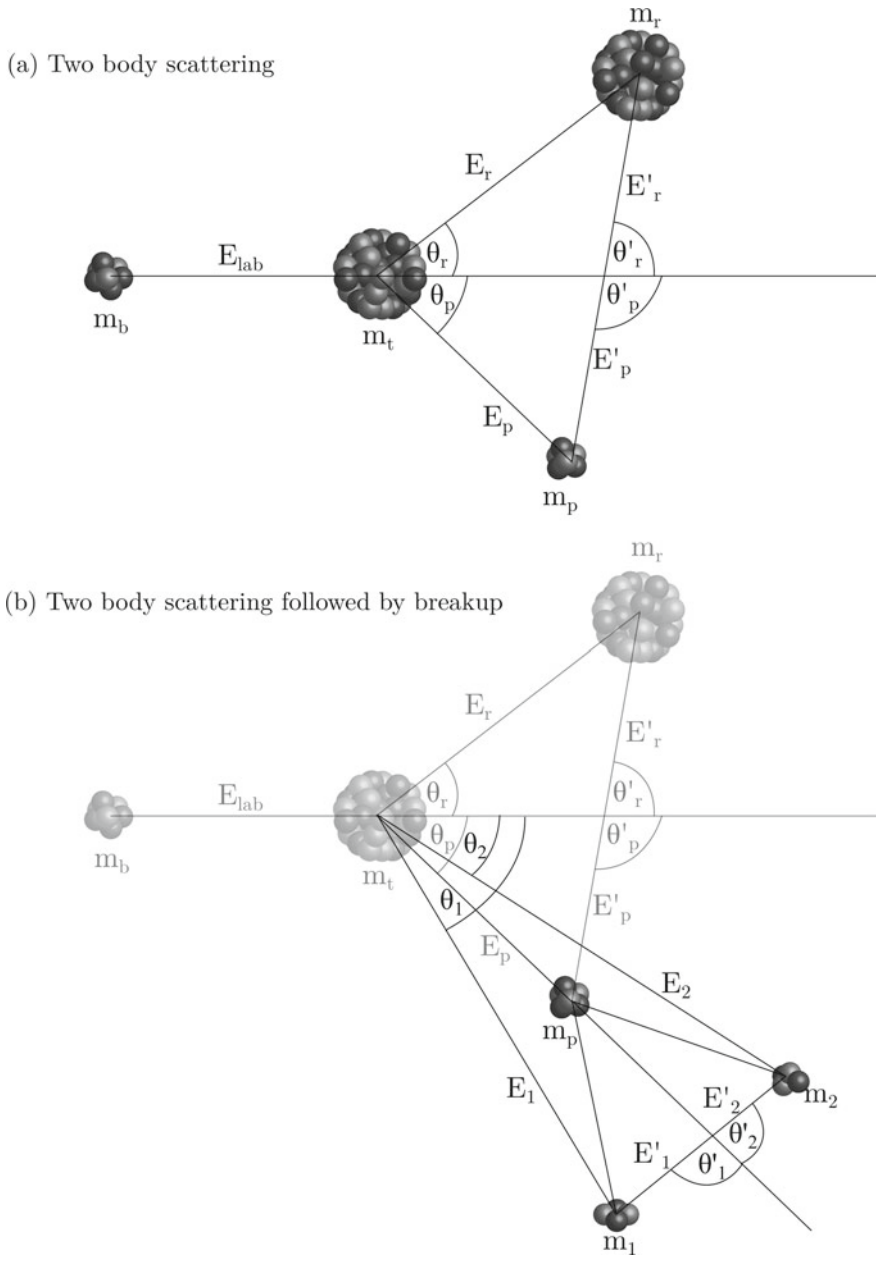

Fig. 2.12 KAITKIN simulates the kinematics of breakup in a two-step process. **a** First, the transfer process is simulated **b** then either the projectile-like or recoiling nucleus is allowed to break up isotropically in the centre of mass frame of the nucleus that breaks up

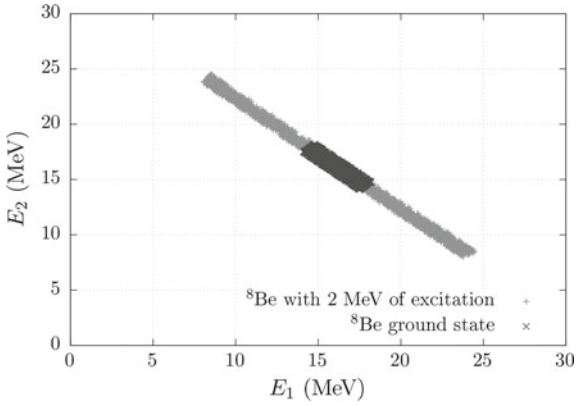

Fig. 2.13 KAITKIN simulation of the (E_1, E_2) distribution of the $\alpha + \alpha$ breakup of ^{8}Be after interactions of ^{7}Li with ^{209}Bi at 37.0 MeV

placed 180° from the first particle. The primed symbols indicate values calculated in the projectile-like nucleus rest frame. The energy available to the breakup fragments in the centre of mass frame is the sum of the internal excitation of the nucleus prior to breakup E^*, and the breakup Q-value Q_{BU}. From energy and momentum conservation, the velocity of the fragments in the projectile-like nucleus rest frame is:

$$v_2' = \frac{2(E^* + Q_{\mathrm{BU}})}{\frac{m_2}{m_1} + m_2} \tag{2.51}$$

$$v_1' = \frac{m_2}{m_1} v_2'. \tag{2.52}$$

Then, the energy of the breakup fragments in the laboratory frame is given by

$$E_i = \frac{1}{2} m_i |v_i|^2 \tag{2.53}$$

$$|v_i|^2 = |v_i'|^2 + |v_p|^2 - 2|v_i'||v_p| \cos\theta_i' \tag{2.54}$$

where v_i is the laboratory velocity of the breakup fragment i with centre of mass velocity v_i' and v_p the velocity of the projectile-like nucleus calculated in the laboratory frame, using Eq. 2.47. The angle of the breakup fragments in the lab frame is then given by

$$\cos\theta_i = -\sin\theta_p \sin\theta_i^p \cos\phi_i' + \cos\theta_p \cos\theta_i^p \tag{2.55}$$

$$\cos\phi_i = (\sin\theta_p \sin\theta_i^p \sin\phi_i' + \cos\theta_p \cos\phi_p \sin\theta_i^p \cos\phi_i^p + \sin\theta_p \cos\phi_p \cos\theta_i^p)/\sin\theta_i \tag{2.56}$$

where θ_i^p is the angle with respect to the projectile-like nucleus, such that

$$\sin\theta_i^p = \frac{v_i' \sin\theta_i'}{v_i}. \tag{2.57}$$

Thus, given the following inputs:

1. the masses of the beam, target, projectile-like nucleus, recoiling nucleus, and the masses of each breakup fragment,
2. the beam energy,
3. the ground-state to ground-state Q-value, as well as the breakup Q-value,
4. the excitation of the projectile-like and recoiling nuclei and
5. whether the projectile or target-like nucleus breaks up,

the code will return a distribution of the energy and scattering angles of the projectile and recoiling nucleus, as well as the energy and angles of the breakup fragments. An example of the simulated (E_1, E_2) distribution is shown in Fig. 2.13 for ^{9}Be + ^{209}Bi$\rightarrow^{8}$Be$(\alpha+\alpha)$+^{210}Bi at $E_{\text{lab}} = 37.0$ MeV – the same lab energy as that of Fig. 2.8. For ease of comparison between these figures, the KaitKin simulation has been performed with the recoil carrying 3 MeV of excitation, reproducing the maximum intensity of the experimental data (this corresponds a peak of excitation at $Q = 0$ MeV, at Q_{opt}). ^{8}Be has been simulated in its ground state, as well as with an excitation of 2 MeV. As can be seen by comparing the two figures, KaitKin reproduces the experimental data fairly well. Further examples of KaitKin outputs will be shown in later chapters. There are limitations however: all breakup is assumed to occur asymptotically far from the target nucleus, and KaitKin does not simulate cross-sections. Where these assumptions are inadequate, classical dynamical models are used in this thesis.

2.9.2 *Classical Dynamical Models: PLATYPUS, KOOKABURRA*

Ideally, the best way to model transfer-triggered breakup is by use of a fully quantum mechanical model since transfer-triggered breakup is ultimately a quantum mechanical process. However, no such model currently exists. Even most CDCC calculations for direct breakup do not make the energies and angles of the individual breakup fragments readily accessible. The problem lies in both treating the transfer ^{7}Li + (^{208}Pb + p) $\rightarrow$ (^{7}Li + p) + ^{208}Pb and breakup $(\alpha+\alpha)\rightarrow(\alpha+\alpha)^*$. Instead, classical simulations must be performed. Clearly, it is important that a classical model captures the key physics of the breakup processes. Namely, (a) the location of transfer, (b) the properties of the intermediate nucleus populated after transfer, and (c) the subsequent decay and post-breakup acceleration of the fragments. The acceleration of the fragments after breakup has the capacity to change their relative energy and is

the classical analogue of continuum-continuum couplings in quantum mechanical models.

Two classical dynamical breakup models have been used in this thesis. The first is PLATYPUS, developed by A. Diaz-Torres [41, 42], with some major modifications by E.C. Simpson, D.H. Luong and the author. The code, following modifications, was tested extensively by Sunil Kalkal and the author. PLATYPUS is a three-body classical trajectory model with stochastic breakup that enables calculations of breakup observables as well as incomplete and complete fusion cross-sections. PLATYPUS considers a target and a weakly-bound pseudoprojectile (here, ^{8}Be) that initially follow Rutherford trajectories. Originally, breakup probabilities and locations are defined through an experimentally determined breakup function $P(R)$. At the point of breakup, the properties of the fragments (excitation energy, separation, orientation) are stochastically sampled before propagating in the fragment-fragment and fragment-target fields.

The creation of a modified version of PLATYPUS arose as a result of the experimental measurements made in this work. As will be discussed in Chap. 6, accurate determination of the coincidence efficiency of BALiN depends on good reproduction of the experimental energy and angular distribution of fragments. Therefore, in order to find the coincidence efficiency of BALiN for measurements of breakup fragments after reactions of ^{7}Li with ^{58}Ni (and lighter targets), PLATYPUS calculations were performed. It was soon seen that there was no set of input parameters that could adequately reproduce the experimental distributions. Thus, it became clear that PLATYPUS was missing some essential physics.

Several significant modifications to PLATYPUS had to be made to more accurately capture the details of breakup dynamics. The modified version of PLATYPUS will be called M-PLATYPUS in this thesis, for clarity, and to denote the significant amount of extra physics and bug-fixes included in M-PLATYPUS. The modifications made in collaboration with E.C. Simpson, are listed in Table 2.1, and described below. The extent of these changes, and the desire to include physics not easily incorporated due to the design of PLATYPUS led to the creation of a new classical dynamical simulation code, called KOOKABURRA.

KOOKABURRA was written by E.C. Simpson, tested and improved over the course of this thesis. KOOKABURRA is also a Monte-Carlo three-body classical dynamical model, which includes the same physics as PLATYPUS, the modifications in M-PLATYPUS, and also simulates the transfer process. Thus modelling a pseudoprojectile is not needed, eliminating the need to adjust projectile energies to match trajectories.

There are a few key differences between M-PLATYPUS and KOOKABURRA, besides the ability to simulate transfer. Firstly, in KOOKABURRA not every trajectory results in breakup, eliminating the need to normalise cross-sections at the end of the simulation as needed in PLATYPUS and M-PLATYPUS. Instead, the input breakup function is used to determine the appropriate fraction of breakup and elastic scattering. Secondly, KOOKABURRA does not simulate integer values of l. Instead a range of impact parameters, up to a user-set value, is sampled. This also eliminates the need that was in M-PLATYPUS to provide an input weighted l distribution. As KOOKABURRA was

Table 2.1 Summary of the differences in the modelling of transfer-triggered breakup between PLATYPUS, M-PLATYPUS and KOOKABURRA. Differences in the mechanics of the code (e.g. the fact that KOOKABURRA is parallelized) have been omitted

	PLATYPUS	M-PLATYPUS	KOOKABURRA
Projectile or pseudoprojectile?	Pseudoprojectile	Pseudoprojectile	Projectile
Projectile-like excitation	Constant or exponentially decreasing	From R-matrix	From R-matrix
Projectile-like lifetime	Time taken to pass potential barrier	$\tau(E) = \hbar/\Gamma_l(E)$ from R-matrix	$\tau(E) = \hbar/\Gamma_l(E)$ from R-matrix
Target-like excitation	No	Yes	Yes
Local breakup functions	Unphysical - Goes to zero at closest approach	Peaked at closest approach	Peaked at closest approach
Does every trajectory lead to breakup?	Yes	Yes	No
Depletion of breakup functions along trajectory	No	No	Yes
σ_{ICF} only considers probabilities on the incoming trajectory?	No	Yes	Yes
How many projectile-like states?	1	1	>1
Capture occurs when nuclei pass	R_B	R_B	$1.1r_0$
What happens at the point of transfer?	l is conserved	Direction is conserved	Either l or direction is conserved
Integer l?	Yes	Yes	No
Angular distribution of breakup fragments in their CM?	Incorrect	Isotropic	Isotropic
Multiple reactions?	No	No	Yes

developed during the work described in this thesis, results from both M-PLATYPUS and KOOKABURRA will be shown, though KOOKABURRA may be regarded as a more realistic model than M-PLATYPUS. Many of the key differences between PLATYPUS and KOOKABURRA are the same as those between PLATYPUS and M-PLATYPUS, which will be discussed below.

2.9.2.1 Incorporation of Excitation Energies and Lifetimes of Resonant States of the Projectile-Like Nucleus

The energies and angles of breakup fragments produced after the decay of a projectile-like nucleus populated in a transfer reaction depends critically on (i) the excitation of the projectile-like nucleus that breaks up, and (ii) the location of breakup with respect to the target-like nucleus, which is in turn sensitive to the lifetime of the projectile-like nucleus after transfer. It was therefore necessary to include the known low-energy structure of the projectile-like nucleus in M-PLATYPUS. In the previous versions of PLATYPUS, the excitation of the projectile-like nucleus was given as a range from E_{min} to E_{max} with either a flat or exponentially decreasing distribution [42]. Although lifetimes were not treated explicitly, breakup fragments would take some time to propagate from their assumed initial Gaussian distribution of separations to beyond their mutual barrier [41]. This effective lifetime is sensitive to the fragment-fragment potential, and did not produce a realistic distribution of lifetimes (which should follow an exponential). In M-PLATYPUS and KOOKABURRA, excitation energies are sampled from realistic distributions of excitation energy and have a corresponding mean life associated with each excitation energy, calculating using R-matrix theory, as was discussed in Sect. 2.5.

Including these probability distributions of excitation energy and associated mean-life, the distribution of decay (breakup) times of short-lived resonance states are now handled explicitly in M-PLATYPUS and KOOKABURRA. This is implemented by first randomly choosing a "transfer radius", R_{Tr}, according to the breakup function as was originally done. Then a classically allowed excitation energy E_p^* (with corresponding mean life τ) is chosen from the probability distribution of excitation energies as shown in Fig. 2.5. The projectile then propagates along its trajectory for some time t, sampled from the exponential distribution of times expected from the mean life, $e^{-t/\tau}$, before breaking up into two fragments with relative energy corresponding to E_p^* . If their energy is above the barrier, the fragments are initially placed at a separation radius corresponding to their mutual barrier radius. At energies below the barrier, they are placed at the external turning point. Breakup is thus defined to occur when the two fragments are beyond their mutual barrier radius. Crucially, unbound projectile-like nuclei such as ^{8}Be, produced by transfer before the distance of closest approach may pass the turning point and begin to recede from the target before breaking up.

This explicit handling of excitation energies and mean lives gives a more physically realistic (though still phenomenological) distribution of (i) breakup fragment energies and (ii) the time taken between transfer and breakup, and thus positions of breakup along the trajectories. The latter modification in particular removes a significant sensitivity to the fragment-fragment potential. In addition, these modifications allows long-lived states, such as the ^{8}Be ground state, to be simulated with M-PLATYPUS or KOOKABURRA rather than requiring an additional model such as that used in Ref. [36]. It also means that it is no longer necessary to draw a firm boundary between "near-target" and "asymptotic" breakup, since M-PLATYPUS and KOOKABURRA can handle the full time evolution of the system. Further, requiring

that the distribution of excitation energies used in M-PLATYPUS and KOOKABURRA be determined by the known resonance properties of ^{8}Be removes this quantity as a parameter in the model. As will be further discussed in Chap. 7, the explicit inclusion of resonance lifetimes eliminates a significant uncertainty in predicted ICF and CF cross-sections above the barrier.

2.9.2.2 Incorporation of Effects of Excitation of Target-Like Nuclei

As can be seen by the spread of Q in Fig. 2.11, the target-like nucleus is populated with a large range of excitations (up to ∼8 MeV) in these reactions. Trivially, as the excitation energy of the target-like nucleus increases, the energy available for the excitation of the projectile-like nucleus decreases. This results in a decrease in the maximum E_{rel} (as can also be seen in Fig. 2.11), and thus a decrease in average opening angle θ_{12}. Therefore, the fidelity of the reproduction of experimental results in classical dynamical models is also dependent on the distribution of target-like excitations.

PLATYPUS, M-PLATYPUS and KOOKABURRA, being classical models, have radii around the classical turning point where transfer is classically forbidden due to energy conservation. The size of this region depends on the beam energy, angular momentum and the excitation energy of the projectile-like and target-like nuclei. The latter excitation energy was not incorporated in the original version of PLATYPUS, which was thus modified to include the excitation energy distribution of the target-like nucleus, obtained from the experimentally determined Q distribution. To model the excitation energy, at R_{Tr} an equivalent amount of kinetic energy is deducted from the projectile-like nucleus such that either the direction of the relative velocity of the system is maintained, or the total angular momentum l of the system is maintained. In a classical model, you can have one or the other. Conserving l results in a sudden jump in the relative velocity of the system at the point of breakup, while conserving the relative velocity of the system results in a change in l at the point of breakup. The resulting energy and angular distributions of the breakup fragments depends on the choice of either maintaining the direction or conserving l. As a result of including the target-like nucleus excitation energy, M-PLATYPUS and KOOKABURRA simulations now reflect both the excited states of the target-like nucleus and the probability of populating those states in the neutron transfer reactions studied in this work. The total E_{rel} and θ_{12} distributions for breakup modes that populate a large number of states in the target-like nucleus are better reproduced, improving the efficiency determination.

2.9.2.3 Modifications to the Local Breakup Function

An aim of the below-barrier measurements of breakup performed for this work is to determine the breakup probabilities P as a function of R_{min}, the distance of closest approach on a Coulomb trajectory. The experimental data were fitted with the functional form

$$P(R_{\min}) = e^{\mu R_{\min}+\nu}, \tag{2.58}$$

where μ and ν are the (logarithmic) slope and intercept of the function, respectively. This function is interpreted as the integral of the local probability $\mathcal{P}(R)$ along the classical orbit of the projectile,

$$P(R_{\min}) = 2\int_{R_{min}}^{\infty} \mathcal{P}(R)dR. \tag{2.59}$$

$\mathcal{P}(R)$ is a function of the projectile-target separation R, and $\mathcal{P}(R)dR$ gives the probability between R and $R + dR$. The factor of two reflects the initial assumption that taking breakup to be instantaneous, it can occur with equal probability on the incoming and outgoing trajectories. With the incorporation of resonance lifetimes, the local probability must now be interpreted as that for the trigger event for breakup, in this case transfer. At above-barrier energies, when using PLATYPUS or KOOKABURRA to estimate $\sigma_{\rm ICF}$, the distance of closest approach is inside the barrier radius, thus only the transfer probabilities on the ingoing trajectory should be included. This change by a factor of two has been taken into account in M-PLATYPUS and KOOKABURRA calculations of $\sigma_{\rm ICF}$, resulting in a decrease in contributions to $\sigma_{\rm ICF}$ from trajectories with angles within the grazing angle by approximately a factor of two.

The distribution of transfer positions along the projectile-target trajectory has also been modified. In the original PLATYPUS, when determining the probability along the trajectory it is assumed that since

$$2\int_{R_{min}}^{\infty} \mathcal{P}(R)dR = e^{\mu R_{min}+\nu}, \tag{2.60}$$

the local probability must then have the form [41]:

$$\mathcal{P}(R) \propto e^{\mu R}. \tag{2.61}$$

However, this neglects the fact that interacting nuclei spend more time near the distance of closest approach than at other distances. Because of this, $dP(R_{min})/dt$ goes to zero at the point of closest approach, as can be demonstrated for a classical Coulomb trajectory, where

$$\frac{dt}{dr} = \frac{r}{v\sqrt{(r - a_0(1+\epsilon))(r - a_0(1-\epsilon))}}, \tag{2.62}$$

and $a_0 = Z_p Z_t e^2/\mu v^2$, $\epsilon = \sqrt{1 + (L/\eta)^2}$ and the Sommerfeld parameter $\eta = Z_p Z_t e^2/v$, where μ is the reduced mass, and v the incident velocity. Then,

$$\frac{dP}{dt} = \frac{dP}{dr}\frac{dr}{dt} \propto e^{-\mu r}\frac{v\sqrt{(r - a_0(1+\epsilon))(r - a_0(1-\epsilon))}}{r}. \tag{2.63}$$

For a trajectory corresponding to scattering at 180°, $\epsilon = 1$ and the distance of closest approach, $R_{min} = 2a_0$, this results in $dP(R_{min})/dt = 0$ at the distance of closest approach, which does not seem reasonable.

Instead, each time step on the projectile trajectory is assigned a relative probability assuming a local (transfer) probability $\widetilde{\mathcal{P}}^L(t) \propto e^{\mu R(t)}$ and is normalised to the full trajectory such that

$$P(R_{min}) = \int_{-\infty}^{\infty} \widetilde{\mathcal{P}}^L(t)dt. \tag{2.64}$$

The local probability is then peaked at the distance of closest approach, which is more physical.

2.9.3 *Using Classical Models of Breakup to Map Experimental Observables to "Unobservables"*

The key goals of modelling breakup in this thesis is to determine the coincidence efficiency of BALiN to extract below-barrier breakup functions and to use these functions to predict above-barrier ICF and CF cross-sections. Aside from these goals, detailed models of breakup can be used to examine the details of near-target breakup by mapping what can be observed experimentally to what cannot.[7] These parameters include the projectile-like excitation energy, the radius and time of transfer and decay, and the impact parameter of the reaction. This will be explored in more detail in Chap. 5 by making comparisons to experimental data. Here we show an illustrative example which complements the material of this chapter, which is a comparison between the input projectile-like excitation (E_p^*, given by $\rho(E)$, shown in Fig. 2.5) and the simulated relative energy of the fragments. As discussed in Sect. 2.8.4, the relative energy of the fragments results from the sum of Q_{BU}, E_p^*, and post-breakup acceleration. The simulated relative energy of $\alpha + p$ breakup pairs after reactions of ^{7}Li with ^{58}Ni at 11.7 MeV, populating ^{5}Li in its $\frac{3}{2}^-$ resonant state, is shown in Fig. 2.14. Here the effect of the post-breakup acceleration on E_{rel} is seen. For small E_p^*, the E_{rel} peaks at $E_{\mathrm{rel}} = Q_{\mathrm{BU}} + E_p^*$, indicating that post-breakup acceleration is small. Then, as E_p^* increases, the E_{rel} distribution broadens. As seen in Fig 2.5, low projectile-like excitation energies map to long lifetimes before breakup. The latter translates to negligible post-breakup acceleration (Fig. 2.10a) as the fragments will experience little differential acceleration in the Coulomb field. This result is not particularly unexpected, but it is a nice illustration of the effect of breakup close to the target, and of the usefulness of classical models such as PLATYPUS and KOOKABURRA.

[7] The caveat is that these models are classical.

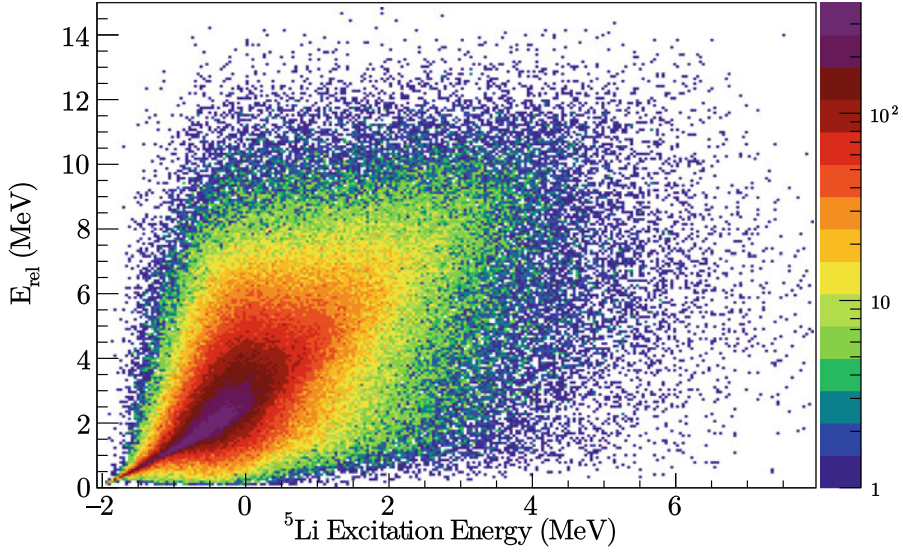

Fig. 2.14 KOOKABURRA simulation of the relationship between relative energy and projectile-like excitation energy (relative to the ground-state of ^{5}Li) for $\alpha + p$ breakup after reactions of ^{7}Li with ^{58}Ni at 11.7 MeV, populating ^{5}Li in its $\frac{3}{2}^-$ ground-state resonance

2.10 Summary

In this chapter, a number of key concepts have been introduced. We have seen that the study of transfer-triggered breakup must include the understanding that nuclear structure and nuclear theory are intertwined. We have also seen that there are a number of experimentally accessible observables that provide insight into this interplay, and introduced models of breakup that will prove invaluable to the aims of this thesis: to understand the trends of breakup across the nuclear chart and to understand the influence of breakup on fusion suppression. In order to address these aims, a number of experimental studies were undertaken, as will be discussed next.

References

1. Chamon, L.C., Carlson, B.V., Gasques, L.R., Pereira, D., De Conti, C., Alvarez, M.A.G., Hussein, M.S., Cândido Ribeiro, M.A., Rossi, E.S., Silva, C.P.: Toward a global description of the nucleus-nucleus interaction. Phys. Rev. C **66**(1), 014610 (2002)
2. Woods, R.D., Saxon, D.S.: Diffuse surface optical model for nucleon-nuclei scattering. Phys. Rev. **95**, 577 (1954)
3. Dasgupta, M., Gomes, P.R.S., Hinde, D.J., Moraes, S.B., Anjos, R.M., Berriman, A.C., Butt, R.D., Carlin, N., Lubian, J., Morton, C.R., Szanto de Toledo, A.: Effect of breakup on the fusion of ^{6}Li,^{7}Li, and ^{9}Be with heavy nuclei. Phys. Rev. C **70**(2), 024606 (2004)
4. Tarasov, O.B., Bazin, D.: Development of the program LISE: Application to fusion-evaporation. Nucl. Instrum. Methods Phys. Res. B **204**, 174 (2003)
5. Simpson, E.C.: The colorful nuclear chart. http://people.physics.anu.edu.au/ecs103/chart/index.php (2018)
6. Merzbacher, E.: Quantum Mechanics, 3rd edn. Wiley, New York (1997)
7. Thompson, I.J., Nunes, F.M.: Nuclear Reactions for Astrophysics, 1st edn. Cambridge University Press, Cambridge (2009)
8. Tilley, D.R., Kelley, J.H., Godwin, J.L., Millener, D.J., Purcell, J.E., Sheu, C.G., Weller, H.R.: Energy levels of light nuclei A = 8,9,10. Nucl. Phys. A **745**, 155 (2004)
9. Lane, A.M., Thomas, R.G.: R-matrix theory of nuclear reactions. Rev. Mod. Phys. **30**(2), 257 (1958)
10. Barker, F.C., Treacy, P.B.: Nuclear levels near thresholds. Nucl. Phys. **38**, 33 (1962)
11. Barker, F.C.: Consistent description of unbound states observed in scattering and reactions. Aust. J. Phys. **41**, 743 (1988)
12. Tilley, D., Cheves, C., Godwin, J., Hale, G., Hofmann, H., Kelley, J., Sheu, C., Weller, H.: Energy levels of light nuclei A = 5,6,7. Nucl. Phys. A **708**, 3 (2002)
13. Clayton, D.: Principles of Stellar Evolution and Nucleosynthesis, 2nd edn. University Of Chicago Press, Chicago (1983)
14. Rolfs, C., Rodney, W.: Cauldrons in the Cosmos. University Of Chicago Press, Chicago (1998)
15. Barker, F.C., Crawley, G.M., Miller, P.S., Steele, W.F.: The ghost anomaly in the ^{9}Be(p, d)^{8}Be reaction. Aust. J. Phys. **29**(1967), 245 (1976)
16. Berkowitz, E., Marolt, G., Rollefson, A., Browne, C.: Survey of the ^{8}Be ghost anomaly. Phys. Rev. C **4**(5), 1564 (1971)
17. Overway, D., Jänecke, J., Becchetti, F., Thorn, C., Kekelis, G.: Reaction dependence of nuclear decay linewidths. Nucl. Phys. A **366**(2), 299 (1981)
18. Freer, M.: The clustered nucleus - cluster structures in stable and unstable nuclei. Rep. Prog. Phys. **70**(12), 2149 (2007)

19. Buck, B., Dover, C., Vary, J.: Simple potential model for cluster states in light nuclei. Phys. Rev. C **11**(5), 1803 (1975)
20. Itagaki, N., Okabe, S.: Molecular orbital structures in ^{10}Be. Phys. Rev. C **61**(04), 044306 (2000)
21. Seya, M., Kohno, M., Nagata, S.: Nuclear binding mechanism and structure of neutron-rich be and b isotopes by molecular-orbital model. Prog. Theor. Phys. **65**(1), 204 (1981)
22. von Oertzen, W.: Two-center molecular states in ^{9}B,^{9}Be,^{10}Be, and ^{10}B. Z. Phys. Hadron. Nucl. **354**(1), 37 (1996)
23. Wiringa, R., Pieper, S.C., Carlson, J.: V.R P. Quantum Monte Carlo calculations of A = 8 nuclei. Phys. Rev. C **62**(1), 014001 (2000)
24. Nishioka, H., Tostevin, J.A., Johnson, R.C., Kubo, K.I.: Projectile excitation and structure effects in ^{6}Li and ^{7}Li scattering. Nucl. Phys. A **415**(2), 230 (1984)
25. Hafstad, L.R., Teller, E.: The alpha-particle model of the nucleus. Phys. Rev. **54**, 681 (1938)
26. Rafferty, D.C., Dasgupta, M., Hinde, D.J., Simenel, C., Simpson, E.C., Williams, E., Carter, I.P., Cook, K.J., Luong, D.H., McNeil, S.D., Ramachandran, K., Vo-Phuoc, K., Wakhle, A.: Multinucleon transfer in ^{16,18}O, ^{19}F + ^{208}Pb reactions at energies near the fusion barrier. Phys. Rev. C **94**(2), 024607 (2016)
27. Schiffer, J.: Isospin in Nuclear Physics. North-Holland, Amsterdam (1969)
28. Siemssen, R.H., Fink, C.L., Greenwood, L.R., Körner, H.J.: ^{18}O-Induced transfer reaction. Phys. Rev. Lett. **28**(10), 626 (1972)
29. Brink, D.M.: Kinematical effects in heavy-ion reactions. Phys. Lett. B **40**(1), 37 (1972)
30. Schiffer, J.P., Kijrner, H.J., Siemssen, R.H., Jones, K.W., Schwarzschild, A.: Experimental study of angular distributions and optimum Q values in heavy-ion reactions. Phys. Lett. B **44**(1), 47 (1973)
31. Wilczynski, J.: Optimum Q-value in multinucleon transfer reactions. Phys. Lett. B **47**(2), 124 (1973)
32. Wilczynski, J., Wilschut, H.W.: Partition of excitation energy in the optimum Q-value model. Phys. Rev. C **39**(6), 2475 (1989)
33. Buttle, P.J.A., Goldfarb, L.J.B.: Systematics of nucleon transfer between heavy ions at low energies. Nucl. Phys. A **176**(2), 299 (1971)
34. Rehm, K.E., Henning, W., Müller, R., Richter, M., Rother, H.P., Schaller, H.: Study of optimum Q-value in ^{16}O induced reactions on even Zr isotopes. Phys. Lett. B **46**(3), 353 (1973)
35. Luong D.H. Mechanisms and time-scales in breakup of ^{6,7}Li. Ph.D. thesis, Australian National University (2012)
36. Rafiei, R., du Rietz, R., Luong, D.H., Hinde, D.J., Dasgupta, M., Evers, M., Diaz-torres, A.: Mechanisms and systematics of breakup in reactions of ^{9}Be at near-barrier energies. Phys. Rev. C **81**(2), 024601 (2010)
37. Luong, D.H., Dasgupta, M., Hinde, D.J., Du Rietz, R., Rafiei, R., Lin, C.J., Evers, M., Diaz-torres, A.: Insights into the mechanisms and time-scales of breakup of ^{6,7}Li. Phys. Lett. B **695**, 105 (2011)
38. Luong, D.H., Dasgupta, M., Hinde, D.J., du Rietz, R., Rafiei, R., Lin, C.J., Evers, M., Diaz-Torres, A.: Predominance of transfer in triggering breakup in sub-barrier reactions of ^{6,7}Li. Phys. Rev. C **88**(3), 34609 (2013)
39. Catford, W.: Catkin. http://personal.ph.surrey.ac.uk/~phs1wc/kinematics/ (2004)
40. Marion, J.B., Young, F.C.: *Nuclear Reaction Analysis*. North Holland Publishing Company (1968)
41. Diaz-Torres, A., Hinde, D.J., Tostevin, J.A., Dasgupta, M., Gasques, L.R.: Relating breakup and incomplete fusion of weakly bound nuclei through a classical trajectory model with stochastic breakup. Phys. Rev. Lett. **98**(15), 152701 (2007)
42. Diaz-Torres, A.: PLATYPUS: a code for reaction dynamics of weakly-bound nuclei at near-barrier energies within a classical dynamical model. Comput. Phys. Commun. **182**(4), 1100 (2011)

Chapter 3
Experimental Methods

Data! Data! Data! I can't make bricks without clay!
Sir Arthur Conan Doyle 1859 – 1930

Three principal goals of these thesis are: (1) to systematically study the mechanisms of breakup in reactions of ^{7}Li and ^{9}Be with target nuclei from *d* to ^{209}Bi, (2) to measure breakup probabilities in order to estimate the contribution of breakup to above-barrier complete fusion suppression and (3) to examine the feasibility of applying the experimental and analysis techniques used for the study of breakup to the astrophysically relevant reaction ^{7}Be(d,p)^{8}Be. The unifying theme of these goals is the need to detect charged particles in coincidence with high efficiency. These measurements were performed with the ANU Breakup Array for Light Nuclei (BALiN), an array of four double-sided silicon strip detectors. In this chapter, the details of the measurement apparatus and techniques will be described, with a focus on the advances made to allow measurements with light to medium mass targets. The target nuclei studied in this work can be broadly categorised into "heavy mass" (^{144}Sm, ^{168}Er, ^{186}W, ^{196}Pt, ^{208}Pb and ^{209}Bi), "medium mass" (^{58}Ni, ^{27}Al and ^{28}Si) and "light mass" ($(C_2D_4)^n$, ^{12}C and ^{16}O). It will be shown that the different masses result in different characteristic energy and angular distributions. This results in different experimental requirements that will be discussed here. All measurements in this thesis were made at the Australian National University Heavy Ion Accelerator Facility (HIAF).

3.1 Beam Production

Beams of ^{7}Li and ^{9}Be at below-barrier energies for each beam-target combination were produced at the ANU HIAF, using the 14UD tandem accelerator, a National

K. J. Cook, *Zeptosecond Dynamics of Transfer-Triggered Breakup*,
Springer Theses, https://doi.org/10.1007/978-3-319-96017-3_3

Electrostatic Corporation Pelletron accelerator, which operates at over 15 MV. The accelerator is shown schematically in Fig. 3.1. Negative ions for injection are produced using a Source of Negative Ions by Caesium Sputtering (SNICS II) source. This source works by producing a vapour of caesium gas in an enclosed space with a cooled cathode containing a sample of the material to be accelerated. Some of the caesium gas condenses on the cathode, while some of it is ionised by contact with an ionising surface kept at a potential of 5 kV. The ionised caesium then accelerates towards the cathode, sputtering the material on the surface of the cathode. The sputtered material then may pick up an electron from the neutral caesium that it passes through, producing a negative ion. $^{7}Li^{-}$ beams of good intensity were produced using a sample comprising 34% natural LiO_2 and 66% Ag (to increase conductivity) by weight. The sample was baked at 180 °C for an hour to remove moisture. Beams of ^{9}Be were produced with a Be metal cathode. The most intense beams were of $^{9}BeO^{-}$ molecules, contrary to the expectation that $^{9}BeH^{-}$ beams, produced by introducing ammonia into the cathode, would be more intense. Therefore, $^{9}BeO^{-}$ beams were used.

After the negative ions are produced in the SNICS II source, they are pre-accelerated in a potential of $V_i = 150$ keV and passed through a mass selection electromagnet which is tuned to the mass of the desired beam so as to remove negative ions of different masses.

In this work, a pulsed beam was required to determine the time of flight (ToF) of breakup fragments. Therefore, the beams of ^{7}Li and ^{9}Be were bunched prior to injection into the accelerator. A longitudinal sinusoidal potential is applied at 9.375 MHz to the negative ions travelling at 150 keV, which are stochastically distributed in time. The field acts to decrease the velocity of the particles within the buncher acceptance with phase greater than π, and to increase the velocity of the particles with phase less than π (with respect to the RF signal). This produces a bunched beam with 106.6 ns separation between peaks, with some left over dark current of ions spread in time due to ions outside the buncher acceptance.

The bunched beam is then injected into the accelerator. The positive terminal, located in the centre of the accelerating structure, can operate at over 15 MV. The terminal is charged via three charging chains, and the accelerating structure is kept at six atmospheres of SF_6 to reduce sparks. In the experiments performed for this work, terminal potentials ranging from 1.314[1] to 4.249 MV were used. The injected negative ions are accelerated towards the positive terminal, where they are passed through a thin carbon foil. Interactions between the beam and foil results in electron stripping from the beam, and the ions become positively charged. The positively charged ions then accelerate away from the positive terminal, giving a final beam energy of:

$$E_{\text{beam}} = V_T(1 + q) + V_i, \tag{3.1}$$

[1]This is the lowest terminal potential ever to be used at the 14UD to deliver beam, to the extent of the author's knowledge.

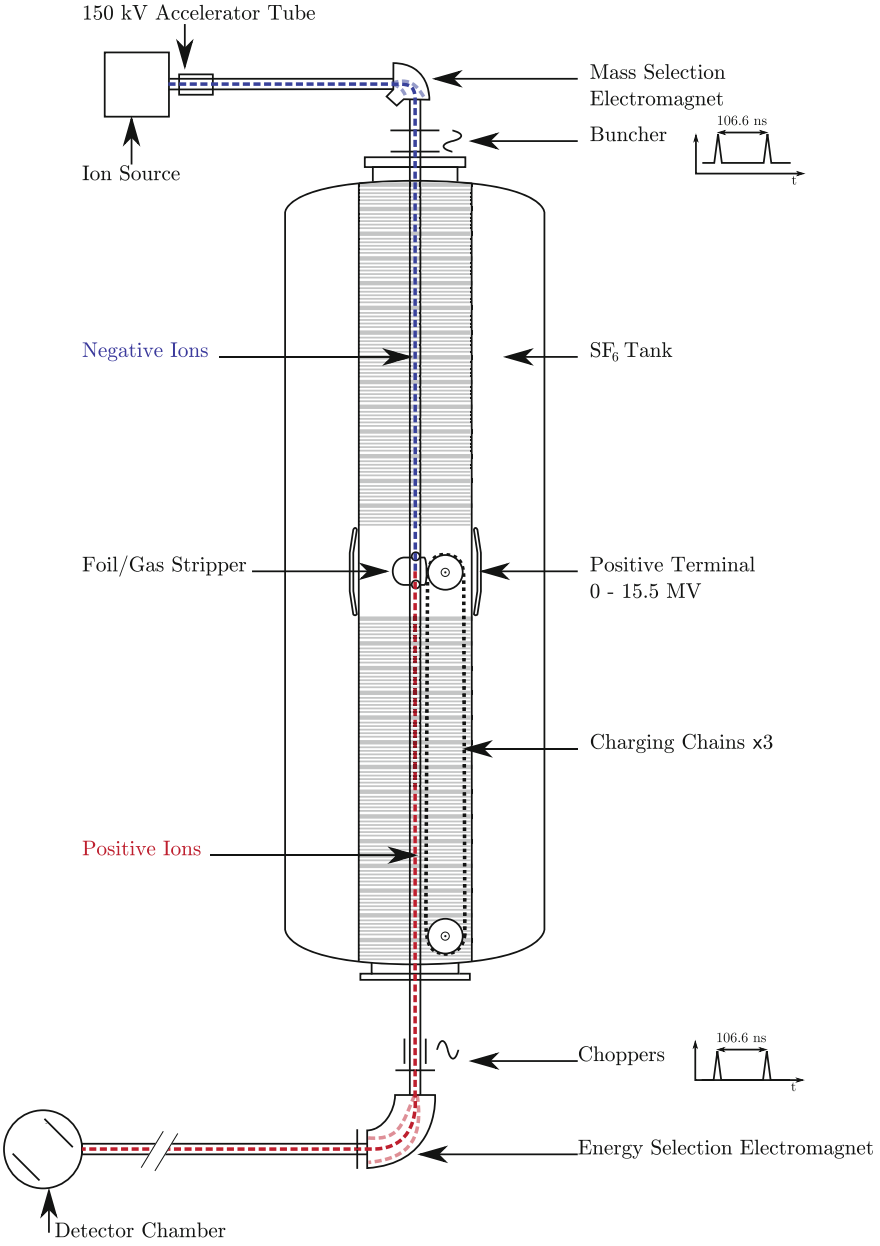

Fig. 3.1 Simplified schematic of the 14UD tandem accelerator, with focusing elements omitted. The process of beam production and acceleration is detailed in the text

where V_T is the terminal potential, and q the charge state of the ions after stripping. When a molecular beam is accelerated, as is the case for $^{9}BeO^{-}$, the stripping process disassociates the molecules, resulting in $^{9}Be^{+q}$ ions. In this case, the O^{+} and $^{9}Be^{+q}$ share their energy in proportion to their masses, and

$$E_{^{9}\mathrm{Be}} = (V_T + V_i)\frac{m_{^{9}\mathrm{Be}}}{m_{^{9}\mathrm{BeO}}} + qV_T \tag{3.2}$$

The stripping process produces a range of charge states, and therefore a range of final beam energies. To remove all but the charge state of interest, the beams are bent through a 90° energy selection electromagnet, set with reference to a calibrated nuclear magnetic resonance reference signal [1]. The magnet was last calibrated in 2004 with the method of [1] where the $^{12}C(p, \alpha)^{9}Be$ resonance at 14.23 MeV is used as the calibration point. Repeat measurements indicate an absolute beam energy uncertainty of ±0.1% for a 60.0 MeV beam of ^{16}O. As the precise energy of the beam is not a limiting uncertainty in this work, the magnet field was not cycled to remove differential hysteresis [1], resulting in an estimated uncertainty in beam energy of ±0.3%. During the acceleration process as well as during subsequent beam transport, a number of beam focusing elements are used, the details of which are not necessary for this thesis.

Prior to entering the energy analysing magnet, the beam passes through two orthogonal choppers, where the beam is swept across slits set at a fixed separation. The phase is set such that the peak in intensity of the bunched beam passes through the slits, removing any beam that is not in the beam bunch (the dark current). After bunching and chopping, a pulsed beam is produced with repetition rate 106.6 ns and typical width of 1–1.5 ns.

Finally, the beam is transported to a target chamber containing the BALiN array. At this point, the beam has a typical diameter of ∼1 mm, with typical currents between 1–10 nA. The limiting factor of the beam currents is due to a limit on the count rate in the detector array and electronics, rather than what can be provided by the 14UD accelerator.

3.2 Targets

The beam impinged onto thin targets of ^{58}Ni, ^{27}Al, $^{28}SiO_2$, C and $(C_2D_4)^n$ in the measurements made in this thesis. In addition, previous measurements for beams of ^{9}Be bombarding thin targets of ^{144}Sm, ^{168}Er, ^{186}W, ^{196}Pt, ^{208}Pb and ^{209}Bi were re-analysed in this work. A summary of all beam-target combinations analysed in this thesis is shown in Table 3.1. In general, several factors are important for good quality breakup measurements. Firstly, the targets must be thin, minimising energy loss in the target. Secondly, the targets should be relatively free of impurities. Scattering from impurities with higher Z than that of the target can overwhelm that from light targets. Ideally, the targets are also free of light impurities: below-barrier measurements on

the target nucleus of interest will likely be above-barrier for light impurities of C and O. Therefore, the light and medium mass targets used here were self-supporting. For reactions with heavy nuclei, carbon backings were used where required. In reactions with heavy targets, breakup from carbon is kinematically distinct from that from the heavy targets. It is not possible to completely eliminate light impurities: for example, the $^{28}SiO_2$ target contains double the number of oxygen atoms compared to the number of silicon atoms. Further, the targets may oxidise over time, and carbon can be deposited onto the surface of the target by the beam if the vacuum in the target chamber is poor. In Chap. 4, kinematic methods for the removal of light impurities will be discussed; these methods are taken into account in the determination of cross-sections in Chap. 6. Where backings have been used, they have been placed downstream of the target material of interest, minimising the effect of energy loss of the beam in the backings.

3.3 Experimental Apparatus: The ANU BALiN Array

Breakup fragments produced in the reactions listed in Table 3.1 were detected with BALiN. BALiN is composed of four 60° wedge-shaped Double-sided Silicon Strip Detectors (DSSDs)[2]. The detectors are mounted on either one or two central hubs, and tilted at an angle of 45° towards the beam axis so as to increase their angular coverage. Depending on the kinematics of the reaction, they are mounted in one of two configurations: either with all four detectors at scattering angles greater than 90° – in the back angle "lampshade" configuration, shown in Fig. 3.2a, c; or with a pair of detectors at forward scattering angles and the other pair at back angles – in the "front-back" configuration, shown in Fig. 3.2b, d. These configurations will be discussed in more detail in Sect. 3.3.1. A summary of the experiments analysed in this thesis can be found in Table 3.2. With the exception of the BEX run, all experiments were performed during the course of this thesis work.

The distance between the target and each hub could be varied, resulting in different angular coverages and angular resolutions from run to run. Before each run, the array was aligned along the beam axis via an optical alignment telescope. To aid in beam tuning, an aperture with a diameter of 2 mm was placed either on the downstream hub (in the front-back configuration) or on the target ladder (in the lampshade configuration) to ensure that the beam is travelling centrally along the beam axis. The aperture on the downstream hub was fixed in place throughout the experiment, while the aperture on the target ladder was replaced by the target after beam tuning. The aperture was placed on the downstream hub in the front-back configuration to avoid high intensity elastic scattering from the edge of the aperture impinging on the detectors placed at forward angles.

The detectors, labelled A through D, are identical save for their different depletion voltages and deadlayers. Detectors A, B and D are fully depleted at −90 V, while

[2]Design MMM, Manufactured by Micron Semiconductor Limited, Sussex, UK.

Table 3.1 Summary of target-beam combinations performed for this work

Beam	Target	Backing	Areal density (μg cm^{-2})	Beam energies (MeV)	E_{CM}/V_b
^{7}Li	$(^{nat}C_2D_4)_n$	Self-supporting	115,131	2.8	1.09
	^{nat}C	Self-supporting	25	4.5	0.90
	^{27}Al	Self-supporting	25	6.75	0.88
				7.5	0.97
	$^{28}SiO_2$†	Self-supporting	50,80	6.75	0.81 (^{28}Si)
				7.5	0.90 (^{28}Si)
				4.5	0.78 (^{16}O)
	^{58}Ni	Self-supporting	60	11.7	0.86
				13.1	0.96
	^{144}Sm	20 μg cm^{-2} C	250	9.70	0.29‡
	^{197}Au	Self-supporting	200	13.1	0.45‡
^{9}Be	$(^{nat}C_2H_4)_n$	Self-supporting	90	2.2	0.24§
	$(^{nat}C_2D_4)_n$	Self-supporting	90,130	2.2	0.50
	^{nat}C	Self-supporting	25	2.2	0.30§
				6.6	0.90
	^{27}Al	Self-supporting	25	8.90	0.82
				10.0	0.93
	^{28} SiO_2	Self-supporting	80	10.0	0.86
				11.0	0.95
	^{144}Sm	20 μg cm^{-2} C	100	25.0	0.85
				28.0	0.94
	^{168}Er	20 μg cm^{-2} C	50	28.0	0.80
				31.0	0.89
	^{186}W	20 μg cm^{-2} C	80	28.0	0.75
				31.0	0.83
				34.0	0.91
	^{196}Pt	20 μg cm^{-2} C	120	25.0	0.65
				28.0	0.73
				31.0	0.80
				34.0	0.88
	^{208}PbS	20 μg cm^{-2} C	80	28.0	0.70
	^{209}Bi	Self-supporting	400	31.0	0.77
				34.0	0.85
				37.0	0.92
				28.0	0.69
				31.0	0.76
				34.0	0.84
				37.0	0.91

$*$ E_{CM} has been corrected for energy loss through the target half-thickness
† Used as a Si and as an O target
‡ For solid angle normalisation
§ Used to examine contribution of contaminant H nuclei to spectra in measurements of $(^{nat}C_2D_4)_n$

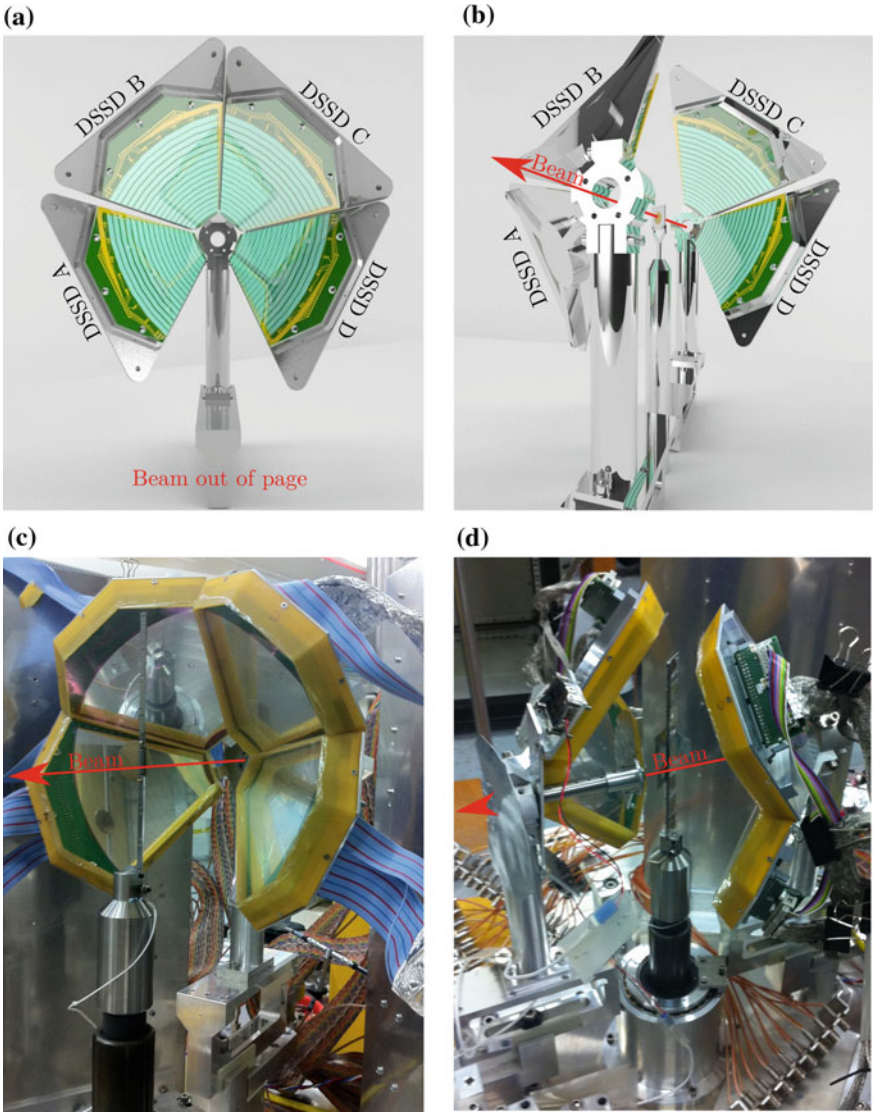

Fig. 3.2 CAD drawings and photographs of the BALiN array in the "lampshade" (**a**, **c**) and "front-back" (**b**, **d**) configuration. The array is composed of four wedge-shaped DSSDs, denoted A through D, angled at 45° towards the beam axis. The photograph of the BALiN array in the lampshade configuration (**c**) shows the target ladder with a mixed α source for energy calibration, while the target ladder loaded with targets is shown in (**d**)

Table 3.2 Summary of experimental runs, with date of run, beams, targets, configurations and whether or not the beam was pulsed

Run	Date	Beams	Targets	Configuration	Pulsed beam?
BEX	6/2008	^{9}Be	^{144}Sm, ^{168}Er, ^{186}W ^{196}Pt, ^{208}Pb, ^{209}Bi	Lampshade	No
LIBEX	8/2013	^{7}Li, ^{9}Be	$^{28}SiO_2$, ^{27}Al	Lampshade	Yes (^{7}Li) No (^{9}Be)
BELICK	9/2013	^{7}Li, ^{9}Be	C, $(^{nat}C_2D_4)_n$ $(^{nat}C_2H_4)_n$	Front-back	Yes
LIAL	4/2014	^{7}Li	C, ^{27}Al, $^{28}SiO_2$, ^{58}Ni	Front-back $\theta > 55°$	Yes
RDUX	1/2015	^{7}Li, ^{9}Be	^{27}Al, $^{28}SiO_2$, ^{58}Ni	Front-back $\theta > 60°$	Yes

detector C is fully depleted at −20 V across the detector. A 0.7 μm thick polyethylene terephthalate (PET) film was placed in front of each detector to stop low-energy electrons produced during collisions. Further, to prevent back-scattered particles from downstream obstacles from reaching the detectors, an aluminium mask was placed behind the targets (in the lampshade configuration) or behind the downstream hub (in the front-back configuration). When the array was used in the front-back configuration with targets of $Z \geq 13$, an additional aluminium mask was mounted on the downstream hub so as to block the most forward arcs from experiencing a large elastic flux. This limited the angular coverage of the array to $\theta > 55°$ for the LIAL run, and $\theta > 60°$ for the RDUX run.

To provide beam normalisation, two small ion-implanted monitor detectors were placed at forward angles, where the elastic yield will follow Rutherford expectations. This allowed experimentally determined breakup cross-sections to be normalised to the precisely known Rutherford cross-section (see Sect. 2.3.1). Further, to characterise the data acquisition dead time, a pulser signal was introduced into an arc and sector of each DSSD, triggered by one of the monitor detectors. The detector electronics will be described in Sect. 3.3.3.

Each DSSD is segmented into sixteen arcs (each 6.4 mm wide) on the junction side of the detector, and eight sectors on the ohmic side (each of which subtends 6.8° in the plane of the detector). The intersections between arcs and sectors give an effective pixelisation of 128 pixels for each DSSD. The DSSDs are 400 μm thick and have a total active area of 80 cm^2, with an outer radius of 135.1 mm and an inner radius of 32.6 mm. To provide a good electrical contact for charge collection, each detector has an 0.2 μm thick layer of Al sputtered on the surface.

Semiconductor detectors, such as the ion-implanted monitor detectors or the DSSDs of BALiN, all follow same general principle. By doping a crystal of a semiconducting material (here silicon) with impurities, imperfections are created in the crystal lattice. Depending on the impurity, this will produce either a p- or n-type

semiconductor, with an excess of positive charge carriers (holes) or negative charge carriers (electrons), respectively. If the dopant produces an n-type semiconductor it is a "donor". If it produces a p-type semiconductor, it is an "acceptor". By bringing the two types of semiconductor in contact, a junction diode is created. At the junction of the two semiconductors, the electrons from the n-type semiconductor diffuse into the p-type and combine with the holes, and vice-versa. This diffusion results in a central area that is depleted of charge carriers. Outside this area, the diffusion of charge carriers results in ionised donor and acceptor sites, resulting in an electric field. This field brings the diffusion of charge carriers (into the depletion region) to equilibrium with the reverse drift of charge carriers. If a large reverse bias is applied, the size of this electric field increases, and so increases the size of the depletion region. This makes charge collection more efficient and reduces noise [2].

When heavy charged particles are incident on the silicon detector, they deposit energy in the material of the detector. The energy deposition per unit length (the "stopping power") dE/dx is commonly given by the Bethe-Bloch equation. For high velocity ions in the non-relativistic limit, dE/dx is inversely proportional to the energy of the incoming particle E_i, which has an ionic charge z_i and mass A_i, and the atomic number Z_d and atomic mass A_d of the stopping material (here, Si) such that [3]:

$$-\frac{dE}{dx} \propto \frac{z_i^2 Z_d A_i}{E_i A_d}. \tag{3.3}$$

We will return to the Bethe-Bloch equation in later sections of this chapter. When energy is deposited in the depletion region of the silicon detector, electron-hole pairs are created, which then move in opposite directions due to the electric field. This produces a pulse that is proportional to the energy lost by the incoming particle, which is then delivered to the pre-amplifiers via a readout from the end of each arc and sector in the DSSD.

The detector array and pre-amplifiers[3] are located inside a multi-purpose scattering chamber, pumped to 1.3×10^{-5} Pa. The pre-amplifiers are located in the vacuum chamber close to the DSSDs to reduce capacitive load, which introduces noise into the system.

3.3.1 Detector Configurations

As mentioned briefly in Sect. 3.3, the BALiN array was used in two configurations in this work. In the first, all four DSSDs were placed at backward angles, and in the second, two detectors were placed at forward angles, and two at backward angles. These configurations were motivated by consideration of the varying angular distribution of breakup fragments for targets with masses that span the periodic table, from ^{2}H to ^{209}Bi.

[3]Model MPR-16, mesytec GmbH & Co. KG, Putzbrunn, Germany.

Prior to this work, all breakup measurements using BALiN were made on heavy targets ranging from ^{144}Sm to ^{209}Bi [4–8]. In measurements with these targets, the breakup fragments have relatively small opening angles, and peak in intensity at backward angles (see for example, p. 110 of Ref. [6]). In addition, placing the detectors at forwards angles is damaging due to the large flux of elastic scattered beam at forwards angles in reactions with heavy targets. Therefore in reactions with heavy targets, the BALiN array was used in the lampshade configuration.

In lighter systems, the angular distribution of breakup fragments becomes much more broad. To guide the location of BALiN, distribution of breakup fragments had to be simulated. In particular:

1. We are interested in the kinematic signatures of breakup that occurs prior to the distance of closest approach. The results of Ref. [9] indicated that the opening angle of the fragments is an important observable. The BALiN configuration should be such that it is sensitive to breakup that results in a large range of opening angles.
2. We are interested in the fraction of direct breakup that occurs in these light systems. It is essential then that BALiN is efficient for direct breakup. This is of particular concern due to the negative Q-value of direct breakup, compared to transfer-triggered breakup, which generally have positive Q-values. The angular distribution of direct breakup will differ to that from positive Q-value transfer-triggered breakup.
3. In reactions of ^{9}Be and ^{7}Li with d, the beam energies are very low relative to the Q-value of the transfer-triggered breakup process. The kinematics of breakup are the dominant factor determining the distribution of fragments. Since we are most interested in the relative populations of the 0^+, 2^+ and 4^+ states, it is important that BALiN is sensitive to these states, which may result in very different angular distributions and fragment-fragment correlations.

These requirements are fulfilled when BALiN is placed in the front-back configuration. The requirement of sensitivity to a large range of opening angles is trivially fulfilled by a front-back configuration. In regards to the second requirement: in Fig. 3.3, (θ_1, θ_2) distributions simulated using KaitKin are shown for the direct breakup $^{7}\text{Li} \rightarrow \alpha + t$ after population of the 4.652 MeV $\frac{7}{2}^-$ state at below-barrier energies in interactions with ^{209}Bi, ^{58}Ni and ^{27}Al. As the mass of the target decreases, the (θ_1, θ_2) distribution moves to more and more forward angles, and the relationship between the fragment scattering angles approaches $\theta_1 = 180° - \theta_2$ as the energy of the beam approaches the energy threshold for direct breakup. It is apparent from these distributions that, to be sensitive to direct breakup in light to medium mass targets, it is necessary to have a pair of detectors at forward scattering angles and a pair of detectors at backward scattering angles.

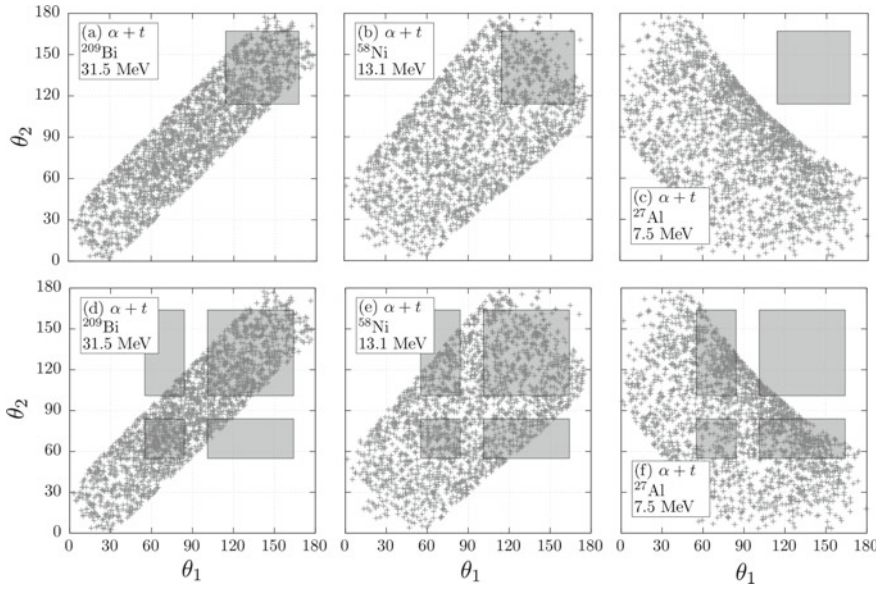

Fig. 3.3 The (θ_1, θ_2) distribution, simulated using KAITKIN, of direct breakup of ^{7}Li in below-barrier reactions with (**a**) ^{209}Bi, (**b**) ^{58}Ni, and (**c**) ^{27}Al. The shaded box represents the (θ_1, θ_2) coverage of BALiN in the lampshade configuration with hub-target distance as for the work of Refs. [6–8]. Panels (**d**), (**e**) and (**f**) show the same distributions, and the shaded boxes represent the (θ_1, θ_2) coverage of BALiN in the front-back configuration with the hub-target distance that of the LIAL experimental run, where angles forward of 55° were blocked. It is apparent that for interactions with heavy targets, the lampshade configuration is sensitive to direct breakup of ^{7}Li, but as the target mass (and therefore beam energy) decreases, the $\alpha + t$ distribution moves to more forward angles, and the front-back configuration must be used, even though the lampshade configuration will still be appropriate for breakup modes with positive Q-value

For measurements of d(^{7}Li,^{8}Be)n, d(^{9}Be,^{8}Be)t, and d(^{7}Be,^{8}Be)p, we are only concerned with one reaction outcome: the population and decay of ^{8}Be. The relative contributions of the 0^+, 2^+ and 4^+ resonances are of key interest. These resonances have quite different on-resonance energies of 0, 3.03 and 11.35 MeV. Since the energy of the beam is low at 2.8 MeV, and the transfer Q-value of 15.022 MeV is so high, the excitation energy of the projectile-like nucleus will have a large effect on the final distribution of fragments. The predicted (θ_1, θ_2) distributions of the α fragments produced after the decay of ^{8}Be with excitations of 0, 3.03 and 11.35 MeV after the d(^{7}Li,^{8}Be)n reaction, for a ^{7}Li beam energy of 2.8 MeV are shown in Fig. 3.4. As expected, the angular distributions of the fragments are very different, but in all cases, a lampshade configuration is inappropriate and the front-back configuration is more suitable. Thus, to fulfil all of the above requirements, measurements of breakup in interactions of ^{7}Li with light and medium mass targets were made in the front-back configuration.

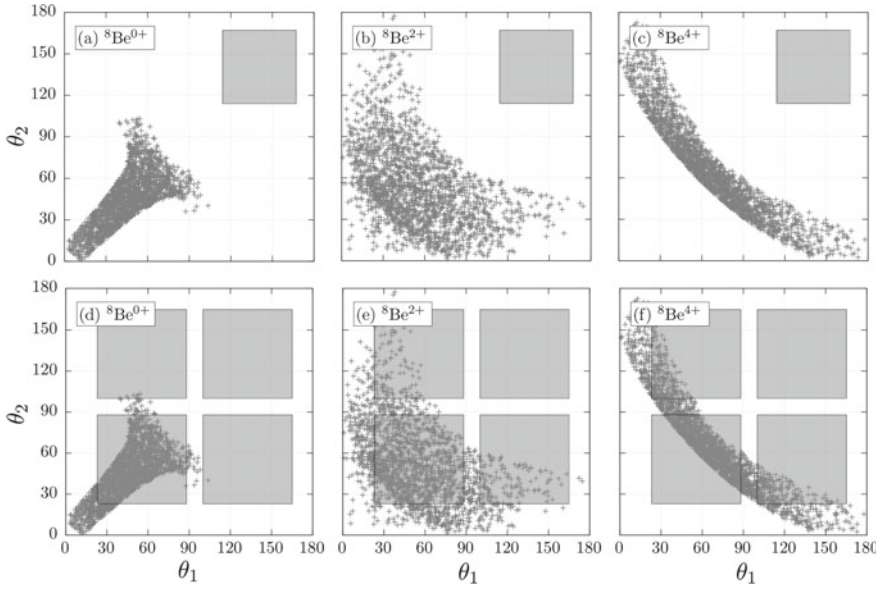

Fig. 3.4 Top row: KAITKIN simulation of the distribution of $\alpha + \alpha$ scattering angles in ^{7}Li + ^{2}H $\rightarrow$ ^{8}Be($\rightarrow 2\alpha$) + n at $E_{\text{beam}} = 2.8$ MeV, populating ^{8}Be with excitation energy corresponding to the resonance energy of its 0^+ ground, first 2^+ and first 4^+ resonances. The shaded box indicates the (θ_1, θ_2) coverage of the BALiN lampshade configuration. It is clear that this configuration is unsuitable for this measurement. Bottom row: The same KAITKIN simulation, with the shaded boxes (θ_1, θ_2) coverage of the array in its front-back configuration as used in the BELICK experimental run, which best suits this measurement

3.3.2 Time of Flight

In breakup after interactions with heavy target nuclei, the reconstructed Q-values and relative energies of the fragments alone are sufficient to enable identification of different breakup modes. This is because the Q-values of the different modes are in general well separated, and the energy of the recoiling nucleus is low. In addition, if there are ambiguities, the energies of the breakup fragments are such that placing one BALiN DSSD in front of another makes a $\Delta E - E$ detector for direct particle identification [6]. As the mass of the target nucleus decreases, the reaction Q-values for different modes become closer together. When transfer populates states in the target-like recoil nucleus, the Q-values for different modes overlap. This meant that for light systems, reconstructed kinematic quantities alone are not sufficient to allow clean separation of different breakup modes.

Some form of direct particle identification is therefore required. The energies of the breakup fragments are in general too low to use the 400 μm thick detectors as a $\Delta E - E$ telescope. This would restrict the energy range to between 7.5 and 11.0

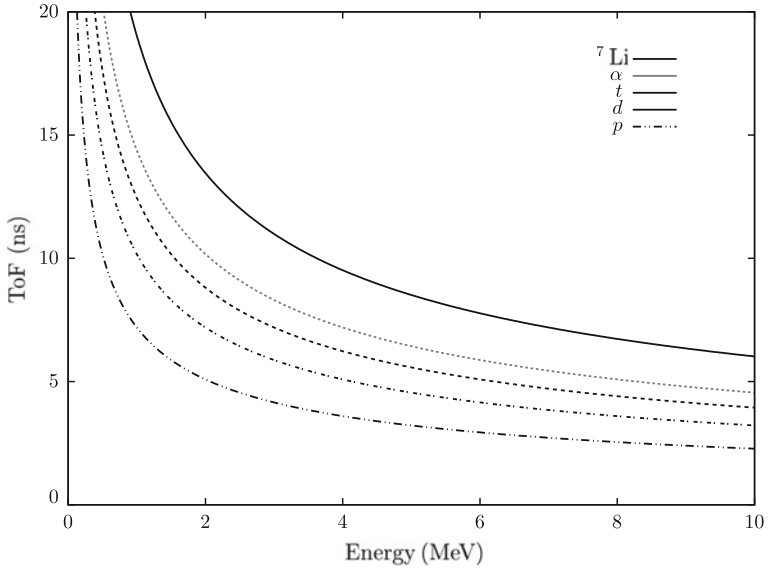

Fig. 3.5 Energy-Time of flight relationship of ^{7}Li, α, t, d and p calculated using Eq. 3.4 over a flight path of 10 cm

MeV for protons, 10.0 and 15.0 MeV for deuterons, and from 11.5 to 17.0 MeV for tritons [6].

Time of Flight (ToF) allows direct particle identification of low energy breakup fragments. By measuring the ToF of each fragment with respect to the pulsed beam over the detector-target distance d, as well as the energy of the fragments E, the relationship:

$$ToF = d\sqrt{\frac{m}{2E}} \tag{3.4}$$

gives a direct measure of the mass m of the fragment. Shown in Fig. 3.5 are calculated Energy-ToF relationships for ^{7}Li, α, t, d and p for a 10 cm flight path. If the ToF resolution is sufficiently good, this relationship provides direct particle identification. However, the requirements of good ToF identification, namely large time differences due to long flight paths, competes with the desire to increase detector efficiency by moving the detectors closer to the target. Therefore, implementing ToF measurements in BALiN allows us to differentiate protons from α particles, but deuterons, tritons and protons don't show sufficiently different times of flight to allow separation of these fragments. Fortunately, the Q-values of transfer-triggered breakup giving $\alpha + p$ pairs are very different from that giving $\alpha + d$ and $\alpha + t$ pairs in all systems studied in this work. This fact enables the use of a combination of reconstructed kinematic quantities as well as direct particle identification via ToF to obtain unambiguous identification of breakup modes.

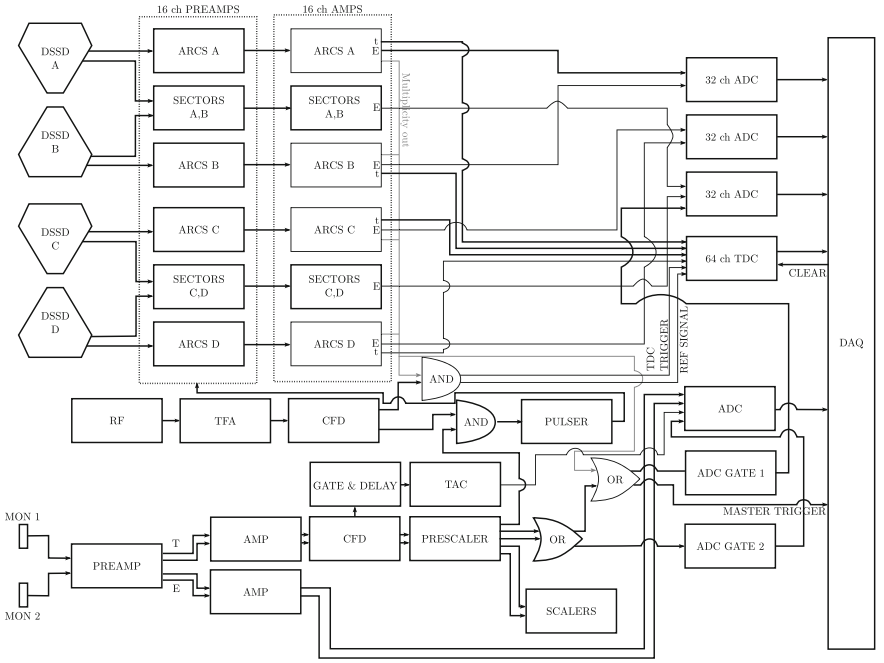

Fig. 3.6 Electronics diagram for the signal processing of BALiN, described in text

It is desirable for future measurements to have direct particle identification that can separate $Z = 1$ isotopes. Such direct particle identification may be achieved by use of a gas ΔE detector in front of the BALiN DSSDs. The close geometry of the BALiN array makes the development of such a detector challenging. Simulations and calculations were performed to maximise ΔE active area, while maintaining the close packing of BALiN. The development of this detector is still in progress.

To enable ToF measurements, pulsed beams were delivered from the 14UD, as described in Sect. 3.1. Calibrating the time of flight requires accounting for the different flight paths from the target to different pixels of each DSSD, as well as a consideration of the different intrinsic pulse shape and rise time of each detector, and the different travel times through the processing electronics. This process will be outlined in Sect. 3.4.6.1, but first the electronic processing of the energy and timing signals delivered from each arc and sector of the DSSD will be discussed.

3.3.3 Electronic Processing

The electronics block diagram for the measurements made for this thesis is shown in Fig. 3.6. The signals from the BALiN array were passed to six 16-channel MPR-16[4]

[4]Mesytec GmbH & Co. KG, Putzbrunn, Germany.

pre-amplifiers, then to six STM-16+[5] amplifiers. Energy signals from the amplifiers were passed to three 32-channel CAEN V785[6] analogue-to-digital (ADC) converters, and the time signals passed to a CAEN V1190B[7] 64-channel multihit time-to-digital converter (TDC).

The MPR-16 preamplifiers, located inside the vacuum chamber, were grounded to a clean earth, separate to the main power earth. The preamplifiers have an 11 MΩ bias resistor. Because of this, the DSSDs were biased[8] such that, when taking into account the voltage drop across the preamplifiers as well as the leakage currents, detectors A, B and D were biased to their fully depleted voltages of −90 V, and C was fully biased to −20 V. The detectors had leakage currents ranging from 1.72 to 3.02 μA, which increased over the course of each experimental run. Therefore, the biases were increased regularly to compensate, maintaining the full depletion of the detectors.

Signals from the preamplifiers were then passed to the amplifiers. Each set of arcs had their own amplifier and preamplifiers, while two sets of sector signals (8 sectors per DSSD) shared one amplifier and preamplifier. Both the preamplifiers and amplifiers used differential outputs to minimise the effect of electronic interference and crosstalk coupling. The multiplicity outputs of the amplifier signals were chained, allowing for hardware based multiplicity selection across all of the DSSDs. An energy above threshold in any arc channel across the array contributes to the multiplicity level, and a logic signal is generated once the number of signals rises to the set multiplicity level. The time interval that defines the multiplicity level was set to 100 ns. In the experiments in this work, the multiplicity level was set to either one ("singles mode") or two ("coincidence mode"). The energy thresholds of the amplifiers were set such that elastic-noise coincidences did not contribute significantly to the rate of the multiplicity two trigger.

Following preamplification and amplification,[9] energy signals from the monitor detectors were sent to a third CAEN V785 ADC. The timing signals from the pre-amplifier were sent to a Phillips Scientific 715 constant fraction timing discriminator.[10] Timing signals from one monitor were then sent to an ORTEC 416A Gate and Delay Generator,[11] then to an ORTEC 567 time-to-amplitude converter (TAC). The TAC output was sent to the 14UD control room to aid beam pulsing setup, and also to the third CAEN V785 analogue to digital converter. In addition, signals from the constant fraction discriminator were prescaled using an EG&G-ESN RD2000 rate divider. The outputs were then sent to scalers in order to monitor data acquisition deadtime, and passed into a Phillips Scientific 755 quad four-fold logic unit. Here,

[5] Differential version. mesytec GmbH & Co. KG, Putzbrunn, Germany.

[6] CEAN S.p.A, Viareggio, Italy.

[7] CEAN S.p.A, Viareggio, Italy.

[8] Using an ORTEC 710 quad 1-kV bias supply, Advanced Measurement Technology Inc., Oak Ridge, Tennessee, USA.

[9] 777 octal variable gain amplifier, Phillips Scientific, Mahwah, New Jersy, USA.

[10] Phillips Scientific, Mahwah, New Jersy, USA.

[11] Advanced Measurement Technology Inc., Oak Ridge, Tennessee, USA.

if a prescaled signal from either monitor detector was present (OR logic), a logic signal was generated. One output was sent to a LeCroy 222 Dual Gate Generator,[12] which generated a gate for the ADC for the monitor signals.

The gate for the BALiN ADCs was generated by the logical OR of the prescaled monitors and the signal generated by the BALiN STM-16+ multiplicity requirement, that is, [BALiN || (Monitor 1 || Monitor 2)]. This was also the master trigger for the data acquisition system (DAQ). The DAQ was developed in-house by N. Withers.

The TDC trigger was generated from the logical AND of the BALiN multiplicity signal and a signal generated from the RF reference signal phase locked to the beam pulses. This coincidence ensured that time signals were referenced to the correct beam pulse, since this signal was also sent to a channel of the TDC (sacrificing the smallest arc of DSSD D) as a reference signal from which to generate the time-of-flight of particles. Finally, when a signal from Monitor 2 occurred, a coincidence with the RF reference signal was made, triggering a BNC model BL2 Fast Tail Pulse generator,[13] used to generate pulses that were fed into the preamplifier channels corresponding to the middle arcs and sectors of each DSSD (8 signals in total). By recording the number of pulser signals presented, the DAQ deadtime of BALiN was monitored.

This setup changed slightly from run to run, though it was very similar for the LIBEX, BELICK, LIAL and RDUX runs. In the BEX run, the beam was not pulsed, so no time of flight information was recorded, and the related logic was simplified. In addition, no ion-implanted monitor detectors were placed at forward angles, and no pulsers were injected into the preamplifiers. Instead, a forward-angle bin in BALiN was used to normalise to elastic scattering. All measurements used in the re-analysis of the BEX data were taken in hardware multiplicity one mode, making each measurement self-normalising.

3.4 Analysis Procedure

Signals from the DAQ were collected using an in-house data collection program (DCP), developed by G.S. Foote. For offline processing, the data were converted to ROOT format [10], using a library written by M.L. Brown. ROOT is an object oriented data analysis framework, written in C++ and developed by CERN. Data files in ROOT format are hierarchical. Each file contains one or more "trees" made of "branches". Branches can be objects of any class, including other trees. Branches contain "leaves" which can be simple objects such as variables, structures, arrays or objects. This data format allows event-by-event access to and processing of data, as well as interactive creation and gating of multidimensional histograms. Scripts for post-processing of data were originally written by D.H. Luong [6], and modified significantly by the author. These scripts make use of a library written by R. du Rietz for efficient access and storage of data.

[12] LeCroy Corporation, Chestnut Ridge, New York, USA.

[13] Berkeley Nucleonics Corporation, San Rafael California, USA.

Data processing had six stages:

1. The raw data were converted to ROOT format from DCP. Each detector had its own branch, with a leaf corresponding to each energy and time channel.
2. Using the known geometry of BALiN, the position of each event was converted from the intersection of an arc and sector to spherical polar coordinates (r, θ, ϕ). This is described in Sect. 3.4.1. The energy signals were calibrated as will be discussed in Sect. 3.4.4. If the time signals were taken in "differences mode"[14] where the RF reference signal was subtracted prior to being recorded, the timing signals were calibrated using the method to be shown in Sect. 3.4.6.1. If the time signals were taken in "raw mode"[15] the RF reference signal was first subtracted in ROOT, followed by the calibration of the time signals. At this stage, an additional software threshold could be applied channel by channel to remove energy and time signals arising from noise.
3. The fact that the pixels of BALiN are defined by intersections of arcs and sectors leads to ambiguities in pixel identification if, for example, two fragments fall on the same arc. The calibrated data were sorted to correct these ambiguities, the process of which will be described in Sect. 3.4.5.
4. The energy loss of the particles entering the array was corrected event by event, and key kinematic quantities were reconstructed. As both the energy loss correction and kinematic reconstruction depends on the charge and mass of the particle, these corrections were evaluated for each possible particle pair, with each breakup mode assigned its own branch in ROOT.
5. Spurious coincidence events due to elastic-random ("elastic-X") coincidences, crosstalk, and reactions from light target impurities were removed using the ToF of particles as well as the reconstructed kinematical quantities. Following this, each valid breakup event was tagged with its breakup mode.
6. The breakup cross-sections and probabilities were extracted.

In the rest of this chapter, the process for stages one through three of the data analysis listed above will be shown. After these stages, the basic quantities measured by BALiN, (θ, ϕ, E, t) are found. The processes of kinematic reconstruction and extraction of breakup modes is the subject of Chaps. 4 and 5, and the extraction of cross-sections will be discussed in Chap. 6 and presented in Chap. 7.

3.4.1 Position Sensitivity

The first part of data analysis of the events gathered in BALiN is to associate each event in a pixel with a coordinate on the sphere (r, θ, ϕ). All energy calibration and kinematic reconstruction relies on these coordinates. The intersection between each arc and sector on a DSSD defines a pixel at the coordinate (R, γ), in the detector

[14] The case for the LIBEX, BELICK and LIAL runs.

[15] As in the RDUX run.

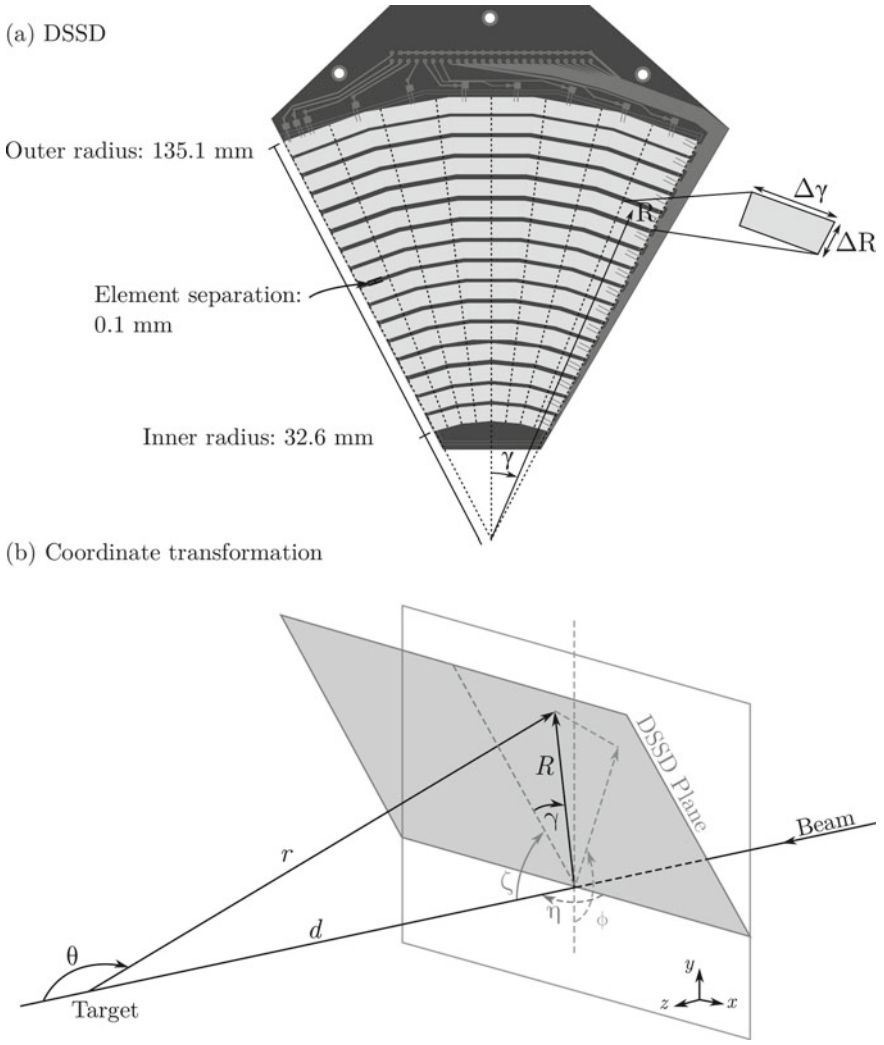

Fig. 3.7 Definition of coordinates used defining the position of pixels in the BALiN array. (**a**) The location of each pixel on each DSSD is defined by the coordinates (R, γ), where R is the radial distance from the focal point of the DSSD wedge, and γ the angle between the middle of the DSSD and the pixel. (**b**) These local coordinates on each DSSD are then transformed into spherical coordinates with respect to the beam-target interaction point by the successive application of rotation matrices, as discussed in text. Adapted from [6]

plane. Here, R is the radial distance from the focal point of the DSSD wedge, and γ the angle between the middle of the DSSD and the pixel, as shown in Fig. 3.7a. The pixels have finite size, parameterised by $(\Delta R, \Delta\gamma)$. As particles can land in any part of the pixel, the location of the particle within the pixel is uniformly randomised.

The coordinates of the pixel with respect to the DSSD are then transformed into Cartesian coordinates within the plane of the detector using the relations

$$x = R \sin \gamma \tag{3.5}$$
$$y = R \cos \gamma \tag{3.6}$$
$$z = 0. \tag{3.7}$$

In a coordinate frame centred on the target, this defines a detector located at the origin, in the (x, y) plane [the definition of (x, y, z) is shown in Fig. 3.7b]. The true location of each DSSD is then defined by a series of translation and rotation matrices. First, any twist in the (x, z) plane by the angle η (in these measurements, this angle was always zero), was accounted for through the relations

$$x \rightarrow z \sin \eta + x \cos \eta \tag{3.8}$$
$$z \rightarrow z \cos \eta - x \sin \eta. \tag{3.9}$$

Secondly, the all detectors lean towards the target by $\zeta = 45°$ in the (y, z) plane

$$z \rightarrow z \cos \zeta - y \sin \zeta \tag{3.10}$$
$$y \rightarrow z \sin \zeta + y \cos \zeta. \tag{3.11}$$

Thirdly, the detectors are distributed in the (x, y) plane, with angle corresponding to the azimuthal angle of the middle of the DSSD ϕ_{mid} (67.68°, 143.38°, 219.68° and 295.68° for detectors A through D, respectively)

$$x \rightarrow x \cos \phi_{\text{mid}} - y \sin \phi_{\text{mid}} \tag{3.12}$$
$$y \rightarrow x \sin \phi_{\text{mid}} + y \cos \phi_{\text{mid}}. \tag{3.13}$$

Finally, the detectors are offset from the origin by

$$x \rightarrow x + x_{\text{offset}} \tag{3.14}$$
$$y \rightarrow y + y_{\text{offset}} \tag{3.15}$$
$$z \rightarrow z + z_{\text{offset}} + z_{\text{hub-target}}, \tag{3.16}$$

where the offsets are as given in Table 3.3 and $z_{hub-target}$ is the hub-target distance.

These coordinates are then converted into spherical polar coordinates by the usual relations

$$r = \sqrt{x^2 + y^2 + z^2} \tag{3.17}$$
$$\theta = \cos^{-1} \frac{z}{\sqrt{x^2 + y^2 + z^2}} \tag{3.18}$$
$$\phi = \tan^{-1} \frac{x}{y}. \tag{3.19}$$

Table 3.3 Summary of the offsets of the focal point of each DSSD from the central point of the face of each hub

	x offset (mm)	y offset (mm)	z offset (mm)
A	−3.29	−0.39	4.97
B	−1.17	3.10	4.97
C	2.72	1.19	4.97
D	2.48	−2.18	4.97

r is the radial distance between the centre of the target and the detected particle, θ is the scattering angle in the laboratory frame, and ϕ the azimuthal angle. If the detector is located in the backward hemisphere, $\theta \rightarrow (180^\circ - \theta)$. These angles are shown in Fig. 3.7b. Examples of the (θ, ϕ) position of breakup events after transformation are shown in Fig. 3.8.

3.4.2 Precision Determination of Spatial Positioning of Array

As the mass of the target nucleus decreases, the energy carried by the recoiling target-like nucleus increases. An increasing fraction of the total kinetic energy of the reaction must therefore be reconstructed. As a result, the sensitivity to the precision of the kinematic reconstruction increases, which depends on (a) the quality of the correction of energy loss through the array, which changes the reconstructed energy and (b) the precision of the spatial positioning of the array, which changes the reconstructed (θ, ϕ), and therefore also the reconstructed energy loss. These results are sensitive to movements of ∼1 mm in light systems. Using CAD models as well as physical measurements of the detector mounts, the offsets of the focal points of the wedge of each DSSD from the beam axis [which defines (x,y) = (0,0)] and the face of each hub (z = 0) were re-determined. These offsets are shown in Table 3.3 and are related to the relationship between the location of the detector PCB and the Si detector focal point. The re-determination of these offsets allowed more reliable reconstruction of quantities such as the Q-value and relative energy of the fragments.

This adjustment in the BALiN positioning resulted in a slight change in the angular coverage of BALiN compared to the ^{9}Be + ^{144}Sm, ^{168}Er, ^{186}W, ^{196}Pt, ^{208}Pb and ^{209}Bi reactions reported in [4, 5]. This adjustment has been incorporated in the re-analysis of these data [11], and changes the elastic yields in the forward arc used for normalisation by ∼9%, thus decreasing the breakup probability by the same factor (as will be discussed in Chap. 6) over the previous work.

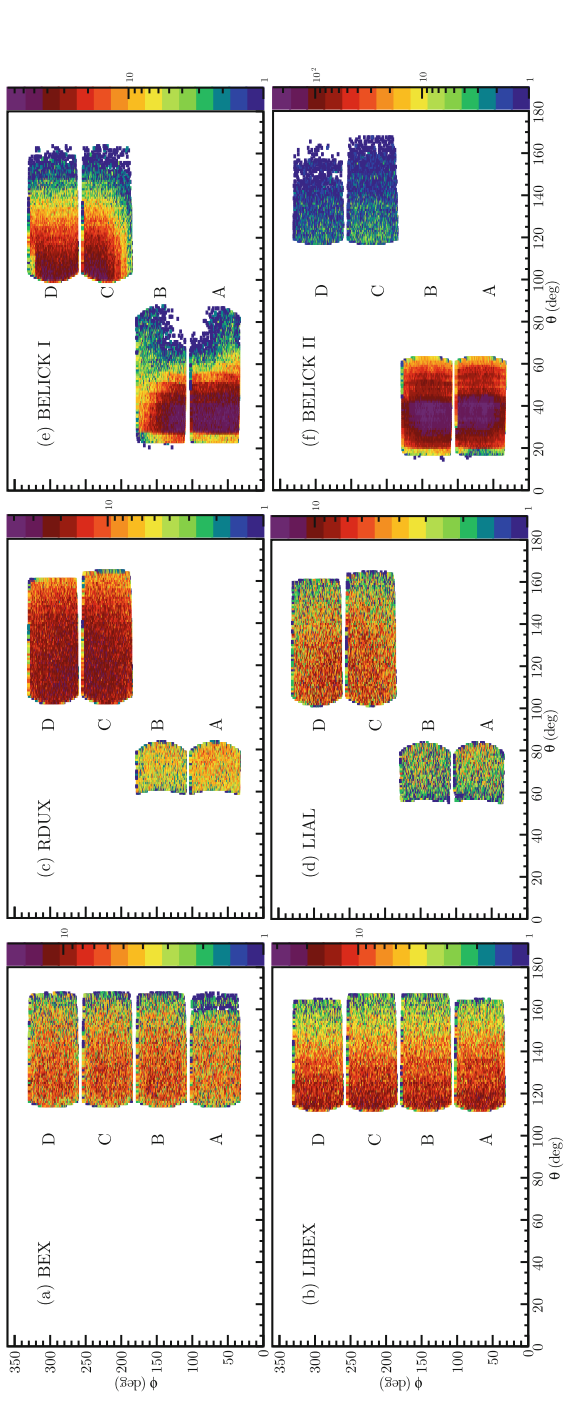

Fig. 3.8 Angular coverage of the BALiN array during the (**a**) BEX (**b**) LIBEX (**c**) RDUX (**d**) LIAL and (**e**), (**f**) BELICK runs. The colour scale represents the number of valid breakup events in each bin. The patterns in intensity reflect the distribution of breakup events combined with the coincidence efficiency of BALiN. Each region in (θ, ϕ) is associated with a particular DSSD, and has been labelled by the identity of the detector. In the case of the BELICK run, two detector-target distances were used, so both are shown here. In the BEX run, faults in the electronics resulted in three arcs (arc 1 and 3 of DSSD A and arc 5 of DSSD B) not contributing to the trigger. The only events in these arcs are due to spurious cross-talk coincidences with neighbouring arcs. In the LIBEX, LIAL and RDUX runs, the smallest arc of one DSSD (DSSD A in LIBEX and DSSD D in RDUX and LIAL) was sacrificed to introduce the RF reference signal into the TDC. As a result, in these runs (shown in panels (**b**), (**c**) and (**d**)) one DSSD is missing its most backward arc. In the RDUX and LIAL runs, the most forward arcs of DSSDs A and B were blocked to protect the detectors from intense elastic flux. In the BELICK I run (panel (**e**)) some measurements were taken where the bottom of the target ladder shadowed DSSDs A and D, near $\theta = 90°$ and $\phi \sim 30°$ and 340°. The gap in events seen in the most backward parts of DSSDs A and B in panel (**e**) is due to the combination of the angular distribution of fragments in ^{7}Li(d,n)^{8}Be reactions, and the coincidence efficiency of BALiN, and is not due to any hardware fault. This will be addressed further in Chap. 8. In all cases, the losses in solid angle coverage due to hardware faults or blocking of the DSSDs are taken into account in the efficiency correction

3.4.3 Energy Loss Correction

As particles pass through the target, PET foil, aluminium layer and detector deadlayer, they deposit energy. The amount of energy lost per unit length dE/dx can be described by the Bethe-Bloch equation, defined in Eq. 3.3. For kinematic reconstruction of the breakup fragments, the measured energy of the particles in BALiN must be corrected for their energy loss. This energy loss correction must be performed for each inactive layer of the array, in reverse order to the sequence of energy loss. Thus, correction begins with the inactive volume of the detectors ("deadlayers") and moves outwards through the aluminium layer, the PET foil, and finally the target.

3.4.3.1 Energy Loss Through PET, Aluminium and Deadlayers

Since the energy loss depends on the distance a particle travels in the stopping material, the angle of incidence β of the particle with respect to the face of the DSSD is important. This angle is shown in Fig. 3.9 and is given by

$$\beta = \cos^{-1}\left(\frac{\vec{n}\cdot\vec{r}}{|r|}\right) \tag{3.20}$$

where $\vec{n}$ is the unit vector normal to the face of each pixel and $\vec{r} = (x, y, z)$ is the position vector of the particle with respect to the intersection between the beam axis and the centre of the target.

Therefore, given a measurement of an energy E in BALiN, the original energy of the fragment E_0 before passing through a thin layer of thickness ΔT made of a given element or compound M can be estimated as

$$E_0 = E + \frac{dE}{dx}(E, M)\frac{\Delta T}{\cos\beta}. \tag{3.21}$$

dE/dx for each material was calculated using an energy loss code written by E. Williams, based on the procedure of Ref. [12]. This energy loss reconstruction is performed for every particle, considering every layer, with the reconstructed energy E_0 of the particle corrected for energy loss through the next layer.

3.4.3.2 Energy Loss Through a Rotated Target

The angle of incidence β of a particle with respect to the face of the DSSD is not the relevant angle to calculate energy loss through the target. Instead, it is the angle between the position vector of the fragment and a vector normal to the face of the target, κ, such that

$$E = E_0 + \frac{dE}{dx}(E, M)\frac{\Delta T/2}{\cos\kappa}, \tag{3.22}$$

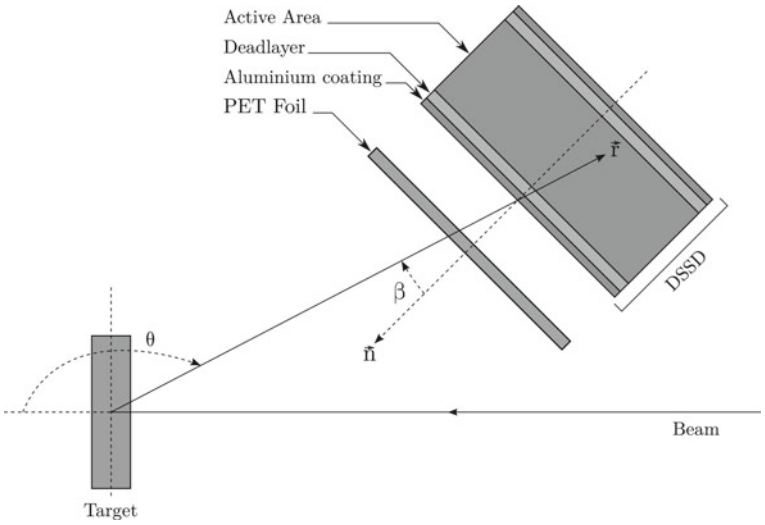

Fig. 3.9 Scattered particles travel through the target, the PET foil layer, the aluminium coating and the deadlayer before reaching the active area of the DSSDs. They lose energy at each step as described by the Bethe-Bloch equation. The energy loss depends on the distance the particle travels in each layer and therefore the angle of the particle with respect to the unit vector normal of the face of the DSSD, β. Adapted from Ref. [6]

where ΔT is the thickness of the target, and the scattering event is assumed to occur in the centre of the target.

In the measurements with the lampshade detector geometry, all the detectors were placed in the backward hemisphere, and the target was placed such that it was normal to the beam axis. In that case, the angle between the vector normal to the face of the target and the position vector of the scattered beam is given by the scattering angle θ. When BALiN is in the front-back configuration, the target was rotated by 45° to minimise energy loss for events that are scattered forwards, and to avoid any shadowing of the detectors by the target frame. κ is then defined by

$$\cos\kappa = \sin\theta_{target}\sin\theta\cos(\phi_{target} - \phi) + \cos\theta\cos\theta_{target}, \tag{3.23}$$

where (θ, ϕ) are the scattering angles of the detected fragment and $\theta_{target} = 45°$ and $\phi_{target} = 90°$ are the angles of the target normal in the same coordinate system as BALiN.

3.4.3.3 Deadlayer Measurement

A significant source of energy loss through the BALiN array is due to the deadlayer of each DSSD outside the active area of the detector where deposited energy is

not collected. Knowing the thickness of the deadlayer is important for accurate energy loss reconstruction. The thickness of the deadlayers depends on several factors during the fabrication process, and also on the bias applied to the detector. When a semiconductor detector with applied reverse bias V is partially depleted, the depletion layer thickness is proportional to $\sqrt{V}$. At full depletion, the size of the deadlayer is minimised. In the previous measurement of the deadlayers of the DSSDs in Ref. [6] the detectors were partially biased, whereas in these measurements they were fully biased. Due to this the deadlayer thicknesses had to be remeasured, and were found to be between 0.95 μm (for DSSD C) and 2.1 μm (for DSSD D), as described in detail in Appendix A.

3.4.4 Energy Calibration

Immediately prior to and immediately following each experimental run, each of the 96 arcs and sectors of BALiN were calibrated by use of the known α energies from a mixed (^{239}Pu, ^{241}Am, ^{244}Cm) α source. These data were combined with elastically scattered beam particles measured during the experimental run. When they reach the active area of the detectors, the elastically scattered particles produced with energy E_0^{elas} have a measured energy E^{elas} of

$$E^{\text{elas}} = E_0^{\text{elas}} - \Delta E_{\text{tgt}}^{\text{elas}} - \Delta E_{\text{PET}}^{\text{elas}} - \Delta E_{\text{Al}}^{\text{elas}} - \Delta E_{\text{deadlayer}}^{\text{elas}}. \tag{3.24}$$

In the α particle calibration, the α particles do not traverse a target, and thus have energy

$$E^{\alpha} = E_0^{\alpha} - \Delta E_{\text{PET}}^{\alpha} - \Delta E_{\text{Al}}^{\alpha} - \Delta E_{\text{deadlayer}}^{\alpha}. \tag{3.25}$$

Here ΔE_i^j is the energy loss of a particle j through the layer i, calculated for the centre of each arc and sector, based on the known geometry of BALiN. The initial energy of the elastically scattered beam E_0^{elas} was calculated using Eq. 2.47. Accounting for energy loss, the measured pulse height in each arc and sector was energy calibrated with respect to the predicted energy of the particles after traversing through the absorbing layers of the array.

The arcs (junction side) of the DSSDs have an energy resolution of $\lesssim$0.1 MeV FWHM, while the sectors (ohmic side) have an energy resolution of ∼0.3 MeV [6]. Therefore, the calibrated arc energies (AE) are used for energy determination.

The relationship between energy and angle provides a verification of the energy calibration as well as the coordinate transformation. The calibrated arc energy of detected particles as a function of their scattering angle θ, for reactions of ^{7}Li with ^{58}Ni at $E_{\text{beam}} = 11.70$ MeV is shown in Fig. 3.10. The intense peak with a maximum of ∼9 MeV corresponds to elastically scattered beam particles. Particles with scattering angles falling forward of 90° correspond to particles falling in detectors A and B, while angles backward of 90° correspond to particles falling in detectors C and D. These energies have not been corrected for energy loss throughout the array.

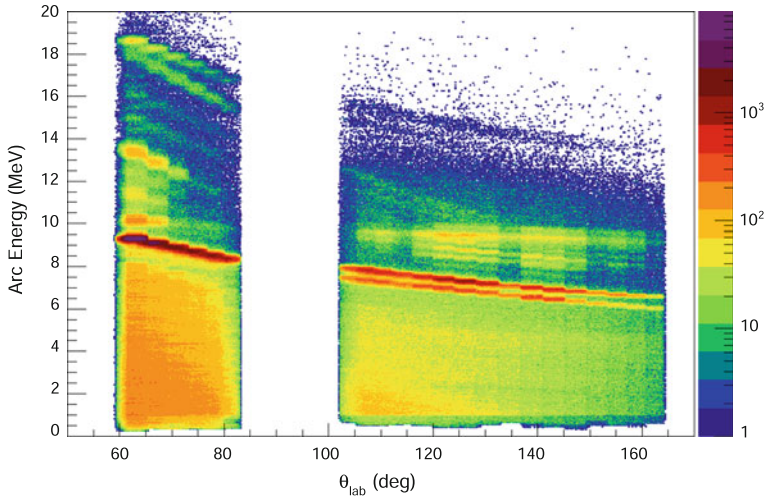

Fig. 3.10 Calibrated energy against scattering angle for reactions of ^{7}Li with ^{58}Ni at $E_{\text{beam}} = 11.70$ MeV. The steps in energy every $\sim 5°$ correspond to particles falling in different arcs, and is due to the randomisation of events within each pixel. The fact that the elastic energies are smoothly decreasing with energy indicates that the energy calibration is consistent from arc-to-arc. These data have not been corrected for energy loss. Due to the large difference in deadlayer thickness in detectors C and D, scattered particles in each detector experience a different amount of energy loss. Because of this, two peaks are seen in the energy at back angles

As a result, the elastic peak splits into two at back angles due to the very different deadlayer thicknesses of detectors C and D (see Table A.1 in Appendix A) and so the scattered beam loses different amounts of energy. The bands of events with well defined energy above the elastic peak correspond to different transfer modes. These data were taken with a hardware multiplicity two requirement, and so any transfer products and elastically scattered beam particles can only be detected if they have a spurious coincidence with another particle, producing the strange patterns of intensity. The events with a broad distribution of energy as a function of angle correspond to breakup events. Compared to Fig. 2.7 (where the measured energies and scattering angles of ^{7}Li in reactions with ^{209}Bi were shown), the different reaction outcomes are not nearly as well separated, due to the increased portion of the total energy carried by the undetected recoiling target-like fragment as the mass of the target nucleus decreases.

3.4.5 Pixel Identification

The fact that the pixels of BALiN are defined by the intersection of arcs and sectors can lead to ambiguity in the exact location and energy of fragments when two coincident

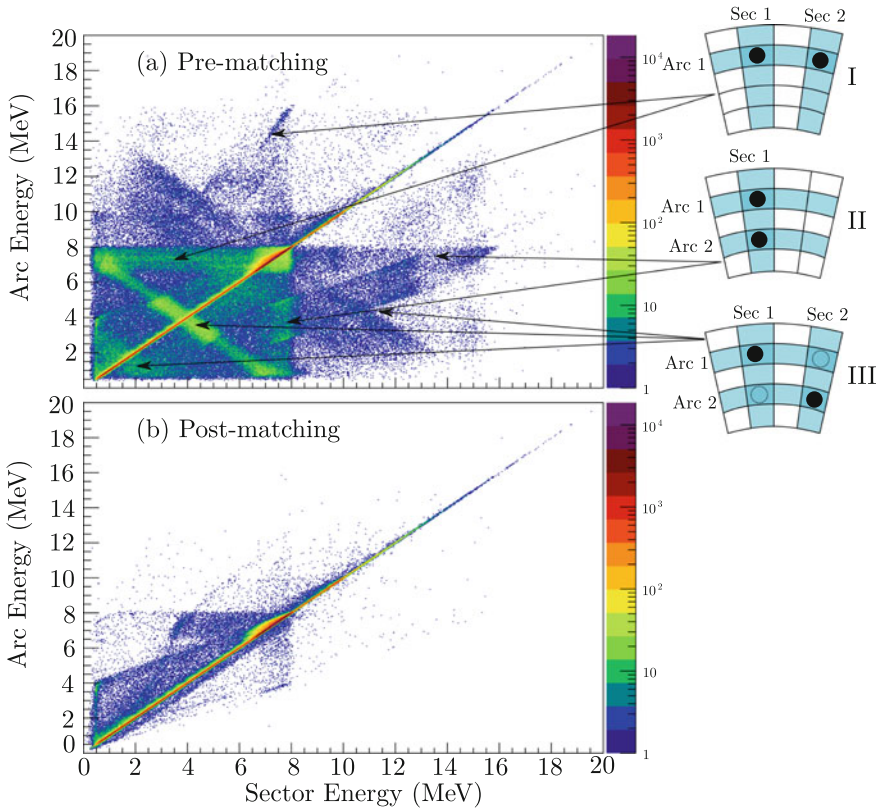

Fig. 3.11 Measured arc energy against sector energy for reactions of ^{7}Li with ^{58}Ni at $E_{\text{beam}} = 11.70$ MeV (**a**) prior to energy matching. Here, the arc energies and sector energies for a given event can be badly mismatched, due to (I) two particles falling in one arc, (II) two particles falling in one sector and (III) "ghost" correlations where, without energy matching, it is unclear which sector signal is associated with which arc signal. (**b**) The same data after energy matching, where the energy mismatches have been corrected, as explained in the text

particles are incident on the same DSSD. For example, both particles may be incident on a single arc, but on two different sectors, and vice-versa (Fig. 3.11 I and II). In these cases, the energy measured by the arc and that in the sector will be mismatched. By requiring that the arc and sector energies be well matched, ambiguities in pixel identification can be removed. The arc energy against sector energy for particles measured after reactions of ^{7}Li with ^{58}Ni at $E_{\text{beam}} = 11.70$ MeV before requiring energy matching is shown in Fig. 3.11a. In this figure, three sources of ambiguity are seen. In the first, two particles fall on one arc, but two sectors. In this case (I), the energy measured in that arc will be the sum of the energy measured in the two sectors. In the second (II), two particles fall on one sector but two arcs, and the energy measured in the sector is the sum of that in the arcs. Thirdly (III), there are events that have arc and sector energies perpendicular to the 45° line in arc energy versus

sector energy. This arises from events that land on the same DSSD, each producing a signal in one arc and one sector. This results in two pairs of arc-sector overlaps; one genuine and one "ghost" pair of correlations.

The arc energy against sector energy of events after the mismatched energies have been resolved is shown in Fig. 3.11b. To resolve events in case I that fall in one arc and two sectors, the energy in the arc was divided in proportion to the measured sector energies. Similarly, when particles fell in two arcs and one sector, the energy in the sector was divided in proportion to the measured arc energies. Finally, the "ghost" correlations were removed by choosing the pair of events with well matched arc and sector energies, deleting the correlations with mismatched arc and sector energies.

After transforming the position of pixels to spherical polar coordinates, energy calibrating each arc and sector taking into account energy loss and correcting mismatched arc and sector energies, the position and energy of detected particles has been extracted. The final basic quantity collected by the BALiN array is the time of flight of the particles.

3.4.6 Particle Identification Using Time of Flight

As discussed in Sect. 3.3.2, direct particle identification using ToF was required to distinguish between different modes of breakup following interactions with medium-mass target nuclei. This was achieved by production of pulsed beams of separation 106.6 ns and width ∼1 ns by the 14UD, as described in Sect. 3.1. The time signals from BALiN were collected, as well as an RF reference signal. These signals were used along with the BALiN multiplicity signal to start the TDC, as described in Sect. 3.3.3. ToF measurements were achieved by measuring all times relative to the RF reference. The CAEN V1190B TDC has a clock frequency of 40 MHz, and so TDC triggers (logical AND of RF and BALiN multiplicity out) have a jitter of one clock cycle: 25 ns. Taking the difference between any two TDC channels, such as the arc times from the RF reference, cancels out this jitter. The 40 MHz clock is multiplied to 320 MHz, with 32 delay elements, giving a 98 ps/channel timing resolution. In the LIBEX, BELICK and LIAL runs, the difference was taken online, whereas in the RDUX run, the subtraction was performed offline, such that

$$ToF = RF - T_{\text{measured}} + 4550, \tag{3.26}$$

where 4550 is an arbitrary offset in channels applied to ensure that all ToF are positive. The measured ToF in this way have time "running backwards" – faster particles have higher channel number.

The measured ToF deviates from the true ToF of a particle between the target and BALiN due to a number of contributing factors, shown schematically in Fig. 3.12. The first is the time offset between the RF trigger, recorded in the TDC, and the moment when the beam interacts with the target T_0. This offset is taken to be constant for a given experimental run, and independent of particle species. The second is an energy

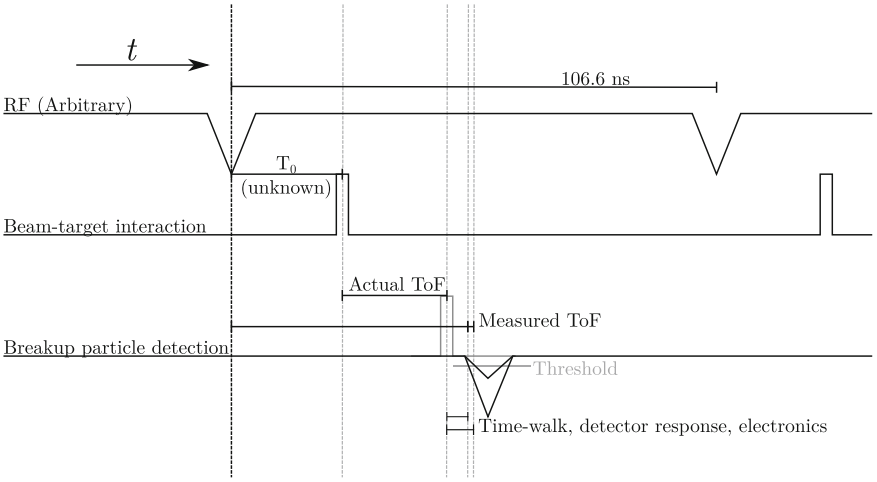

Fig. 3.12 Sketch of the contributions to the measured ToF in BALiN. Compared to the real target-detector travel time, there is a T_0 offset due to the difference between the arrival time of the RF reference signal and the beam-target interaction time. Due to the leading edge discriminator used, there is an additional offset T_{walk}. In leading edge discriminators, timing signals are generated when the energy signal rises above an adjustable threshold. Higher voltage signals will therefore cross the threshold before a lower voltage signal with the same rise time. However, different particles will also have different rise-times, and the arcs have different characteristic responses and go through different electronics channels, leading to an additional offsets T_{detector} and $T_{\text{electronics}}$ (see text)

dependent time-walk. The mesytec STM-16+ amplifiers make use of leading-edge discriminators for timing: timing signals are generated when the energy signal rises above a given threshold voltage, shown schematically in Fig. 3.12. Therefore, the timing signals are energy dependent: when the pulse height is smaller, the timing signal will be generated after that of a larger pulse height, provided that the rise time is the same. This effect is known as "time-walk", T_{walk}. This changes the shape of the energy-ToF curve, away from that given by Eq. 3.4. In addition, it is not necessarily true that the rise time of different particles should be the same.[16] Neither is it true that the rise time of the same particle in different detectors, or in different arcs of the same detector will be the same. In fact, when tested with a mixed-α source used for energy calibration, the rise time of ~5 MeV α particles was found to vary between 25 and 38 ns, depending on the area (and so the capacitance) of the arcs of the DSSD. As a result there is an additional factor T_{detector}, dependent on the arc, detector and particle. Further, there is an offset between timing signals from different arcs due to slightly different travel times through the detector electronics, $T_{\text{electronics}}$. Put together,

$$ToF_{\text{measured}} = ToF + T_0 + T_{\text{walk}} + T_{\text{detector}} + T_{\text{electronics}}. \tag{3.27}$$

[16] Indeed, the difference in pulse shape between different particles in DSSDs has been exploited in direct particle identification via "pulse shape analysis" (e.g. [13]).

These factors are in principle correctable – the ToF for increasingly energetic particles will asymptote to T_0, $T_{\text{walk}}(E) + T_{\text{detector}}(\text{arc}, Z, E) + T_{\text{electronics}}(\text{arc})$ can be characterised using beams of different species on thick targets and compared to predictions of Eq. 3.4, enabling the extraction of absolute ToF. The goal of this work, however, is to separate particles with different masses based on their energy-ToF relationship. As such, determining the *relative* ToF between different particles is sufficient, provided they can be gated on. The task then is to calibrate the ToF spectra, so that the energy-ToF relationship is aligned across a single DSSD.

3.4.6.1 Time of Flight Calibration

Unlike the energy calibration, which was performed for every arc and sector, the ToF calibration was performed for every pixel, as the detector-target distance varies across each arc. This creates 512 separate calibration factors across the array. In each experimental run, the data were calibrated using elastic scattering from a far below-barrier measurement on a heavy target, where the dominant feature in the ToF spectra is the peak due to elastic scattering. By running an automatic peak search on data from every pixel, the positions of the elastic peak in ToF were measured with respect to a pixel in the center of the detector (chosen to be arc 12 sector 4). The difference between these two peaks is T_{offset}, and takes into account the effect of different flight paths, T_0 and $T_{\text{electronics}}$. To account for T_{detector} and T_{walk}, an energy dependent calibration factor was applied in the form A/E, where E was the measured energy and A some constant. This form of energy dependence was chosen by approximating the pulse shape as triangular, meaning that the voltage of the signal is changing linearly when passing E_{thr}, such that

$$T_{\text{walk}} \approx \frac{E_{\text{thr}} * t_{\text{rise}}}{E} = \frac{A}{E}. \tag{3.28}$$

This correction is made with respect to the reference pixel, thus A can be positive or negative. Since this term should depend on the properties of each arc, this term was applied arc-by-arc, and A was chosen by eye to best match the energy-ToF curve of the reference pixel. When plotted as a function of arc number (shown in Fig. 3.13) there is a clear systematic dependence on the arc size. Since this factor is a result of the detector and amplifier properties, these factors are constant from one experimental run to the next.

Together, the calibrated ToF are determined from the measured ToF via the expression:

$$ToF_{\text{calibrated}} = ToF_{\text{measured}} + T_{\text{offset}} + \frac{A}{E}. \tag{3.29}$$

The progressive change in the measured ToF as the aforementioned corrections are implemented is shown in Fig. 3.14. The top panel shows the measured ToF in DSSD B prior to calibration for particles detected in reactions of ^{7}Li with ^{27}Al at 7.5 MeV in

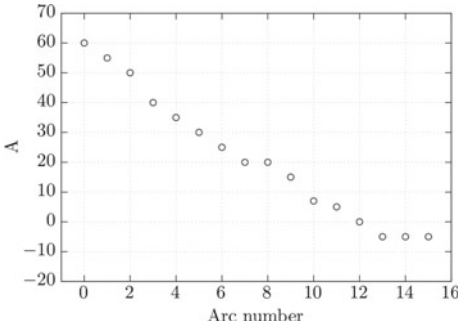

Fig. 3.13 Energy dependent calibration factor A for detector B, plotted as a function of arc number. There is a systematic dependence on the arc number

the LIBEX run. There are sixteen different energy-ToF curves, corresponding to the sixteen arcs of DSSD B. After introducing the T_{offset} correction, the sixteen curves collapse into one, as shown in the second panel. Further shaping due to the energy dependent term yields a correction that is relatively modest, but acts to improve the correspondence of ToF between different arcs, and is most visible at low energies, as can be seen in the bottom panel. As the times are measured with respect to the RF signal, the time axis is reversed. In the figure, it is apparent that there are two main groups in the energy-ToF curve. The particles with highest measured ToF correspond to the lowest real ToF, and are thus protons. The particles with lower measured ToF (the higher real ToF) for the same energy correspond to α particles. The relatively tight group of events at $E \sim 9$ MeV correspond to elastically scattered ^{7}Li.

Shown in Fig. 3.15 is the final ToF for a slice in energy $4 < E < 4.5$ MeV for reactions of ^{7}Li with ^{27}Al at 7.5 MeV in the LIBEX run – the same as for Fig. 3.14c. Here, the ToF resolution and extent of the separation between α particles and protons can be seen. The peaks are separated by 4 ns, and have a FWHM of 2.3 ns. The separation between the peaks is comparable to expectations from Eq. 3.4, where over the 10.5 cm beam-target separation, 4.25 MeV α particles and protons should be separated by 3.66 ns. That the predicted and measured separations differ by 0.34 ns should not be too surprising considering the aforementioned particle-dependent detector response of the DSSDs.

3.4.7 Deadtime

For the extraction of breakup cross-sections, it is necessary to understand the losses of events that can occur after being incident on the DSSDs and being written to file by the DAQ – this is the *deadtime*, and is characterised by

$$D = \frac{N_{\text{recorded}}}{N_{\text{presented}}}, \tag{3.30}$$

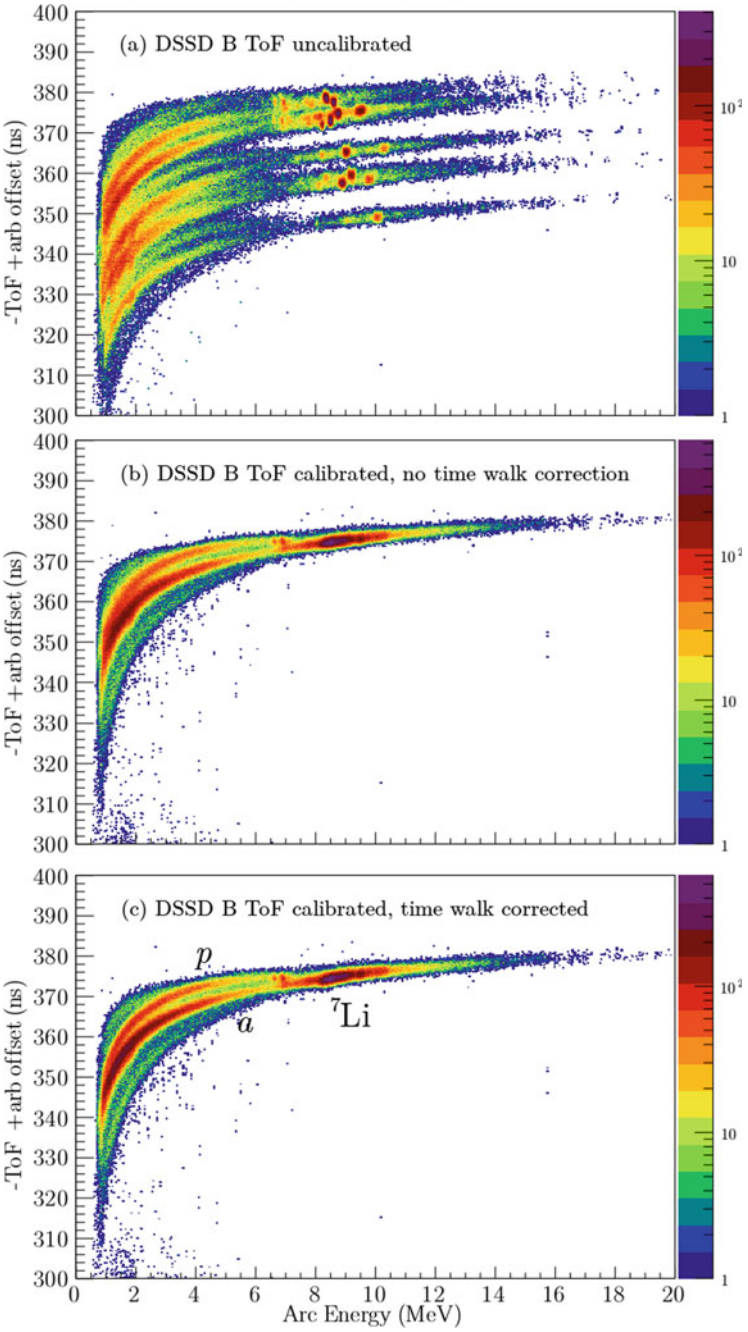

Fig. 3.14 Energy-ToF spectra for particles measured by DSSD B in reactions of ^{7}Li with ^{27}Al at 7.5 MeV in the LIBEX run (**a**) prior to calibration, (**b**) when corrected for the ToF offset and (**c**) when the time walk term A/E is applied

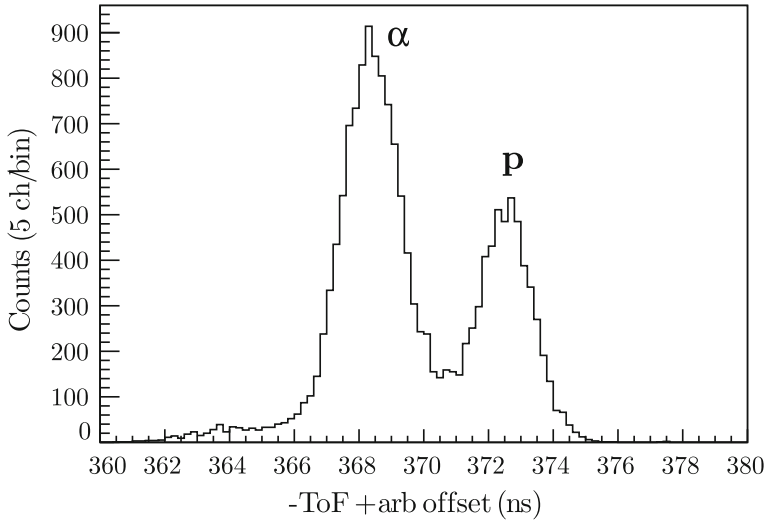

Fig. 3.15 Calibrated ToF for a slice in energy of $4 < E < 4.5$ MeV in a measurement of ^{7}Li with ^{27}Al at a beam energy of 7.5 MeV in the LIBEX run (panel **c** of Fig. 3.14). Peaks have been labelled corresponding to the particle type. The peaks are separated by 4 ns and each have a FWHM of 2.3 ns

where $0 \leq D \leq 1$ is the fractional deadtime, N_{recorded} is the number of signals written to file and $N_{\text{presented}}$ is the number of signals presented by the array. In the BALiN array there are three sources of deadtime: D_{ADC}, associated with the CAEN V785 ADCs that trigger together and record energy signals from BALiN; D_{TDC} associated with the CAEN V1190B TDC that record time signals from BALiN; and D_{Mon} from a separate CAEN V785 ADC that records the energy signals from the monitors. Each of these quantities must be characterised.

3.4.7.1 ADC Deadtimes

To monitor D_{ADC}, a signal from a pulser was injected into the BALiN preamplifiers, shown schematically in Fig. 3.6. To ensure that the pulser is present only when beam is on target, it was triggered by a coincidence between a monitor and the RF reference. The number of pulser triggers were recorded in a scaler. In order to best mimic the experimental signals, the pulsers were injected into one arc and one sector of each DSSD. The comparison between the number of pulsers recorded in the BALiN energy spectra and that recorded in the scalers yields D_{ADC}.

Similarly, D_{Mon} was monitored by sending prescaled monitor counts into a set of scalers, and comparing the number of monitor counts that appear in the monitor spectra and the number of counts in the scalers.

In the BEX run, no pulser was used. As the forward arcs were used to normalise the breakup cross-sections, rather than a monitor detector, $D_{\mathrm{ADC}} = D_{\mathrm{Mon}}$, and so the deadtimes cancel out. In the LIAL and RDUX runs, a probable fault in the monitor CFD resulted in an unreliable number of monitor time signals being produced, changing D_{Mon} and D_{ADC} by a factor of two from run to run. Instead of the monitors, a forward arc was used for normalisation (as in the BEX run), cancelling out the deadtimes. This will be discussed in more detail in Chap. 6.

3.4.7.2 TDC Deadtimes

Section 3.4.6.1 outlined the calibration of the ToF spectra. However, as detailed in Appendix B, not all ToF signals are valid. Invalid signals occur due to either a coincidence event arising from different beam bunches, or one or all of the time and RF signals being zero. Valid breakup events that fall outside the "good" ToF region constitute an additional deadtime, D_{TDC}.

The cause of these invalid ToFs is not immediately obvious – the multiplicity requirement of the STM-16+ amplifiers, and therefore the DAQ trigger, is based on the fast timing signal from BALiN. If an event is recorded by the DAQ, there *must* therefore be a timing signal in the amplifiers. A plausible cause of these zeros is if the time presented to the TDC falls outside the time window (-180 to $+500$ ns relative to the trigger) defined in the TDC.

Regardless of the cause, the loss of valid breakup events due to a gate on ToF for particle identification must be characterised. Naively, this is just the ratio of events that fall within the "good" ToF region to all events. However, this is only true if the likelihood of a coincidence event falling within the good ToF window is independent of event type. To test this, we can consider the θ-E relationship for ^{7}Li + ^{58}Ni at 11.7 MeV, as previously seen in Fig. 2.7. The θ versus E plot, when gated on events where all times are valid, is shown in Fig. 3.16a, whereas the plot when events with one or more invalid ToF is shown in Fig. 3.16b. Clearly, there is an uneven distribution of events that have good ToF compared to those that do not. It appears that it is far more probable for an elastically scattered particle or transfer product detected in coincidence with another particle to miss a ToF signal being recorded than a breakup event. As we are interested in the D_{TDC} *for breakup events*, the naive approach will not work. This presents a challenge: to cleanly identify breakup events, gating on ToF is required, but finding D_{TDC} requires us to identify breakup events without making use of ToF gates. Where there is a large amount of ^{8}Be ground-state breakup, these events can be cleanly picked out in Q-value versus E_{rel}. However, ^{8}Be ground-state breakup is not always present.

Instead, to determine D_{TDC}, we can make use of a good proxy for breakup events that have a strong signature: elastic cross-talk. These events will be discussed in more detail in Chap. 4. Briefly: when particles are incident on arc or sector boundaries, the energy is shared between both arcs or sectors, producing two ToF signals. This

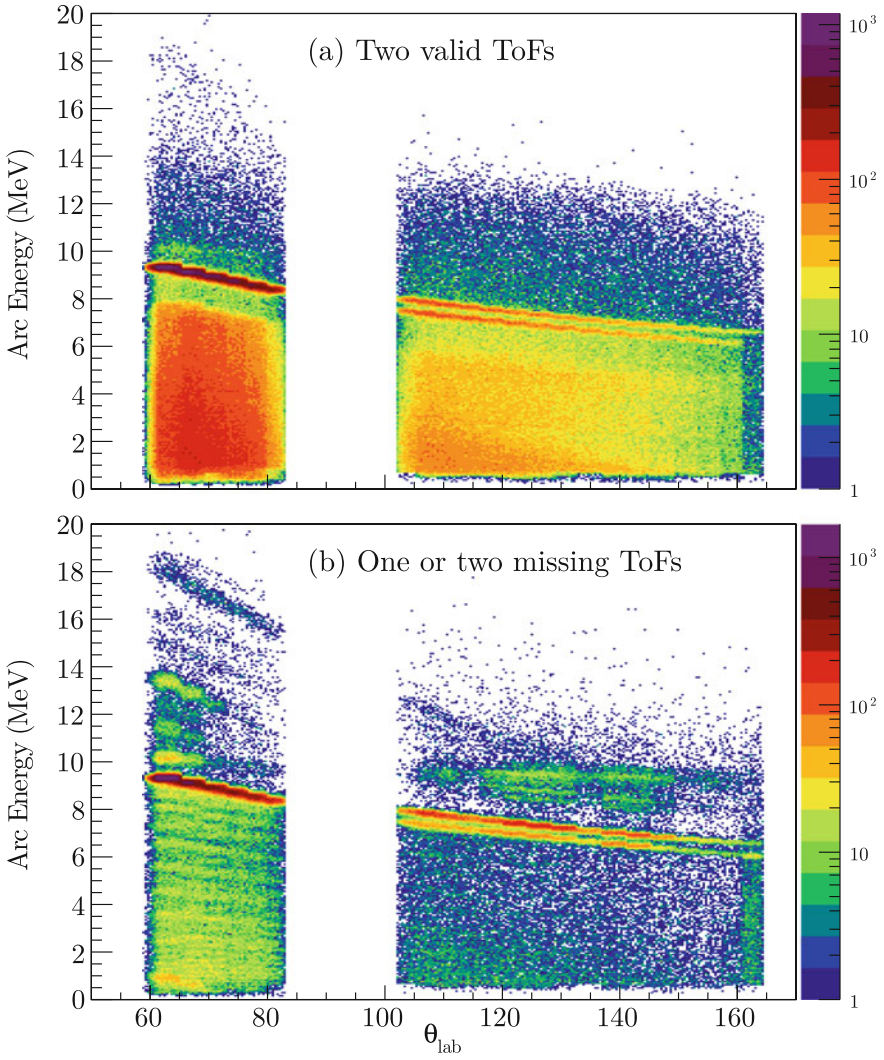

Fig. 3.16 θ-energy relationship for ^{7}Li + ^{58}Ni at 11.7 MeV when **a** gating on coincidence events with two valid ToFs and **b** gating on coincidence events *without* two valid ToFs. It is readily apparent that the distribution of events with and without a valid ToF is inhomogeneous. Therefore, there is some dependence of T_{TDC} on the event type

is closely analogous to breakup from the ^{8}Be ground-state, where the opening angle between the fragments is small. The cross-talk events typically arise from elastic scattering (due to the very high probability of elastic scattering) and so the sum of the energy of the coincidence events should equal that of elastic scattering, i.e.

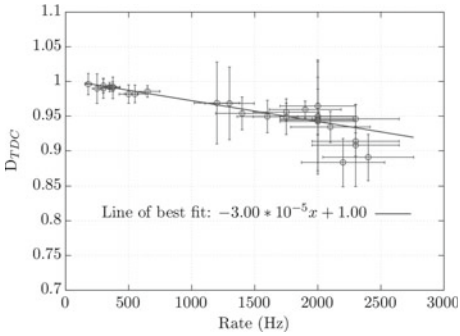

Fig. 3.17 D_{TDC} for the RDUX run, evaluated using cross-talk associated with elastic scattering. Error bars in D_{TDC} are statistical, while error bars in the DAQ rate represent an estimated 15% uncertainty

$E_1 + E_2 = E_{\mathrm{elas}}$. By choosing events that fall in a pair of adjacent arcs,[17] and gating on events with $E_1 + E_2 = E_{\mathrm{elas}}$, a clean set of coincidence two events that mimic breakup were selected without having to gate on a valid ToF. The ratio of events with and without valid ToFs was then examined as a function of DAQ trigger rate (with an estimated uncertainty of 15%), and the results are shown in Fig. 3.17. A line of best fit yields a relationship between D_{TDC} and DAQ rate of $-3.00 * 10^{-5}x + 1.00$ in the RDUX run.[18] Where available, a comparison to D_{TDC} for ground-state ^{8}Be breakup was made to check the reliability of D_{TDC} as determined as outlined above. D_{TDC} determined from ^{8}Be ground-state and cross-talk events give identical D_{TDC} to within 2%. These results indicate that except for very high rates, the loss of valid breakup events through ToF gating is relatively modest and was corrected for.

3.5 Summary

Using the BALiN detector, coincidence measurements of particles produced during breakup reactions of ^{7}Li and ^{9}Be with targets ranging in mass from d to ^{209}Bi were performed at below-barrier energies using beams delivered by the ANU 14UD accelerator. The position sensitivity of DSSDs allowed the extraction of the scattering and azimuthal angles (θ, ϕ). In addition, the energy of the fragments was collected. Through characterisation of the target and the inactive layers of BALiN, these energies can be corrected for energy loss. Finally, the development of time of flight analysis with the BALiN array allowed direct particle identification to be used as a tool to extract breakup leading to fragments of differing masses.

[17] Events in adjacent sectors but in the same arc are suppressed in measurements with a hardware multiplicity two requirement, as coincidence events falling in one arc will only produce a multiplicity one signal.

[18] For reasons that are not entirely clear, neither the LIAL nor LIBEX runs show any TDC deadtime associated with valid coincidence events. This is perhaps due to the fact that in these runs, ToFs were collected by taking the RF differences online, while in the RDUX runs, the difference was taken offline, though the mechanism for this is unclear.

In the following chapter, we will make use of the energy, time of flight and angles of particles detected in coincidence to identify the variety of breakup modes that are present in reactions of ^{7}Li and ^{9}Be. From these, key kinematic quantities are reconstructed that allow the near-target behaviour of breakup fragments to be examined in Chap. 5. It has been shown here that it is possible to characterise the loss of valid breakup events through the data acquisition process, which will allow for cross-sections to be extracted. This is the subject of Chaps. 6 and 7. Finally, further experimental methods will be presented in Chap. 8 examining the experimental conditions required for coincidence measurements of α particles produced in ^{7}Be(d,p)^{8}Be reactions.

References

1. Spear, R.H., Kean, D.C., Esat, M.T., Joye, A.M.R., Fewell, M.P.: Energy calibration of the A.N.U. 14UD Pelletron accelerator. Nucl. Instrum. Methods **147**(3), 455 (1977)
2. Knoll, G.F.: Radiation Detection and Measurement, 4th edn. Wiley, New York (2010)
3. Krane, K.S.: Introductory Nuclear Physics. Wiley, New York (1988)
4. Rafiei, R., du Rietz, R., Luong, D.H., Hinde, D.J., Dasgupta, M., Evers, M., Diaz-torres, A.: Mechanisms and systematics of breakup in reactions of ^{9}Be at near-barrier energies. Phys. Rev. C **81**(2), 024601 (2010)
5. Rafiei, R.: Dynamics of breakup and quasifission - mechanisms inhibiting fusion. Ph.D. thesis, The Australian National University (2010)
6. Luong, D.H.: Mechanisms and time-scales in breakup of ^{6,7}Li. Ph.D. thesis, Australian National University (2012)
7. Luong, D.H., Dasgupta, M., Hinde, D.J., Du Rietz, R., Rafiei, R., Lin, C.J., Evers, M., Diaz-torres, A.: Insights into the mechanisms and time-scales of breakup of ^{6,7}Li. Phys. Lett. B **695**, 105 (2011)
8. Luong, D.H., Dasgupta, M., Hinde, D.J., du Rietz, R., Rafiei, R., Lin, C.J., Evers, M., Diaz-Torres, A.: Predominance of transfer in triggering breakup in sub-barrier reactions of ^{6,7}Li. Phys. Rev. C **88**(3), 34609 (2013)
9. Simpson, E.C., Cook, K.J., Luong, D.H., Kalkal, S., Carter, I.P., Dasgupta, M., Hinde, D.J., Williams, E.: Disintegration locations in ^{7}Li$\rightarrow^{8}$Be transfer-triggered breakup at near-barrier energies. Phys. Rev. C **93**(2), 024605 (2016)
10. Brun, R., Rademakers, F.: ROOT - an object oriented data analysis framework. Nucl. Instrum. Methods Phys. Res. A **389**, 81 (1997)
11. Cook, K.J., Simpson, E.C., Luong, D.H., Kalkal, S., Dasgupta, M., Hinde, D.J.: Importance of lifetime effects in breakup and suppression of complete fusion in reactions of weakly bound nuclei. Phys. Rev. C **93**, 064604 (2016)
12. Ziegler, J.F., Biersack, J.P., Littmark, U.: The Stopping and Range of Ions in Solids. Pergamon, New York (1985)
13. von Schmid, M., Egelhof, P., Eremin, V., Gernhuser, R., Krll, T., Mutterer, M., Pietralla, N., Streicher, B., Weber, M.: First application of pulse-shape analysis to silicon micro-strip detectors. Nucl. Instrum. Methods Phys. Res. A **629**(1), 197 (2011)

Chapter 4
Identifying Breakup Modes

In the previous chapter, the process of making measurements of charged particles in coincidence with the BALiN array was described. It was shown that measurements made with the BALiN array yield information on the energy, position and ToF of detected particles. This information will be utilised in this chapter to reconstruct key kinematic quantities and to identify different modes of breakup in reactions with ^{7}Li and ^{9}Be. Discussion of the kinematic quantities that indicate near-target breakup will be presented in the following chapter. Since not all charged particle coincidences arise from breakup, the first task is to identify spurious coincidence events to enable their separation from genuine breakup coincidences.

4.1 Identification and Removal of Spurious Coincidence Events

There are two principal sources of spurious coincidence events. The first source is random coincidence between unrelated events. As elastic scattering is by far the most likely process, random coincidences between an elastically scattered beam particle and another scattered nucleus X or an electronic noise signal above threshold are the predominant cause of random spurious coincidences. In this thesis, these events are termed "elastic-X" coincidences. The second form of spurious coincidences arise from particles that cross the boundary of either an arc or a sector. In this situation, the energy of the particle is shared between the two adjacent arcs or sectors. This class of spurious event is referred to as "cross-talk" in this thesis.

The relationship between the energy of coincidence fragments was introduced in Sect. 2.8.2, where it was discussed that in reactions with heavy targets, breakup fragments should have energy such that $E_1 + E_2 \approx E_{\text{beam}} + Q$, giving diagonal features

K. J. Cook, *Zeptosecond Dynamics of Transfer-Triggered Breakup*,
Springer Theses, https://doi.org/10.1007/978-3-319-96017-3_4

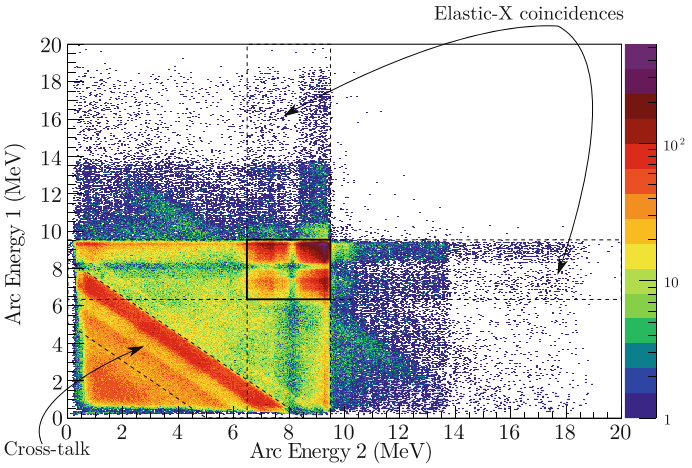

Fig. 4.1 Measured AE_1 against AE_2 of particles detected in coincidence in the reactions of ^{7}Li with ^{58}Ni at $E_{\text{beam}} = 11.70$ MeV, without any energy loss correction performed. The dominant features of this spectrum are spurious coincidences. The vertical and horizontal bands between 6.5 and 9.5 MeV correspond to random coincidences between elastically scattered beam particles and other reaction products, such as transfer products. The diagonal bands between $AE_1 + AE_2 = 5$ and $AE_1 + AE_2 = 8$ MeV correspond to elastic cross-talk. The dip in intensity at ~8 MeV corresponds to the gap in the angular coverage of BALiN between 80 and 100°

in arc energy one vs arc energy two (AE_1, AE_2), (i.e. prior to energy loss correction). An example was shown in Fig. 2.8 for ^{9}Be + ^{209}Bi at $E_{\text{beam}} = 37.0$ MeV, after the removal of spurious coincidences. Shown in Fig. 4.1 is the (AE_1, AE_2) relationship for *all* coincidence events measured in reactions of ^{7}Li with ^{58}Ni at $E_{\text{beam}} = 11.70$ MeV. The dominant features of this spectrum are spurious coincidences.

4.1.1 Elastic-X Coincidences

The vertical and horizontal bands between 6.5 and 9.5 MeV in AE_1 or AE_2 indicated by the vertical and horizontal dashed lines in Fig. 4.1 correspond to random coincidences between elastically scattered beam particles and other reaction products that have a large range of AE_1 and AE_2. Events where both AE_1 and AE_2 have an energy between 6.5 and 9.5 MeV (indicated by the solid box in Fig. 4.1) correspond to the detection of two elastically scattered particles in coincidence. As evidenced by the intensity of events in the box in Fig. 4.1, elastic-elastic coincidences are the most common form of elastic-X coincidence. Events with energy greater than 9.5 MeV correspond to coincidences between elastically scattered particles and transfer products produced in positive Q reactions. Below the energy of the elastic peak, the

elastic-random coincidences are peaked in intensity at low energies, indicating that these events arise from coincidences between elastically scattered particles and low energy particles, such as those produced in scattering from light impurities.

The width of these bands is due to the energy variation of elastic scattering between 60 and 170°. In reactions with heavy targets when the BALiN array is in the lamp-shade configuration, the bands of elastic-X scattering are much more narrow since the energy of the elastically scattered particles do not change significantly between 110 and 170°. The reduction of intensity in the distribution of events near 8 MeV in this measurement is due to the gap in the angular coverage of BALiN between 80 and 100°.

To remove these spurious coincidences, it is sufficient to remove any event where either of the fragments detected in coincidence has the expected energy of elastic scattering (at the angle at which it was detected). This was achieved by drawing tight gates on the (θ_1, AE_1) and (θ_2, AE_2) distributions [an example of which was shown in Fig. 3.10 for ^{7}Li + ^{58}Ni]. As this was done prior to energy loss reconstruction, these gates were drawn separately for each DSSD due to the different deadlayer thicknesses of each DSSD, resulting in 8 gates in total.

Spurious coincidences that occur between two particles, where one of them is *not* a full energy elastic particle, are not removed through this method. In general, these events occur in coincidence with low energy particles, and their reconstructed Q-values are such that they can be removed. However, this does not exclude the possibility of a small background wash of spurious coincidence events.

4.1.1.1 Energy-Degraded Beam Particles

A small contributor to random coincidence events, not readily apparent in Fig. 4.1, is that between energy-degraded beam particles and another particle. These events only appear in downstream detectors when the BALiN array is placed in the forward-back configuration, and do not appear in all such measurements. They likely arise due to scattering from obstructions upstream of the scattering chamber. The (AE_i, ToF_i) relationship of these particles allows these events to be removed. Shown in Fig. 4.2 is the (AE_1, ToF_1) spectrum for DSSD B in reactions of ^{7}Li with ^{58}Ni at $E_{\text{beam}} = 11.70$ MeV. Energy-degraded beam particles appear as a well separated band of particles that are slower than either alpha particles or protons, and join the full energy elastic peak. These events were removed by tight gates on (AE_1, ToF_1) and (AE_2, ToF_2) in each detector.

4.1.2 Cross-Talk

Elastic cross-talk events appear as diagonal bands in Fig. 4.1 between $AE_1 + AE_2 = 5$ and $AE_1 + AE_2 = 8$ MeV. As the spectrum has not been corrected for energy loss it

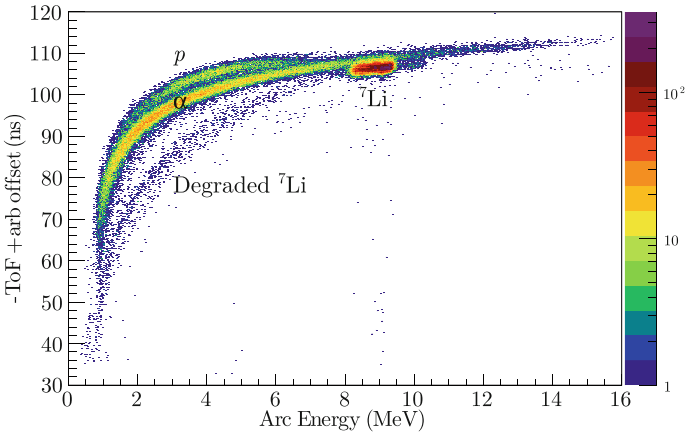

Fig. 4.2 (AE_1, ToF_1) spectrum for DSSD B in reactions of ^{7}Li with ^{58}Ni at $E_{\text{beam}} = 11.70$ MeV. Energy-degraded beam particles appear as a band of events with maximum energy equal to that of elastic scattering, and have ToF slower than α or p, with differences approximately that expected from the mass of the beam

appears that these events have a sum of energy less than that of the elastic peak. When corrected for energy loss, the cross-talk and elastic-X coincidence bands intersect at each axis. As with the elastic-X coincidences, the width of the cross-talk band corresponds to the variation in the energy of the elastically scattered particle across the array.

Cross-talk has the characteristic property that it occurs across arc and sector boundaries, and will only arise in adjacent pixels. Therefore, it can be removed by selecting events that fall in adjacent pixels. In general, coincidence events from breakup will have opening angles such that the chance of valid events appearing in adjacent pixels is small. The exception to this is breakup from ^{8}Be in its 92 keV resonance. In heavy systems, due to kinematic focusing, most of these events will fall in adjacent pixels. Since this breakup is kinematically distinct from cross-talk, gating on the reconstructed Q-value of events that land in adjacent pixels is sufficient to separate ground-state ^{8}Be breakup from elastic cross-talk.

After removal of all spurious coincidences, the (AE_1, AE_2) distribution for genuine breakup events in the measurement of ^{7}Li + ^{58}Ni at $E_{\text{beam}} = 11.70$ MeV is shown in Fig. 4.3. Genuine breakup coincidences comprised 29.7% of the total coincidence yield in this measurement. This yield includes any contribution to breakup from light impurities in the target, the removal of which is the subject of Sect. 4.3.

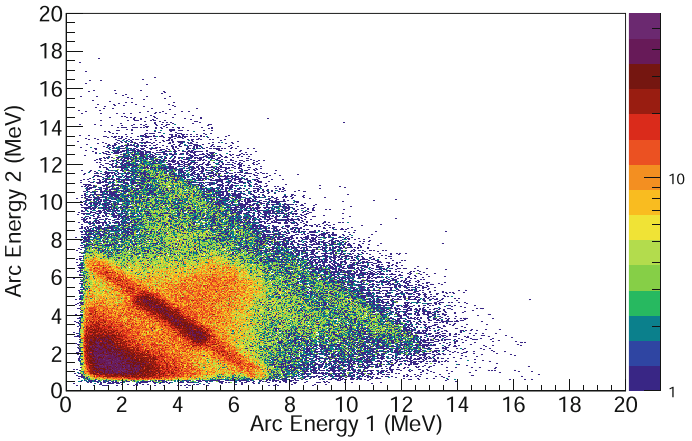

Fig. 4.3 (AE_1, AE_2) distribution for genuine breakup coincidences in the measurement of ^{7}Li + ^{58}Ni at $E_{\text{beam}} = 11.70$ MeV, after removal of spurious coincidence events, but includes breakup from light impurities in the target. In a marked improvement to Fig. 4.1, the diagonal bands of events corresponding to different breakup modes are now evident

4.2 Identification of Breakup Modes

After removing spurious coincidence events, the next task was to identify the breakup mode – that is, the identity of each fragment – associated with each valid coincidence breakup event. This was done using the reconstructed Q-value against E_{rel} together with the ToF of the fragments. In medium mass targets, neither method alone is sufficient to uniquely identify the breakup modes, but together they provide complete separation of breakup modes. The general method for extracting breakup modes will be presented below, and the results for all systems shown in the following sections.

4.2.1 Q-Value Against E_{rel}

The process of kinematically reconstructing Q-value and E_{rel} based on the measured energies and angles of the breakup fragments was described in Sects. 2.8.3 and 2.8.4. Both of these quantities are reconstructed using energy and momentum conservation. Because of this, as seen from Eqs. 2.38 and 2.44, the reconstructed Q-value and E_{rel} depend on the masses of the beam, recoiling nucleus and breakup fragments. Further, the measured energies must be corrected to account for energy loss of the breakup fragments through the target, PET, Al and detector deadlayers. Particles of different mass and charge experience different degrees of energy loss. The energy loss correction also relies on the correct identification of the particles. As a result, to correctly reconstruct the Q-value and E_{rel} for a given event, and so identify its breakup mode, one must first know the breakup mode.

Table 4.1 Ground-state to ground-state breakup Q-values for reactions of ^{7}Li with the targets studied in this work. The breakup modes shown here are those that are expected to occur in these reactions as they either have positive or small negative Q-values

Beam + Target	$Q_{\alpha+\alpha}$ (MeV)	$Q_{\alpha+p}$ (MeV)	$Q_{\alpha+d}$ (MeV)	$Q_{\alpha+t}$ (MeV)
Transfer	$1p$ pickup	$2n$ stripping	$1n$ stripping	–
Breakup	$^{8}\text{Be} \rightarrow \alpha + \alpha$	$^{5}\text{Li} \rightarrow \alpha + p$	$^{6}\text{Li} \rightarrow \alpha + d$	$^{7}\text{Li} \rightarrow \alpha + t$
^{7}Li + ^{58}Ni	9.174	9.437	0.274	−2.467
^{7}Li + ^{28}Si	5.761	8.133	−0.251	−2.467
^{7}Li + ^{27}Al	9.075	6.201	−1.000	−2.467
^{7}Li + ^{16}O	5.219	1.239	−4.582	−2.467
^{7}Li + ^{12}C	1.389	2.173	−3.788	−2.467

To achieve this, the Q-value and E_{rel} for every possible breakup mode leading to two charged fragments is reconstructed for every event. Further, for breakup modes leading to fragments with different masses (e.g. $\alpha + p, \alpha + d, \alpha + t$), every breakup event is reconstructed for each permutation of fragment masses. For example, $\alpha + p$ breakup is reconstructed where the first fragment is assigned the mass of the α and the second fragment is assigned the mass of the p, and vice versa. If the Q-value has been reconstructed for a particular breakup mode, it is indicated as Q_{i+j}, where i, j are the breakup fragments, e.g. $Q_{\alpha+\alpha}$.

It was shown in Fig. 2.11 for the example of ^{7}Li+ ^{209}Bi, that when correctly reconstructed, breakup forms bands in E_{rel} that are constant in Q-value, and the reconstructed Q-value is characteristic of the ground-state to ground-state Q-value and the energy of excited states of the recoiling target-like nucleus. If the correct breakup mode (and so masses of the fragments) has been chosen for a given group of particles, a band of constant Q-value should result at the energy expected from the ground-state to ground-state Q-value of the breakup mode, as well as bands in Q-value with spacing corresponding to the differences between excited states of the recoiling target-like nucleus. For reference, the ground-state to ground-state Q-values Q_{gg} for reactions studied in this work have been tabulated in Tables 4.1 and 4.2 for reactions with ^{7}Li and ^{9}Be, respectively. In addition, if the breakup mode populates a narrow resonance in the projectile-like nucleus (as is the case for breakup populating ^{8}Be and ^{6}Li) the narrow resonance should appear at the expected E_{rel}.

If, on the other hand, the breakup mode has been incorrectly identified, there will still be bands of events, but they will be broad and they will not have a constant Q-value as a function of E_{rel}, and the Q-value will not match expectations. For example, if a breakup mode producing an $\alpha + p$ pair is misidentified as an $\alpha + \alpha$ pair, the reconstructed Q-value will be higher than expected, and the bands in Q-value against E_{rel} will have a negative slope. In the reverse case, misidentified $\alpha + \alpha$ pairs will have a lower reconstructed Q-value than expectation, and the bands in Q-value against E_{rel} will have a positive slope.

The fact that the reconstructed Q-value is sensitive to the assumed breakup mode can be exploited for the identification of breakup modes. This method alone works

Table 4.2 Ground-state to ground-state breakup Q-values for reactions of ^{9}Be with the targets studied in this work. The breakup modes shown here are those that are expected to occur in these reactions as they either have positive or small negative Q-values. Reactions forming $\alpha + p$ fragments in the exit channel have been included as these reaction Q-values are positive for some targets studied in this thesis

Beam + Target	$Q_{\alpha+\alpha}$ (MeV)	$Q_{\alpha+p}$ (MeV)	$Q_{\alpha+\alpha+n}$ (MeV)
Transfer	$1n$ stripping	$1p$, $2n$ stripping	–
Breakup	$^{8}\text{Be} \rightarrow \alpha + \alpha$	$^{5}\text{Li} \rightarrow \alpha + p$	$^{9}\text{Be} \rightarrow \alpha + \alpha + n$
^{9}Be + ^{209}Bi	3.032	−9.970	−1.573
^{9}Be + ^{208}Pb	2.364	−11.996	−1.573
^{9}Be + ^{196}Pt	4.274	−2.386	−1.573
^{9}Be + ^{186}W	3.894	−5.241	−1.573
^{9}Be + ^{168}Er	4.430	−3.981	−1.573
^{9}Be + ^{144}Sm	5.184	−4.031	−1.573
^{9}Be + ^{28}Si	6.901	4.447	−1.573
^{9}Be + ^{27}Al	6.152	7.386	−1.573
^{9}Be + ^{12}C	3.374	−4.049	−1.573

well for the different breakup modes of reactions of ^{7}Li + ^{209}Bi, as shown in Fig. 2.11, and it is sufficient to cleanly identify breakup modes in reactions of ^{9}Be with ^{144}Sm, ^{168}Er, ^{186}W, ^{196}Pt, ^{208}Pb and ^{209}Bi. In reactions of ^{9}Be with targets of ^{144}Sm to ^{209}Bi only two breakup modes are expected to contribute: direct breakup into $\alpha + \alpha + n$ and neutron stripping forming ^{8}Be, which subsequently breaks up into $\alpha + \alpha$ pairs. These modes are well separated in Q, as seen in Table 4.2; as BALiN is not sensitive to n, only $\alpha + \alpha$ pairs can be measured, arising from either breakup mode.

However, when the mass of the target decreases, two factors work against the efficacy of separating different breakup modes by their Q-E_{rel} relationship alone. Firstly, the results of Ref. [1] (shown in Fig. 2.11) indicate that target-like excitations extending to ∼10 MeV may be observed. Therefore, even if ground-state to ground-state Q-values are well separated, bands corresponding to different breakup modes will intersect if the excitation of the target-like recoil is sufficiently high. In particular, the reaction of ^{7}Li with ^{58}Ni has the p pickup breakup mode just 263 keV below the $2n$ stripping breakup mode. These breakup modes will overlap completely in Q-E_{rel} and cannot be separated on this basis. Secondly, as the mass of the recoiling nucleus decreases, the kinetic energy of the recoiling target-like nucleus represents a larger portion of the total energy budget of the reaction. Therefore, an incorrect assignment of breakup mode can result in very broad bands in Q-E_{rel}, as the energy of the recoil will not have been correctly calculated. As a result, very weakly populated breakup modes may appear as a background "wash" of events when incorrectly identified.

The above challenges are illustrated in Fig. 4.4, where $Q_{\alpha+\alpha}$ is plotted against E_{rel} for breakup of ^{8}Be after interactions of ^{7}Li with ^{28}Si at 7.50 MeV. Bands of constant Q appear at the expected values of $Q_{\alpha+\alpha} \sim 5.8$ and ∼5 MeV, indicating that the $\alpha + \alpha$ breakup mode has been correctly assigned for the events that fall within these

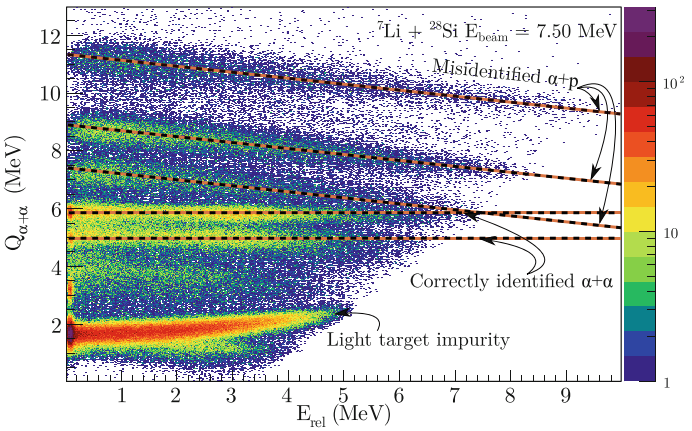

Fig. 4.4 Reconstructed Q-value assuming breakup into $\alpha + \alpha$ pairs ($Q_{\alpha+\alpha}$) for all breakup fragments detected in reactions of ^{7}Li with ^{28}Si at $E_{\text{beam}} = 7.50$ MeV with BALiN in the lampshade configuration. Bands of events with constant Q-value against E_{rel} appear at $Q_{\alpha+\alpha} = 5.8$ and 5 MeV, indicating that the $\alpha + \alpha$ breakup mode has been correctly assigned for the events that fall within these bands. On the other hand, the diagonal bands starting at $Q_{\alpha+\alpha} \sim 11$, 9 and 7 MeV actually correspond to breakup into $\alpha + p$ pairs that have not been correctly reconstructed, as they have been reconstructed with the assumption of the $\alpha + \alpha$ mass partition. The band of events starting at $\sim$1.7 MeV arises from $\alpha + \alpha$ breakup after interactions with a light impurity in the target. Breakup after interactions with light impurities will be discussed in Sect. 4.3

bands. The peak in intensity at E_{rel}= 92 keV, corresponding to breakup from the 92 keV resonance of ^{8}Be confirms this assignment. However, there are a large number of breakup events forming diagonal bands with negative slopes starting at $Q_{\alpha+\alpha} \sim 11$, 9 and 7 MeV. These events are incorrectly reconstructed $\alpha + p$ pairs. These bands are relatively well separated from the $\alpha + \alpha$ breakup, but it is reasonable to suspect that there are $\alpha + p$ pairs originating from reactions with higher target-like excitations that are being masked by the intense $\alpha + \alpha$ bands. It is therefore necessary to use direct particle identification through ToF to separate these events.

The Q-E_{rel} spectrum in Fig. 4.4 shows a sharp diagonal threshold. When BALiN is in the lampshade configuration, as is the case for the data shown in Fig. 4.4, there is a limited θ_{12} acceptance. This results in a limited E_{rel} acceptance that changes with fragment energy, resulting in a diagonal threshold. In the front-back configuration, BALiN has sensitivity to all θ_{12}. Nevertheless, in this configuration there is still a diagonal threshold, though at higher E_{rel}. In the front-back configuration, the diagonal threshold reflects the limit in E_{rel} due to energy conservation. An example of this will be shown in Fig. 4.6a in the context of removal of light impurities.

4.2.2 Time of Flight

As was shown in Sect. 3.4.6, the relationship between energy and ToF of fragments measured in BALiN allows the identification of their mass. The resolution of the detector is sufficient to separate α from p and d, but p and d are not sufficiently distinct in ToF to allow separation of p from d with this method. ToF can then be used to distinguish between breakup producing $\alpha + \alpha$ fragments and that producing $\alpha + p$ or $\alpha + d$ fragments, but $\alpha + p$ and $\alpha + d$ breakup modes are not separated by this method. Fortunately, as shown in Table 4.1, the ground-state to ground-state Q-values for $\alpha + p$ and $\alpha + d$ breakup modes are always separated by more than 5.8 MeV in the systems studied in this work, making identification on the basis of a joint gate on ToF and Q possible. Further, breakup forming $\alpha + d$ will populate ^{6}Li in its 3^{+} resonance state, which is sharply peaked at ~700 keV in E_{rel}.

When Q and E_{rel} is reconstructed, it is always reconstructed on the basis of the *expected* breakup modes: $\alpha + \alpha$ breakup is expected, so events are kinematically reconstructed for this mode. The benefit of direct particle identification is that no assumption as to breakup mode is required. Therefore, unexpected breakup modes can be identified through ToF gating, as will be shown.

To fully identify breakup modes in medium mass systems, identification via Q against E_{rel} and ToF must be combined. The general procedure to identify breakup modes is as follows:

1. After removing spurious coincidences, Q against E_{rel} spectra are generated for each expected breakup mode.
2. If $\alpha + \alpha$ and $\alpha + d$ or $\alpha + t$ are present, a tight gate is drawn around the $\alpha + d$ or $\alpha + t$ bands.
3. In each detector, two dimensional gates on the (AE_1, ToF_1) and (AE_2, ToF_2) curves for protons are drawn. If the $\alpha + d$ or $\alpha + t$ modes are present, a gate for the deuterons and/or tritons is drawn in (AE_1, ToF_1) and (AE_2, ToF_2) in each detector for events within the Q-E_{rel} gate drawn in step 2.
4. Breakup modes are then identified via the possible combinations of gates on protons and deuterons, and the logical not (denoted by "!") of the gates, together with gates on Q against E_{rel} where relevant. These combinations are listed in Table 4.3. The last set of gates – coincidences between two protons or deuterons – completes the enumeration of the possible combinations of gates.

Through this method, breakup modes in the light and medium mass targets studied in this thesis (^{12}C, ^{16}O, ^{27}Al, ^{28}Si, ^{58}Ni) were identified. In reactions of ^{9}Be on ^{144}Sm, ^{168}Er, ^{186}W, ^{196}Pt, ^{208}Pb and ^{209}Bi, and reactions with d (where there is no target-like excitation) it was sufficient to use Q-E_{rel} identification.

As an example of the application of this method, $\alpha + \alpha$ and $\alpha + p$ pairs detected in a measurement of ^{7}Li + ^{28}Si at $E_{\mathrm{beam}} = 7.50$, and identified using ToF and Q-value gates are shown in Fig. 4.5a, b respectively. They are plotted as a function of Q and E_{rel} reconstructed assuming $\alpha + \alpha$ breakup (i.e. $Q_{\alpha+\alpha}$). This is the same data and reconstructed quantities as were shown in Fig. 4.4, prior to ToF identification. It is

Table 4.3 General gating method used to separate breakup modes in light and medium mass targets. Separation is achieved through a combination of gates on Q-E_{rel}, (AE_1, ToF_1), and (AE_2, ToF_2). In heavy and light systems, Q-E_{rel} is sufficient to separate all breakup modes. Exclamation points "!" indicate the logical not of a gate

Q-E_{rel} Gate	Gate on ToF_1	Gate on ToF_2	Breakup mode
$!(Q_{\alpha+d})$	!p	!p	$\alpha+\alpha$
$!(Q_{\alpha+d})$	!p	p	$\alpha+p$
$!(Q_{\alpha+d})$	p	!p	$p+\alpha$
$Q_{\alpha+d}$	!d	!d	$\alpha+\alpha$
$Q_{\alpha+d}$	!d	d	$\alpha+d$
$Q_{\alpha+d}$	d	!d	$d+\alpha$
–	p	p	$p+p$
–	p	p	$p+d$
–	p	p	$d+d$

apparent that the use of ToF to identify the mass of breakup fragments event-by-event is crucial to separate these otherwise overlapping bands in $Q_{\alpha+\alpha}$ against E_{rel}. Panel (c) of Fig. 4.5 shows the same $\alpha+p$ pairs as in panel (b), now plotted as a function of $Q_{\alpha+p}$ and E_{rel}, showing clear horizontal bands. In all panels, a band of events at low Q is present. These events are due to the presence of light impurities in the target, which must be removed.

4.3 Removal of Breakup Originating from Interactions with Target Impurities

If the mass of the target has been misidentified, the Q-E_{rel} bands will have either a positive slope (if the true mass of the target is lighter than what was assumed) or negative slope (if the true mass of the target is heavier than what was assumed). This effect can be seen in Fig. 4.4, where there is an intense band of events starting at ∼1.7 MeV, curving upwards with increasing E_{rel}. The peak in E_{rel} at ∼100 keV indicates that $\alpha+\alpha$ pairs from ^{8}Be have been produced, but it does not have constant Q when reconstructed assuming $\alpha+\alpha$ breakup from ^{28}Si. Instead, these events are due to proton pickup from ^{16}O resulting in ^{8}Be, which subsequently breaks up into $\alpha+\alpha$ pairs. This is not surprising – the target is $^{28}SiO_2$, and the beam energy is above-barrier for reactions with ^{16}O.

In reactions with heavy targets, breakup from ^{16}O or ^{12}C is sufficiently kinematically distinct that reconstructed Q-E_{rel} bands do not overlap with breakup from the heavy nucleus. On the other hand, in medium mass nuclei, as seen in Fig. 4.4, this is no longer the case. The data shown in Fig. 4.4 were taken with BALiN in the lampshade configuration, which is a better configuration to use to minimise the influence of light target impurities. When the array is placed in the front-back configuration, the increased efficiency for detecting breakup pairs from light target impurities results

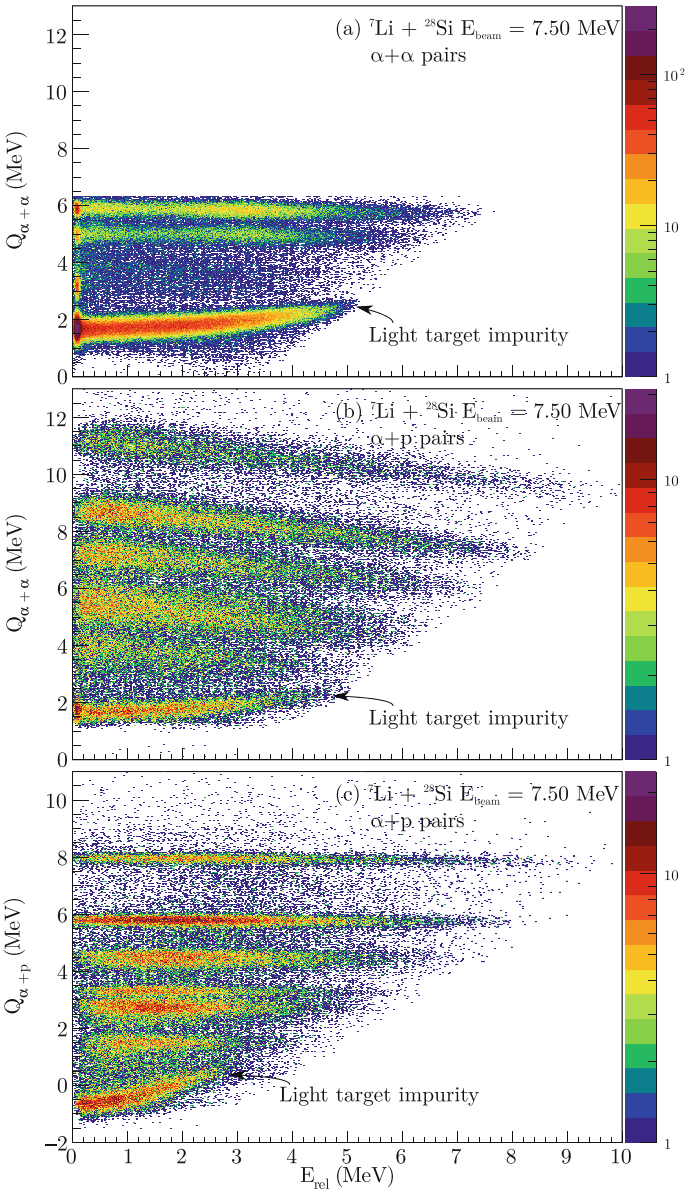

Fig. 4.5 Reconstructed Q-value (assuming the $\alpha + \alpha$ mass partition) against E_{rel} for ToF identified $\alpha + \alpha$ pairs (**a**) and ToF identified $\alpha + p$ pairs (**b**) for breakup fragments detected in reactions of ^{7}Li with ^{28}Si at $E_{\text{beam}} = 7.50$ MeV with BALiN in the lampshade configuration. Figure 4.4, shown previously, contains the sum of events in panels (**a**) and (**b**), prior to separation via ToF. This demonstrates the utility of ToF identification in separating kinematically overlapping breakup modes. Panel (**c**) shows the same $\alpha + p$ pairs, now reconstructed assuming the $\alpha + p$ mass partition, forming clear horizontal bands in Q against E_{rel} indicating that they have indeed been correctly identified. The band of events at low Q arise from breakup after interactions with a light impurity in the target. Breakup after interactions with light impurities will be discussed in Sect. 4.3

in a much higher ratio of breakup from impurities to breakup from the nucleus of interest. Further, the increased efficiency of the detector to low Q breakup from the target of interest results in a larger overlap between breakup that is of interest and breakup from a light impurity.

To identify and remove breakup from light impurities, breakup fragments were reconstructed assuming that they were the result of interactions with the light nuclide of interest. The impurities seen in the targets are typically carbon, oxygen and nitrogen. As an example, a measurement of breakup after interactions of ^{7}Li with an ^{27}Al target at $E_{\text{beam}} = 6.75$ MeV is presented in Fig. 4.6. This measurement represents a "worst case" for contamination due to light impurities as this target showed the largest presence of these impurities, and the data were taken with BALiN in the front-back configuration.

The reconstructed data assuming $\alpha + \alpha$ breakup from the ^{27}Al target is shown in Fig. 4.6a. Narrow horizontal bands do appear at the expected $Q_{\alpha+\alpha}$ values for $\alpha + \alpha$ breakup from ^{27}Al. However, a number of intense bands of events do not reconstruct in a manner that is consistent with breakup from ^{27}Al, and are due to lighter impurities. Reconstructing the data assuming that the $\alpha + \alpha$ breakup pairs result from interactions with ^{16}O provides the spectrum shown in Fig. 4.6b. The straight band at $Q \sim 5.5$ MeV corresponds to $\alpha + \alpha$ breakup from ^{16}O, populating ^{15}N in its ground state. Another band appears at ~0.5 MeV, which could be a result of breakup populating an excited state of ^{14}N, however, this band is not very straight. Instead, if the reaction is assumed to be with ^{12}C, then the band appears at 1.8 MeV and is straight, as seen in Fig. 4.6c. Thus, these events are most likely to correspond to $\alpha + \alpha$ breakup after interactions with ^{12}C leaving ^{11}B in its ground state. A fairly weak band of $\alpha + \alpha$ events at $Q_{\alpha+\alpha} \sim 10$ MeV is reconstructed when breakup is assumed to occur after interactions with ^{14}N, shown in Fig. 4.6d. Finally, $^{8}\text{Be} \rightarrow \alpha + \alpha$ breakup is not the only positive-Q breakup mode following interactions of ^{7}Li with light impurities. Shown in Fig. 4.6e are the same data, reconstructed assuming $\alpha + p$ breakup pairs were produced after interactions of ^{7}Li with ^{12}C. A sharp band of events in $Q_{\alpha+p}$ results at the expected Q for $^{5}\text{Li} \rightarrow \alpha + p$ breakup after interactions of ^{7}Li with ^{12}C. Reconstructing assuming $p + \alpha$ breakup from ^{12}C also yields a sharp band.

To most cleanly remove events due to reactions with target impurities, it is desirable to be able to draw a tight gate around data of interest. As shown in the sequence of panels in Fig. 4.6 this is fulfilled by the reconstructed Q-E_{rel} spectra. However, when ^{8}Be is populated in its ground-state resonance, the resulting 92 keV peak reconstructed in E_{rel} is almost independent of the assumed target mass. It is therefore difficult to identify whether or not breakup populating the ^{8}Be ground state results from interactions with the target or with a light impurity. Instead, breakup resulting from interactions with light impurities was removed by gating on Q against θ_p, where θ_p is the reconstructed scattering angle of the ^{8}Be nucleus prior to breakup (as introduced in Sect. 2.8.6). As with Q-E_{rel}, reconstructed events assuming the correct target nucleus form sharp, straight bands in Q-θ_p, and incorrectly reconstructed breakup events form broad bands with strong Q-θ_p correlations. In addition, breakup from ^{8}Be in its ground-state resonance is spread over all θ_p, making identification of

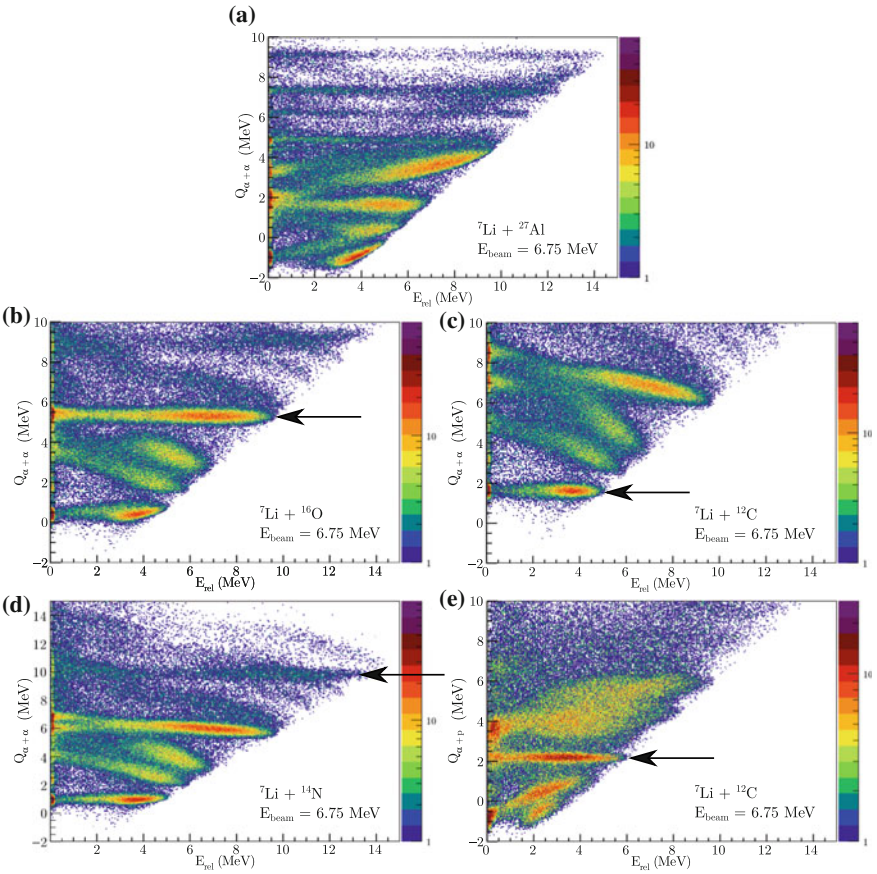

Fig. 4.6 (**a**) Reconstructed Q-value assuming breakup into $\alpha + \alpha$ pairs ($Q_{\alpha+\alpha}$) for all breakup fragments detected in reactions of ^{7}Li with ^{27}Al at $E_{\text{beam}} = 6.75$ MeV in the RDUX experimental run. Bands of events with constant Q-value against E_{rel} are reconstructed, indicating the presence of the $\alpha + \alpha$ breakup mode. However, there are several very intense bands of events due to breakup from light target impurities. The mode of breakup and the identity of the light impurity can be found by reconstructing all breakup events assuming they are from reactions with the light impurity. (**b**) The same events as in (**a**), reconstructed assuming the target was ^{16}O. The straight band at ∼5.5 MeV (indicated by the arrow) corresponds to $\alpha + \alpha$ breakup from ^{16}O. (**c**) The data reconstructed for $\alpha + \alpha$ breakup, assuming the target was ^{12}C. The band at ∼1.8 MeV corresponds to breakup from ^{12}C. (**d**) The data reconstructed for $\alpha + \alpha$ breakup assuming target was ^{14}N. The band at ∼10 MeV corresponds to breakup from ^{14}N. Finally, (**e**) reconstructed for $\alpha + p$ breakup as if the target were ^{12}C. The band at ∼2.2 MeV corresponds to $\alpha + p$ breakup from ^{12}C. A similar band will appear if the data are reconstructed for $p + \alpha$ breakup. Arrows in panels (**b**–**e**) indicate the peak of interest. The diagonal thresholds in all cases reflect the maximal E_{rel} due to energy conservation

the origin of these fragments clear. By application of narrow gates in Q-θ_p, all identified breakup that resulted from interactions with ^{12}C, ^{16}O, and ^{14}N was removed. The Q against E_{rel} spectra after ToF identification of fragments and the application of these narrow gates may be found in Fig. 4.11. As breakup from interactions with the target of interest and that from light impurities overlaps in Q-E_{rel} and Q-θ_p, removing breakup from light impurities inevitably results in a loss of breakup events from the target of interest. These cuts must be taken into account in the determination of the coincidence efficiency of BALiN for each measurement.

The modes of breakup after interactions of ^{7}Li and ^{9}Be with each target have been extracted using the procedures described in Sects. 4.1 and 4.2, and will now be presented. The discussion of the modes will be separated by projectile, and then the Z range of the targets: $Z = 6, 8$, $Z = 13, 14, 28$ and $62 \leq Z \leq 83$. Signatures of near-target breakup will be discussed in Chap. 5. A single beam energy will be shown for each reaction. In all measurements except for those of ^{9}Be with ^{144}Sm, ^{168}Er, ^{186}W, ^{196}Pt, ^{208}Pb and ^{209}Bi, data shown was taken with the BALiN array in the front-back configuration. Where measurements were made at a different beam energy or detector configuration, they appear in Appendix C. Breakup in reactions of ^{7}Li with ^{58}Ni, ^{28}Si, and ^{27}Al show the largest diversity of breakup modes. Therefore, it is appropriate to turn to this set of reactions first.

4.4 Breakup after Interactions of ^{7}Li with Targets $13 \leq Z \leq 28$

4.4.1 ^{58}*Ni*

The Q-E_{rel} (top row), Q (centre row) and E_{rel} (bottom row) distributions for reactions of ^{7}Li with ^{58}Ni at 11.70 MeV are shown in Fig. 4.7. Three dominant transfer-triggered breakup modes are identified through ToF and Q-E_{rel} identification: (a) $\alpha + \alpha$ pairs, resulting from proton pickup forming ^{8}Be which subsequently decays; (b) $\alpha + p$ pairs, resulting from two-neutron stripping forming ^{5}Li followed by its decay; (c) $\alpha + d$ pairs, which result when ^{6}Li is populated by neutron stripping above its 1.47 MeV breakup threshold. Results for reactions of ^{7}Li with ^{58}Ni at a higher beam energy of 13.1 MeV are similar and are shown in Appendix C in Fig. C.1.

Several key features are apparent: narrow bands are reconstructed in Q-E_{rel} confirming the assignment of each breakup mode, with peaks in the Q spectra, shown in Fig. 4.7d–f corresponding to the population of the ground and excited states of ^{57}Co, ^{60}Ni and ^{59}Ni, respectively. In the case of $\alpha + \alpha$ and $\alpha + p$ breakup, these peaks are well defined in Q-E_{rel} plots up to target-like excitations ($E_{\mathrm{r}}^{*} = Q_{\mathrm{gg}} - Q$) of approximately 7 MeV, after which, peaks are no longer able to be distinguished. Much of this is due to the increasing level density of ^{57}Co and ^{60}Ni with increasing excitation energy. In addition, as briefly discussed in Sect. 3.3.2, protons will punch through the BALiN array if their energy is greater than 7.5 MeV. This incomplete

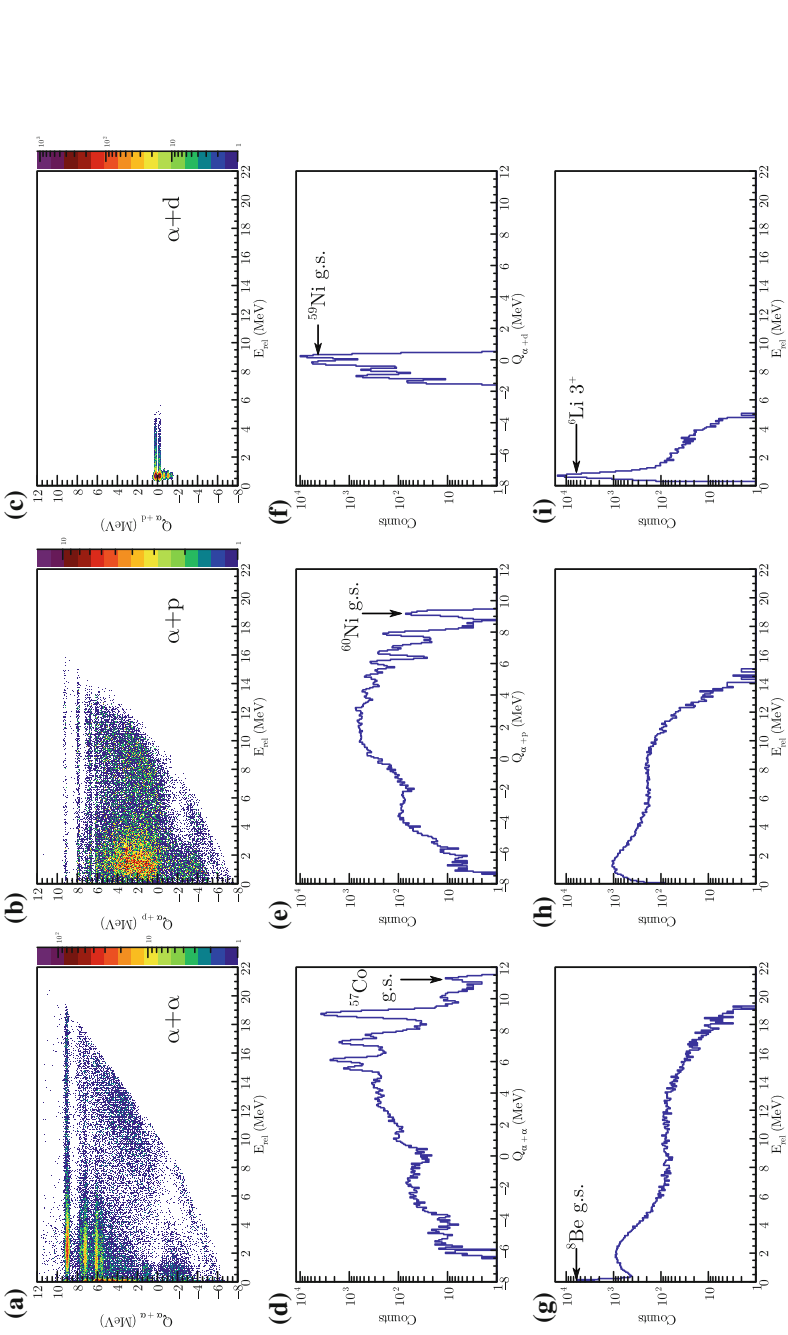

Fig. 4.7 Breakup after interaction of ^{7}Li with ^{58}Ni at E_{beam} = 11.70 MeV. (**a**) Q-E_{rel} spectrum for ToF and Q-E_{rel} identified $\alpha + \alpha$ pairs resulting from proton pickup forming ^{8}Be. (**b**) $\alpha + p$ pairs resulting from two-neutron stripping, (**c**) $\alpha + d$ pairs resulting from one-neutron stripping. (**d**)–(**f**), the associated Q spectra for $\alpha + \alpha$, $\alpha + p$ and $\alpha + d$ breakup, respectively, and (**g**)–(**i**) the associated E_{rel} spectra for $\alpha + \alpha$, $\alpha + p$ and $\alpha + d$ breakup, respectively

energy deposition results in a spread in reconstructed Q towards smaller values of Q, which corresponds to lower energy of the breakup fragments that originally arose from higher Q reactions. However, these punch-through events still fall within the ToF gate identifying protons, and are therefore assigned the $\alpha + p$ breakup mode. In the case of $\alpha + \alpha$ breakup, there can be no effects of punch-through, yet below $Q = 1.5$ MeV, there is no population of the 0^+ ground-state of ^{8}Be. This suggests that events below $Q = 1.5$ MeV may not be due to $\alpha + \alpha$ breakup from ^{58}Ni. Therefore, coincidence fragments identified as the $\alpha + \alpha$ breakup mode with $Q \leq 1.5$ were removed from determination of breakup cross-sections. As there is no such strong indication for any misidentified $\alpha + p$ breakup, no such Q threshold can be placed on this breakup mode.

In the Q-E_{rel} spectra for $\alpha + \alpha$ and $\alpha + p$ breakup (Fig. 4.7a, b), there are apparent "holes" in the data below $Q = 0$ MeV. These holes are due to the cuts performed in Q-θ_p to remove breakup that resulted from interactions with light impurities. This will be accounted for in the efficiency correction described in Chap. 6.

There is no "dominant" breakup mode for the breakup after interactions of ^{7}Li with ^{58}Ni in the measurements made here. For example, in the measurement at 11.70 MeV, shown in Fig. 4.7, the different transfer-triggered breakup modes have almost identical yields: 54 894 $\alpha + \alpha$ pairs (above $Q = 1.5$ MeV), 53 831 $\alpha + p$ pairs, and 51 597 $\alpha + d$ pairs. Although these yields have not been efficiency corrected, the conclusions do not change significantly after efficiency correction, as will become apparent in Chap. 7.

The final quantity presented in Fig. 4.7 is E_{rel}. The E_{rel} spectra of $\alpha + \alpha$ [panel (g)] and $\alpha + d$ [panel (i)] breakup show strong peaks at ~100 and ~700 keV, respectively. In $\alpha + \alpha$ breakup, this peak arises from the population of ^{8}Be in its narrow ground-state resonance, 92 keV above the breakup threshold into $\alpha + \alpha$ fragments. In $\alpha + d$ breakup, the peak in E_{rel} is due to the population of ^{6}Li in its 2.186 MeV 3^+ resonance, located 712 keV above the $\alpha + d$ breakup threshold of ^{6}Li. These peaks, arising from narrow, and therefore long lived resonances, correspond to breakup occurring far from the target-like nucleus. Since breakup occurs as the projectile-like nucleus is receding from the target-like nucleus, such breakup cannot suppress complete fusion at above-barrier energies, as will be discussed in more detail in Chap. 5. No such narrow peaks appear in the E_{rel} distribution for $\alpha + p$ pairs [panel (h)], since ^{5}Li has no narrow resonances to populate. In all breakup modes, breakup that results in large relative energies is significant. These large E_{rel} events (up to ~19 MeV in the case of $\alpha + \alpha$ breakup) result from breakup that occurs close to the target-like nucleus, where Coulomb effects perturb E_{rel}. It is these events that have the potential to suppress complete fusion.

4.4.1.1 Direct Breakup into Projectile Cluster Constituents

The yield of direct breakup is expected to monotonically decrease with decreasing Z: as direct breakup should depend principally on the strength of the Coulomb field. Therefore, the probability of direct breakup of ^{7}Li after interactions with ^{58}Ni is

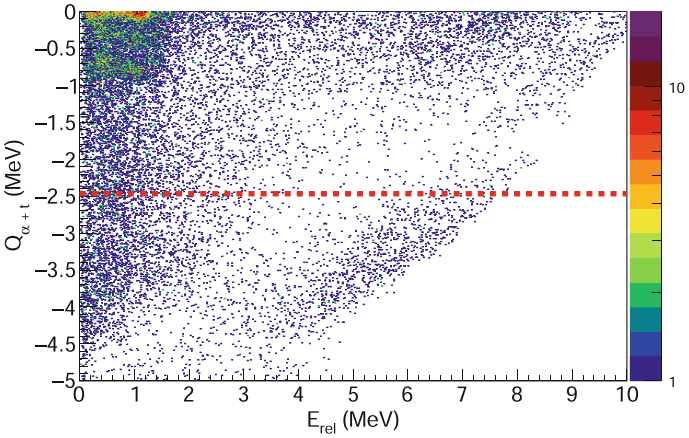

Fig. 4.8 The Q-E_{rel} spectrum for pairs of particles detected in coincidence, reconstructed assuming direct breakup, in the reaction of ^{7}Li with ^{58}Ni at $E_{\mathrm{beam}} = 11.70$ MeV. The dashed line indicates the expected location of direct breakup. It is apparent that no band is present here

expected to be less than was observed in reactions with ^{207,208}Pb and ^{209}Bi [2]. In fact, no direct breakup of ^{7}Li was observed in reactions with ^{58}Ni or with any target lighter than ^{58}Ni studied in this thesis.

Shown in Fig. 4.8 are all measured breakup fragments produced in the ^{7}Li + ^{58}Ni reaction at $E_{\mathrm{beam}} = 11.70$ MeV, now reconstructed for $\alpha + t$ breakup. Spurious coincidences as well as breakup from light impurities have been removed. The dashed red line indicates the expected Q for direct breakup, $Q_{\mathrm{gg}} = -2.467$ MeV. It is readily apparent that there is only smooth background present. To give an upper limit on direct breakup, taking a generous 0.5 MeV window around $Q = -2.467$ yields some 1157 events. This corresponds to a direct breakup contribution of at most 0.7% in this measurement.

4.4.2 ^{28}Si

The Q-E_{rel}, Q and E_{rel} spectra shown in Fig. 4.9 show the dominant breakup modes in interactions of ^{7}Li with ^{28}Si at $E_{\mathrm{beam}} = 6.75$ MeV. Similar results are seen for a higher beam energy of 7.5 MeV and in the lampshade configuration, and are presented in Appendix C in Figs. C.2, C.6 and C.7.

Proton pickup forming ^{8}Be followed by decay into $\alpha + \alpha$ pairs and two-neutron stripping forming ^{5}Li followed by decay into $\alpha + p$ are the two dominant breakup modes. The features in E_{rel} are broadly similar, although the high E_{rel} features of $\alpha + \alpha$ breakup differ somewhat to that seen in ^{58}Ni, due to the different degree of post-breakup acceleration experienced by the breakup fragments. Unlike in the reaction with ^{58}Ni, there is a clearly dominant breakup mode. In this measurement, there were

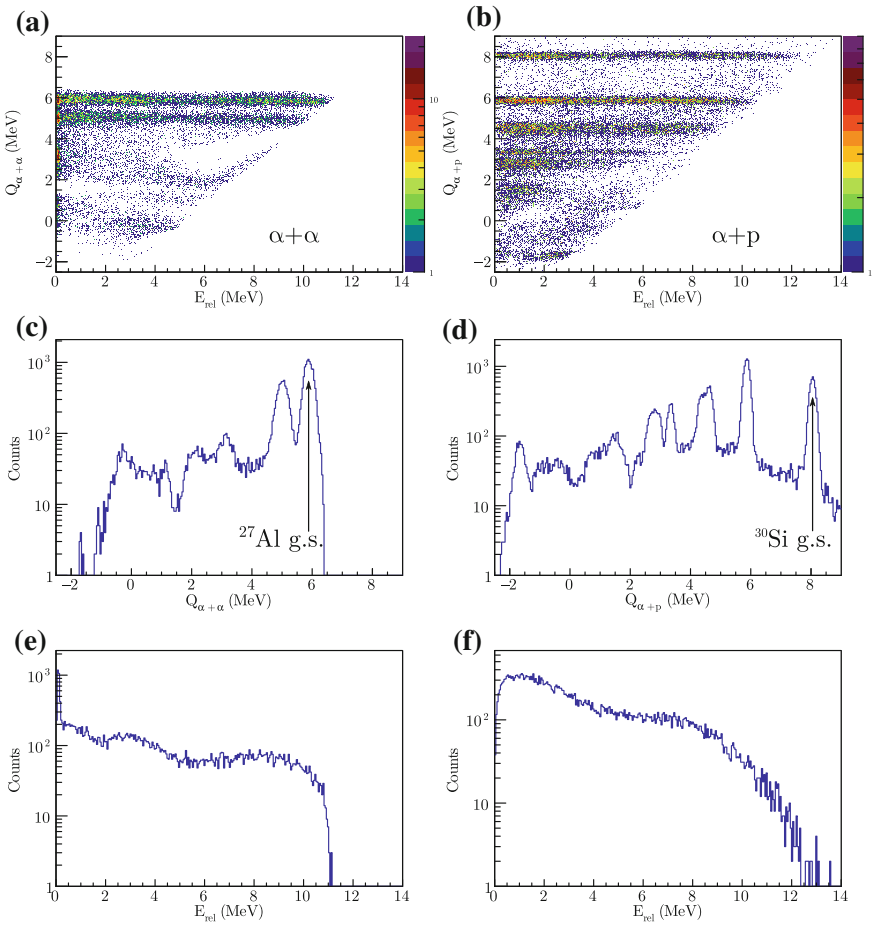

Fig. 4.9 The dominant breakup modes for reactions of ^{7}Li with ^{28}Si at $E_{\text{beam}} = 6.75$ MeV are **a** proton pickup forming ^{8}Be and its subsequent decay into $\alpha + \alpha$ fragments and **b** two neutron stripping forming ^{5}Li followed by decay into $\alpha + p$ fragments. Shown in **c** and **d** are the corresponding reconstructed $Q_{\alpha+\alpha}$ and $Q_{\alpha+p}$ spectra, showing a peak corresponding to ground-state to ground-state transfer and breakup, as well as peaks corresponding to the excitation of the ^{27}Al and ^{30}Si recoiling target-like nuclei. The E_{rel} spectra for $\alpha + \alpha$ and $\alpha + p$ pairs are shown in panels (**e**) and (**f**), respectively. The characteristic peak associated with the narrow ground-state resonance of ^{8}Be is seen at $E_{rel} = 92$ keV for the $\alpha + \alpha$ pairs, while the $\alpha + p$ pairs show no such narrow resonances

1.46 times the number of $\alpha + p$ fragments detected than $\alpha + \alpha$ fragments, perhaps driven by the high two neutron stripping Q_{gg} compared to that of proton pickup.

In contrast to reactions with ^{58}Ni, no one-neutron stripping forming ^{6}Li above its breakup threshold is observed. Further, no evidence of ^{6}Li produced in its stable ground state is seen. Shown in Fig. 4.10 is the energy of detected particles with no coincidence requirement, in the ^{7}Li + ^{28}Si reaction, between 69 and 71°. This angle

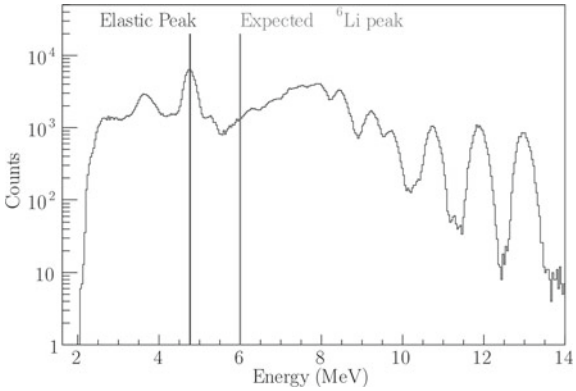

Fig. 4.10 Energy of particles detected in reactions of ^{7}Li + ^{28}Si at $E_{\text{beam}} = 6.75$ MeV, detected between 69 and 71°. The dark grey line indicates the expected position of elastically scattered ^{7}Li, consistent with the experimental data. On the other hand, the light grey line indicating the expected position of ^{6}Li populated below its breakup threshold, has no matching peak in the experimental energy distribution. Peaks at higher energy are associated with different high Q transfer modes

is fairly forward, but away from any detector edge effects. The measured energies were reconstructed for the energy loss of elastically scattered ^{7}Li. The calculated position of the elastic peak is indicated by the dark grey line, matches well with the experimental data. There is no peak consistent with the expected location of the ^{6}Li transfer products (light grey line), even accounting for the modest difference in energy loss between ^{6}Li and ^{7}Li. This result is somewhat surprising: one-neutron stripping has a positive Q-value, $Q_{\text{gg}} = 1.222$ MeV in this reaction, and two-neutron stripping forming ^{5}Li is plentiful, although the difference between Q_{gg} and Q_{opt} for two-neutron stripping means that there will be a strong population of highly excited states in the latter case, as seen in Fig. 4.9.

4.4.3 ^{27}Al

As with reactions of ^{7}Li with ^{28}Si, the dominant breakup modes seen in reactions of ^{7}Li with ^{27}Al are via proton pickup ($\alpha + \alpha$) and two-neutron stripping ($\alpha + p$). The associated Q-E_{rel}, Q and E_{rel} spectra are shown in Fig. 4.11 for $E_{\text{beam}} = 6.75$ MeV. Similar results for measurements made at $E_{\text{beam}} = 6.75$ and $E_{\text{beam}} = 7.50$ MeV with the BALiN array in both its front-back and lampshade configuration are shown in Appendix C in Figs. C.3, C.4, and C.5.

The reconstructed E_{rel} spectra for the $\alpha + \alpha$ mode differ little between ^{28}Si and ^{27}Al, except for the difference in the extent of E_{rel}, due to the difference of 3.3 MeV in the Q_{gg} values for proton pickup of ^{7}Li from ^{27}Al compared to ^{28}Si. In particular, there is a sharp peak in E_{rel} at 92 keV in both cases, as well as a broad peak in intensity at approximately 3 MeV. The $\alpha + p$ E_{rel} spectrum for ^{27}Al extends to ∼10.5 MeV, compared to ∼12.5 MeV, in the case of ^{28}Si. This is due to the 1.93 MeV lower

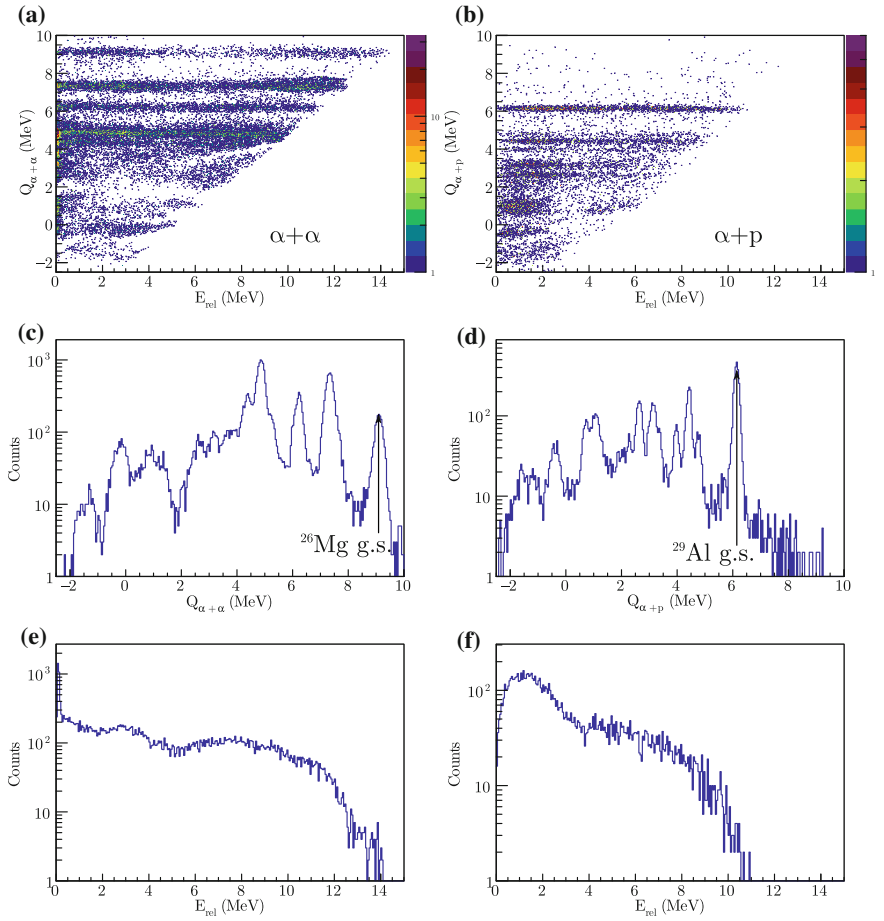

Fig. 4.11 The dominant breakup modes for reactions of ^{7}Li with ^{27}Al at $E_{\text{beam}} = 6.75$ MeV are **a** proton pickup forming ^{8}Be and its subsequent decay into $\alpha + \alpha$ fragments and **b** two neutron stripping forming ^{5}Li followed by decay into $\alpha + p$ fragments shown by their Q-E_{rel} spectra. Shown in (**c**) and (**d**) are the corresponding reconstructed $Q_{\alpha+\alpha}$ and $Q_{\alpha+p}$ spectra, showing a peak corresponding to ground-state to ground-state transfer and breakup, as well as peaks corresponding to excitation of the ^{26}Mg and ^{29}Al recoiling target-like nuclei. The E_{rel} spectra of $\alpha + \alpha$ fragments is shown in panel (**e**), where the characteristic peak at 92 keV is seen, and of $\alpha + p$ fragments in panel (**f**)

Q_{gg} for two-neutron stripping for reactions with ^{27}Al compared with ^{28}Si. These differences in Q are manifest in the reconstructed $Q_{\alpha+\alpha}$ and $Q_{\alpha+p}$ spectra, shown in Fig. 4.11c, d respectively.

Breakup following interactions of ^{7}Li with ^{27}Al shows a clearly dominant breakup mode: there are 2.8 times the number of $\alpha + \alpha$ fragments than $\alpha + p$ fragments in this measurement. This is an opposite result to the breakup modes seen in reactions of ^{7}Li with ^{28}Si, where the $\alpha + p$ yield was dominant. This demonstrates the presence of structure effects in determining the dominant breakup modes in interactions of

^{7}Li. These differences are likely attributable to pairing effects. In both ^{28}Si and ^{27}Al, the dominant transfer-triggered breakup mode corresponds to that in which the recoiling nucleus (^{30}Si and ^{26}Mg) has an even number of protons and neutrons. The less dominant breakup mode in both cases leaves a nucleus with an odd number of protons and an even number of neutrons.

4.4.4 Rare Coincidence Modes

A benefit of the identification of breakup modes via direct particle identification of both breakup fragments is that by examining every possible combination of the mass of breakup fragments, it is possible to comprehensively determine the breakup modes present. This removes disadvantages of identifying breakup via Q-E_{rel} reconstruction. Firstly, if the breakup mode is not expected to occur, it may not be reconstructed in the first place. Secondly, if the breakup mode is weak and overlapping with other, stronger, breakup modes, it will not be apparent in a Q-E_{rel} spectrum without separation via direct particle identification. Such coincidence modes will inevitably be rare, and therefore should not be expected to contribute to complete fusion suppression to any great extent. However, they are curiosities and present an opportunity to use the sensitivity of BALiN and the analysis method to their full extent. Such is the case of $p + p$ pairs detected in coincidence. Looking for $p + p$ pairs is the logical next step after looking for $\alpha + p$ and $\alpha + \alpha$ pairs.

Shown in Fig. 4.12 are the reconstructed Q_{p+p} distributions for $p + p$ pairs detected by ToF gating after interactions of ^{7}Li with **a** ^{28}Si and **b** ^{27}Al at $E_{\mathrm{beam}} = 6.75$ MeV. Clear peaks emerge in both spectra, associated with the ground-state Q-value for $^{7}\mathrm{Li} + {}^{28}\mathrm{Si} \rightarrow p + p + {}^{33}\mathrm{P}$ and $^{7}\mathrm{Li} + {}^{27}\mathrm{Al} \rightarrow p + p + {}^{32}\mathrm{Si}$, respectively. There are also strong peaks associated with excited states of ^{33}P and ^{32}Si. The presence of these excited states indicate that these pairs do not arise through random coincidence.

In the measurement with ^{28}Si there is an $\alpha + p$ background, where, due to slightly overlapping ToF bands, $\alpha + p$ pairs have been misidentified as $p + p$ pairs. In reactions with ^{27}Al there is a peak at $Q_{p+p} \sim -1$ MeV, potentially due to reactions producing $p + d$ pairs. However, there may also be a peak in intensity at $Q_{p+p} \sim -1$ MeV due to the optimum Q of $Q_{\mathrm{opt}} = -1.69$ MeV for this process. In total, events identified as $p + p$ pairs comprise 4.9% of the total valid coincidence yield in the measurement of ^{7}Li with ^{28}Si. The $p + p$ yield in reactions of ^{7}Li with ^{27}Al is much smaller – totalling 1.9% of the total valid coincidence two yield.

It is not immediately obvious that pairs of protons detected in coincidence can be considered a "breakup mode" in any way. There are two possible mechanisms: either the $p + p$ pairs are due to the stripping of four neutrons and one proton from ^{7}Li; or they arise from complete fusion followed by two proton evaporation, populating discrete states in the recoiling target-like nuclei. The transfer of four neutrons and one proton doesn't seem likely on the face of it. Nor is it expected that complete fusion should have a significant cross-section in these reactions since both measurements are performed at below-barrier energies: $E/V_b = 0.82, 0.88$ for reactions with ^{28}Si

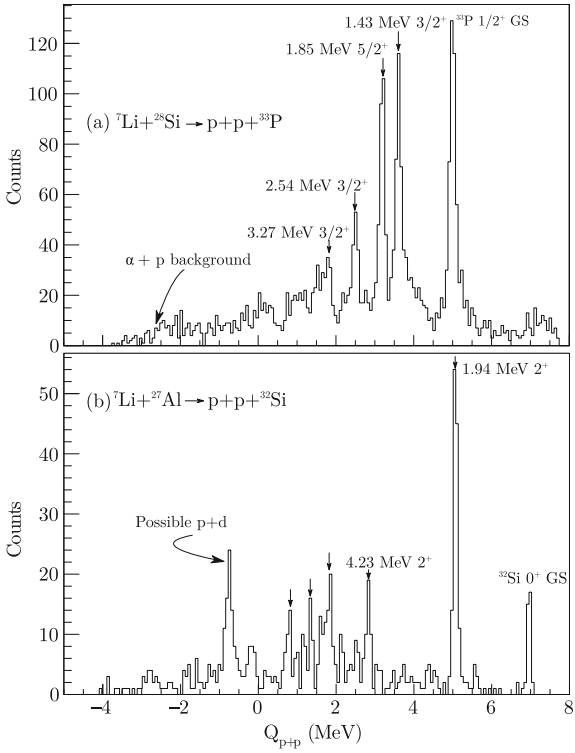

Fig. 4.12 Reconstructed Q_{p+p} for pairs of protons identified using ToF gating in reactions of (**a**) ^{7}Li + ^{28}Si at $E_{\text{beam}} = 6.75$ MeV ($Q_{\text{gg}} = 5.173$ MeV) and (**b**) ^{7}Li + ^{27}Al at $E_{\text{beam}} = 6.75$ MeV ($Q_{\text{gg}} = 7.210$ MeV). Clear peaks, indicated with arrows, appear corresponding to population of ^{33}P and ^{32}S in their ground and excited states demonstrating that the identity of the pairs has been correctly assigned

and ^{27}Al respectively. The fact that reactions with ^{28}Si yield a higher proportion of $p + p$ pairs than those with ^{27}Al, even though the reaction is more below-barrier demonstrates the role of structure (reflected in Q-values) in this process.

The Q_{gg} leading to $p + p$ pairs in reactions of ^{7}Li with ^{27}Al and ^{28}Si is highly positive in both cases. This is also true in reactions of ^{7}Li with ^{58}Ni, producing $p + p$ pairs and a recoiling ^{63}Cu, with $Q_{\text{gg}} = 5.680$ MeV. In the ^{58}Ni case, if ToF gating is used, $p + p$ pairs comprise 2.59% of the total valid coincidence yield at a beam energy of $E_{\text{beam}} = 11.70$ MeV. However, unlike the ^{28}Si and ^{27}Al case, the Q spectrum does not show narrow peaks, likely due to punchthrough.

4.4.5 Q-Value and E_{rel} Resolution

A key quantity dictating the utility of using Q-value spectra to identify the state of the target-like nucleus that was populated is the Q-value resolution. For low target-like excitation energies, where the level density of the target-like nucleus is low, it is possible to extract the FWHM of a Q-value peak arising from a single target-like nucleus state. The evaluated Q-value FWHM for reactions of ^{7}Li + ^{58}Ni, ^{28}Si and ^{27}Al are shown in Table 4.4, for the spectra shown in Figs. 4.7, 4.9, 4.11 and 4.12.

Table 4.4 Q-value and E_{rel} resolutions evaluated for reactions of ^{7}Li with ^{58}Ni, ^{28}Si and ^{27}Al, evaluated from the spectra shown in Figs. 4.7, 4.9, 4.11 and 4.12. The thickness of the target used in each measurement is given in brackets

	^{7}Li + ^{58}Ni (60 μg cm^{-2})	^{7}Li + ^{28}Si (80 μg cm^{-2})	^{7}Li + ^{27}Al (25 μg cm^{-2})
$Q_{\alpha+\alpha}$ FWHM (keV)	240	330	260
$Q_{\alpha+d}$ FWHM (keV)	150	-	-
$Q_{\alpha+p}$ FWHM (keV)	100	240	200
Q_{p+p} FWHM (keV)	-	150	100
E_{rel} ^{8}Be 0^{+} FWHM (keV)	90	70	70
E_{rel} ^{6}Li 3^{+} FWHM (keV)	180	-	-

From this table, it is clear that the resolution in Q-value is not constant. The $Q_{\alpha+\alpha}$ peaks are always the broadest, and the peak widths decrease with decreasing Z and A of the breakup fragments. When both fragments are protons, the resolution in Q-value is smallest. This is because the Q-value depends critically on the reconstruction of energy loss of the breakup fragments. This energy-loss reconstruction relies on accurate knowledge of the location of the detected particle in BALiN which is only known to within a pixel. Since the α particles experience a greater amount of energy loss than the protons (for example), the uncertainty in the energy loss reconstruction due to the size of the pixels affects the $\alpha + \alpha$ resolution in the breakup mode to a greater extent than the $\alpha + p$ breakup mode. In addition, the uncertainty in Q-value depends on the target thickness, as well as identity target nucleus. As the target nucleus decreases in Z, at constant E_{CM}/V_b, the energy of the breakup fragments decrease, thus increasing their energy loss. In addition, as the mass of the recoiling target-like nucleus decreases, it carries proportionately more kinetic energy, and so increasing the sensitivity of Q to the reconstruction of its kinetic energy. All of these quantities contribute to the variation in Q-value resolution seen in Table 4.4.

It is also possible to evaluate the resolution of E_{rel} spectra, provided that the projectile-like nucleus is left in a long-lived (narrow) resonance, where no effects of post-breakup acceleration are expected to perturb the E_{rel} distribution. This is the case for ^{8}Be in its 0^{+} resonance, which peaks at 92 keV, and ^{6}Li in its 3^{+} resonance, which has a peak at 700 keV. Shown in Table 4.4 are the evaluated E_{rel} resolutions for these states for reactions of ^{7}Li with ^{58}Ni, ^{28}Si and ^{27}Al. These widths are primarily due to the finite pixel size of BALiN. In simulations of breakup from the 0^{+} state of ^{8}Be and the 3^{+} state of ^{6}Li, including the pixelisation of BALiN alone is sufficient to reproduce the widths seen here [2].

4.5 Breakup After Interactions of ^{9}Be with ^{28}Si and ^{27}Al

Let us now examine breakup after interactions of ^{9}Be with ^{28}Si and ^{27}Al. In measurements of breakup after reactions of ^{9}Be with ^{144}Sm, ^{168}Er, ^{186}W, ^{196}Pt, ^{208}Pb and ^{209}Bi, it was found that breakup following neutron stripping forming ^{8}Be is the dominant breakup mode in interactions of ^{9}Be with these targets [3]. Direct breakup $^{9}\text{Be} \rightarrow \alpha + \alpha + n$ was found to contribute ∼2% to the raw breakup yield. At the other end of the periodic table, in reactions of ^{9}Be with ^{28}Si and ^{27}Al, breakup triggered by neutron stripping once again is by far the dominant breakup mode. Shown in Fig. 4.13 is the Q-E_{rel} spectrum for ToF identified $\alpha + \alpha$ pairs produced in interactions of ^{9}Be with (a) ^{28}Si and (b) ^{27}Al. Clear bands are reconstructed in Q-E_{rel} which

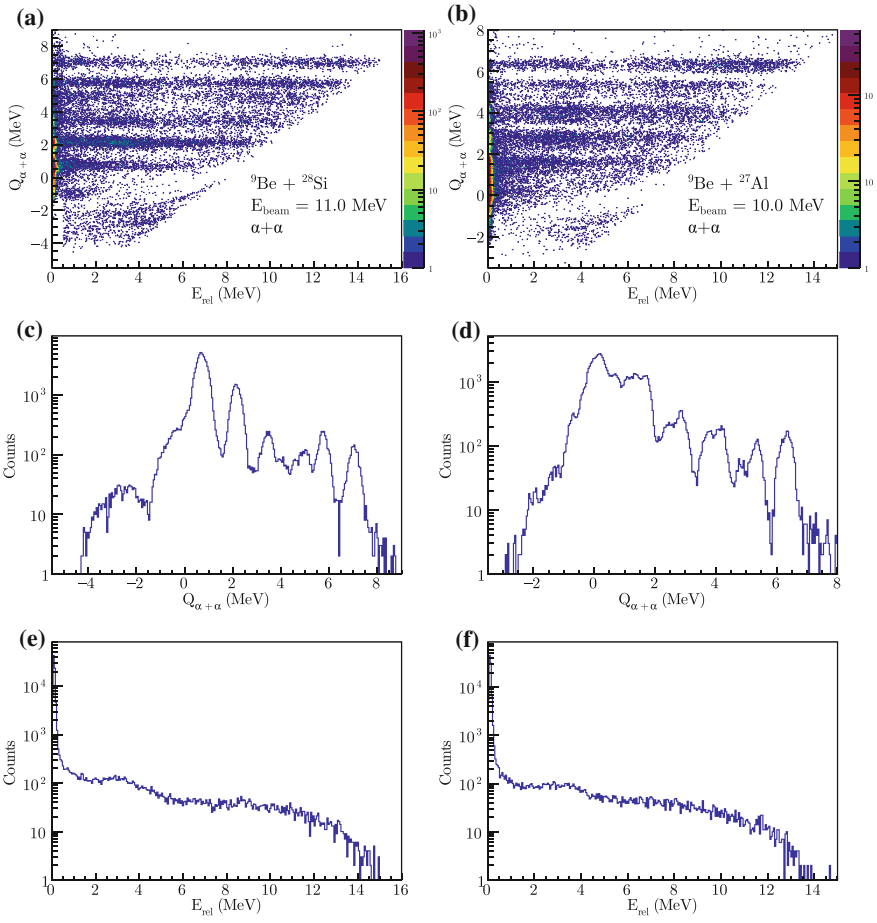

Fig. 4.13 Reconstructed Q-E_{rel}, Q and E_{rel} spectra for ToF identified $\alpha + \alpha$ pairs produced after interactions of ^{9}Be with ^{27}Al and ^{28}Si. In **a**, **c** and **e** the spectra for $^{9}\text{Be} + {}^{28}\text{Si}$ at $E_{\text{beam}} = 11.0$ MeV is shown, and in **b**, **d** and **f** the spectra for $^{9}\text{Be} + {}^{27}\text{Al}$ at $E_{\text{beam}} = 10.0$ MeV is shown

are also seen in the peaks in the Q-value spectrum shown in Fig. 4.13c, d for ^{28}Si and ^{27}Al, respectively. A large fraction of breakup goes through the 92 keV ground-state resonance in ^{8}Be, evident from the $E_{\rm rel}$ spectra presented in Fig. 4.13e, f.

The $Q_{\alpha+\alpha}$ spectra for reactions with both targets are very similar, except for a 0.75 MeV offset due to the different $Q_{\rm gg}$ for $\alpha+\alpha$ produced in reactions with ^{28}Si and ^{27}Al ($Q_{\rm gg} = 6.901$ and 6.152 MeV, respectively, as shown in Table 4.2). The similar spectra arise from the fact that the neutron numbers of ^{27}Al and ^{28}Si are the same. As a result, neutron stripping populates the same neutron levels in both targets. This will be discussed in more detail in Sect. 4.6.1 for the case of breakup after interactions of ^{9}Be with ^{209}Bi and ^{208}Pb where a similar situation is encountered.

The $E_{\rm rel}$ spectra for $\alpha+\alpha$ fragments produced in interactions with ^{9}Be and ^{28}Si compared to those produced after interactions with ^{27}Al are also very similar. On average, $82 \pm 5\%$ of the (not yet efficiency corrected) $\alpha+\alpha$ pairs are contained in the peak centred around $E_{rel} = 92$ keV, resulting from the population of ^{8}Be in its ground state resonance. This is in contrast to reactions with ^{7}Li populating ^{8}Be, where on average $19 \pm 3\%$ of $\alpha+\alpha$ pairs result from the ground state resonance of ^{8}Be. Both $E_{\rm rel}$ spectra show a peak in intensity at $\sim$3 MeV and show a broad, essentially flat $E_{\rm rel}$ distribution extending to high energies. The slightly larger extent of $E_{\rm rel}$ distribution for reactions with ^{28}Si is attributable to the slightly larger $Q_{\rm gg}$ for neutron stripping triggered breakup for this target, as well as the slightly larger beam energy.

In measurements of the breakup of ^{9}Be with ^{144}Sm, ^{168}Er, ^{186}W, ^{196}Pt, ^{208}Pb and ^{209}Bi, direct breakup of $^{9}\text{Be} \rightarrow \alpha+\alpha+n$ was identified via the characteristic Q vs $E_{\rm rel}$ of breakup via the $\frac{5}{2}^{-}$ state in ^{9}Be [3]. Since BALiN is not sensitive to neutrons, the energy of the breakup process is not captured completely, leading to an extended peak in Q below the direct breakup threshold of ^{9}Be (-1.57 MeV). However, since the $\frac{5}{2}^{-}$ state of ^{9}Be is narrow, there is a fairly narrow peak in $E_{\rm rel}$, enabling these events to be clearly identified. Direct breakup of ^{9}Be in reactions with ^{144}Sm, ^{168}Er, ^{186}W, ^{196}Pt, ^{208}Pb and ^{209}Bi may be seen in Fig. 4.15, and will be discussed in Sect. 4.6. However, in reactions of ^{9}Be with ^{27}Al and ^{28}Si, such structure is apparent in Fig. 4.13, demonstrating that direct breakup is not a significant portion of the breakup yield. However, the presence of cuts removing light impurities at negative Q-values precludes the estimation of an upper limit. The lack of direct breakup in these reactions echoes what was seen in reactions of ^{7}Li with ^{27}Al, ^{28}Si, and ^{58}Ni. It would be interesting to "bridge the gap" between these measurements, to study the evolution of ^{7}Li and ^{9}Be direct breakup with decreasing target Z.

In addition to the two measurements shown in this section, measurements of coincidence fragments produced after interactions of ^{9}Be with ^{27}Al at $E_{\rm beam} = 8.90$ MeV and ^{9}Be with ^{28}Si at $E_{\rm beam} = 10.0$ MeV were performed. Q-$E_{\rm rel}$, Q and $E_{\rm rel}$ spectra for the ToF gated breakup modes are shown in Appendix C in Figs. C.8 and C.9 for ^{27}Al and ^{28}Si, respectively.

4.5.1 Rare Coincidence Modes

As with reactions of ^{7}Li, ToF identification can enable the study of rare coincidence modes in reactions of ^{9}Be, the details of which may be found in Appendix D. In summary, $\alpha + p$ pairs populating states of ^{32}P and ^{31}Si were found to comprise $3.60 \pm 0.06\%$ and $2.65 \pm 0.05\%$ of the total (valid) coincidence yield for reactions of ^{9}Be with ^{28}Si at $E_{\text{beam}} = 11.0$ MeV and ^{27}Al at $E_{\text{beam}} = 10.0$ MeV, respectively. The E_{rel} spectra for these events were consistent with the E_{rel} spectra for two neutron stripping reactions with ^{7}Li beams forming ^{5}Li, suggestive of a common mechanism (transfer). Breakup functions for these reactions will be extracted in Chap. 7. In addition, a small yield of $p + p$ pairs were detected populating states in ^{35}S and ^{34}P, comprising $0.57 \pm 0.02\%$ and $0.12 \pm 0.01\%$ of the total valid coincidence yield, respectively. With greater statistics, it may be possible to use this reaction mode producing $p + p$ pairs after two-proton five-neutron transfer to examine the structure of neutron rich isotopes.

4.6 Breakup After Interactions of ^{9}Be with Targets $62 \leq Z \leq 83$

A re-analysis was carried out of measurements performed in the 2008 BEX run for breakup in reactions of ^{9}Be with ^{144}Sm, ^{168}Er, ^{186}W, ^{196}Pt, ^{208}Pb and ^{209}Bi. The main purpose of the re-analysis was to re-determine the breakup functions using the improved efficiency determination described in Chap. 6 and, using these breakup functions as input, to predict the resulting above-barrier suppression of complete fusion when resonant state lifetimes are explicitly treated in M- PLATYPUS. Due to the advances made in data analysis in the intervening years, the yields of breakup fragments used as input into the breakup functions were also re-determined in the course of this thesis, and will be described briefly. Further experimental detail and discussion of the breakup mechanisms of reactions of ^{9}Be with ^{144}Sm, ^{168}Er, ^{186}W, ^{196}Pt, ^{208}Pb and ^{209}Bi may be found in [3, 4].

Determining the breakup modes for these data proceeded slightly differently to the process described above. Prior to the work of this thesis, measurements with BALiN did not record ToF. For reactions of ^{9}Be with heavy targets, the breakup modes can be identified solely on the basis of Q-E_{rel}. As has been previously found [3, 4] ^{9}Be has two breakup modes in this mass region; breakup yields are dominated by neutron stripping forming ^{8}Be ($^{8}\text{Be} \rightarrow \alpha + \alpha$), with a small contribution from direct breakup ($^{9}\text{Be} \rightarrow \alpha + \alpha + n$). Therefore, all breakup modes produce two α particles, and no direct particle identification is required (this is in contrast to the ^{27}Al and ^{28}Si targets just under discussion, which energetically favour $^{9}\text{Be} \rightarrow {}^{5}\text{Li} \rightarrow \alpha + p$, and a small yield of $\alpha + p$ pairs are observed).

The challenge is then only in separating coincident breakup events from all other reaction outcomes. As in the experiments performed in this thesis, energy matching

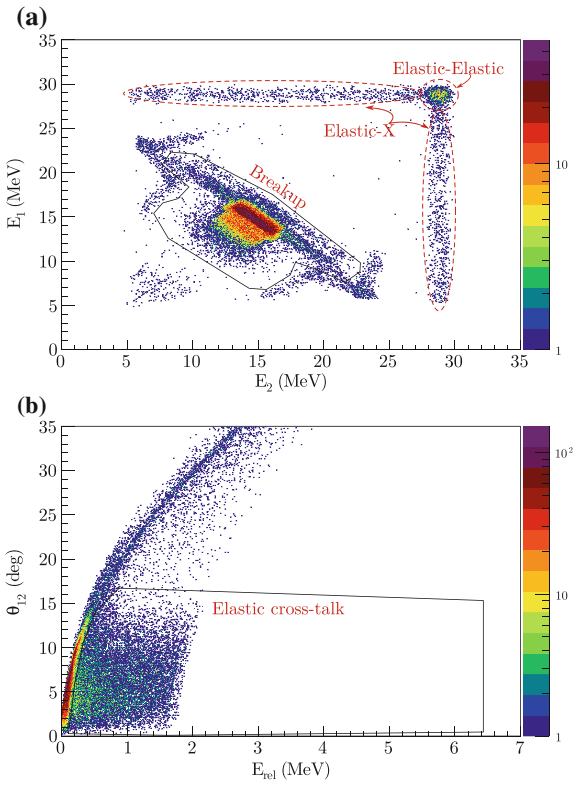

Fig. 4.14 The gating scheme used for the re-analysis of breakup after interactions of ^{9}Be with ^{144}Sm, ^{168}Er, ^{186}W, ^{196}Pt, ^{208}Pb and ^{209}Bi, shown using ^{9}Be + ^{209}Bi at 34 MeV as an example. (**a**) E_1 against E_2 distribution of coincidence signals detected in BALiN. The solid black polygon indicates the gate drawn around the genuine coincidence breakup events, removing the elastic-elastic and elastic-X events (see text), indicated by the dashed red ellipses. (**b**) θ_{12} against E_{rel} distribution of coincidence signals detected in BALiN. Events with small opening angle but large ($\gtrsim$0.5 MeV) relative energy correspond to elastic cross-talk events, and are removed using the solid black polygon shown

was performed to remove incorrect pixel identification, as described in Sect. 3.4.5. Then, the elastic-elastic and elastic-random events were removed through gating on the diagonal bands in E_1 against E_2, shown for ^{9}Be + ^{209}Bi at $E_{\text{beam}} = 37.0$ MeV in Fig. 4.14a. As shown in Sect. 4.1.1, events in these diagonal bands correspond to breakup reactions, whereas the horizontal and vertical bands correspond to elastic-elastic and elastic-X events. A direct gate in (AE_1, AE_2) can be drawn in these reactions, as the energy of the elastically scattered beam is well separated from that of the breakup fragments. In addition, the energy of the recoiling nucleus is small, leading to a tight grouping of $\alpha + \alpha$ pairs in (AE_1, AE_2) along bands of $AE_1 + AE_2 \approx E_{\text{beam}} + Q$. Finally, elastic cross-talk events are removed by removing those events with θ_{12} vs. E_{rel} correlations that are unphysical, shown in Fig. 4.14b.

In the analysis of Ref. [3], spurious coincident events resulting from charge-sharing across adjacent pixels due to particles incident on the inter-strip partition (elastic cross-talk), were removed by rejecting *any* event in adjacent pixels (thus rejecting genuine ^{8}Be 0^{+} events). With greater experience in analysis of such data, it was realised that spurious events can be rejected by their unphysical relative energy (E_{rel}), with respect to their opening angle (θ_{12}). In this analysis, spurious events were removed by applying cuts in the $E_{\text{rel}} - \theta_{12}$ spectra. This alternate method for extracting breakup events resulted in an approximately four times larger yield of the

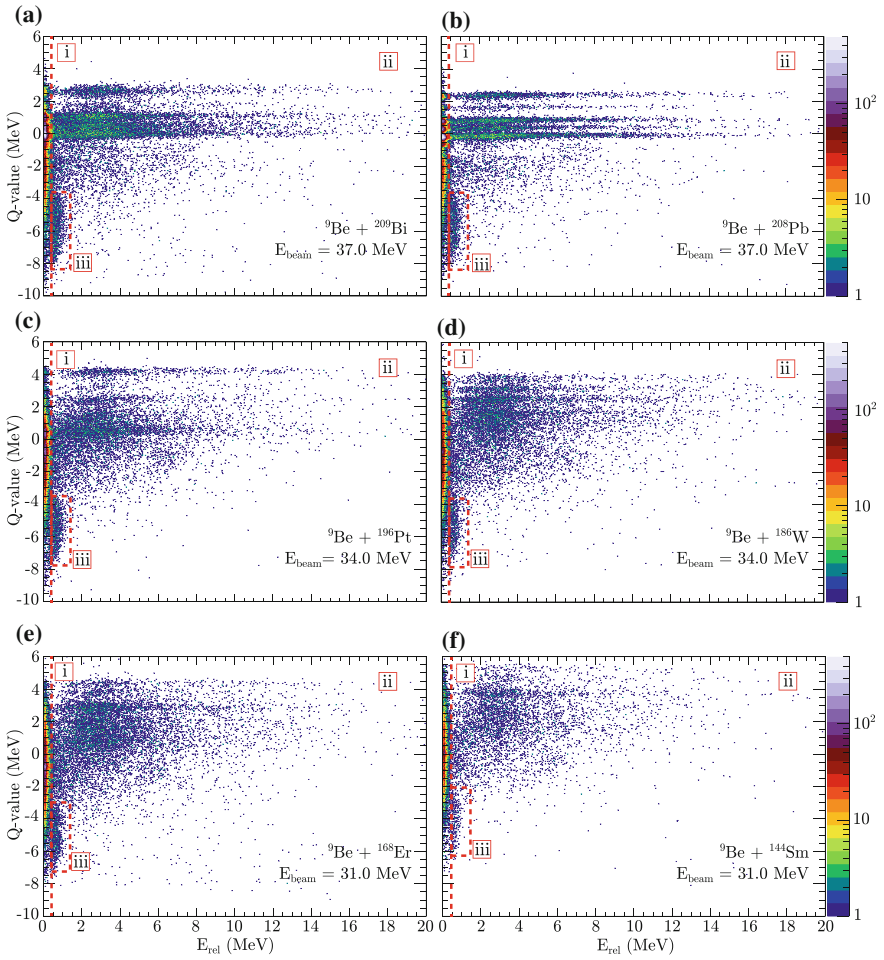

Fig. 4.15 Reconstructed E_{rel} against Q-value spectra for the systems studied in the re-analysis of ^{9}Be + ^{144}Sm, ^{168}Er, ^{186}W, ^{196}Pt, ^{208}Pb and ^{209}Bi breakup reactions. Reactions shown here were taken at beam energies of $\sim 0.9E/V_B$. Events arising from the breakup of ^{8}Be from its 0^+ ground state, which includes contributions from direct (^{9}Be$\rightarrow^{8}$Be$+n$) and transfer-triggered breakup are shown to the left of the vertical dashed line denoted region (i). Events from breakup of ^{8}Be from either the high excitation energy tail of the 0^+ state or the 2^+ and 4^+ states lie to the right of the line [region (ii)], except those marked by the dashed box (iii), which contains direct breakup events from the decay of ^{9}Be from its $5/2^-$ state

ground-state ^{8}Be events, as the vast majority of genuine ^{8}Be ground-state breakup events result in signals in adjacent pixels. These lost events would otherwise have had to be restored by a larger efficiency correction as in the previous work [3].

The resulting $\alpha + \alpha$ Q-value against E_{rel} spectra for all the systems studied in this work at beam energies of $\sim$0.9 E/V$_B$ are shown in Fig. 4.15. Events with E_{rel} around 92 keV, identified as region (i), correspond to breakup following neutron stripping producing ^{8}Be in its 0^+ ground state, whilst events in region (ii) correspond

to breakup following neutron stripping producing ^{8}Be either in the high excitation energy tail of the 0^{+} state (see Sect. 2.5.2.1), or in its first 2^{+} or 4^{+} resonant states, with $E_p^* = 3.03$ MeV and $E_p^* = 11.35$ MeV, respectively. Region (iii) corresponds to the direct breakup of ^{9}Be through the $\frac{5}{2}^{-}$ state, producing $^{5}\text{He} + \alpha \rightarrow \alpha + \alpha + n$. The energy of the neutron cannot be measured by BALiN, resulting in the incomplete capture of the energy of this breakup process. As such, the reconstruction of breakup modes through energy and momentum conservation of three particles (two breakup fragments and the target-like recoil) does not accurately reconstruct the Q-value for the direct breakup of ^{9}Be.

4.6.1 Breakup in Interactions of ^{9}Be with ^{208}Pb and ^{209}Bi

There is a distinct similarity between the Q-value against E_{rel} spectra for the $\alpha + \alpha$ pairs produced in neutron stripping reactions of ^{9}Be with ^{209}Bi and ^{208}Pb, shown in Fig. 4.15a, b respectively. In fact, the target-like excitation energy distribution ($E_r^* = Q - Q_{\text{gg}}$) in ^{9}Be + ^{209}Bi breakup reactions, shown in Fig. 4.16b looks somewhat like a "poorer-resolution" version of the ^{9}Be + ^{208}Pb spectrum shown in Fig. 4.16a. The similarity arises as in both cases, the transferred neutron populates the same set of neutron states. In the case of ^{209}Bi, the levels excited in neutron transfer will correspond to multiplets built on the strongly populated levels in the ^{208}Pb reaction [5]. That is, the neutron transferring to ^{210}Bi will couple to the proton in the $g_{\frac{9}{2}}$ shell, resulting in a splitting of levels, and the broader Q-value distribution that is observed due to the many more levels contributing. For example, the spectroscopic factor S (from ^{209}Bi(d,p) measurements [6]) weighted average of the lowest lying 0^{-} to 9^{-} states in ^{210}Bi [arising from $\pi(1\text{h}_{\frac{9}{2}}) \otimes \nu(2\text{g}_{\frac{9}{2}})$] is indicated by the vertical red line in Fig. 4.16b, which well reproduces the peak seen in the experimental data. The Q-value resolution of these spectra (250 keV FWHM for the ground state of ^{209}Pb) is insufficient to resolve these states individually. This is the same effect that has been previously seen in (p, p') studies of ^{208}Pb and ^{209}Bi [7].

4.7 Breakup in Interactions of ^{9}Be and ^{7}Li with ^{12}C and ^{16}O

Breakup after interactions of ^{7}Li and ^{9}Be with ^{12}C and ^{16}O is presented separately to breakup with the heavier targets of ^{27}Al and ^{28}Si. This is for two reasons. First, in below-barrier reactions of ^{9}Be and ^{7}Li with ^{12}C and ^{16}O the low beam energy and small ground-state Q-values ensure that the energy available to excite the recoiling target-like nuclei is relatively small. Further limiting the possible excitations of the target-like nuclei is the fact that light nuclei have fewer low-lying excited states compared with heavier nuclei. The energy threshold of BALiN also limits the number

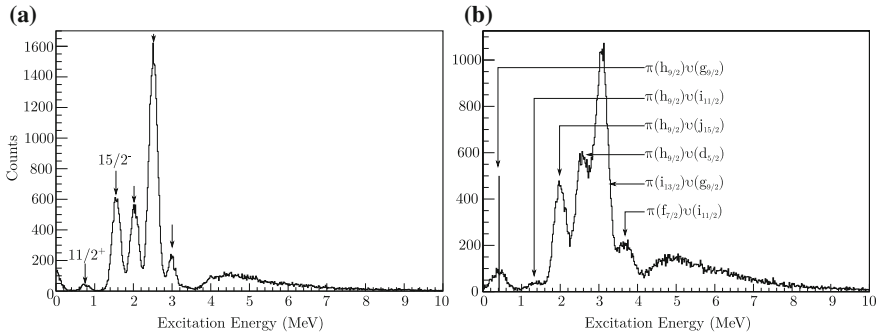

Fig. 4.16 Excitation energy distributions of **a** ^{209}Pb and **b** ^{210}Bi after neutron transfer from ^{9}Be at $E_{\text{beam}} = 37.0$ MeV. The solid vertical line in **b** indicates the S weighted average of the 0^- to 9^- states corresponding to the $\pi(1h\frac{9}{2})\nu(2g\frac{9}{2})$ configuration. Multiplet configurations from [5] have been assigned to each peak

of measured target-like recoil states. The second reason is an additional complication in the data analysis for these reactions, as will now be discussed.

4.7.1 $^{9}Be + ^{12}C$

After removing spurious coincidence events in the manner described in Sect. 4.1, the reconstructed $Q_{\alpha+\alpha}$ spectrum for reactions of ^{9}Be with ^{12}C at $E_{\text{beam}} = 6.60$ MeV in data taken in the BELICK run are shown in Fig. 4.17a. The expected bands of $\alpha + \alpha$ breakup events appear at $Q = 3.4$, 0.3 and -0.3 MeV, corresponding to the population of ^{13}C in its ground, first and second excited states, which are located at 3.08 and 3.68 MeV respectively [9]. There is also a very small peak at $Q_{\alpha+\alpha} = 2.2$ MeV, which does not correspond to a state in ^{13}C, but may be due to a small amount of ^{16}O contamination in the target.

There is also a large, tightly grouped set of events that reconstruct to large E_{rel} with a very large range of reconstructed $Q_{\alpha+\alpha}$, indicated by the dashed box in Fig. 4.17a. These are clearly not breakup events, but they are also not obviously random coincidences, as these were already removed. Plotting the energy and angle of each of the pairs (within the dashed box), as shown in Fig. 4.17b, yields the solution: these are transfer-recoil coincidences. High energy α particles at back angles produced in the ^{9}Be $+^{12}$C $\rightarrow \alpha+^{17}$O reaction ($Q_{\text{gg}} = 9.732$ MeV), are detected in coincidence with the low energy recoiling ^{17}O nucleus detected at forward angles. Summing the measured energies, as shown in Fig. 4.17c, yields peaks with spacing corresponding to the ground and first three excited states of ^{17}O [8]. The tight groups disappear below $AE_1 + AE_2 \sim 6.5$ MeV corresponding to a target-like excitation of $E_r^* = 4.1$ MeV. This is due to the neutron decay threshold of ^{17}O$\rightarrow n+^{16}$O. The energy carried by the neutron will result in the smooth distribution of $AE_1 + AE_2$ seen here.

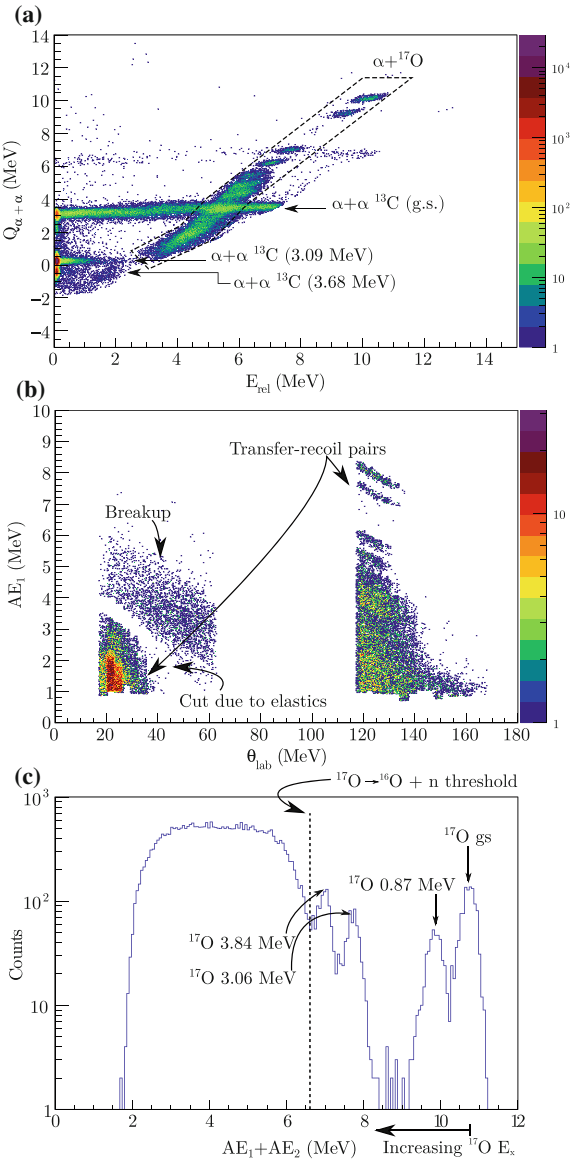

Fig. 4.17 (**a**) Reconstructed Q-E_{rel} spectrum for coincidence pairs detected in reactions of ^{9}Be with ^{12}C at $E_{\text{beam}} = 6.60$ MeV, after the removal of random coincidences. There are a large number of events that are tightly grouped at high E_{rel} with a large span of reconstructed $Q_{\alpha+\alpha}$, indicated in the dashed box. (**b**) When the energy and scattering angle of these events are projected into AE_1 vs θ_1, they show groups of events at high energies at backward angels, and low energies at forward angles. This is characteristic of transfer-recoil coincidences. (**c**) When the measured energies of the transfer-recoil coincidences are summed, peaks corresponding to the ground and first three excited states of ^{17}O appear. At lower summed energies, corresponding to higher excitation of ^{17}O, the peaks disappear, leaving a smooth distribution of energies. This occurs when the excitation of ^{17}O is above the neutron decay threshold, indicated by the dashed line [8]. These energies have not been corrected for energy loss through BALiN

These coincidence events appear when measuring breakup on very light targets with detectors placed at forward angles. For heavier targets, the forward arcs of BALiN were blocked to reduce the elastic flux, removing the possibility of measuring recoiling nuclei. Further, in higher mass targets, the energy of the recoiling nucleus is low enough that it is stopped in the deadlayers, or is below the energy threshold of BALiN.

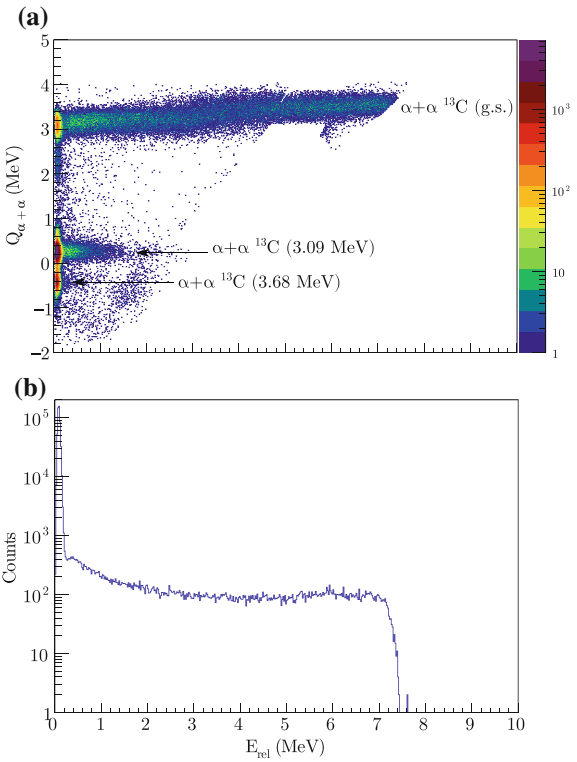

Fig. 4.18 **a** Q-E_{rel} spectrum for $\alpha + \alpha$ pairs detected in coincidence in the breakup after interactions of ^{9}Be with ^{12}C at $E_{\mathrm{beam}} = 6.60$ MeV. Peaks are seen in $Q_{\alpha+\alpha}$ corresponding ^{13}C in its ground and first three excited states, confirming the neutron stripping triggered breakup mechanism in this reaction. **b** The projected E_{rel} spectrum for the same data. A large fraction of events have an E_{rel} near 0.092 MeV, demonstrating a large population of the ground-state of ^{8}Be in the transfer process

These transfer-recoil coincidence events are easily removed: a gate on Q-E_{rel} is able to remove the majority, except for those that overlap with the high E_{rel} portion of the $\alpha + \alpha$ band corresponding to breakup populating the ground state of ^{13}C. When the overlapping region of Q-E_{rel} is projected into AE_1 vs θ_1 and AE_2 vs θ_2, the breakup pairs are kinematically distinct from the transfer-recoil pairs: the breakup pairs have highest energy at smallest θ, and the reverse is true for transfer-recoil pairs, as seen in Fig. 4.17b. This property allows breakup pairs to be separated from transfer-recoil pairs where they overlap in Q-E_{rel}. The resulting Q-E_{rel} spectrum for the neutron stripping triggered breakup of ^{8}Be in interactions of ^{9}Be with ^{12}C is shown in Fig. 4.18a, and is projected in E_{rel} in Fig. 4.18b. A very strong population of ^{8}Be in its ground state is evident, with a virtually flat distribution of events extending to high E_{rel}. There is a slight jump in the reconstructed $Q_{\alpha+\alpha}$ spectrum at $E_{\mathrm{rel}} \sim 3$ MeV, which corresponds to breakup pairs with opening angles such that one α falls on the forward angle pair of detectors, and one on the backward angle pair of detectors. This is an indication that the detector-target distance for one of the BALiN pairs is slightly ($\sim$1 mm) incorrect. It is, however, a small jump, and does not effect the conclusions drawn in regards to the breakup mechanisms in reactions of ^{9}Be with ^{12}C, that is, neutron stripping triggered breakup forming $\alpha + \alpha$ pairs is dominant. As the other modes have large negative Q_{gg}, this further demonstrates the importance of reaction Q-value.

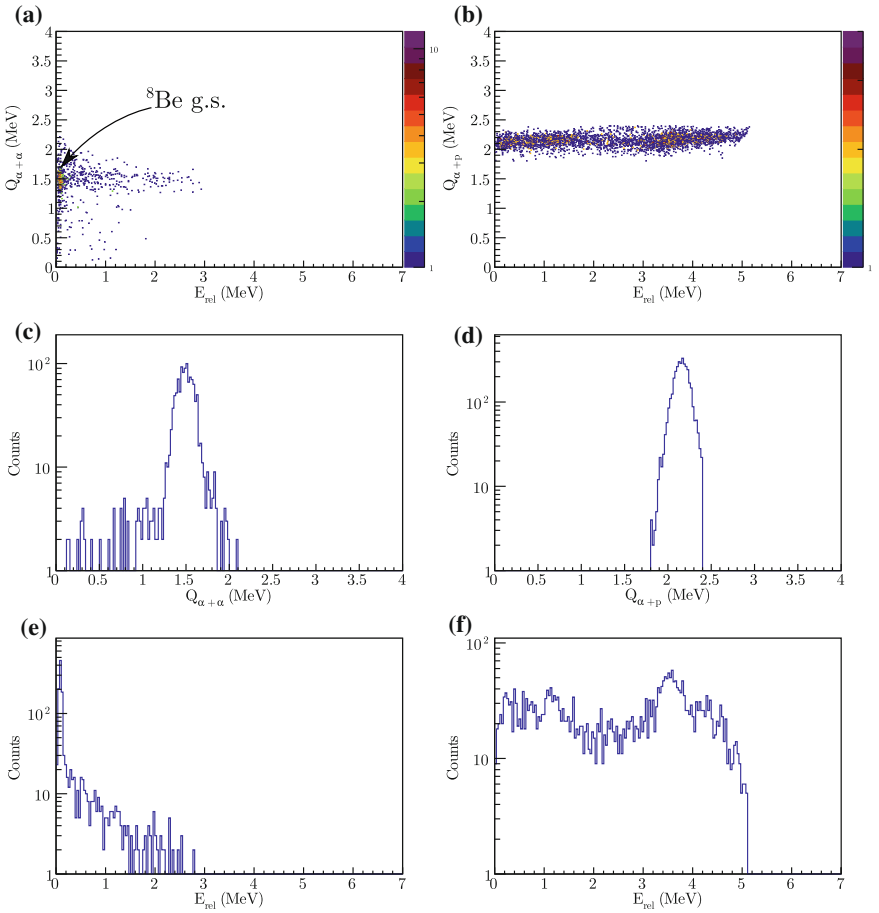

Fig. 4.19 Q-E_{rel} spectra of **a** $\alpha+\alpha$ and **b** $\alpha+p$ breakup pairs produced after interactions of ^{7}Li with ^{12}C at $E_{\mathrm{beam}} = 4.50$ MeV. Corresponding Q spectra are shown in **c** and **d** for the $\alpha+\alpha$ and $\alpha+p$ pairs, respectively, along with their E_{rel} spectra shown in **e** and **f**

4.7.2 ^{7}Li + ^{12}C

In reactions of ^{7}Li with ^{12}C proton pickup forming ^{8}Be and two-neutron stripping forming ^{5}Li have positive Q, and therefore both should be expected to occur. This is indeed the case. Shown in Fig. 4.19a, b are the ToF gated Q-E_{rel} spectra for $\alpha+\alpha$ and $\alpha+p$ pairs, respectively, detected in reactions of ^{7}Li with ^{12}C at $E_{\mathrm{beam}} = 4.50$ MeV. The yields of $\alpha+\alpha$ and $\alpha+p$ pairs indicate that breakup producing $\alpha+p$ pairs is the dominant breakup mode at this energy, comprising $76 \pm 2\%$ of the raw yield (prior to efficiency correction). Proton pickup populating ^{8}Be in its long-lived 92 keV ground state peak (with $E_{\mathrm{rel}} < 0.2$ MeV) comprises $73 \pm 3\%$ of the $\alpha+\alpha$ yield. The efficiency for detecting $\alpha+\alpha$ pairs in the 92 keV peak is much higher than the high E_{rel} portion of the spectrum, especially in light systems, as will be

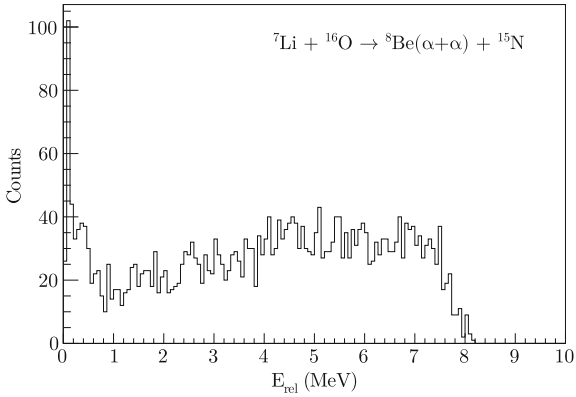

Fig. 4.20 E_{rel} spectrum for $\alpha + \alpha$ pairs detected in coincidence in the breakup of ^{8}Be produced in interactions of ^{7}Li with ^{16}O at $E_{\mathrm{beam}} = 4.50$ MeV in data taken during the LIAL experimental run

discussed in Chap. 6, making definitive conclusions tenuous at this point. However, the low beam energy and reaction Q-value leaves little energy available to excite ^{8}Be in its first 2^{+} state at $E_p^{*} = 3.03$ MeV ($E_{CM} + Q_{\mathrm{gg}} = 2.84 + 1.40 = 4.24$ MeV).

4.7.3 ^{7}Li + ^{16}O

The use of a $^{28}SiO_2$ target to measure below-barrier breakup after interactions of ^{7}Li and ^{9}Be with ^{28}Si also enabled the examination of the interaction of ^{7}Li with ^{16}O. By lowering the beam energy to below the fusion barrier for ^{7}Li + ^{16}O, (far below the barrier for reactions with ^{28}Si) no contamination due to breakup in interactions with ^{28}Si was observed. Only breakup resulting in $\alpha + \alpha$ pairs, populating ^{15}N in its ground state was observed. The E_{rel} spectrum for these events is shown in Fig. 4.20. These data were taken in the LIAL run, where angles forward of 55° were blocked. Based on kinematic expectations, most of the breakup flux from light targets should be forward focussed. As a result, blocking forward angles significantly reduces the efficiency of detecting breakup pairs after interactions with light nuclei. However, KAITKIN simulations indicate BALiN should be sensitive to $\alpha + p$ pairs in this reaction. The low beam energy, coupled with the slightly negative transfer Q-value may have suppressed this breakup mode.

4.8 Summary

In this chapter, the modes of breakup after interactions of ^{7}Li and ^{9}Be with targets ranging in mass from ^{12}C to ^{209}Bi have been identified through kinematic reconstruction of reaction Q-values as well as through direct identification of the masses of fragments through ToF.

In interactions of ^{9}Be with the heavy target nuclei, ^{144}Sm, ^{168}Er, ^{186}W, ^{196}Pt, ^{208}Pb and ^{209}Bi, the dominant breakup mode is neutron stripping producing ^{8}Be followed by its decay into $\alpha + \alpha$ fragments. The next most likely mode is direct breakup into $\alpha + \alpha + n$ fragments. On the lighter end of the periodic table, in interactions of ^{9}Be with ^{28}Si, ^{27}Al, and ^{12}C, breakup triggered by neutron stripping remains the dominant breakup mode. However, direct breakup through the $\frac{5}{2}^{-}$ state of ^{9}Be was not observed in the Q against $E_{\rm rel}$ spectra for these measurements. In addition, in reactions of ^{9}Be with ^{28}Si and ^{27}Al, an additional breakup mode with large positive $Q_{\rm gg}$ was observed, leading to $\alpha + p$ pairs. The presence of these pairs, even though a large amount of mass transfer must occur, is indicative of the effect that Q-values have in dictating whether or not a breakup mode will be present. In addition, $p + p$ pairs were observed, with Q-values consistent with population of the recoiling target-like nucleus. The origin of these events is unclear, and may be a result of transfer or two proton evaporation following fusion.

Measurements of breakup in interactions of ^{7}Li with ^{58}Ni, ^{28}Si, ^{27}Al, and ^{12}C yielded a variety of breakup modes. In interactions of ^{7}Li with all targets, $\alpha + \alpha$ pairs were observed resulting from proton pickup forming ^{8}Be, as well as $\alpha + p$ pairs resulting from two-neutron stripping forming ^{5}Li. In addition, in reactions of ^{7}Li with ^{58}Ni, $\alpha + d$ pairs resulting from one-neutron stripping into ^{6}Li above its breakup threshold were observed. Direct breakup $^{7}\text{Li} \rightarrow \alpha + t$ was not observed in any ^{7}Li measurement reported in this thesis. Unlike reactions with ^{9}Be, no single breakup mode dominated in reactions of ^{7}Li. Instead, the presence of one fewer proton in ^{27}Al compared to ^{28}Si resulted in the dominant breakup mode switching from that producing $\alpha + p$ pairs to $\alpha + \alpha$ pairs. Clearly, target structure plays a significant role in transfer-triggered breakup in reactions with ^{7}Li.

The effect of projectile structure is evident in the $E_{\rm rel}$ spectra. In ^{9}Be a higher proportion of the measured $\alpha + \alpha$ pairs had $E_{rel} = 0.092$ MeV than was seen in reactions with ^{7}Li producing $\alpha + \alpha$ pairs. This is important: at above-barrier energies, only breakup that occurs prior to the nuclei reaching the fusion barrier can suppress complete fusion. Below the barrier, this corresponds to breakup that occurs prior to reaching the distance of closest approach. As has been discussed, $\alpha + \alpha$ pairs with $E_{rel} = 0.092$ MeV correspond to breakup of the long-lived ground-state resonance of ^{8}Be. This breakup cannot suppress complete fusion as the breakup of ^{8}Be will not occur before passing inside the fusion barrier. In reactions with ^{9}Be, a larger fraction of the $\alpha + \alpha$ pairs are therefore not able to suppress complete fusion compared to the $\alpha + \alpha$ pairs measured in reactions with ^{7}Li. If the ability of breakup to suppress complete fusion depends on the location of breakup, it is not only the mode of breakup that is relevant to fusion suppression: it is also the timescale of breakup. In the following chapter, kinematic signatures of near-target breakup will be discussed.

References

1. Luong, D.H., Dasgupta, M., Hinde, D.J., Du Rietz, R., Rafiei, R., Lin, C.J., Evers, M., Diaz-torres, A.: Insights into the mechanisms and time-scales of breakup of ^{6,7}Li. Phys. Lett. B **695**, 105 (2011)
2. Luong, D.H., Dasgupta, M., Hinde, D.J., du Rietz, R., Rafiei, R., Lin, C.J., Evers, M., Diaz-Torres, A.: Predominance of transfer in triggering breakup in sub-barrier reactions of ^{6,7}Li. Phys. Rev. C **88**(3), 34609 (2013)
3. Rafiei, R., du Rietz, R., Luong, D.H., Hinde, D.J., Dasgupta, M., Evers, M., Diaz-torres, A.: Mechanisms and systematics of breakup in reactions of ^{9}Be at near-barrier energies. Phys. Rev. C **81**(2), 024601 (2010)
4. Rafiei, R.: Dynamics of breakup and quasifission - mechanisms inhibiting fusion. Ph.D. thesis, The Australian National University (2010)
5. Cline, C.K., Alford, W.P., Gove, H.E., Tickle, R.: Multiplet structure of ^{210}Bi from the ^{209}Bi(d, p) and ^{209}Bi(α,^{3}He) reactions. Nucl. Phys. A **186**, 273 (1972)
6. Shamsuzzoha Basunia, M.: ^{209}Bi(d,p) (Data extracted from the ENSDF database). Nucl. Data Sheets **121**(561) (2014)
7. Wagner, W., Crawley, G., Hammerstein, G.: High resolution (p, p') on ^{207}Pb and ^{209}Bi. Phys. Rev. C **11**(2), 486 (1975)
8. Tilley, D.R., Weller, H.R., Cheves, C.M.: Energy levels of light nuclei A = 16–17. Nucl. Phys. A **564**, 1 (1993)
9. Ajzenberg-Selove, F.: Energy levels of light nuclei A = 13–15. Nucl. Phys. A **523**(1), 1 (1991)

Chapter 5
Examining Breakup Mechanisms

In the previous chapter, the mechanisms of breakup in interactions of ^{7}Li and ^{9}Be with targets ranging in Z from 6 to 83 were identified. In this chapter the importance of the structure of projectile-like nuclei in influencing reaction outcomes will be explored. In particular, the nature of the states populated in the projectile-like nucleus formed after transfer is a key factor in determining the extent to which transfer-triggered breakup can suppress complete fusion. At below-barrier energies, breakup that occurs prior to the nuclei reaching the distance of closest approach translates above the barrier into breakup that occurs prior to the nuclei passing the fusion barrier, reducing the probability of complete charge capture. Conversely, breakup that occurs after the nuclei reach the distance of closest approach translates into capture of the nuclei at above-barrier energies. This equivalence is shown schematically in Fig. 5.1. Therefore, the locations of breakup are important. These locations are intimately connected to the lifetime of resonance states. In general, broad resonances populated in a reaction will quickly decay, resulting in breakup near to the target. This has the capacity to suppress complete fusion if it occurs prior to passing inside the fusion barrier radius. Transfer populating narrow resonances will break up asymptotically far from the target nucleus, long after the distance of closest approach, so cannot suppress complete fusion.

It is thus desirable to separate asymptotic breakup that cannot suppress complete fusion from breakup near the target which may. This can be achieved by the use of kinematic quantities that are sensitive to behaviour of fragments near the target. In this chapter, the experimental results from breakup at sub-barrier energies will be compared to simulations from KOOKABURRA to verify the ability of KOOKABURRA to reproduce experimental results to a reasonable extent. With guidance from KOOKABURRA, the kinematic signatures of breakup that occurs on the incoming and on the outgoing trajectory will be explored.

K. J. Cook, *Zeptosecond Dynamics of Transfer-Triggered Breakup*,
Springer Theses, https://doi.org/10.1007/978-3-319-96017-3_5

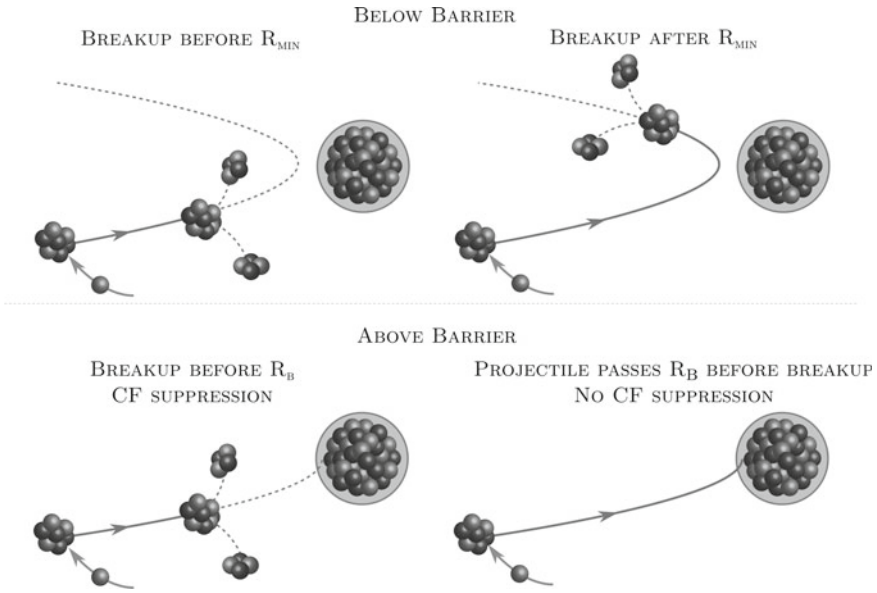

Fig. 5.1 At below-barrier energies, breakup that occurs prior to the projectile-like nucleus passing R_{min} translates at above-barrier energies to breakup prior to the projectile-like nucleus reaching R_B. In this case, breakup can suppress complete fusion at above-barrier energies. Conversely, breakup at below-barrier energies that occurs after the projectile-like nucleus passes R_{min} translates to capture of the projectile at above-barrier energies

As is apparent from Chap. 4, the number of reactions measured in this thesis is large. It is therefore not appropriate to discuss each system in detail. Instead, breakup after interactions of ^{7}Li with ^{58}Ni will be discussed as a representative case. Where there are significant differences between ^{7}Li + ^{58}Ni and other systems, other systems will be mentioned. ^{7}Li + ^{58}Ni was chosen for three reasons. Firstly, it is the projectile-target combination with the largest variety of intense breakup modes; $\alpha + \alpha$, $\alpha + d$ and $\alpha + p$. Secondly, it lies in-between the reactions with very heavy target nuclei (such as ^{208}Pb) and those with very light target nuclei (such as ^{12}C). Thirdly, due to its intermediate Z, it is a sensitive test of the new physics incorporated in M-Platypus and Kookaburra. In high Z targets, the acceleration experienced by the breakup fragments due to the strong Coulomb field 'washes out' the nuances of target-fragment interactions. In low Z targets, the efficiency of BALiN plays a larger role in dictating the shape of spectra. In this way, ^{58}Ni is neither too light nor too heavy, it is 'just right'. To distinguish between near-target and asymptotic breakup, we begin with examining E_{rel} distributions of breakup fragments produced in the transfer-triggered breakup after interactions of ^{7}Li with ^{58}Ni.

5.1 Separating Near-Target and Asymptotic Breakup Using Relative Energy

The utility of E_{rel} for the separation of near-target and asymptotic breakup was introduced in Sect. 2.8.4. With the example of breakup after interactions of ^{7}Li with ^{208}Pb, it was shown that it is possible to separate breakup that occurs from long-lived (narrow) resonances from that which occurs close to the target and/or from broad resonances.

In previous work [1–5], the idea that the very short lifetimes of broad resonant structures were relevant was not incorporated in the interpretation of E_{rel} and further analysis. Instead, all breakup that did not populate a narrow resonance was designated "prompt" and assumed to occur effectively instantly after transfer. As a result, it was assumed that an equal amount of breakup occurred on the incoming trajectory and on the outgoing trajectory. However, when lifetimes (even of broad resonances) are taken into account transfer that occurs on the incoming trajectory can result in breakup on the outgoing trajectory. As a result, more breakup will occur on the outgoing trajectory than on the incoming trajectory when the projectile-like nucleus has a finite lifetime. In the context of broad resonances, a more detailed understanding of the physics behind E_{rel} distributions is desirable.

Many E_{rel} distributions have already been shown in Chap. 4, such as in Fig. 4.7g through (i) (p. 103), which shows the E_{rel} distribution for breakup after interactions of ^{7}Li with ^{58}Ni producing $\alpha+\alpha$, $\alpha+p$ and $\alpha+d$ pairs, respectively. In the E_{rel} distribution for $\alpha+\alpha$ pairs, there is a peak in intensity at 92 keV, corresponding to breakup from the narrow ground-state resonance of ^{8}Be, such that $E_{\mathrm{rel}} = Q_{\mathrm{BU}} + E_{\mathrm{p}}^{*} + \Delta E_{\mathrm{acc}} = 92 + 0 + 0$ keV (as previously discussed in Sect. 2.8.4). Beyond this peak, there is a broad band of events with E_{rel} up to ~19 MeV, with a broad peak at ~2 MeV. These events may be due to (a) breakup from the high E_{p}^{*} tail of the 0^{+} resonance, (b) breakup from the broad 2^{+} resonance or (c) breakup from the broad 4^{+} resonance, all of which may experience distortion due the Coulomb field of the target-like nucleus, contributing to E_{rel} via the ΔE_{acc} term. Since for any given E_{p}^{*}, there is a non-zero probability of populating ^{8}Be in any particular resonance, as seen in Fig. 2.5, it is not possible to definitively identify a given E_{rel} to a given resonance. Therefore the high E_{rel} band of events almost certainly arises from a mixture of (a), (b) and (c).

In the E_{rel} distribution for $\alpha+p$ fragments, shown in Fig. 4.7h, there is no sign of a narrow resonance: this is unsurprising, as ^{5}Li is unbound and has no narrow resonances. All breakup forming $\alpha+p$ pairs will be short-lived. This should predominantly be due to the low-lying $\frac{3}{2}^{-}$ and $\frac{1}{2}^{-}$ resonances of ^{5}Li. However, contributions from different partial waves are possible.

Finally, the E_{rel} distribution for breakup after neutron stripping from ^{7}Li producing ^{6}Li which decays into $\alpha+d$ pairs is shown in Fig. 4.7i. There is a narrow peak at E_{rel} ~ 0.7 MeV corresponding to breakup from the first 3^{+} resonance in ^{6}Li, such that $E_{\mathrm{rel}} = Q_{\mathrm{BU}} + E_{\mathrm{p}}^{*} + \Delta E_{\mathrm{acc}} = -1.4743 + 2.186 + 0 = 0.712$ MeV. The origin of the tail of events extending to ~5 MeV is unclear. There are no nearby broad resonances

of ^{6}Li. However, as has been discussed in detail in Sect. 2.5 all excitation energies above a particle decay threshold have some probability of being populated in some partial wave. The high E_{rel} region will be a result of this probability, modulated by ΔE_{acc}. The fact that the E_{rel} distribution for $\alpha + d$ pairs extends to lower energies than for $\alpha + \alpha$ pairs is principally due to the fact that neutron transfer forming ^{6}Li has a low transfer Q-value $Q_{\mathrm{gg}} = 0.274$ MeV, in contrast to $Q_{\mathrm{gg}} \sim 9$ MeV for $\alpha + p$ and $\alpha + \alpha$ pairs. Because of this, less energy is available for excitation.

From the above discussion it is clear that the reconstructed E_{rel} distributions arise from a complex interplay between the structure of the projectile-like nuclei, the lifetimes of the resonant states populated, and the effects of the proximity of breakup to the target-like nucleus. The extent of the role of ΔE_{acc} is difficult to determine in E_{rel}. Using E_{rel} distributions, it is not possible to distinguish between breakup that occurs from a broad resonance far from the target-like nucleus with $E_{\mathrm{rel}} = Q_{\mathrm{BU}} + E_{\mathrm{p}}^*$ and breakup that occurs close to the target-like nucleus (from a broad or narrow resonance) with $E_{\mathrm{rel}} = Q_{\mathrm{BU}} + E_{\mathrm{p}}^* + \Delta E_{\mathrm{acc}}$. As broad resonances are short-lived, usually, breakup that occurs after populating broad resonances will occur close to the target.[1] As discussed in Sects. 2.8.4 and 2.9.3, ΔE_{acc} depends on a number of factors, including, but not limited to, target proximity and orientation of the fragments.

5.2 Orientation of the Relative Momentum of Breakup Fragments

To examine the effects of target proximity on the observed energy and angular distribution of fragments in more detail, a new breakup observable was constructed, that of the orientation β of relative momentum of the breakup fragments with respect to the direction of the centre of mass of the nucleus undergoing breakup, reconstructed assuming that the projectile-like nucleus decays far from the target [6, 7]. The relationship between β and the opening angle θ_{12} provides crucial insight into the location of breakup. β can also be described as the breakup angle in the projectile-like nucleus rest frame. The relationship between β and θ_{12} is shown schematically in Fig. 5.2. β can be reconstructed from measured quantities by considering the laboratory velocities of the breakup fragments $|\vec{v}_1| = \sqrt{\frac{2E_1}{m_1}}$, $|\vec{v}_2| = \sqrt{\frac{2E_2}{m_2}}$ as well as their scattering angles. A brief derivation follows.

Using the definition of E_{rel}, shown in Eq. 2.41, and conserving momentum, the velocities of the breakup fragments in the rest frame of the projectile-like nucleus are given by:

[1] Recall that the on-resonance width of states corresponds to an on-resonance mean-life τ, such that the time taken from transfer to decay follows an exponential distribution following $e^{-t/\tau}$. Therefore, a small fraction of transfer products populated in broad resonances will break up far from the target, especially if E_{p}^* is small, as can be seen in Fig. 2.14.

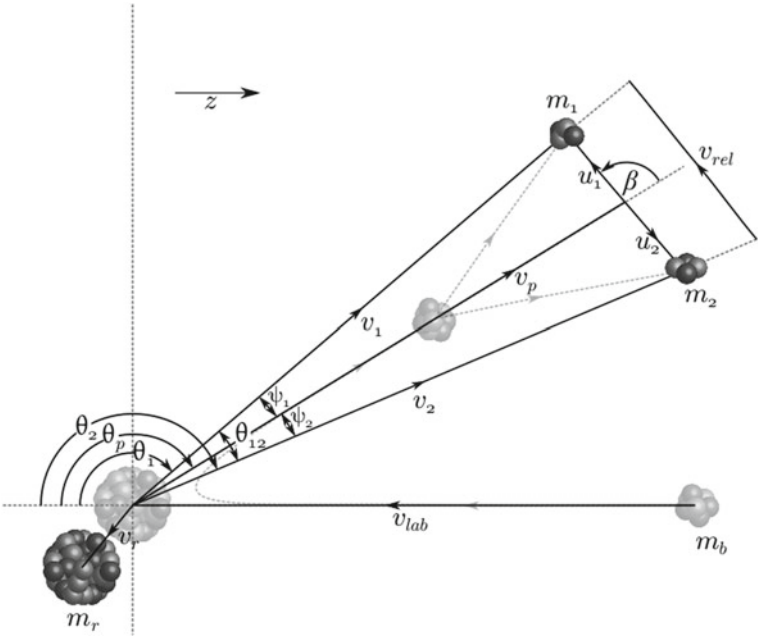

Fig. 5.2 Schematic demonstrating the velocity vectors used to determine Q, opening angle θ_{12}, relative energy and β angle. v_{lab}, v_{p}, v_{r}, v_1 and v_2 are the laboratory velocities of the beam, projectile-like nucleus, recoiling nucleus and breakup fragments, respectively. The masses of the beam, recoiling nucleus and breakup fragments are given by m_b, m_{r}, m_1 and m_2. The velocities of the breakup fragments in their centre of mass is given by u_1 and u_2 and their relative velocity is v_{rel}. The scattering angles of the projectile and breakup fragments are given by θ_{p}, θ_1 and θ_2. (Figure reproduced from Chap. 2)

$$|\vec{u}_1| = \sqrt{\frac{2m_2 E_{\text{rel}}}{m_1(m_1+m_2)}}$$
$$|\vec{u}_2| = \sqrt{\frac{2m_1 E_{\text{rel}}}{m_2(m_1+m_2)}}. \tag{5.1}$$

We can relate β and θ_{12} using geometry by considering the angles $\psi_{1,2}$ between the laboratory velocity of each fragment $\vec{v}_{1,2}$ and the velocity of the projectile nucleus $\vec{v}_{\text{p}}$, shown in Fig. 5.2. Using geometry, ψ_i can be related to $|\vec{u}_i|$, $|\vec{v}_i|$ and β, so that

$$\sin\psi_1 = \sin(\pi-\beta)\frac{|\vec{u}_1|}{|\vec{v}_1|} \tag{5.2}$$
$$\cos\psi_1 = \frac{|\vec{v}_{\text{p}}| + |\vec{u}_1|\cos\beta}{|\vec{v}_1|} \tag{5.3}$$

$$\sin\psi_2 = \sin\beta\frac{|\vec{u}_2|}{|\vec{v}_1|} \tag{5.4}$$

$$\cos\psi_2 = \frac{|\vec{v}_\mathrm{p}| - |\vec{u}_2|\cos\beta}{|\vec{v}_2|}. \tag{5.5}$$

Noting that $\psi_{1,2}$ are related to θ_{12} via $\psi_1 + \psi_2 = \theta_{12}$, β can be written in terms of θ_{12} using these expressions, giving

$$\sin\beta = \frac{|\vec{v}_1||\vec{v}_2|\sin\theta_{12}}{|\vec{v}_\mathrm{p}|(|\vec{u}_1| + |\vec{u}_2|)}. \tag{5.6}$$

All that is not known in this expression is the reconstructed laboratory velocity of the transfer product $\vec{v}_\mathrm{p}$. It has previously been defined in Eq. 2.36, but it is convenient to rewrite it in terms of θ_{12} and $|\vec{u}_i|$, $|\vec{v}_i|$. This can be done using the cosine law:

$$\cos\beta = \frac{|\vec{v}_1|^2 - |\vec{u}_1|^2 - |\vec{v}_\mathrm{p}|^2}{2|\vec{u}_1||\vec{v}_\mathrm{p}|} = \frac{|\vec{v}_\mathrm{p}|^2 + |\vec{u}_2|^2 - |\vec{v}_2|^2}{2|\vec{u}_2||\vec{v}_\mathrm{p}|}. \tag{5.7}$$

Rearranging for $|\vec{v}_\mathrm{p}|$ and multiplying by $(|\vec{u}_1| + |\vec{u}_2|)$ gives the denominator to Eq. 5.6, which after some simplification can be expressed as:

$$|\vec{v}_\mathrm{p}|(|\vec{u}_1| + |\vec{u}_2|) = \sqrt{|\vec{v}_2|^2|\vec{u}_1|^2 + |\vec{v}_1|^2|\vec{u}_2|^2 + |\vec{u}_1||\vec{u}_2|(|\vec{v}_1|^2 + |\vec{v}_2|^2 - (|\vec{u}_1| + |\vec{u}_2|)^2)}. \tag{5.8}$$

Then, using the cosine law,

$$\cos\theta_{12} = \frac{|\vec{v}_1|^2 + |\vec{v}_2|^2 - (|\vec{u}_1| + |\vec{u}_2|)^2}{2|\vec{v}_1||\vec{v}_2|}. \tag{5.9}$$

Substituting this into Eq. 5.8 gives β as a function of θ_{12} and the velocities of the fragments in a fairly compact form:

$$\sin\beta = \frac{|\vec{v}_1||\vec{v}_2|\sin\theta_{12}}{(|\vec{v}_2|^2|\vec{u}_1|^2 + |\vec{v}_1|^2|\vec{u}_2|^2 + 2|\vec{u}_1||\vec{u}_2||\vec{v}_1||\vec{v}_2|\cos\theta_{12})^{1/2}}. \tag{5.10}$$

Due to the sine term, this expression does not distinguish between β and $(180 - \beta)$. β may be disambiguated by noting that if $|\vec{v}_1|\cos\psi_1 > |\vec{v}_2|\cos\psi_2$, then $\beta < 90°$. Thus, writing $\psi_{1,2}$ in terms of velocity vectors, we obtain the inequality

$$|\vec{v}_1|^2 - |\vec{u}_1|^2 > |\vec{v}_2|^2 - |\vec{u}_2|^2. \tag{5.11}$$

If this inequality is satisfied, $\beta < 90°$, otherwise $\beta \to 180° - \beta$. This expression enables β to be determined for each pair of breakup fragments.

β is reconstructed assuming that the breakup has occurred asymptotically far from the target-like nucleus. If breakup occurs close to the target-like nucleus,

post-breakup fragment-target interactions will distort the reconstructed values of β. These distortions mean that β will not reflect the initial breakup angle in the rest frame of the projectile-like nucleus. This fact enables us to examine the effects of post-breakup acceleration in the energy and angular distribution of fragments: deviations from asymptotic β distributions indicate the presence of post-breakup acceleration. Therefore, it is useful to know what the expected asymptotic distributions are.

When breakup occurs asymptotically far from the target-like nucleus from a transfer product in a long-lived resonant state with $E_{\rm rel} = E_{\rm p}^{*} + Q_{\rm BU}$, we can obtain β in terms of $E_{\rm p}^{*} + Q_{\rm BU}$ and the sum of the energies of the fragments, $E_0 = E_1 + E_2$. We can write

$$|\vec{v}_{\rm p}| = \sqrt{\frac{2(E_0 - E_{\rm p}^{*})}{m_1 + m_2}}. \tag{5.12}$$

Then, since

$$\vec{v}_1 = \vec{v}_c + \vec{u}_1, \tag{5.13}$$

the cosine rule gives

$$\begin{aligned} |\vec{v}_1| &= \sqrt{|\vec{u}_1|^2 + |\vec{v}_{\rm p}|^2 + 2|\vec{u}_1||\vec{v}_{\rm p}|\cos\beta} \\ |\vec{v}_2| &= \sqrt{|\vec{u}_2|^2 + |\vec{v}_{\rm p}|^2 - 2|\vec{u}_2||\vec{v}_{\rm p}|\cos\beta}. \end{aligned} \tag{5.14}$$

Substituting Eqs. 5.1, 5.12 and 5.14 into Eq. 5.9 yields an expression for the relationship between β and θ_{12} in terms of $E_{\rm rel}$, $E_1 + E_2$, m_1 and m_2 only:

$$\begin{aligned} \cos(\theta_{12}) = \left(E_0 - 2E_{\rm rel}\left[m_2\sqrt{\frac{m_2(E_0 - E_{\rm rel})E_{\rm rel}}{m_1(m_1+m_2)^2}} - m_1\sqrt{\frac{m_1(E_0 - E_{\rm rel})E_{\rm rel}}{m_2(m_1+m_2)^2}} \right]\cos\beta \right) \Bigg/ \\ \left[\frac{1}{m_1 m_2}\left(m_2 E_0 + (m_1 - m_2)E_{\rm rel} - 2\sqrt{m_1 m_2 (E_0 - E_{\rm rel})E_{\rm rel}}\cos\beta \right) \right. \\ \left. \left(m_1 E_0 + (m_2 - m_1)E_{\rm rel} + 2\sqrt{m_1 m_2 (E_0 - E_{\rm rel})E_{\rm rel}}\cos\beta \right) \right]^{1/2}. \end{aligned} \tag{5.15}$$

This expression enables the comparison between reconstructed $\theta_{12} - \beta$ distributions and the asymptotic expectation for a given $E_{\rm p}^{*}$, $Q_{\rm BU}$ and $E_1 + E_2$.

The experimental $\theta_{12} - \beta$ distributions for the three different modes of breakup seen in reactions of ^{7}Li with ^{58}Ni at $E_{\rm beam} = 11.70$ MeV are shown in Fig. 5.3. One thing is immediately clear: the three distributions are very different. We will discuss each in turn. The reconstructed $\theta_{12} - \beta$ distribution for proton pickup triggered breakup forming $\alpha + \alpha$ pairs, shown in Fig. 5.3a, extends across all θ_{12}, with two sets of intense bands of events below $\theta_{12} \lesssim 80°$, and a peak in intensity at $\beta = 90°$. The dip in intensity at $\beta = 90°$ and $\theta_{12} \sim 60°$ is due to the removal of elastically scattered beam particles, which also removes some genuine $\alpha + \alpha$ pairs in this region of $\theta_{12} - \beta$. This is taken into account in the efficiency correction discussed in Chap. 6. In the previous section, it was discussed that the $E_{\rm rel}$ distribution of ^{8}Be may arise

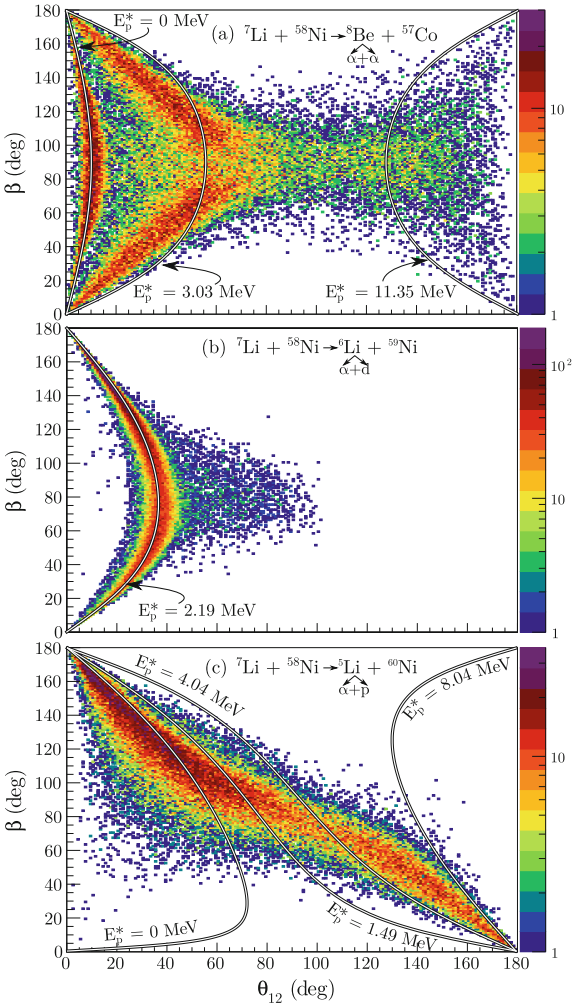

Fig. 5.3 **a** $\theta_{12} - \beta$ distribution for $\alpha + \alpha$ pairs produced in the proton-pickup triggered breakup of ^{8}Be in ^{7}Li interactions with ^{58}Ni at $E_{\text{beam}} = 11.70$ MeV. Lines indicate the expected asymptotic $\theta_{12} - \beta$ distribution corresponding to breakup of ^{8}Be in its first 0^+, 2^+ and 4^+ resonances with on-resonant excitation $E_{\text{p}}^* = 0, 3.03$ and 11.70 MeV. The deficit of events around $\beta = 90°$ and $\theta_{12} \sim 60°$ is due to the removal of elastically scattered beam particles, which also removes some genuine $\alpha + \alpha$ pairs in this region of $\theta_{12} - \beta$. **b** The same experiment, for neutron stripping forming ^{6}Li produced above its breakup threshold, followed by the production of $\alpha + d$ pairs. The line indicates the asymptotic prediction for ^{6}Li populated in its first 3^+ resonance at $E_{\text{p}}^* = 2.19$ MeV. **c** The same experiment, for two neutron stripping forming ^{5}Li which subsequently decays into $\alpha + p$ pairs. Lines indicate asymptotic predictions for breakup of ^{5}Li with E_{p}^* corresponding to the on-resonance energies of its $\frac{3}{2}^-$ ground-state resonance and first $\frac{1}{2}^-$ resonance. Additional lines have been drawn at $E_{\text{p}}^* = 4.04$ and 8.04 MeV, and will be discussed in the text

through the ^{8}Be 0^+, 2^+ and 4^+ resonances. The black and white lines in Fig. 5.3a, calculated using Eq. 5.15, indicate the expected location of the bands in $\theta_{12} - \beta$ for asymptotic breakup of ^{8}Be from its 0^+, 2^+ and 4^+ resonances with $E_p^* = 0$, 3.03 and 11.35 MeV, respectively. There is clear correspondence between the asymptotic expectation for $E_p^* = 0$ and a band of experimental $\alpha + \alpha$ events. These are the same events that have $E_{rel} = 0.092$ MeV. This confirms the interpretation that these events experienced no post-breakup Coulomb acceleration by the target-like nucleus, since the 0^+ resonance of ^{8}Be is narrow and has $\tau \sim 10^{-16}$ s, and so breakup occurs far from the target-like nucleus. The excellent match between asymptotic expectations and measurement of breakup from a long-lived state where no post-breakup acceleration can occur furthers the validity of using $\theta_{12} - \beta$ as a probe of target nucleus proximity effects.

Near-target effects in the angular correlation of $\alpha + \alpha$ breakup fragments can be seen at higher θ_{12} in Fig. 5.3a. The calculated band for asymptotic breakup from $E_p^* = 3.03$ MeV does not agree well with the shape of the experimental band of events located nearby. The intensity of events near the calculated curve indicates that the 2^+ resonance has indeed been populated, but the shape is not consistent with asymptotic breakup. The on-resonance width of this state is 1.51 MeV, corresponding to a lifetime τ of $\tau = 0.44 \times 10^{-21}$ s. This means that these distortions are expected to be due to breakup near the target-like nucleus. As a result of post-breakup acceleration, events are pushed into higher θ_{12}, and $\beta \sim 90°$ compared to asymptotic breakup expectations. This deviation from asymptotic expectations can be understood by examining the role of the potential. For breakup close to the target, a large part of the energy is stored in the fragment-target potential, and thus initial kinetic energy of the fragments is small. Because of this, there is an increased probability for $E_1 \sim E_2$ and thus of deduced values of $\beta \sim 90°$ for breakup into identical mass fragments, as shown in projection in Fig. 5.4a for all $\alpha + \alpha$ events with $E_{rel} > 0.3$ MeV. Without prior knowledge of the state that is populated, the concentration of events around $\beta \sim 90°$ (when the mass of the fragments are identical) indicates breakup close to the target nucleus. Breakup far from the target-like nucleus will have a $\sin\beta$ distribution of intensity consistent with an isotropic distribution. This can be seen in projection in Fig. 5.4b for $\alpha + \alpha$ events with $E_{rel} < 0.3$ MeV. There is a deficit of events for $\beta \lesssim 45°$ and $\beta \gtrsim 135°$ relative to expectations from the $\sin\beta$ distribution drawn to guide the eye. This is due to fact that there is an increased probability of both α fragments landing in the same arc of BALiN at small θ_{12} (and thus small β). These events are not recorded as a coincidence event and must be efficiency corrected, as discussed in Chap. 6. Finally, there is no increase in intensity of reconstructed $\theta_{12} - \beta$ near to the line that indicates the asymptotic $\theta_{12} - \beta$ relationship for on-resonance breakup from the ^{8}Be 4^+ state in the same way as was seen for the 2^+ state. This suggests that the 4^+ resonance is not significantly populated in this reaction.

The reconstructed $\theta_{12} - \beta$ distribution of $\alpha + d$ particles detected in coincidence in the same measurement is shown in Fig. 5.3b, along with a line indicating the asymptotic prediction for breakup from the first 3^+ resonance at $E_p^* = 2.19$ MeV, which has an on-resonance lifetime of $\tau = 2.74 \times 10^{-20}$ s. As expected from the

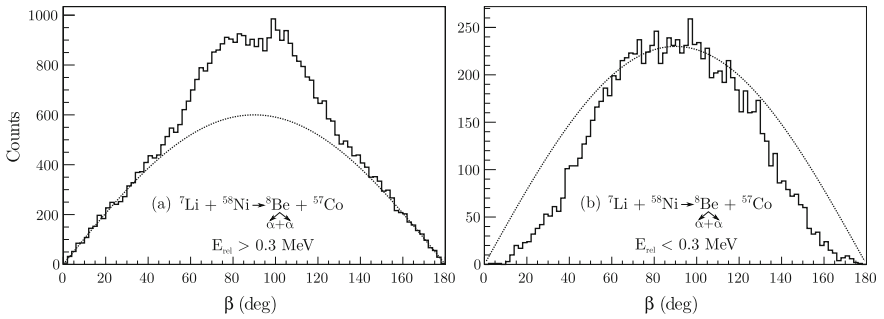

Fig. 5.4 β distribution of $\alpha + \alpha$ pairs produced in the proton-pickup triggered breakup of ^{8}Be in ^{7}Li interactions with ^{58}Ni at $E_{\text{beam}} = 11.70$ MeV where the E_{rel} of the fragments is larger than 0.3 MeV, associated with near-target breakup (**a**), and smaller than 0.3 MeV and associated with breakup from the 0^+ state of ^{8}Be (**b**). Curves of $\sin\beta$ have been drawn in both panels to guide the eye. In panel **a** there is an enhancement of events around $\beta \sim 90°$ indicating the presence of breakup close to the target-like nucleus (as discussed in the text). The events at β significantly away from 90° follow a $\sin\beta$ distribution. In panel **b** the events around $\beta \sim 90°$ follow expectations from a $\sin\beta$ distribution, but drop more rapidly around $\beta \lesssim 45°$ and $\beta \gtrsim 135°$. The deficit can be explained solely by the increased likelihood of both breakup fragments being incident on the same pixel of BALiN and are thus not recorded as a coincidence event

(relatively) long lifetime of this state, there is once again excellent correspondence between the asymptotic expectation and a band of measured points, confirming that it is this resonance that is dominantly populated. There is also a long tail of events extending to $\theta_{12} \sim 100°$. As in the case the $\alpha + \alpha$ distribution, these events correspond to near-target breakup, though there is no nearby broad resonance to populate. These events must therefore be due to either a short-lived tail of events from the 3^+ resonance,[2] or from non-resonant excitation of ^{6}Li.

Turning now to the reconstructed $\theta_{12} - \beta$ distribution of $\alpha + p$ pairs, shown in Fig. 5.3c, we see a fairly narrow diagonal band of events with $\theta_{12} + \beta \sim 180°$. In the figure, lines are shown corresponding to asymptotic breakup of ^{5}Li with excitations $E_{\text{p}}* = 0$, 1.49, 4.04 and 8.04 MeV (the on-resonance energy of the $\frac{3}{2}^-$ ground state and $\frac{1}{2}^-$ resonances, and energies corresponding to 6 and 10 MeV above the breakup threshold, respectively). The band of events follow the $E_{\text{p}}* = 0$ line fairly closely up to $\theta_{12} \sim 40°$ before deviating, perhaps indicating the longest-lived ^{5}Li that was produced. Otherwise, the asymptotic breakup lines are not representative of the data. Unlike ^{6}Li and ^{8}Be there is no narrow resonance in ^{5}Li to populate. As a result, there is little correspondence between the experimental and predicted asymptotic distributions as there is a great deal of post-breakup acceleration occurring. Thus, much of the shape of the measured $\theta_{12} - \beta$ spectrum is due to ΔE_{acc}.

Since the $\theta_{12} - \beta$ distributions are distorted by post-breakup acceleration of the breakup fragments, they will also be sensitive to the Z of the target-like nucleus. As

[2] Or from the presence of the target nucleus modifying the lifetime of the nucleus – this requires further investigation.

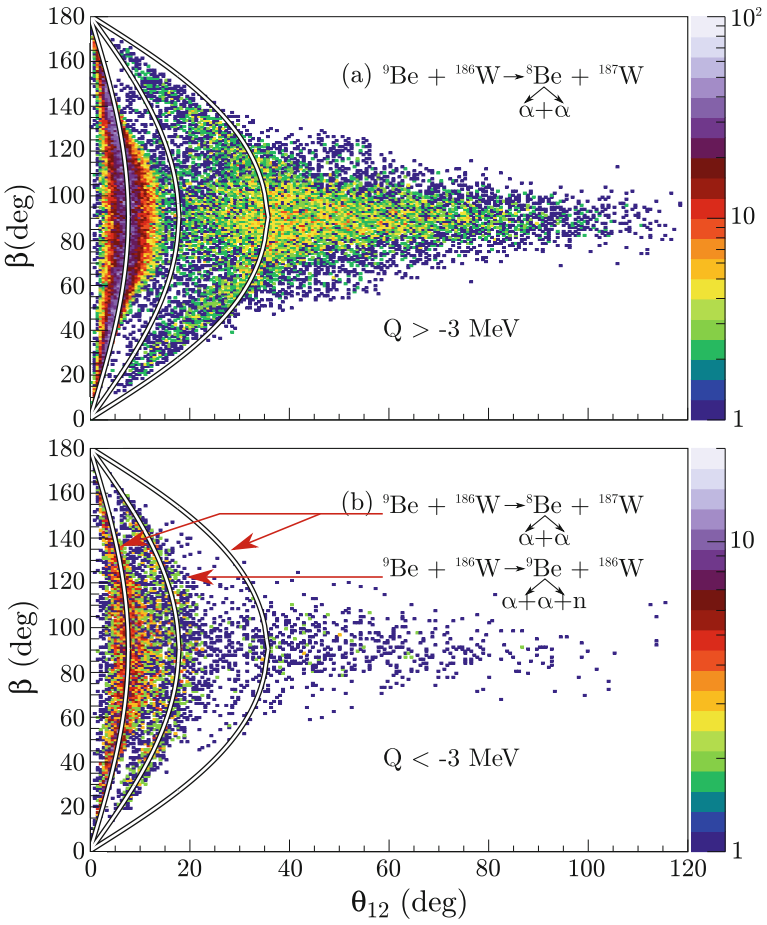

Fig. 5.5 Deduced experimental $\theta_{12} - \beta$ distribution for the direct breakup of ^{9}Be and the breakup of ^{8}Be formed after neutron transfer from ^{9}Be in interactions with ^{186}W at $E_{\text{beam}} = 37.0$ MeV. Panel **a** shows $Q > -3$ MeV, highlighting transfer-triggered breakup, and **b** the same system, for events with $Q < -3$ MeV, where the direct ^{9}Be $\frac{5}{2}^{-}$ curve is more clearly seen. Lines indicate $\theta_{12} - \beta$ curves calculated for the asymptotic breakup of (left to right) ^{8}Be 0^{+}, ^{9}Be $\frac{5}{2}^{-}$ and ^{8}Be 2^{+}. Distributions that deviate from these curves are from breakup close to the target-like nucleus where the final trajectories are perturbed by the Coulomb field. If particles fall into the same pixel of BALiN, they do not register as coincidence events, resulting in a reduced number of events observed near $\beta = 0$–$180°$

Z decreases, the strength of post-breakup acceleration will decrease, and in the limit of $Z = 0$, all breakup, regardless of projectile-target distance at the point of breakup, will follow asymptotic expectations. This will be shown to be the case in the ^{7}Li(d, n)^{8}Be reaction in Chap. 8. On the other hand, as Z increases, the strength of the post-breakup acceleration will also increase. To see this, the experimental $\theta_{12} - \beta$

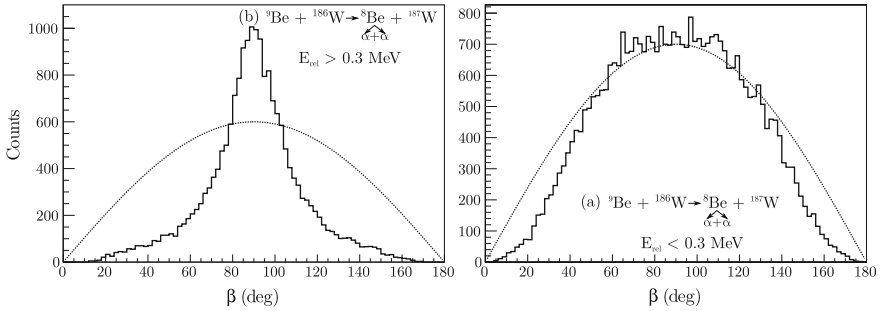

Fig. 5.6 β distribution of $\alpha + \alpha$ pairs produced in the proton-pickup triggered breakup of ^{8}Be in ^{9}Be interactions with ^{186}W at $E_{\text{beam}} = 37.0$ MeV where the E_{rel} of the fragments is larger than 0.3 MeV, associated with near-target breakup (**a**), and smaller than 0.3 MeV and associated with breakup from the 0^{+}state of ^{8}Be (**b**). Curves of sin β have been drawn in both panels to guide the eye. In panel **a** there is an enhancement of events around $\beta \sim 90°$ indicating the presence of breakup close to the target-like nucleus. In panel **b** the events around $\beta \sim 90°$ follow expectations from a sin β distribution, but drop more rapidly around $\beta \lesssim 45°$ and $\beta \gtrsim 135°$, due to events falling in the same pixel of BALiN. When compared to the same quantities extracted for $\alpha + \alpha$ pairs measured in reactions of ^{7}Li with ^{58}Ni at 11.70 MeV, as shown in Fig. 5.4, there is a significantly sharper peak around $\beta \sim 90°$ in reactions with ^{186}W than with ^{58}Ni, indicating the larger magnitude of post-breakup acceleration due to higher target Z. On the other hand, the β distributions for events with for $E_{\text{rel}} < 0.3$ MeV are almost identical in reactions with ^{58}Ni and with ^{186}W, demonstrating that no significant differential post-breakup acceleration is occurring

distributions for ^{9}Be + ^{186}W at $E_{\text{beam}} = 37$ MeV are shown in Fig. 5.5 for $Q > -3$ MeV (panel a), where transfer-triggered breakup is dominant, and for $Q < -3$ MeV (panel b), where direct breakup is dominant (e.g. region (iii) in Fig. 4.15d). Kinematic focusing of the $\alpha + \alpha$ pairs restrict the extent of the θ_{12} distribution to $\theta_{12} \lesssim 120°$. The lines overlaid on the data in Fig. 5.5 correspond to the expectations for asymptotic breakup for E_{p}^{*} arising from (left to right) ^{8}Be 0^{+} $E_{\text{p}}^{*} = 92$ keV, ^{9}Be $\frac{5}{2}^{-}$ $E_{\text{p}}^{*} = 600$ keV (region (iii) in Fig. 4.15), and ^{8}Be 2^{+} $E_{\text{p}}^{*} = 3.03$ MeV. As was previously seen in the ^{7}Li + ^{58}Ni case, bands with excellent correspondence to the calculations for the asymptotic breakup of ^{8}Be 0^{+} (shown in projection in β in Fig. 5.6b) and ^{9}Be $\frac{5}{2}^{-}$ are present in the experimental $\theta_{12} - \beta$ distribution, confirming the interpretation that these events correspond to breakup asymptotically far from the target-like nucleus. In the case of ^{7}Li + ^{58}Ni, the diagonal bands of events near the 2^{+} asymptotic curve have the highest intensity, while in ^{9}Be + ^{186}W the highest intensity is at $\beta \sim 90°$ (shown in projection in β in Fig. 5.6a). As has been discussed, events around $\beta \sim 90°$ for $\alpha + \alpha$ pairs correspond to events with $E_1 \sim E_2$, and are attributable to near-target breakup. Due to stronger near-target forces, the higher Z targets lead to an increase of deviation from asymptotic expectations.

The fact that $\theta_{12} - \beta$ distributions clearly distinguish between near-target and asymptotic breakup can be exploited to separate these two breakup types, particularly when the amount of asymptotic breakup is very small. This is the case for the direct breakup of ^{7}Li in the ^{7}Li + ^{209}Bi reaction. The Q-E_{rel} distribution for this reaction

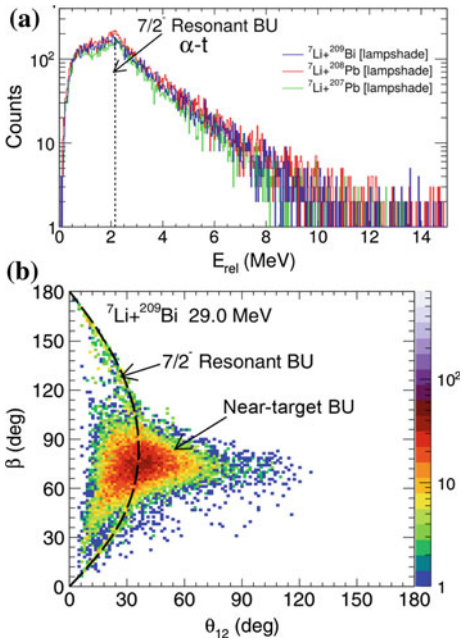

Fig. 5.7 The $E_{\rm rel}$ distribution of direct ^{7}Li breakup in reactions with ^{207,208}Pb and ^{209}Bi is essentially featureless, with only a small peak in intensity at the $E_{\rm rel}$ associated with breakup from the ^{7}Li $\frac{7}{2}^{-}$ state (**a**). When the same events are plotted as $\theta_{12} - \beta$, a clear band of events associated with the $\frac{7}{2}^{-}$ state can be observed. Reproduced from [8]

was shown in Fig. 2.11, where the $E_{\rm rel}$ distribution of $\alpha + t$ pairs was essentially featureless. This aspect of $\theta_{12} - \beta$ distributions was explored in Ref. [8] by Sunil Kalkal in collaboration with E.C. Simpson, D.H. Luong and the author. In that work, we explored the direct breakup of ^{6}Li and ^{7}Li in reactions with heavy and intermediate mass targets. It was found that using $E_{\rm rel}$, it is essentially impossible to identify any evidence of direct breakup via the long-lived $\frac{7}{2}^{-}$ resonance of ^{7}Li at $E_{\rm p}^{*} = 4.652$ MeV, shown in Fig. 5.7a. However, when the same events were plotted in the $\theta_{12} - \beta$ representation, a clear band of events appeared with a curve in $\theta_{12} - \beta$ corresponding to the asymptotic direct breakup of ^{7}Li from its $\frac{7}{2}^{-}$ resonance as well as a far more intense region of near-target breakup, shown in Fig. 5.7b.

5.3 Signatures of Breakup Before and After the Distance of Closest Approach

Thus far, we have only distinguished between two breakup locations: that which occurs "asymptotically far" from the target-like nucleus and cannot possibly suppress complete fusion and that which occurs "near" to the target-like nucleus, which may. Breakup can occur at all distances, and below the barrier, it will occur both before and after the distance of closest approach. The extent to which breakup occurs before the distance of closest approach is a crucial factor in determining the suppression of

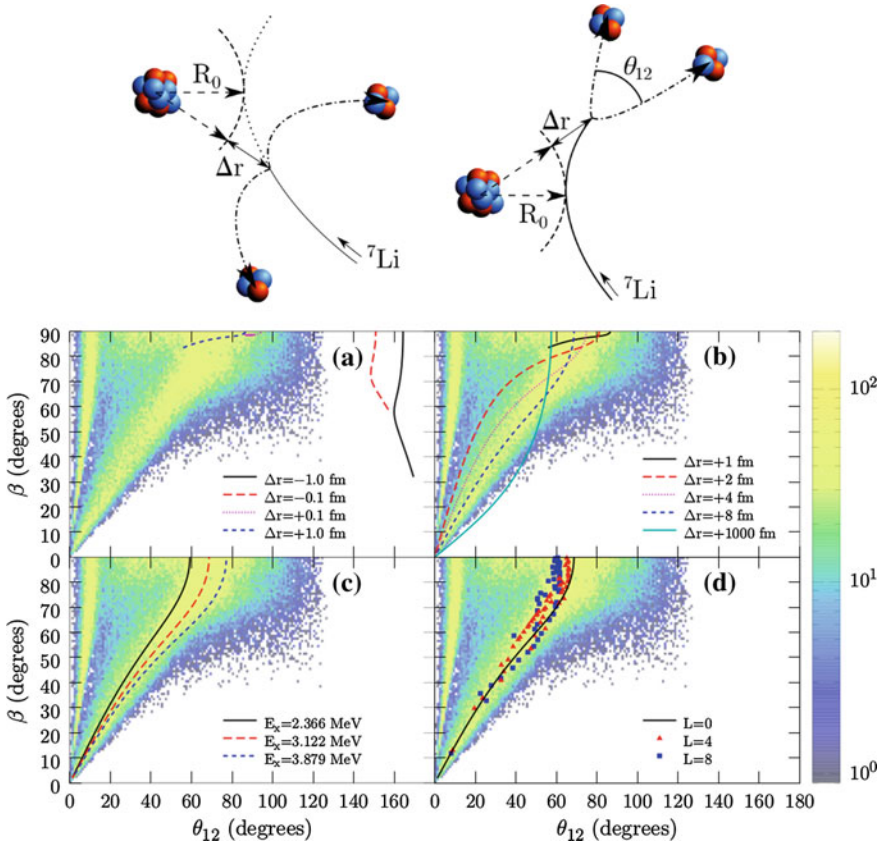

Fig. 5.8 Figure reproduced from [6] demonstrating the sensitivity of the $\theta_{12} - \beta$ distribution to breakup locations and energetics. Data shows $\alpha + \alpha$ pairs produced following interactions of ^{7}Li with ^{58}Ni at $E_{\text{beam}} = 13.1$ MeV populating the ^{57}Co 2.981 MeV $\frac{1}{2}^{+}$ state, measured with the BALiN array in the "lampshade" geometry, discussed in Sect. 3.3.1. Overlaid are PLATYPUS simulations (described in Sect. 2.9.2) exploring the factors that affect $\theta_{12} - \beta$. **a** Curves for breakup that occurs at small radial distances, Δr fm before (negative values) or after (positive values) the distance of closest approach. **b** Curves for breakup that occurs 1–1000 fm after the distance of closest approach. **c** Curves showing the effect of changing the relative energies of the fragments at a fixed radius of $\Delta r = 8$ fm (a distance that best represents the data, as shown in **b**). Values correspond to the on-resonance energy (E_{res}) for the 2^{+} state in ^{8}Be at $E_{\text{x}} = Q_{\text{BU}} + E_{\text{res}} = 3.122$ MeV, $E_{\text{x}} = Q_{\text{BU}} + E_{\text{res}} - \Gamma/2$ (2.366 MeV) and $E_{\text{x}} = Q_{\text{BU}} + E_{\text{res}} + \Gamma/2$ (3.879 MeV), where Γ is the on-resonance width of the 2^{+} state. **d** Points representing the sensitivity to the projectile-target angular momenta (see text) at $\Delta r = 8$ fm

above-barrier complete fusion. Therefore, it is interesting to examine whether useful information about breakup location can be extracted from experimental energy and angular distributions of breakup fragments.

This was explored in Ref. [6] by E.C. Simpson by performing classical trajectory calculations at fixed projectile-target distances and fixed excitation energy. The calculations were compared to experimental $\theta_{12} - \beta$ distributions of proton-pickup triggered breakup ^{8}Be in reactions of ^{7}Li with ^{58}Ni at $E_{\text{beam}} = 13.1$ MeV analysed by the author, and measured by the BALiN array in the lampshade configuration.[3] The main results of that work are shown in Fig. 5.8. In all panels, the experimental $\theta_{12} - \beta$ distribution of $\alpha + \alpha$ pairs is shown, where the selected reaction has left ^{57}Co in its 2.981 MeV $\frac{1}{2}^{+}$ state. The data do not extend past $\theta_{12} \sim 120°$ due to the limited θ_{12} acceptance of BALiN when in the lampshade configuration. In panels (a) and (b), the experimental distribution is compared to PLATYPUS simulations at a fixed radial distance from the distance of closest approach Δr, where negative values indicate breakup prior to the distance of closest approach (the incoming trajectory) and positive values indicate breakup after the nuclei pass the distance of closest approach (the outgoing trajectory). All breakup is assumed to occur from projectile-like excitation corresponding to the on-resonance energy E_{res} of the first ^{8}Be 2^{+} resonance, i.e. $E^{*}_{\text{p}} = E_{res} = 3.03$ MeV. In panel (a), breakup that occurs at 1.0 and 0.1 fm before and after the distance of closest approach is shown. Here we see that in PLATYPUS simulations, the breakup that occurs near to but *before* reaching the distance of closest approach is kinematically distinct from breakup that occurs near to but *after* the distance of closest approach. The former events lie close to $\beta = 90°$ (and so $E_1 \approx E_2$) and at smaller θ_{12} than the latter events, which have a large range in β and fall at large θ_{12}. In panel (b), PLATYPUS simulations of breakup at distances of 1, 2, 4, 8 and 1000 fm after the distance of closest approach are shown. The line of $\theta_{12} - \beta$ is seen to evolve towards the asymptotic prediction shown in panel (a) Fig. 5.3.

Whether or not breakup occurs on the incoming or outgoing trajectory has a large impact on the measured θ_{12} of the fragments, to the extent that a change of breakup location of just 0.2 fm around the distance of closest approach entirely changes where the fragments go. The origin of this effect is the interplay between the initial velocity of the fragments and the direction of the Coulomb field (radially outwards). In the case of breakup on the incoming trajectory, illustrated schematically in Fig. 5.9a, the initial velocity of the fragments is towards the target-like nucleus, and so against the repulsive Coulomb field. This acts to "push" the fragments apart, resulting in large θ_{12}. On the other hand, as illustrated in Fig. 5.9b, when breakup occurs after the distance of closest approach, the initial velocities of the fragments are away from the target-like nucleus. This is in the same direction as the force on the fragments from the Coulomb interaction, acting to narrow the opening angle of the fragments.

Naturally, the $\theta_{12} - \beta$ distribution is not just sensitive to the location of breakup. Shown in panel (c) of Fig. 5.8 is PLATYPUS calculations at $\Delta r = 8$ fm with different excitations of ^{8}Be: At the on-resonance energy of the first 2^{+} resonance $E^{*}_{\text{p}} = E_{res} = 3.03$ MeV and at $E^{*}_{\text{p}} = E_{res} \pm \Gamma/2 = 3.03 \pm 0.76$ MeV. As was seen

[3] This particular measurement is not included in this thesis. Measurements of the same system made with the array in the front-back configuration are included instead. However, these data, which were taken in the lampshade configuration, are discussed in [9].

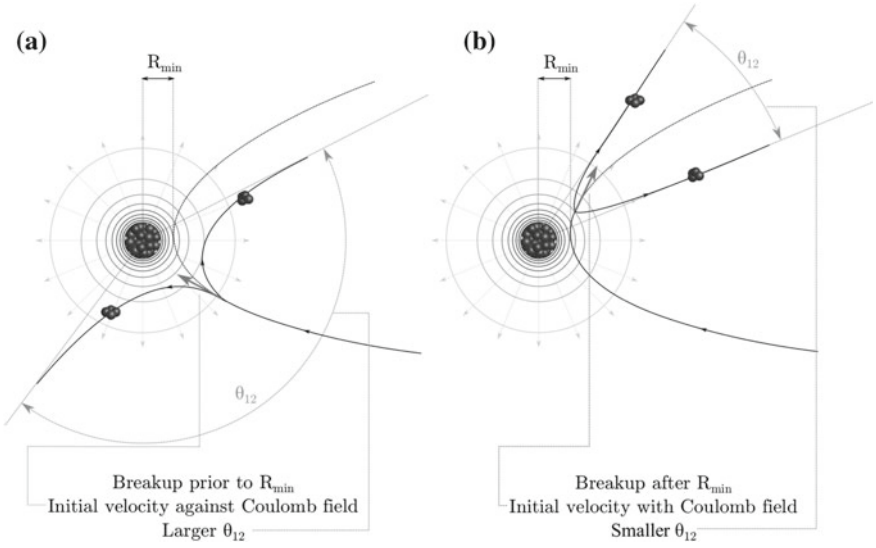

Fig. 5.9 Illustration of the difference in θ_{12} for breakup that occurs **a** prior to the projectile reaching R_{min} and **b** that which occurs after passing R_{min}. Red lines show the direction of the Coulomb field, with circles of radii representing constant steps in potential

when considering the asymptotic prediction of $\theta_{12} - \beta$, different excitation energies result in different $\theta_{12} - \beta$ distributions. A range of internal excitation of the projectile-like nucleus will broaden the $\theta_{12} - \beta$ distribution at a given Δr. In panel (d), the effect of projectile-target angular momentum (i.e. impact parameter) is shown for $\Delta r = 8$ fm and $E^*_{\text{p}} = E_{res} = 3.03$ MeV. Again, a range of angular momenta results in the broadening of the $\theta_{12} - \beta$ distribution for a given Δr, though the qualitative distribution is the same.

From this discussion, it can be seen that the reconstructed $\theta_{12} - \beta$ distribution is sensitive to the location of breakup and the excitation of the projectile-like nucleus. Both of these quantities depend on the resonant structure of the projectile-like nuclei: the projectile-like nuclei are more likely to be populated in resonant states. The resonant states have a characteristic width, and so a particular distribution of lifetimes. This highlights the importance of realistic simulation of projectile-like nucleus excitation and lifetime in KOOKABURRA and M-PLATYPUS calculations. This is especially true for light to intermediate mass targets. In reactions with heavy targets, the strength of Coulomb repulsion is such that all breakup fragments are pushed to backward angles and relatively small θ_{12}, masking the effects of breakup location.

With the above discussion in mind, it is illustrative to reconsider the measured $\theta_{12} - \beta$ distribution for $\alpha + \alpha$ fragments shown in Fig. 5.3a, where the detector configuration was sensitive to all $\theta_{12} - \beta$. There are indeed events with large θ_{12}, where incoming trajectory breakup is expected. These are the events that may contribute to above-barrier complete fusion suppression. However, the bulk of the events appear at

small θ_{12}, which are associated with breakup on the outgoing trajectory. As discussed earlier in this chapter, previous studies [1–5] operated on the assumption that half of the near-target breakup occurred on the incoming trajectory and half occurred on the outgoing trajectory. This assumption is not supported by the measured $\theta_{12} - \beta$ distributions. The link between breakup location and lifetime becomes crucial: the probability of transfer P_{tr} at a given projectile-target distance governs the probability of transfer that occurs on the incoming and outgoing trajectories. However, the fact that the projectile-like nucleus formed after transfer has a finite lifetime means that breakup occurs further along the trajectory than the triggering transfer process. Thus, transfer that occurs on the incoming trajectory may result in breakup on the outgoing trajectory. This explains the general features of Fig. 5.3a, where apparently more breakup occurs on the outgoing trajectory than on the incoming, and limits the extent to which transfer-triggered breakup can suppress above-barrier complete fusion. However, quantitative conclusions require the coincidence data to be corrected for the efficiency of the BALiN array.

5.4 Comparison of Experimental Results and Classical Dynamical Simulations

Realistic simulations are required to determine the coincidence efficiency of BALiN for each measurement, to produce breakup functions, and to predict the contribution of breakup to above-barrier complete fusion suppression using the extracted breakup functions. In this work, the simulations are performed with a realistic distribution of projectile-target distances and angular momenta, and with a range of projectile-like excitation energies and lifetimes, as well as a distribution of target-like excitation energies. The final simulated distribution of fragments, and therefore the extracted efficiency and predicted suppression of complete fusion, is sensitive to all of these quantities. On one hand, this enables us to interpret experimental spectra by varying different quantities, but on the other, reliable efficiencies require good correspondence between simulation and experiment. In the following section, comparisons between simulated and experimental distributions of breakup fragments will be made to verify the ability of KOOKABURRA and M-PLATYPUS to provide accurate efficiency determination in Chap. 6.

5.4.1 Model Inputs

The same general simulation techniques were used throughout this thesis, and will be described here. As mentioned in Chap. 2, KOOKABURRA and M-PLATYPUS were developed over the course of this thesis. Because of this, while KOOKABURRA can be regarded as a more realistic model than M-PLATYPUS, both models are used in

this work. M-PLATYPUS was used for the analysis of ^{9}Be + ^{144}Sm, ^{168}Er, ^{186}W, ^{196}Pt, ^{208}Pb and ^{209}Bi reactions, as KOOKABURRA was being developed at that time. KOOKABURRA was used for the systems that were studied later.

The KOOKABURRA and M-PLATYPUS simulations were performed using the probability distributions of excitation energy $\rho_\ell(E)$ (and associated mean-life) associated with a particular resonance, shown in Fig. 2.5. In all cases, more than one resonance will contribute to the experimental distributions. The relative intensity of the distributions were chosen to best reproduce efficiency corrected experimental data. The determination of these intensities will be described in Chap. 6 along with the input breakup functions used for the simulations. The excitation energy distributions of the target-like nuclei were taken from experimental results.

The projectile-target, fragment-target and fragment-fragment potentials are Wood-Saxon parameterisations of SPP potentials, which were introduced in Sect. 2.1. In the case of the ^{9}Be + ^{144}Sm, ^{168}Er, ^{186}W, ^{196}Pt, ^{208}Pb and ^{209}Bi measurements, the SPP potentials of Ref. [2] were used, to enable full comparisons between this work and that of Ref. [2].

In PLATYPUS and in M-PLATYPUS, nucleon transfer is not simulated. Instead, the trajectory of a pseudoprojectile, being the transfer product is simulated. In simulations of breakup following neutron stripping reactions from ^{9}Be, the "beam" in PLATYPUS and M-PLATYPUS is ^{8}Be. At the same $E_{\rm lab}$ as the experiment, the pseudo-projectile will not reach the same distance of closest approach as the true projectile. Therefore, the beam energy used as input in M-PLATYPUS ($E'_{\rm p}$) was calculated by matching the distance of closest approach to that attained by the ^{9}Be beam. This matching energy can be derived using the same arguments as $Q_{\rm opt}$, and is given by

$$E'_{\rm P} = \frac{m_{\rm T}}{m'_{\rm T}} E_{\rm lab} \left(\frac{Z_{\rm P} Z_{\rm T}}{Z'_{\rm P} Z'_{\rm T}} \right), \tag{5.16}$$

where $Z_{\rm T}, m_{\rm T}, Z_{\rm P}, m_{\rm P}$ and $Z'_{\rm T}, m'_{\rm T}, Z'_{\rm P}, m'_{\rm P}$ is the charge and mass of the target and projectile before and after transfer, respectively. In this case, where only neutron transfer is occurring, the matching energy is very close to the experimental beam energy. In cases such as proton pickup by ^{7}Li forming ^{8}Be, this factor becomes more significant. As nucleon transfer is simulated in KOOKABURRA, the energy of the projectiles in KOOKABURRA is taken to be the laboratory energy $E_{\rm lab}$ corrected for energy loss through half the target thickness.

Both KOOKABURRA and M-PLATYPUS calculate the energy and scattering angles of coincidence breakup fragments. These events are then filtered through the acceptance of BALiN using a post-processing program. This filtering process includes not only the angular coverage of BALiN, but also the randomisation of the events within each pixel (as done with the experimental data) and the inclusion of energy thresholds and cuts in events due to elastic scattering and for the removal of cross-talk. Further, events that are simulated to land in the same pixel of BALiN are removed, as they cannot contribute to the experimental coincidence yield. The limit of angular information to within one pixel of BALiN is a key factor limiting the resolution of

kinematically reconstructed quantities such as Q, and is larger than any spread introduced due to the intrinsic resolution of BALiN (∼0.1 MeV FWHM [1]). The energy spread induced by energy loss of fragments (the central value of which is corrected in the experimental data, as described in Sect. 3.4.3) in the array is not simulated. This is likely to be the reason behind the narrower Q peaks observed in KOOKABURRA simulations than seen in experimental data. For the purposes of efficiency calculations (as will be discussed in Chap. 6), multiple Q are simulated in KOOKABURRA to reproduce the experimental resolution in Q. After the randomisation of angles within each pixel, kinematic quantities such as E_{rel}, θ_{12}, Q, and β are reconstructed in the same manner as the experimental data. This process ensures that the experimental and simulated distributions are directly comparable.

5.4.2 *Comparison Between M-PLATYPUS and PLATYPUS for Heavy Target Nuclei*

The substantial extra physics included in M-PLATYPUS and KOOKABURRA when compared to PLATYPUS, outlined in Sect. 2.9.2, was motivated due to the inability of PLATYPUS to reproduce quantities such as E_{rel} in light systems. Due to the sensitivities of $\theta_{12} - \beta$ to the excitation and lifetime of the projectile-like nucleus (quantities that were not adequately modelled in PLATYPUS) experimental $\theta_{12} - \beta$ distributions cannot be reproduced using PLATYPUS even for the heaviest targets. An example of this can be seen in Fig. 5.10, where panel (a) shows the experimental $\theta_{12} - \beta$ distribution for $\alpha + \alpha$ pairs produced following neutron stripping, forming ^{8}Be in reactions of ^{9}Be with ^{209}Bi at $E_{\text{beam}} = 34$ MeV. The corresponding M-PLATYPUS and PLATYPUS[4] simulations are shown in panels (b) and (c), respectively. The most obvious missing feature in PLATYPUS simulations is the absence of the 0^+ ground state resonance of ^{8}Be seen in the intense purple band at small θ_{12} in Fig. 5.10a. This is because PLATYPUS does not explicitly incorporate lifetimes, and so cannot simulate long-lived resonances. In previous work, this was remedied by running a separate code to simulate long-lived resonances that break up asymptotically [2]. The PLATYPUS simulation does not reproduce the experimental $\theta_{12} - \beta$ distribution, even neglecting the 0^+ resonance. The PLATYPUS simulation has a much higher intensity of events at $\beta \sim 90°$ corresponding to $E_1 \approx E_2$. As previously discussed, $\alpha + \alpha$ pairs that reconstruct to $E_1 \approx E_2$ are associated with near-target breakup. Thus, in PLATYPUS, there is an over-abundance of breakup occurring close to the target, compared with the $\theta_{12} - \beta$ simulation. This is consistent with the fact that PLATYPUS does not correctly model the lifetimes of resonant states.

[4] In PLATYPUS the internal excitation of the pseudoprojectile nucleus can be taken to be a flat or as an exponentially decreasing distribution of energies between a minimum and maximum value. In this simulation, the excitation of the pseudoprojectile was chosen to be a flat distribution of $0.95 \leq E_{\text{p}}^{*} \leq 4$ MeV, approximating the 2^+ resonance.

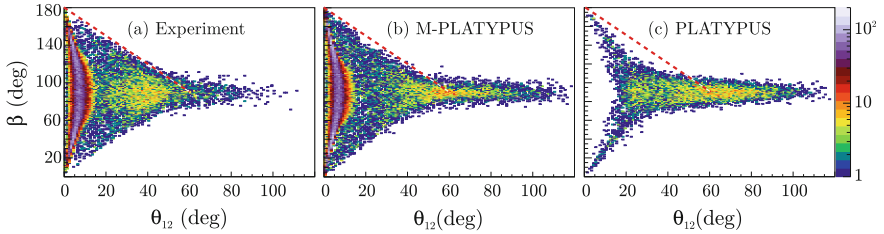

Fig. 5.10 **a** Measured $\theta_{12} - \beta$ distribution for the breakup of ^{8}Be formed following neutron transfer in interactions of ^{9}Be with ^{209}Bi at $E_{\text{beam}} = 34.0$ MeV. **b** The corresponding M-PLATYPUS simulation, which includes contribution from ^{8}Be 0^+ and 2^+ resonances. **c** The corresponding unmodified PLATYPUS simulation, with $0.95 \leq E_{\text{p}}^{*} \leq 4$ MeV, approximating the ^{8}Be 2^+ resonance only. The red diagonal line provides a reference to quantify the differences between the observables for the 2^+ resonance

On the other hand, the simulation using M-PLATYPUS well reproduces the 0^+ peak, and reproduces the high θ_{12} component rather better than the unmodified PLATYPUS. In the M-PLATYPUS simulation, both 0^+ and 2^+ resonances have been simulated in the same ratio of breakup events that populate the $E_{\text{rel}} = 92$ keV 0^+ peak to the total number of events as seen in the experimental data. Some differences between the simulation and experimental data do persist, most noticeably, the simulation contains a higher intensity of events with $\theta_{12} \gtrsim 60°$ and $\beta \sim 90°$ than the experiment. This means that too many breakup events result in coincident fragments with similar energies and large opening angles, but to a much smaller extent than seen in PLATYPUS. This will be discussed in more detail in Sect. 5.4.5. Nevertheless, it is clear that the additional physics incorporated in M-PLATYPUS, which is also included in KOOKABURRA, markedly improves the correspondence between experiment and simulation.

5.4.3 *Comparison Between KOOKABURRA and Experiment*

To verify the ability of KOOKABURRA and M-PLATYPUS to adequately model breakup, it is useful to re-visit breakup in the ^{7}Li + ^{58}Ni reaction. A good measure of how well KOOKABURRA performs are $\theta_{12} - \beta$ distributions, due to their sensitivity to projectile-like excitation as well as near-target effects. However, if detailed kinematic quantities such as $\theta_{12} - \beta$ are to be reproduced, the experimental distributions of basic observables such as energy and scattering angle should be reasonably well reproduced in KOOKABURRA. In addition, the determination of efficiency relies on these quantities, and a check on the reproducibility of these variables is essential. Comparisons between the experimental measurements and simulation for $\alpha + \alpha$ pairs formed in proton pickup during interactions of ^{7}Li with ^{58}Ni at $E_{\text{beam}} = 11.70$ MeV for energies and angles of the two fragments are shown in Fig. 5.11 where the KOOKABURRA simulation has been filtered by the detector acceptance. In addition,

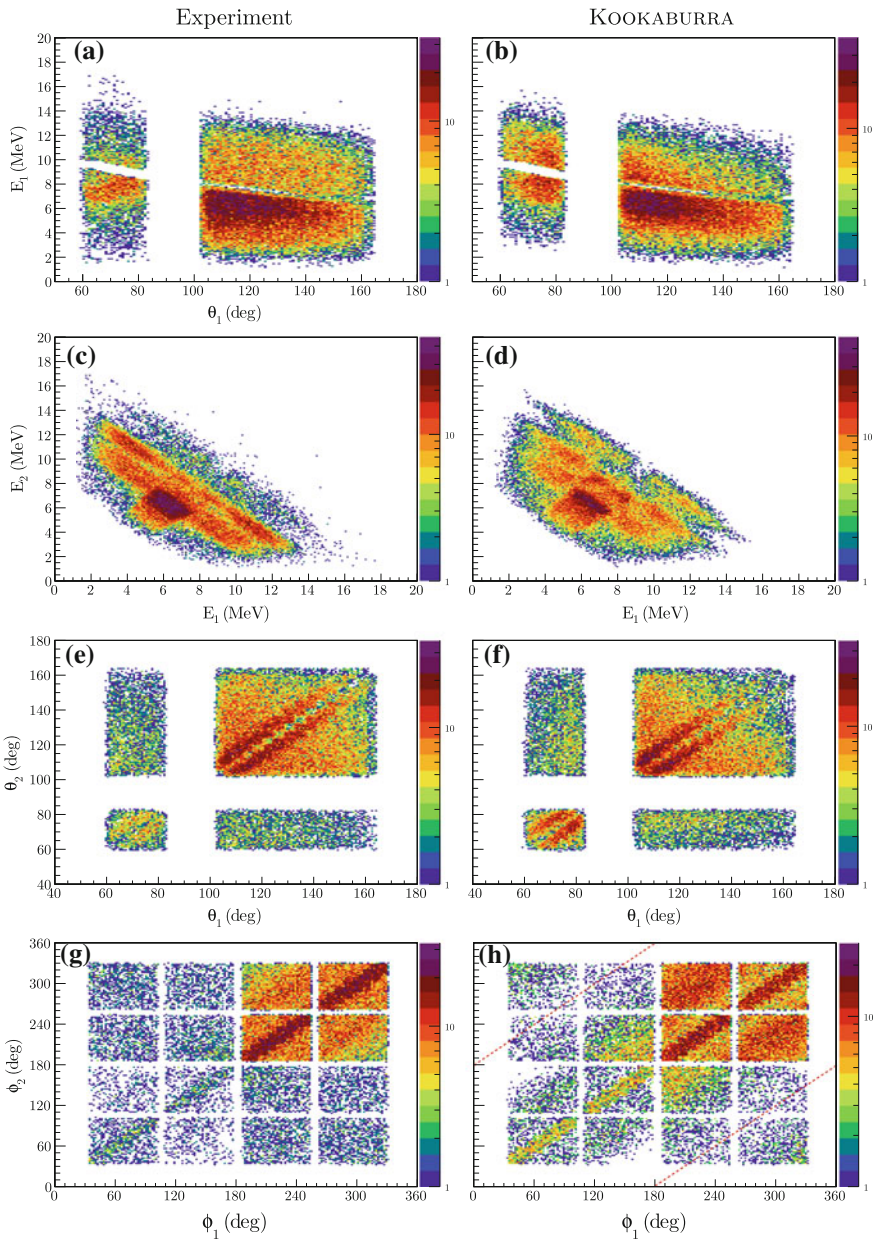

Fig. 5.11 Comparison between experiment (left column) and KOOKABURRA (right column) for the distributions of $\alpha + \alpha$ pairs produced in ^{7}Li + ^{58}Ni reactions at $E_{\text{beam}} = 11.70$ MeV. (**a**), (**b**) θ_1 versus E_1, (**c**), (**d**) E_1 versus E_2, (**e**), (**f**) θ_1 versus θ_2 and (**g**), (**h**) ϕ_1 versus ϕ_2. The KOOKABURRA simulation has been filtered by the acceptance of BALiN and has the same cuts placed on it as the experimental data. The number of $\alpha + \alpha$ pairs in the experimental and simulated distributions is approximately equal. Dotted lines in panel (**h**) indicate $\phi_1 = \phi_2 + 180°$ and $\phi_2 = \phi_1 + 180°$

the same cuts that remove elastic-X and cross-talk coincidences from the experimental data (and inevitably also some valid $\alpha + \alpha$ pairs) have been placed on the KOOKABURRA simulation. In general, the correspondence between KOOKABURRA and experiment is very good. Shown in panels (a) and (b) are the experimental and simulated distributions of the energy of the first α fragment E_1 and its scattering angle θ_1. The gap in events at $E_1 \sim 10$ MeV is due to the cut that removes full-energy elastically scattered ^{7}Li, and the gap between $\sim$80° and 100° is a gap in the coverage of BALiN when placed in the front-back configuration. KOOKABURRA seems to reproduce the experiment reasonably well in terms of the spread and slope of E_1. However, KOOKABURRA simulates too many events at angles forward of 90° relative to experiment, and the intensity of the highest and lowest energy alpha particles drops off slightly too quickly. This lack of events with extreme E_1 in KOOKABURRA is also evident in panels (c) and (d) where the energy of the two fragments are shown plotted against each other. In the experimental E_1 versus E_2 distribution, there are slightly more events extending into the largest differences between E_1 and E_2, though the reproduction is fairly good. The distribution of θ_1 against θ_2 is shown in panels (e) and (f). The bright diagonal bands of events at $\theta_1 \approx \theta_2$ correspond to breakup of ^{8}Be in its narrow 0^+ resonance. Since this resonance is only 92 keV above the breakup threshold, the relative energy and θ_{12} of these fragments is small, thus $\theta_1 \approx \theta_2$. There is a deficit of events at exactly $\theta_1 = \theta_2$. Where both breakup fragments are incident on the same pixel or on the same arc, no coincidence trigger is generated by the amplifiers, and so the event is lost. This loss of events is considered in the efficiency correction. As was seen in panels (a) and (b), too many events are simulated at forward angles in panels (e) and (f) as well.

Panels (g) and (h) show ϕ_1 against ϕ_2. Each square in ϕ_1 against ϕ_2 represents a coincidence between different DSSDs of BALiN (hence 16 (4×4) squares). The very different intensities of the squares is due to the fact that the different pairs of DSSDs have different θ coverages, as shown in Fig. 3.8c. It is much more likely to have both fragments fall in the backward pair of detectors, and so the intensity of events with both $\phi_1 > 180$ and $\phi_2 > 180$ is highest. This general pattern of intensity is seen in both KOOKABURRA and the experimental results. However, the distribution of events in KOOKABURRA is more uneven than seen in experiment. Away from the $\phi_1 \approx \phi_2$ line (which once again corresponds to ^{8}Be ground-state breakup), the experimental distribution is fairly flat. In the simulation, there is a deficit of events at $\phi_1 = \phi_2 + 180$ (and $\phi_2 = \phi_1 + 180$), indicated by the dotted lines in panel (h). These simulations were performed under the assumption that the direction of relative motion of the nuclei is conserved at the point of breakup. Test simulations that instead conserve L largely ameliorated this deficit. Therefore, the ϕ_1 against ϕ_2 distribution is sensitive to the model assumptions made at the point of breakup. In a classical simulation, some assumption has to be made as to what occurs to the nuclei at the point of transfer and at breakup. Conserving L results in large jumps in the trajectories of the nuclei, which have a significant effect on above-barrier ICF and CF. On the other hand, conserving direction results in more physical trajectories, but a deficit of events at $\phi_1 = \phi_2 + 180$. This is a limitation of a classical model. While this discussion has focused on where KOOKABURRA does not reproduce the experimental distributions,

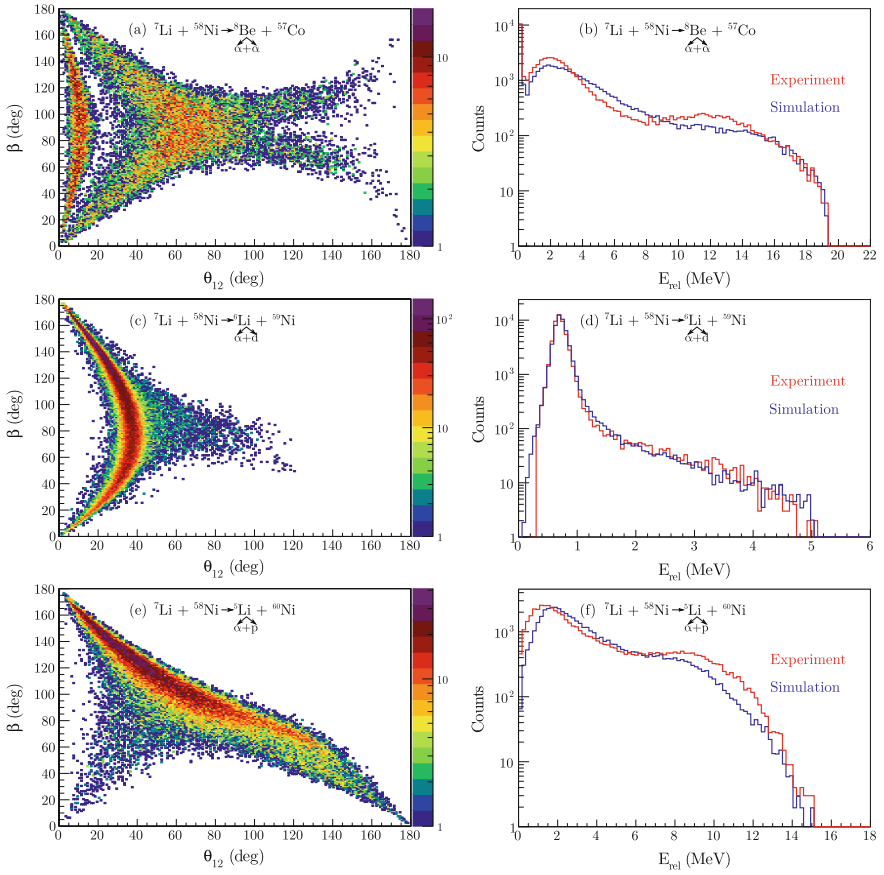

Fig. 5.12 Simulated $\theta_{12} - \beta$ and E_{rel} distributions for breakup in interactions of ^{7}Li with ^{58}Ni at $E_{\text{beam}} = 11.70$ MeV. The simulated $\theta_{12} - \beta$ distributions shown on the left can be compared directly to the experimental $\theta_{12} - \beta$ distributions shown in Fig. 5.3. The simulated E_{rel} distributions are shown on the right in blue, with the experimental distributions shown in red

it is important to note that these are (minor) details that do not significantly affect the conclusions.

Breakup triggered by proton pickup is not the only breakup mode occurring in reactions of ^{7}Li with ^{58}Ni. Shown in Fig. 5.12 are the filtered simulated $\theta_{12} - \beta$ distributions (left) and the simulated and experimental E_{rel} distributions (right) for $\alpha + \alpha$, $\alpha + d$ and $\alpha + p$ pairs detected in coincidence. The simulated $\theta_{12} - \beta$ simulations can be compared to the experimental distributions presented in Fig. 5.3. The broad features of the $\theta_{12} - \beta$ and E_{rel} distributions are reproduced very well by the simulations. However, for the $\alpha + \alpha$ case (panel (a)) more simulated events appear at $\beta = 90°$ (and so $E_1 \approx E_2$) than at lower θ_{12} and larger β, in the band of the 2^{+} resonance. Experimentally, (Fig. 5.3a) there is a paucity of events at $\beta = 90°$. This

phenomenon was also seen for $\alpha + \alpha$ fragments produced in reactions of ^{9}Be with ^{209}Bi at $E_{\text{beam}} = 34.0$ MeV (Fig. 5.10). Conspicuously, there is also a "hole" in the simulated $\theta_{12} - \beta$ distribution at $\theta_{12} > 100°$ and $\beta \approx 90°$. This region in $\theta_{12} - \beta$ corresponds to fragments that have similar energies but very large opening angles, and so large E_{rel}. Such events are produced in the total KOOKABURRA simulation, but do not fall within the detector acceptance. Further work is required to address this discrepancy. In reactions producing $\alpha + d$ pairs, the KOOKABURRA simulation reproduces the $\theta_{12} - \beta$ and E_{rel} distributions extremely well, as seen in panels (c) (compared with Fig. 5.3b) and (d). The $\theta_{12} - \beta$ and E_{rel} distributions for $\alpha + p$ are shown in panels (e) and (f) respectively. As with the $\alpha + \alpha$ events, there is a deficit of $\alpha + p$ events at large θ_{12} (and thus large E_{rel}) compared to experiment, though the general features of the distributions are reproduced.

The small (but systematic) deviations between experiment and simulation may be due to the fact that whilst the excitation energies and lifetimes of the projectile-like nuclei are modelled realistically, they are calculated fairly simplistically with the one-state one-channel limit of R-matrix theory. As a result, there is uncertainty in the estimates of $\rho_\ell(E)$ and the associated lifetimes τ, especially for nuclei with very broad resonances where the experimental structure information is poor. Thus, while these estimates are certainly reasonable, it is interesting to examine how the experimental distributions change when τ is varied. This tests the sensitivity of the energy and angular distributions of breakup fragments to lifetime, and by comparison to experiment, constrains τ. To that end, shown in Fig. 5.13a is the experimental $\theta_{12} - \beta$ distribution of events for $\alpha + \alpha$ fragments produced in ^{7}Li + ^{58}Ni $\rightarrow$ ^{8}Be + ^{57}Co reactions at $E_{\text{beam}} = 11.70$ MeV, as previously seen in Fig. 5.3a. Shown in (b) is the "baseline" $\theta_{12} - \beta$ simulation, as seen in 5.12a, with the distribution of τ as calculated by Eq. 2.20, using the one-state, one-decay-channel limit of R-matrix theory. Shown in panels (c)–(f) are KOOKABURRA simulations, filtered by the acceptance of BALiN, where the calculated excitation energy dependent τ has been scaled by 0.1, 0.5, 2, and 10. The black line has been drawn to guide the eye: it is located at the edge of the band of events associated with the 2^+ resonance in the experimental data, and is shown in all panels. The baseline simulation shown in panel (b) follows the black line well. If τ is reduced, it can be seen that the band associated with the 2^+ resonance becomes concave, and events move towards $\beta \sim 90°$ and larger θ_{12}. This can be understood since for lower τ, breakup will occur closer to the target-like nucleus on average. As has already been discussed in this chapter, a signature of near-target breakup is that the fragments have similar energies, and so $\beta \sim 90°$. On the other hand, when τ is increased, as shown in (e), the band associated with the 2^+ resonance becomes convex, and in the extreme case of 10τ (panel (f)), approaches the asymptotic prediction shown in Fig. 5.3a. When τ is large, breakup occurs further away from the target-like nucleus on average, and therefore the effect of post-breakup acceleration on the final energies and angles of the fragments is smaller. Therefore, fewer events are focused towards $\beta \sim 90°$.

In all cases, the band of events at small θ_{12} associated with the 0^+ resonance remains unaffected by scaling τ by as much as a factor of ten in either direction. The lifetime of this state ($\tau \sim 10^{-16}$ s) is long enough compared to the reaction

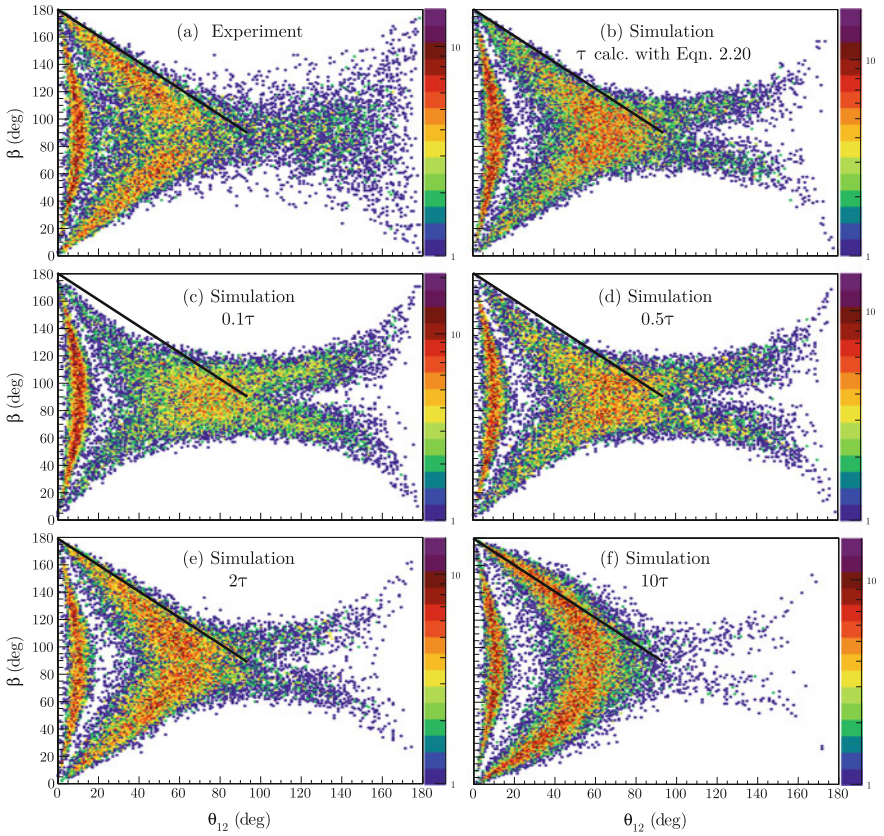

Fig. 5.13 $\theta_{12} - \beta$ simulations are sensitive to the lifetime of the projectile-like nucleus populated after transfer. To explore this, the experimental $\theta_{12} - \beta$ distribution of $\alpha + \alpha$ fragments produced in $^{7}\mathrm{Li} + {}^{58}\mathrm{Ni} \rightarrow {}^{8}\mathrm{Be} + {}^{57}\mathrm{Co}$ reactions at $E_{\mathrm{beam}} = 11.70$ MeV is shown in (**a**). The $\theta_{12} - \beta$ distribution of $\alpha + \alpha$ fragments produced in a KOOKABURRA simulation of the same reaction is shown in (**b**). This simulation uses the mean life of ^{8}Be that was calculated using Eq. 2.20. Panels (**c**)–(**f**) show the same simulation, but with τ scaled by 0.1, 0.5, 2, and 10, respectively. The black line is drawn as a reference to aid comparison between the different distributions

timescale ($\tau \sim 10^{-21}$ s) that a factor of ten in the lifetime cannot affect the energy and angles of the breakup fragments. The fact that the 2^{+} resonance has a lifetime on the same timescale as the reaction makes it particularly sensitive to changes in τ. From this figure, it is apparent that the τ estimated from Eq. 2.20 is quite reasonable. An error in the determination of τ by a factor of ten either way is precluded by these calculations since the experimental $\theta_{12} - \beta$ distribution is not reproduced. A change in τ by as much as a factor of two in either direction is reasonable, based on the distributions shown in Fig. 5.13. However, it is not obvious whether τ should be increased or decreased – a decrease in τ by a factor of two places more events at large θ_{12}, which is desirable, but a increase in τ by a factor of two produces a more

even distribution of events in the 2^+ band, which is also desirable. A change in τ cannot wholly alleviate the discrepancies between KOOKABURRA or M-PLATYPUS and experiment that have been identified in this section. Therefore, the values of τ given by Eq. 2.20 are adopted throughout the rest of this thesis.

5.4.4 *Revisiting Kinematic Signatures of Breakup on the Incoming Trajectory*

In Sect. 5.3, it was noted that breakup on the incoming and outgoing trajectories populate distinct regions in $\theta_{12} - \beta$ for reactions with light to intermediate mass target nuclei. This can be explored further with the full KOOKABURRA simulations described above. Beyond experimentally accessible quantities such as $E_{1,2}$, $\theta_{1,2}$ and $\phi_{1,2}$, KOOKABURRA allows interrogation of quantities such as the radial distance between the nuclei and time of transfer and breakup. Distributions of the transfer radius R_{tr} and time T_{tr} relative to R_{min} are shown in Fig. 5.14a for $^{7}\text{Li} + {}^{58}\text{Ni} \rightarrow {}^{8}\text{Be} + {}^{57}\text{Co}$ reactions at $E_{\text{beam}} = 11.70$ MeV. The corresponding distributions of breakup radius R_{BU} and time T_{BU} are shown in Fig. 5.14b. Here, the effect of lifetime can be seen: while the probability of *transfer* peaks at R_{min} (the dashed vertical line), the probability of *breakup* is pushed to larger distances, beyond the dashed vertical line. In total 16% of all $\alpha + \alpha$ events break up in the incoming trajectory and 84% on the outgoing in this particular simulation, which models contributions from the 0^+ and 2^+ resonances in proportion to the experimental data.

Selecting those events that experience both transfer and breakup on the incoming trajectory, filtered by the acceptance of BALiN, results in the $\theta_{12} - \beta$ distribution shown in Fig. 5.15a. Conversely, the $\theta_{12} - \beta$ distribution of events where breakup occurs on the outgoing trajectory is shown in Fig. 5.15b. These distributions are kinematically distinct, and thus experimental signatures of breakup that occurs on incoming trajectories – that which can suppress above-barrier complete fusion – can be identified.

5.4.5 *Signatures of Orientation Effects*

The discrepancies between experiment and simulations using KOOKABURRA and M-PLATYPUS raises the question: is there some essential physics not being captured in KOOKABURRA and M-PLATYPUS? The obvious answer is yes: these are classical models, and classical models are limited in the extent to which they can model quantum mechanical processes. Looking through this lens, the correspondence between model calculations and experiment is remarkably good.

In a classical model, all key physics has to be included "by hand", either classically or phenomenologically. This has the advantage of being able to interrogate

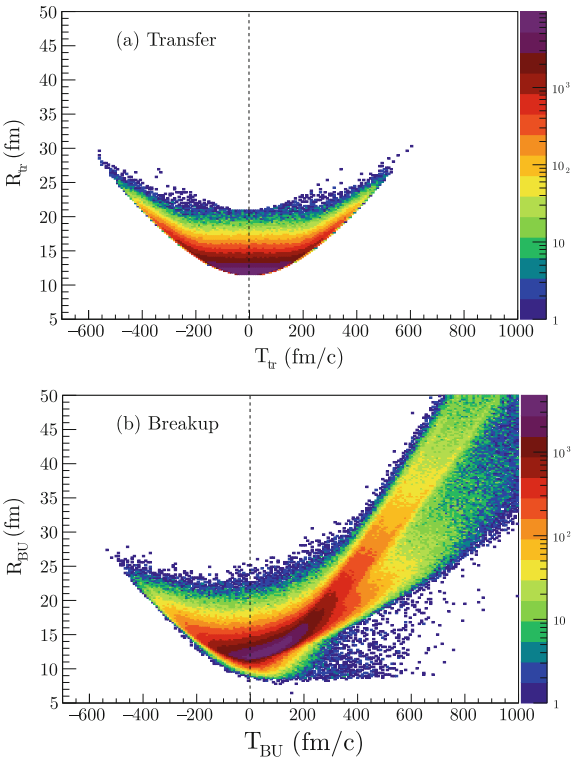

Fig. 5.14 KOOKABURRA simulations of the location and time of **a** transfer and **b** breakup for ^{7}Li + ^{58}Ni $\rightarrow$ ^{8}Be + ^{57}Co reactions at $E_{\text{beam}} = 11.70$ MeV. Times are relative to the time at which the nuclei reach the distance of closest approach. Negative times indicate reactions prior to reaching the distance of closest approach, while positive times indicate reactions after reaching the distance of closest approach. The probability of transfer is peaked at $T_{\text{tr}} = 0$ and $R_{\text{tr}} = R_{\text{min}}$, and reflect the exponential form of the local breakup function (Eq. 2.64), which is peaked at the distance of closest approach. After transfer, the projectile-like nucleus propagates according to the lifetime associated with its excitation energy. As a result, while transfer is peaked at $T_{\text{tr}} = 0$ and $R_{\text{tr}} = R_{\text{min}}$, breakup is peaked at somewhat larger T_{BU} and R_{BU}. Due to the long lifetime of the 0^{+} resonance and the fact that the length of time that the ^{8}Be remains intact is distributed exponentially, there is a long tail of events extending to very large T_{BU} and R_{BU}

the sensitivities of measured variables to the underlying physics, but it also means that it is essential to consider all aspects of the physics. A candidate for physics that has not been included in M-PLATYPUS or KOOKABURRA that may influence the energy and angular distribution of the breakup fragments is the initial orientation of the projectile-like nucleus. In KOOKABURRA and M-PLATYPUS, all breakup occurs isotropically in the rest frame of the projectile-like nucleus. This does not necessarily reflect reality: the projectile-like nuclei may have a preferential orientation

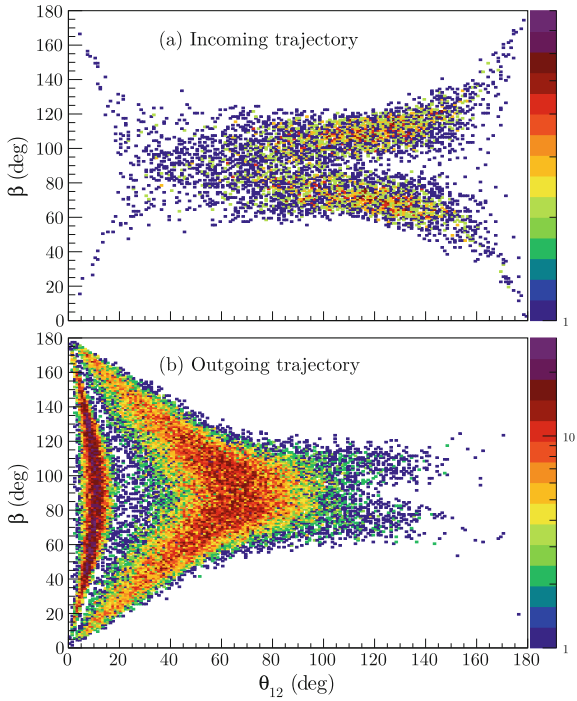

Fig. 5.15 Simulated $\theta_{12} - \beta$ distribution of $\alpha + \alpha$ pairs produced in ^{7}Li + ^{58}Ni $\rightarrow$ ^{8}Be + ^{57}Co reactions at $E_{\text{beam}} = 11.70$ MeV, filtered by the acceptance of BALiN, showing only breakup that **a** occurs on the incoming trajectory and **b** occurs on the outgoing trajectory

with respect to the target due to the effect of the projectile-target potential and the cluster structure of the projectile nucleus. That is, the projectile nucleus should be treated as a non-spherical extended object that has a certain distribution of charge. After transfer, this will translate into a preferential orientation of the projectile-like transfer product, and so the breakup fragments. This has been previously explored for direct breakup of ^{7}Li [10], where it was found that the initial orientation of the ^{7}Li had a large effect on the measured E_{rel}.

The concept of orientation dependent E_{rel} distributions (via the ΔE_{acc}) term was introduced in Fig. 2.10. If the fragments are oriented perpendicular to the field at the point of breakup, E_{rel} will increase, whereas if they are oriented parallel to the field, E_{rel} will decrease. Preferential orientation of the fragments will result in a different E_{rel} distribution to that where the fragments are isotropically distributed. However, without a satisfactory method for reliably parameterising orientation effects, these effects have until now been neglected in KOOKABURRA and M-PLATYPUS. To work towards an understanding of orientation effects in breakup reactions, we can reconstruct the azimuthal orientation of the breakup fragments with respect to the reaction plane.

5.5 Azimuthal Orientation of Breakup Fragments

A complementary quantity to β is the azimuthal orientation of the breakup fragments with respect to the reaction plane, γ, shown schematically in Fig. 5.16. β is analogous to θ_{CM} for two body reactions, and γ is analogous to ϕ. In the absence of any orientation effects, γ should give an isotropic distribution. If there are orientation effects, or if post-breakup acceleration perturbs the fragments, then the γ distribution will not be isotropic. Therefore, the differences between simulated γ distributions, where the initial orientation of the fragments is isotropic, and experimental γ distributions which reflect reality, may provide useful insight into any orientation effects present in breakup.

To reconstruct γ we first define the reaction plane, given by the vector normal to the plane

$$\vec{n}_{\text{reaction}} = \vec{r}_{\text{beam}} \times \vec{r}_{\text{p}}. \tag{5.17}$$

Where $\vec{r}_{\text{beam}} = \{0, 0, -1\}$ is the vector defining the beam direction, and $\vec{r}_{\text{p}} = \{\sin(\theta_{\text{p}})\cos(270 - \phi_{\text{p}}), \sin(\theta_{\text{p}})\sin(270 - \phi_{\text{p}}), -\cos(\theta_{\text{p}})\}$ is the position vector defining the direction of the transfer product prior to breakup. Similarly, the plane joining $\vec{r}_{\text{p}}$ and the position vector of the breakup fragment $\vec{r}_{\alpha} = \{\sin(\theta_{\alpha})\cos(270 - \phi_{\alpha}), \sin(\theta_{\alpha})\sin(270 - \phi_{\alpha}), -\cos(\theta_{\alpha})\}$ is given by

$$\vec{n}_{p-\alpha} = \vec{r}_{\alpha} \times \vec{r}_{\text{p}}. \tag{5.18}$$

The azimuthal orientation of the breakup fragment with position vector $\vec{r}_{\alpha}$ is the angle between the reaction plane and the plane joining the transfer product and the breakup fragment:

$$\cos\gamma = \frac{\vec{n}_{p-\alpha}.\vec{n}_{\text{reaction}}}{|\vec{n}_{p-\alpha}||\vec{n}_{\text{reaction}}|}. \tag{5.19}$$

The orientation of the other breakup fragment with respect to the beam axis is simply $\pi - \gamma$. Like β, determining γ with respect to the first breakup fragment is sufficient to define the orientation of each breakup event.

If there is no preferential orientation of the projectile-like nucleus prior to breakup, $\beta - \gamma$ distributions for breakup fragments of equal mass should be isotropic in γ and have a $\sin\beta$ dependence[5] in β, modulated by the efficiency of BALiN. This should be the case for asymptotic breakup, where projectile-target interactions can have little influence on the orientation of the projectile-like nucleus at the point of breakup. The simulated and experimental $\beta - \gamma$ distributions for $\alpha + \alpha$ fragments are shown in Fig 5.17 for the ^{7}Li + ^{58}Ni $\rightarrow$ ^{8}Be + ^{57}Co reaction at $E_{\text{beam}} = 11.70$ MeV. This is indeed what is seen in the simulation when breakup occurs asymptotically far from the target from the long-lived 0^{+} ground-state of ^{8}Be, which is shown in Fig. 5.17a. The experimental distribution of fragments with $E_{\text{rel}} < 0.5$ MeV, shown in panel

[5]This is equivalent to a set of points evenly distributed on a sphere.

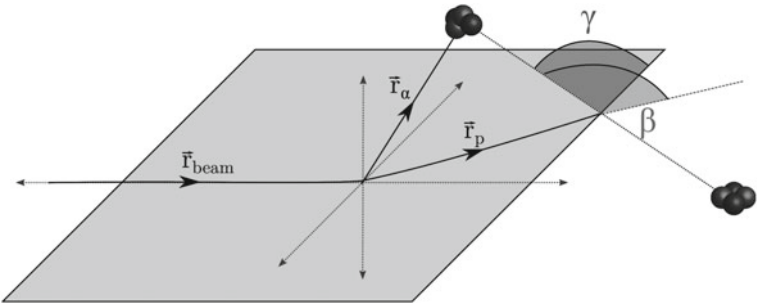

Fig. 5.16 Schematic illustration of the orientation of the breakup fragment relative to the reaction plane γ. The reaction plane is defined by the direction of the beam $\vec{r}_{\text{beam}}$ and the direction of the transfer product $\vec{r}_{\text{p}}$, and γ is the angle between the reaction plane and the plane joining the breakup fragment and transfer product

(c) matches very well with the simulated distribution following filtering through the detector acceptance as shown in panel (e).

On the other hand, the simulated (panel (b) of Fig. 5.17) $\beta - \gamma$ distribution for $E_{\text{rel}} > 0.5$ MeV does not show similar isotropy. In fact, in both experimental (panel (d)) and the simulated distribution filtered by the detector geometry (panel (f)), have a peak in β when $\gamma = 90°$. That is, it is more probable for the fragments to have equal energies $E_1 \approx E_2$ when breakup occurs out of plane. While all breakup in KOOKABURRA is isotropic, the *reconstructed* $\beta - \gamma$ distribution is not. This is an indication of post-breakup acceleration modifying the energy and angle of the breakup fragments, and so β and γ. However, the experimental γ distribution is significantly broader and more flat-topped than the filtered simulated distribution. This is, perhaps, an indication of preferential orientation of the fragments in the reaction plane in near target breakup. Inclusion of this effect in KOOKABURRA will result in a broader distribution of γ and β, and larger values of $E_1 - E_2$. This is encouraging – inclusion of orientation effects in KOOKABURRA may ameliorate discrepancies identified in Sect. 5.4 between experimental and simulated distributions of breakup fragments.

5.6 Summary

This thesis ultimately aims to understand the extent to which breakup in reactions of light weakly bound nuclei may suppress complete fusion. To achieve this, the breakup modes as well the location of breakup needs to be identified. In this chapter, the observables that give insight into the location of breakup were explored. In Sect. 5.1, the utility of E_{rel} in separating near-target from asymptotic breakup was shown using breakup resulting from reactions of ^{7}Li with ^{58}Ni. It was then shown that the reconstructed orientation of the relative momenta of the fragments β compared to their opening angle θ_{12}, when combined with classical trajectory simulations

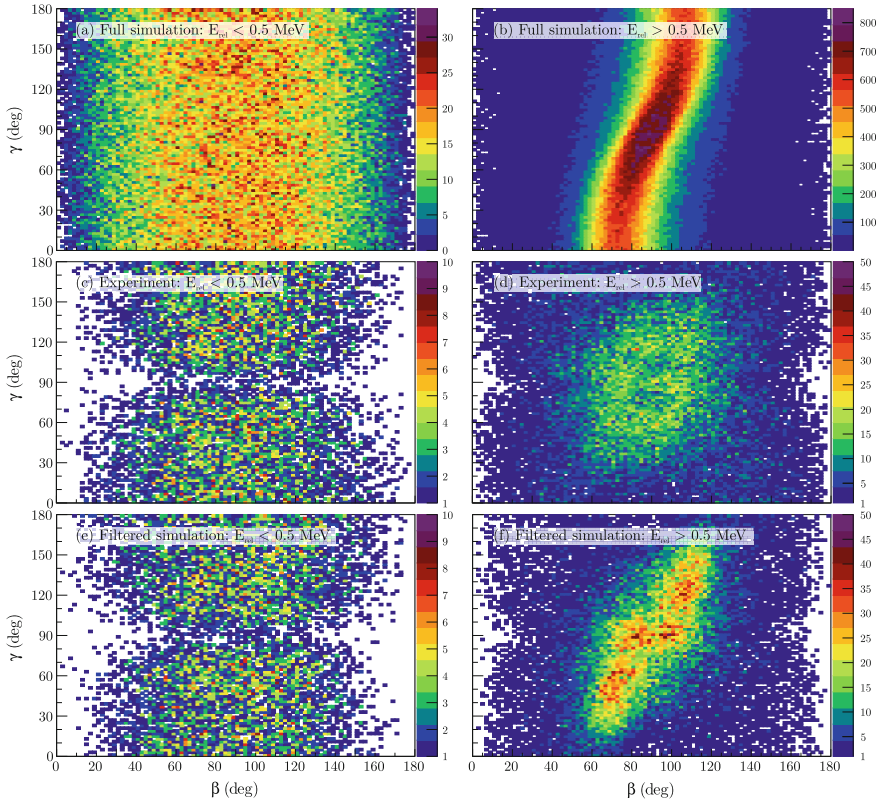

Fig. 5.17 Correlations between β and γ yield insight into the relationship between the orientation of the projectile-like nucleus prior to breakup and target proximity. The simulated reconstructed $\beta - \gamma$ distributions for $\alpha + \alpha$ fragments produced in ^{7}Li + ^{58}Ni $\rightarrow$ ^{8}Be + ^{57}Co reactions at $E_{\text{beam}} = 11.70$ MeV for **a** for $E_{\text{rel}} < 0.5$ MeV, where breakup only occurs asymptotically through the 0^{+} ground state resonance of ^{8}Be and **b** for $E_{\text{rel}} > 0.5$ MeV where breakup occurs near to the target. Panels **c** and **d** show the associated experimental $\beta - \gamma$ simulations for the same system, which are modulated by the coincidence efficiency of BALiN. These experimental distributions can be compared to the simulated distributions after filtering by the acceptance of BALiN, which are shown in panels **e** and **f** for $E_{\text{rel}} < 0.5$ MeV and $E_{\text{rel}} > 0.5$ MeV, respectively. The number of events in the experimental and filtered simulated distributions is equal, as is the colour scale

enables the distinction between near-target breakup on the incoming trajectory and near-target breakup on the outgoing trajectory. These distributions show that more near-target breakup occurs after the distance of closest approach than before, which is a result of the finite lifetime of the projectile-like nucleus. This result indicates that the extent to which near-target breakup can suppress complete fusion is much more limited than was identified in previous work, where it was assumed that breakup is equally likely on the incoming and outgoing trajectories.

Due to the reliance on classical trajectory simulations to interpret measured spectra, to extract below-barrier breakup functions and to predict above-barrier complete fusion suppression, it is critical that these simulations reproduce experimental data reasonably well. In this chapter, comparisons between experimental data, KOOKABURRA, M-PLATYPUS and PLATYPUS were made. It was shown that PLATYPUS cannot reproduce $\theta_{12} - \beta$ distributions even in a heavy system such as ^{9}Be + ^{209}Bi, where the $\theta_{12} - \beta$ distributions are less sensitive to the details of the excitation and lifetime of the projectile-like nucleus. It was then shown that M-PLATYPUS and KOOKABURRA reproduce experimental distributions fairly well, with some discrepancies that may be resolved by considering a preferential orientation of the projectile-like nucleus.

The next step is to move beyond the qualitative discussions of this chapter and of Chap. 4 to make quantitative predictions of the contribution of breakup to above-barrier complete fusion. This is the subject of Chaps. 6 and 7.

References

1. Luong D.H. *Mechanisms and time-scales in breakup of* ^{6,7} *Li*. Ph.D. thesis, Australian National University (2012)
2. Rafiei, R., du Rietz, R., Luong, D.H., Hinde, D.J., Dasgupta, M., Evers, M., Diaz-torres, A.: Mechanisms and systematics of breakup in reactions of ^{9}Be at near-barrier energies. Phys. Rev. C **81**(2), 024601 (2010)
3. Luong, D.H., Dasgupta, M., Hinde, D.J., Du Rietz, R., Rafiei, R., Lin, C.J., Evers, M., Diaz-torres, A.: Insights into the mechanisms and time-scales of breakup of ^{6,7}Li. Phys. Lett. B **695**, 105 (2011)
4. Luong, D.H., Dasgupta, M., Hinde, D.J., du Rietz, R., Rafiei, R., Lin, C.J., Evers, M., Diaz-Torres, A.: Predominance of transfer in triggering breakup in sub-barrier reactions of ^{6,7}Li. Phys. Rev. C **88**(3), 34609 (2013)
5. Diaz-Torres, A., Hinde, D.J., Tostevin, J.A., Dasgupta, M., Gasques, L.R.: Relating breakup and incomplete fusion of weakly bound nuclei through a classical trajectory model with stochastic breakup. Phys. Rev. Lett. **98**(15), 152701 (2007)
6. Simpson, E.C., Cook, K.J., Luong, D.H., Kalkal, S., Carter, I.P., Dasgupta, M., Hinde, D.J., Williams, E.: Disintegration locations in ^{7}Li$\rightarrow^{8}$Be transfer-triggered breakup at near-barrier energies. Phys. Rev. C **93**(2), 024605 (2016)
7. McIntosh, A.B., Hudan, S., Metelko, C.J., De Souza, R.T., Charity, R.J., Sobotka, L.G., Lynch, W.G., Tsang, M.B.: Tidal effects and the proximity decay of nuclei. Phys. Rev. Lett. **99**(13), 132701 (2007)
8. Kalkal, S., Simpson, E.C., Luong, D.H., Cook, K.J., Dasgupta, M., Hinde, D.J., Carter, I.P., Jeung, D.Y., Mohanto, G., Palshetkar, C.S., Prasad, E., Rafferty, D.C., Simenel, C., Vo-Phuoc, K., Williams, E., Gasques, L.R., Gomes, P.R.S., Linares, R.: Asymptotic and near-target direct breakup of ^{6}Li and ^{7}Li. Phys. Rev. C **93**(4), 044605 (2016)
9. Cook, K.J., Luong, D.H., Williams, E., Carter, I.P., Dasgupta, M., Hinde, D.J., Ramachandran, K.: Developing new methods to investigate nuclear physics input to the cosmological lithium problem. EPJ Web Conf. **63**, 03011 (2013)
10. Mason, J.E., Gazes, S.B., Roberts, R.B., Teichmann, S.G.: Coulomb and nuclear effects in direct breakup of 54-MeV ^{7}Li + ^{12}C, ^{197}Au. Phys. Rev. C **45**(6), 2870 (1992)

Chapter 6
Extraction of Below-Barrier Breakup Probabilities

Science doesn't always go forwards. It's a bit like doing a Rubik's cube. You sometimes have to make more of a mess with a Rubik's cube before you can get it to go right. You build up this picture of what there is and you believe it to be true and you work with this picture and you refine it but sometimes you have to abandon the picture. Sometimes you discover the picture you thought you had, that everybody thought we had, actually turns out to be wrong

Jocelyn Bell Burnell 1943–

In Chap. 4, it was shown that breakup in interactions of ^{9}Be and ^{7}Li with the targets studied in this work is dominated by transfer-triggered breakup, producing nuclei in both long- and short-lived resonant states. It has also been shown in Chap. 5 that a small portion of the breakup fragments from short-lived resonances have angular correlations that are consistent with breakup on the incoming trajectory. It is this breakup that may influence complete fusion. This raises the question: what is the quantitative contribution of breakup from short lived states to the suppression of complete fusion cross-sections?

In this chapter, the process of taking breakup yields Y_{BU} determined from the analysis procedure described in Chap. 4 and extracting breakup probabilities is described. This chapter is arranged as follows: (1) the process of normalising to Rutherford scattering is described, which requires (2) the extraction of the Rutherford yield in a monitor as well as (3) the determination of the solid angles of monitors. (4) breakup cross-sections and probabilities are then defined and (5) the process for determining the coincidence efficiency of BALiN shown. (6) Finally, the breakup pseudoangle is mapped to the Rutherford scattering angle of the projectile nucleus. The resulting breakup probability functions are presented in Chap. 7, and are used as input into classical trajectory models to predict the effect on above-barrier complete and incomplete fusion cross-sections.

K. J. Cook, *Zeptosecond Dynamics of Transfer-Triggered Breakup*,
Springer Theses, https://doi.org/10.1007/978-3-319-96017-3_6

6.1 Normalising to Rutherford Scattering

The task at hand is to find the breakup probabilities $P(\theta_{\mathrm{CM}})$ for these reactions, defined as the ratio of breakup $d\sigma_{\mathrm{BU}}/d\Omega$ to Rutherford cross-sections, $d\sigma_{\mathrm{Ruth}}/d\Omega$ as a function of θ_{CM}, such that

$$P(\theta_{\mathrm{CM}}) = \frac{\frac{d\sigma_{\mathrm{BU}}}{d\Omega}}{\frac{d\sigma_{\mathrm{Ruth}}}{d\Omega}}(\theta_{\mathrm{CM}}) \tag{6.1}$$

Mapping θ_{CM} to distance of closest approach R_{min}, assuming a Rutherford trajectory ($\theta_{CM} \sim \theta_{Ruth}$), via

$$R_{\mathrm{min}} = \frac{Z_P Z_T e^2}{2E_{\mathrm{CM}}}\left(1 + \frac{1}{\sin\frac{\theta_{\mathrm{CM}}}{2}}\right), \tag{6.2}$$

yields breakup probabilities as a function of closest approach $P(R_{\mathrm{min}})$.

Differential cross-sections for any process $d\sigma/d\Omega(\theta_{\mathrm{lab}})$ (defined in Sect. 2.3) at a given energy can be related to the total yield of the reaction Y in a detector of solid angle $\Delta\Omega$ placed at an angle of θ_{lab} via the expression

$$Y = IN\epsilon\frac{d\sigma}{d\Omega}(\theta_{\mathrm{lab}})\Delta\Omega, \tag{6.3}$$

where I is the total number of beam particles incident on a target which has a number density of N, and ϵ is the efficiency of the detector. The coincidence efficiency of breakup in BALiN depends on the beam energy, the breakup reaction, and the distribution of fragments. This term also includes data acquisition deadtimes. Finding coincidence efficiencies is the subject of Sect. 6.5.

Since BALiN is large and position sensitive, cross-sections as a function of θ_{bin} can be found by partitioning the yield into bins of constant width $\Delta\theta_{\mathrm{bin}}$, $\Delta\phi_{\mathrm{bin}} = 2\pi$ centred around θ_{bin}, and

$$Y(\theta_{\mathrm{bin}}) = IN\epsilon(\theta_{\mathrm{bin}})\frac{d\sigma}{d\Omega}(\theta_{\mathrm{bin}})\Delta\Omega(\theta_{\mathrm{bin}}). \tag{6.4}$$

As will be discussed in Sect. 6.5, the coincidence efficiencies $\epsilon(\theta_{\mathrm{bin}})$ consider events at all azimuthal angles ϕ, and so the solid angle of each bin is $\Delta\Omega_{\mathrm{bin}}(\theta_{\mathrm{bin}}) = \int\int_{\mathrm{bin}} \sin\theta_{\mathrm{bin}} d\theta d\phi = 2\pi\Delta\theta_{\mathrm{bin}}\sin\theta_{\mathrm{bin}}$.

In general, the number of beam particles I and the number density of a target N are not well known. Firstly, both are difficult to measure precisely. Further, the target may thin over time, and the beam current may fluctuate. It is thus advantageous to take the ratio of yield of the reaction mode of interest – here breakup – and the yield expected from Rutherford scattering Y_{Ruth}, where the associated cross-section is known exactly (see Sect. 2.3.1), giving

$$\frac{Y_{\mathrm{BU}}(\theta_{\mathrm{bin}})}{Y_{\mathrm{Ruth}}(\theta_{\mathrm{bin}})} = \frac{\frac{d\sigma_{\mathrm{BU}}}{d\Omega}(\theta_{\mathrm{bin}})}{\frac{d\sigma_{\mathrm{Ruth}}}{d\Omega}(\theta_{\mathrm{bin}})} \frac{\epsilon_{\mathrm{BU}}(\theta_{\mathrm{bin}})}{\epsilon_{\mathrm{Ruth}}(\theta_{\mathrm{bin}})}. \tag{6.5}$$

The Rutherford yield Y_{Ruth} at all θ_{bin} is needed in Eq. 6.5. As evidenced by the fact that other nuclear reactions are occurring, the elastic yield will deviate strongly from the Rutherford cross-section at backward angles. However, since the Rutherford cross-section can be calculated exactly, a monitor detector can be placed at a forward angle θ_{M}, where the yield Y_{M} is expected to be purely Rutherford at all energies of interest. This detector can be a part of the BALiN array that is at sufficiently forward angles, or can be a separate detector. The yield in this detector can be used to find the expected Rutherford yield at any angle, through the relation

$$Y_{\mathrm{Ruth}}(\theta_{\mathrm{bin}}) = Y_{\mathrm{M}} \frac{\frac{d\sigma_{\mathrm{Ruth}}}{d\Omega}(\theta_{\mathrm{bin}})}{\frac{d\sigma_{\mathrm{Ruth}}}{d\Omega}(\theta_{\mathrm{M}})} \left[\frac{\Delta\Omega_{\mathrm{bin}}(\theta_{\mathrm{bin}})}{\Delta\Omega_{\mathrm{M}}} \right]. \tag{6.6}$$

This expression requires the determination of the solid angle of the monitor detector, $\Delta\Omega_{\mathrm{M}}$, as well as the number of Rutherford scattered beam particles in the monitor detector Y_{M}. We begin with determination of Y_{M}.

6.2 Rutherford Yield

Together with the solid angle of the monitor, the yield of Rutherford scattering from the target nucleus in the monitor Y_{M} must be determined for Eq. 6.6. In principle, finding the Rutherford yield should be fairly straightforward:

1. Place the monitor at a scattering angle where the elastic yield is expected to correspond to Rutherford scattering.
2. In the monitor, do a singles measurement – that is, require no coincidences.
3. Count the number of events in a peak that corresponds to the energy of elastic scattering of the beam from the target.

In practice, each set of measurements used to extract breakup probabilities in this work has a complicating factor. Namely:

- In the BEX run, a forward section of BALiN had to be used as a monitor region. Since this measurement was made in the lampshade configuration, the monitor region is between 124° and 127°. At this angle, the elastic yield deviated from Rutherford expectations by at most 11% in the energies studied here. This can be corrected by evaluation of existing elastic scattering data.
- In the LIAL and RDUX runs, again, a forward section of BALiN had to be used as a monitor region. This was due to a probable fault in the monitor CFD resulting in an unreliable number of monitor time signals. This was not foreseen, so many measurements were made in the hardware coincidence mode (as previously described in Sect. 3.3.3). In the hardware coincidence mode, the only elastically scattered

particles that are detected are those that are detected in random coincidence with another particle or hit an arc-sector boundary. Since the probability of an elastically scattered particle being incident on an arc-sector boundary is governed by the geometry of the detector, the yield of these elastic events can be exploited to determine the Rutherford yield.

These factors make the determination of Y_{M} challenging, and each required a different strategy for an accurate determination. These will be discussed briefly in turn. As the same systems were measured in LIAL and RDUX, which have different normalisation factors, finding consistent breakup functions will give confidence in the final results.

6.2.1 BEX: Monitor Bin at Backward Angles

In the BEX run, elastic events for normalisation were extracted from a bin of the BALiN array in θ from 124° to 127°, where the elastic yield is pure Rutherford for deep sub-barrier measurements. At higher energies, the elastic yield deviates from pure Rutherford scattering, as other reaction channels open. Where measurements were made near to the barrier, the expected Rutherford yield (Y_{M}) is calculated from the measured elastic yield ($Y_{\mathrm{M}}^{\mathrm{elas}}$) by taking the ratio of the elastic cross-sections determined from optical model fits of existing elastic scattering data [1–4] to that of the Rutherford cross section:

$$Y_{\mathrm{M}} = Y_{\mathrm{M}}^{\mathrm{elas}} \frac{\frac{d\sigma_{\mathrm{elas}}}{d\Omega}(\theta_{\mathrm{M}})}{\frac{d\sigma_{\mathrm{Ruth}}}{d\Omega}(\theta_{\mathrm{M}})}. \tag{6.7}$$

There are no elastic scattering data for ^{9}Be + ^{168}Er, ^{186}W and ^{196}Pt available. In these cases, the real part of the potentials were the São Paulo Potential, and the imaginary parts were taken from experimental data for the closest mass nucleus (^{208}Pb for ^{196}Pt and ^{186}W, ^{144}Sm for ^{168}Er). The results of these calculations are shown in Fig. 6.1. This correction was largest for ^{9}Be + ^{208}Pb and ^{209}Bi at $E_{\mathrm{beam}} = 37.0$ MeV, where $\frac{d\sigma_{\mathrm{elas}}}{d\sigma_{\mathrm{Ruth}}}(\theta_{\mathrm{norm}}) = 0.89$.

The results for the BEX run are a re-analysis of the work in Ref. [5], a comparison to the Y_{M} in that work yields an average $9 \pm 1\%$ decrease in the number of elastic particles assigned to the 124°–127° bin for each measurement in this analysis as compared to that of Ref. [5]. This is due to the corrected measurement of the spatial position of the BALiN array, as described in Sect. 3.4.2.

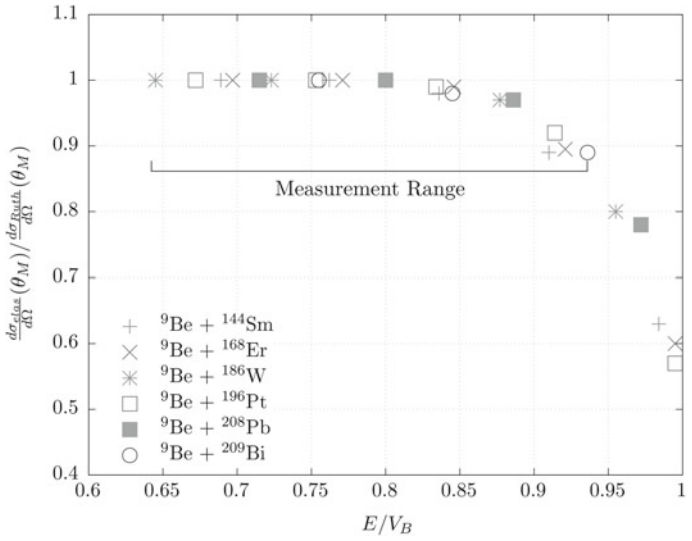

Fig. 6.1 Ratio of elastic and Rutherford cross-sections as a function of energy relative to the barrier at the monitor angle $\theta_{\mathrm{M}} = 125.5°$

6.2.2 LIAL and RDUX: Data Taken with Hardware Multiplicity Two Requirement

As in the BEX run, the breakup data for LIAL and RDUX is normalised to the Rutherford yield in a forward part of BALiN. Two forward arcs were used. For LIAL, arcs 10 and 11 of detectors A and B are used, and for RDUX, arcs 11 and 12 of the same detectors were used. Unlike the BEX run, this was not as originally planned. Instead, some measurements were taken with a hardware multiplicity two requirement, in order to reject the bulk of particles originating from reactions that do not produce two particles in coincidence. Elastically scattered beam particles that are recorded are as a result of events that produce a multiplicity two trigger in BALiN, such as those resulting from elastically scattered beam hitting an arc boundary. The ratio between the expected Rutherford yield in the two arcs to those that cross the boundary between the arcs can be characterised using the measurements that were performed with no multiplicity requirement, as described below.

From geometry, the ratio between the number of elastic events that hit an arc boundary and the total number of elastic events in adjacent arcs is related only to the width of the boundary region and how the elastic cross-section changes over the arcs. This results in a constant value $\frac{Y^{\mathrm{ideal}}_{\mathrm{boundary}}}{Y_{\mathrm{M}}}$ for any measurement. However, as discussed earlier, BALiN has an effective energy threshold E_{thr} due to the energy loss of fragments in the target and array prior to arriving at the active volume of the detector. Particles of initial energy $E < E_{thr}$ will lose energy and be below the amplifier threshold when they are detected. When an elastic event hits an arc

boundary, the energy of the fragment E_{elas} is shared between the two arcs, such that $E_{\text{elas}} = E_1 + E_2$, with a uniform distribution of energy given to each arc, such that the energy of each fragment is evenly distributed in $0 < E_i < E_{\text{elas}}$. This can be seen in Fig. 4.1. As a result, the measured ratio of elastic events that hit an arc boundary to the total is given by the function

$$\frac{Y^{\text{measured}}_{\text{boundary}}}{Y_{\text{M}}} = \frac{Y^{\text{ideal}}_{\text{boundary}}}{Y_{\text{M}}} \left(\frac{E_{\text{elas}} - 2E_{\text{threshold}}}{E_{\text{elas}}} \right). \tag{6.8}$$

The measured $\frac{Y^{\text{measured}}_{\text{boundary}}}{Y_{\text{M}}}$ values for data taken in the RDUX and LIAL runs with no hardware multiplicity requirement are shown as a function of E_{elas} in Fig. 6.2, and has been fitted with Eq. 6.8. In the fit, $\frac{Y^{\text{ideal}}_{\text{boundary}}}{Y_{\text{M}}}$ and $E_{\text{threshold}}$ has been treated as free parameters. The fit goes to zero at $E_{\text{elas}} = 2E_{\text{threshold}}$. At this energy, all elastically scattered particles will be below threshold. Therefore, this fit also allows the determination of the energy threshold for elastically scattered particles in BALiN. With the fitted functions, Y_{M} in data taken with a hardware multiplicity two requirement can be found using the measured $Y^{\text{measured}}_{\text{boundary}}$ and the energy of the elastic peak at θ_{M}, E_{elas}, giving

$$Y_{\text{M}} = \frac{Y^{\text{measured}}_{\text{boundary}}}{\frac{Y^{\text{ideal}}_{\text{boundary}}}{Y_{\text{M}}} \left(\frac{E_{\text{elas}} - 2E_{\text{threshold}}}{E_{\text{elas}}} \right)}. \tag{6.9}$$

6.3 Monitor Solid Angle

The normalisation detector used to determine the Rutherford yield can be either one or more forward arcs of BALiN or a separate, smaller, surface barrier detector. In either case, its solid angle must be determined.

If a separate detector is used, its solid angle coverage either has to be measured physically, which is prone to error, or the expression for the Rutherford cross-section can be used (Eq. 2.13) to relate the relative yields in the monitor detector and in BALiN to the relative solid angle coverage of the detectors at a beam energy E_{cal} where the elastic yields do not deviate from Rutherford scattering (in this work, generally around $E_{\text{cal}} \sim 0.7 \times V_B$). That is, using Eq. 6.4 in the laboratory frame, the ratio of the yields in the monitor and the yields in BALiN at each θ_{bin} may be written as

$$\frac{Y_{\text{Ruth}}(\theta_{\text{M}}, E_{\text{cal}})}{Y_{\text{Ruth}}(\theta_{\text{bin}}, E_{\text{cal}})} = \frac{\frac{d\sigma_{\text{Ruth}}}{d\Omega}(\theta_{\text{M}}, E_{\text{cal}})}{\frac{d\sigma_{\text{Ruth}}}{d\Omega}(\theta_{\text{bin}}, E_{\text{cal}})} \frac{\Delta\Omega_{\text{M}}}{\Delta\Omega_{\text{BALiN}}(\theta_{\text{bin}})} \frac{D_{\text{M}}}{D_{\text{BALiN}}}, \tag{6.10}$$

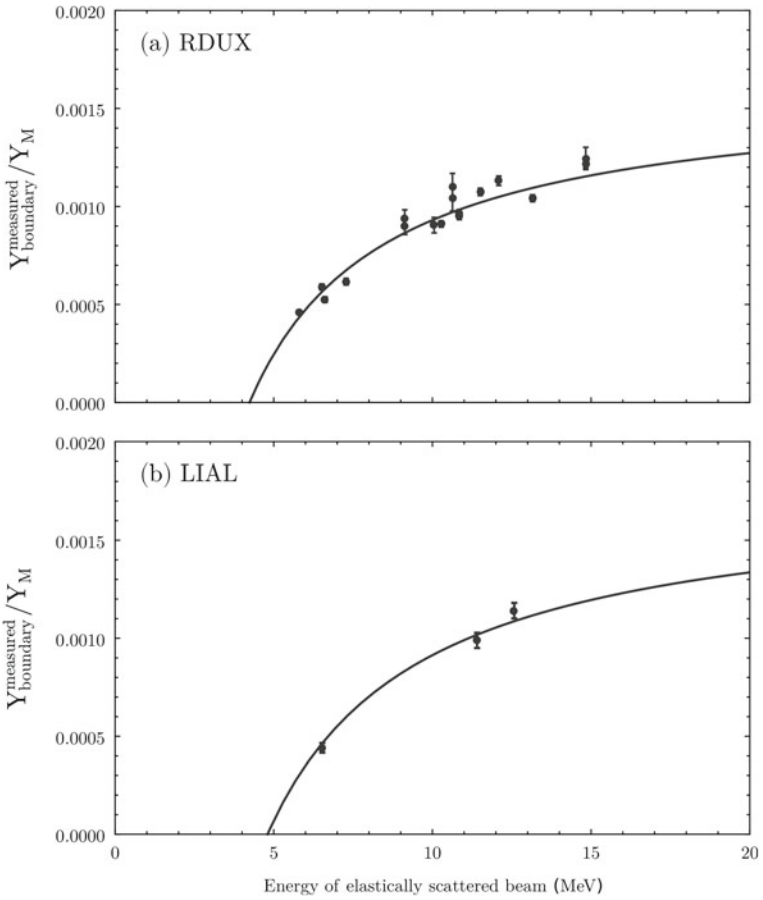

Fig. 6.2 Measured $\frac{Y^{measured}_{boundary}}{Y_M}$ ratios for data taken with no multiplicity requirement, for the **a** RDUX and **b** LIAL runs. A fit with Eq. 6.8 has been performed, allowing for determination of Y_M in data taken with a multiplicity two requirement. The fit goes to zero at $2E_{threshold}$, which is at a value consistent with what is observed in the experimental data

where $\Delta\Omega_{BALiN}(\theta_{bin})$ is the solid angle of BALiN at each θ_{bin}, D_M is the fractional data acquisition deadtime in the monitor, and D_{BALiN} is the data acquisition deadtime for Rutherford scattering in BALiN. When the arcs in BALiN are used as a monitor as in the measurements under discussion here, this method for determining the monitor solid angle is still useful: it provides a cross-check of the geometry of BALiN. Since the monitor solid angle is independent of the region of BALiN used for normalisation, the $\Delta\Omega_M(\theta_{bin})$ deduced must be constant. In the instance where forward arcs of BALiN are used as the beam monitor, $D_M = D_{BALiN}$. Re-arranging Eq. 6.10 for $\Delta\Omega_M$, we obtain

$$\Delta\Omega_{\mathrm{M}} = \frac{Y_{\mathrm{Ruth}}(\theta_{\mathrm{M}}, E_{\mathrm{cal}})}{Y_{\mathrm{Ruth}}(\theta_{\mathrm{bin}}, E_{\mathrm{cal}})} \frac{\frac{d\sigma_{\mathrm{Ruth}}}{d\Omega}(\theta_{\mathrm{bin}}, E_{\mathrm{cal}})}{\frac{d\sigma_{\mathrm{Ruth}}}{d\Omega}(\theta_{\mathrm{M}}, E_{\mathrm{cal}})} \Delta\Omega_{\mathrm{BALiN}}(\theta_{\mathrm{bin}}) \frac{D_{\mathrm{BALiN}}}{D_{\mathrm{M}}}. \tag{6.11}$$

This expression depends on the angle of the monitor θ_{M} being accurately known in the calculation of the Rutherford cross-section $d\sigma_{\mathrm{Ruth}}/d\Omega(\theta_{\mathrm{M}}, E_{\mathrm{cal}})$. However, when substituted into Eq. 6.6, the angular dependence in $d\sigma_{\mathrm{Ruth}}/d\Omega(\theta_{\mathrm{M}}, E_{\mathrm{cal}})$ cancels out, removing this uncertainty. However, the quantities $\Delta\Omega_{\mathrm{BALiN}}(\theta_{\mathrm{bin}})$ and $Y_{\mathrm{Ruth}}(\theta_{\mathrm{bin}}, E_{\mathrm{cal}})$ must be found. A description of the determination of $\Delta\Omega_{\mathrm{BALiN}}(\theta_{\mathrm{bin}})$ appears in Appendix E.

6.3.1 $Y_{\mathrm{Ruth}}(\theta_{\mathrm{bin}})$

To determine the Rutherford yield in BALiN, normalisation measurements were made at far below-barrier energies, where the elastic yield follows Rutherford expectations across the entire array. For the LIAL run, this was ^{7}Li + ^{58}Ni at $E_{\mathrm{beam}} = 7.50$ MeV. For RDUX, this was ^{7}Li + ^{144}Sm at $E_{\mathrm{beam}} = 9.70$ MeV. The energy of ^{7}Li (corrected for energy loss) as a function of scattering angle is shown in Fig. 6.3a. In the RDUX run, the ^{144}Sm target had irregular target thickness. As a result, the elastic peak has a large tail of events extending below the energy of the elastic peak, seen in the projection of the energy of particles scattered in $68-72°$, shown in Fig. 6.3b. As such, it is difficult to obtain a consistent Rutherford yield from drawing a two dimensional gate – small changes in cursor position can change the values significantly. Instead, for consistency, the position of the elastic peak in each 4° bin is found using a peak search routine, and a Gaussian fit made around the peak. The *ratio* of Rutherford events are what is important here, rather than the absolute number of events. Since the forward arcs of BALiN were used as the monitor detector there is no issue with different detectors having different responses. This method enables a more consistent determination of $\Delta\Omega_{\mathrm{M}}$, even if the shape of the peak is somewhat non-Gaussian.

6.3.2 *Resulting* $\Delta\Omega_{\mathrm{M}}$ *Values*

The resulting $\Delta\Omega_{\mathrm{M}}$ for the RDUX run is shown in Fig. 6.4. As required, $\Delta\Omega_{\mathrm{M}}$ shows no dependence on θ_{bin}, indicating that the measured geometry of BALiN matches the true position of BALiN, aside from the first and last bins on each set of detectors, where the value of $\Delta\Omega_{\mathrm{M}}$ deviates somewhat. Since $\Delta\Omega_{\mathrm{BALiN}}$ changes rapidly at the edges of the BALiN array, as seen in Fig. E.1c, slight ($\lesssim$1 mm) differences between the measured and true position of BALiN can result in such discrepancies.

If the geometry were not correctly determined to a larger extent, there would be a mismatch between the measured $Y_{\mathrm{Ruth}}(\theta_{\mathrm{M}})/Y_{\mathrm{Ruth}}(\theta_{\mathrm{bin}})$ and the calculated

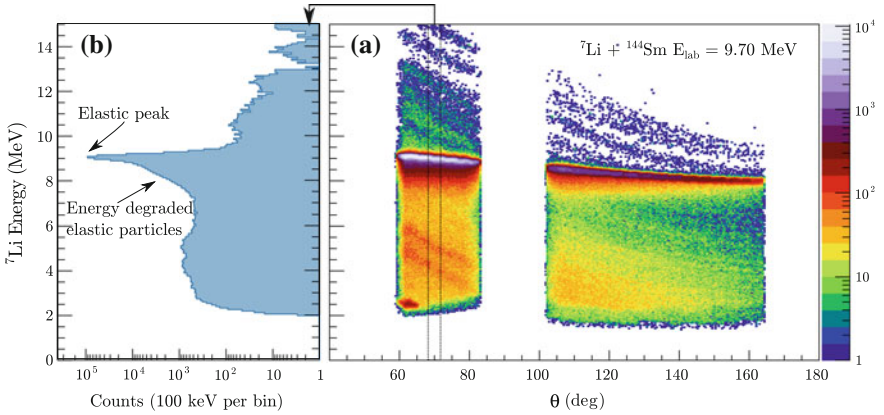

Fig. 6.3 **a** Energy-loss corrected ^{7}Li energy as a function of laboratory scattering angle for the ^{7}Li + ^{144}Sm normalisation measurement at $E_{\text{beam}} = 9.70$ MeV. The elastic peak can be seen at ∼9 MeV, with a large tail extending below the elastic peak. **b** Energy spectrum of the particles that were detected between 68−72°, showing the elastic peak with its energy degraded tail

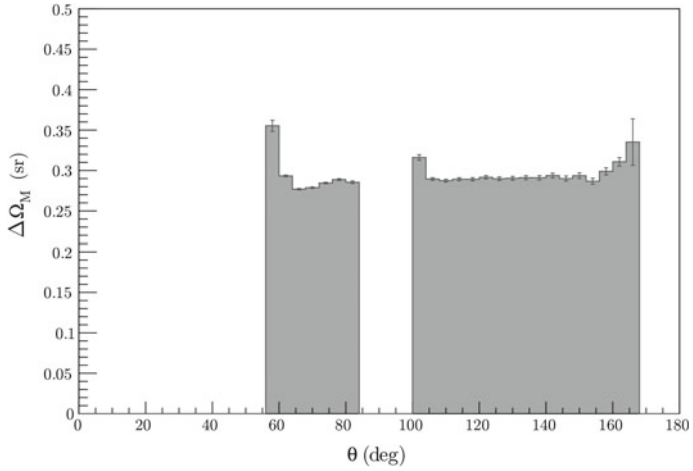

Fig. 6.4 The monitor solid angle $\Delta\Omega_M$ for the RDUX run, where two forward arcs of BALiN were used for normalisation, determined from the scattering of ^{7}Li from ^{144}Sm at $E_{\text{beam}} = 9.70$ MeV. The large value of $\Delta\Omega_M$ reflects the large size of the DSSDs. Deviations are seen at the edges of the distribution. Since $\Delta\Omega_{\text{BALiN}}$ changes rapidly at the edges, this is suggestive of a slight difference ($\lesssim 1$ mm) between the measured and true position of BALiN. Outside these edge effects, the fact that $\Delta\Omega_M$ is constant with changing θ_{bin} indicates that the geometry of BALiN is correctly determined

$\frac{d\sigma_{\text{Ruth}}}{d\Omega}(\theta_{\text{bin}})/\frac{d\sigma_{\text{Ruth}}}{d\Omega}(\theta_M)$ across the entire array, and $\Delta\Omega_M$ would vary with θ_{bin}. An example of this is seen in Fig. 6.5, where the assumed detector-target distance of detectors C and D in the backward hemisphere are moved in 2 mm increments from 121 to 115 mm, keeping detectors A and B fixed at 112 mm. As the detectors move

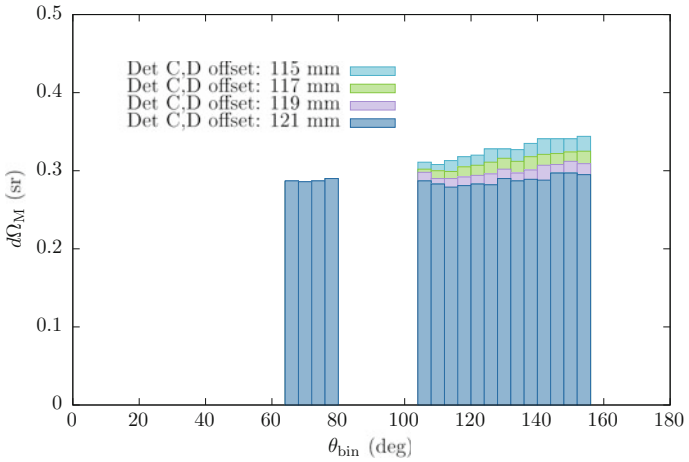

Fig. 6.5 The monitor solid angle $\Delta\Omega_M$ for the LIAL run, where two forward arcs of BALiN are used for normalisation, determined from the scattering of ^{7}Li + ^{58}Ni at 7.50 MeV. The sensitivity of the measured $\Delta\Omega_M$ is demonstrated by varying the assumed location of detectors C and D of BALiN between 115 and 121 mm. The constant value of $\Delta\Omega_M$ at a detector-target distance of 121 mm demonstrates that this is the correct detector-target distance

towards the target, $\Delta\Omega_M$ increases for these values, and gains a slope as a function of θ_{lab}, which increases with distance towards the target, demonstrating that the correct detector-target distance is 121 mm. As such evaluation of $\Delta\Omega_M$ as a function of θ_{bin} provides a useful check of the assumed detector geometry.

Once $\Delta\Omega_M(\theta_{bin})$ has been obtained the next task is to average it over θ_{bin}. For LIAL, the average $\Delta\Omega_M$ is 0.29 ± 0.01 sr and for RDUX it is 0.28 ± 0.01 sr. These values differ due to the slightly different detector-target distances in the two runs.

6.4 Breakup Cross-Sections

Given the solid angle of the monitor $\Delta\Omega_M$ and the Rutherford yield in the monitor $Y_M(\theta_M)$, the Rutherford yield across the array $Y_{Ruth}(\theta_{bin})$ is determined via Eq. 6.6. Re-arranging Eq. 6.5, an expression for the breakup cross-section is obtained,

$$\frac{d\sigma_{BU}}{d\Omega}(\theta_{bin}) = \frac{Y_{BU}(\theta_{bin})}{Y_{Ruth}(\theta_M)} \frac{d\sigma_{Ruth}}{d\Omega}(\theta_M) \frac{\epsilon_{Ruth}(\theta_M)}{\epsilon_{BU}(\theta_{bin})} \frac{\Delta\Omega_{bin}}{\Delta\Omega_M}. \tag{6.12}$$

The efficiency for detecting Rutherford scattering in the monitor is given by $\epsilon_{Ruth}(\theta_M)$. Since the detector solid angle is taken into account in Eq. 6.12, ϵ_{Ruth} is the fractional data acquisition deadtime D_M, the determination of which was discussed in Sect. 3.4.7. Similarly, $\epsilon_{BU}(\theta_{bin})$ is the efficiency for detecting breakup events in

BALiN. As with the efficiency for detecting elastically scattered particles, ϵ_{BU} has a term due to the data acquisition deadtime $D_{\mathrm{BU}} = D_{\mathrm{ADC}} \times D_{\mathrm{TDC}}$, discussed in Sect. 3.4.7, as well as the efficiency for detecting both fragments in coincidence (as will be discussed in Sect. 6.5), giving $\epsilon_{\mathrm{BU}}(\theta_{\mathrm{bin}}) = D_{\mathrm{BU}} \times \epsilon_{\mathrm{Coin}}(\theta_{\mathrm{bin}})$.

The yield of breakup Y_{BU} within the bin located θ_{bin} is defined as the number of events with reconstructed breakup pseudoangle θ_p (as defined in Sect. 2.8.6) within the bin. The desired breakup probabilities as a function of R_{min} require the evaluation of the differential breakup cross-section in the centre of mass frame. The standard approach of evaluating differential cross-sections in the laboratory frame and subsequent transformation into the centre of mass frame (e.g. [6]) requires that the kinetic energy of relative motion in the centre of mass frame and the Q-value of the reaction to be the same for all events. Since the breakup fragments are produced through reactions with a large range of Q-values, the standard method for laboratory to centre of mass frame conversion is not appropriate in this context. However, the energy, pseudoangle and Q-value for every breakup event is known. Therefore, converting from laboratory to centre of mass frame is done *event by event* and Eq. 6.12 is evaluated in the centre of mass frame. Since the centre of mass breakup pseudoangle of each fragment is known, the breakup yield is binned as a function of θ_p in bins of constant width centred around θ_{bin} in the centre of mass frame. The solid angle of each bin is given by

$$\Delta\Omega_{\mathrm{bin}} = 2\pi\Delta\theta_{\mathrm{bin}}\sin(\theta_{\mathrm{bin}}), \tag{6.13}$$

and the coincidence efficiencies are calculated as a function of θ_p and θ_{12}, which will be described in Sect. 6.5.

Finally, $\Delta\Omega_{\mathrm{M}}$ (denoted $\Delta\Omega_{\mathrm{M}}^{lab}$) is transformed from the laboratory frame to the centre of mass frame $\Delta\Omega_{\mathrm{M}}^{\mathrm{CM}}$ for every measurement. Following Ref. [6], since the solid angle is given by $d\Omega = d\theta d\phi \sin\theta$, and ϕ remains unchanged in a transformation between laboratory and centre of mass frames, the relationship between solid angles is given by:

$$\frac{d\Omega_{\mathrm{M}}^{\mathrm{lab}}}{d\Omega_{\mathrm{M}}^{\mathrm{CM}}} = \frac{d\theta_{\mathrm{M}}^{\mathrm{lab}}\sin\theta_{\mathrm{M}}^{\mathrm{lab}}}{d\theta_{\mathrm{M}}^{\mathrm{CM}}\sin\theta_{\mathrm{M}}^{\mathrm{CM}}} = \frac{d\cos\theta_{\mathrm{M}}^{\mathrm{lab}}}{d\cos\theta_{\mathrm{M}}^{\mathrm{CM}}}. \tag{6.14}$$

For elastically scattered projectiles m_p from a target m_t, the relationship between θ_M^{lab} and θ_M^{CM} is given by

$$\cos\theta_{\mathrm{M}}^{\mathrm{lab}} = \frac{\frac{m_p}{m_t} + \cos\theta_{\mathrm{M}}^{\mathrm{CM}}}{\sqrt{1 + (\frac{m_p}{m_t})^2 + 2\frac{m_p}{m_t}\cos\theta_{\mathrm{M}}^{\mathrm{CM}}}}. \tag{6.15}$$

Differentiating this gives

$$\frac{d\cos\theta_{\mathrm{M}}^{\mathrm{lab}}}{d\cos\theta_{\mathrm{M}}^{\mathrm{CM}}} = \frac{1 + \frac{m_p}{m_t}\cos\theta_{\mathrm{M}}^{\mathrm{CM}}}{(1 + (\frac{m_p}{m_t})^2 + 2\frac{m_p}{m_t}\cos\theta_{\mathrm{M}}^{\mathrm{CM}})^{3/2}}. \tag{6.16}$$

And so, after re-arranging for $\theta_{\mathrm{M}}^{\mathrm{lab}}$, the desired transformation:

$$d\Omega_{\mathrm{M}}^{\mathrm{CM}} = d\Omega_{\mathrm{M}}^{\mathrm{lab}} \frac{d\cos\theta_{\mathrm{M}}^{\mathrm{lab}}}{d\cos\theta_{\mathrm{M}}^{\mathrm{CM}}} = d\Omega_{\mathrm{M}}^{\mathrm{lab}} \frac{(1-\frac{m_p}{m_t}^2 \sin^2\theta_{\mathrm{M}}^{\mathrm{lab}})^{1/2}}{[\frac{m_p}{m_t}\cos\theta_{\mathrm{M}}^{\mathrm{lab}} + (1-\frac{m_p}{m_t}^2 \sin^2\theta_{\mathrm{M}}^{\mathrm{lab}})^{1/2}]^2}, \quad (6.17)$$

is obtained. The transformed quantity $\Delta\Omega_{\mathrm{M}}^{\mathrm{CM}}$ is used in Eq. 6.12.

The breakup probability P is defined as the ratio between the breakup cross-section, determined from the yield of breakup fragments with the reconstructed angle of the unbroken projectile falling in the bin centred around θ_p, and the Rutherford scattering cross-section for each θ_p in the centre of mass frame,

$$P(\theta_p) = \frac{\frac{d\sigma}{d\Omega}_{\mathrm{BU}}(\theta_p)}{\frac{d\sigma}{d\Omega}_{\mathrm{Ruth}}(\theta_p)}. \quad (6.18)$$

The desired breakup functions must be as a function of R_{min}, which, as defined in Eq. 6.2, depends on the scattering angle for particles on a Rutherford trajectory, θ_{CM}. The mapping of the reconstructed scattering angle θ_p to the scattering angle for a Rutherford trajectory θ_{CM} is presented in Sect. 6.9. This mapping gives breakup functions $P(R_{\mathrm{min}})$ which may be fitted with the functional form

$$P(R_{\mathrm{min}}) = Ae^{\mu R_{\mathrm{min}}} \quad (6.19)$$

or

$$P(R_{\mathrm{min}}) = e^{\mu R_{\mathrm{min}}+\nu} \quad (6.20)$$

for input into KOOKABURRA or M-PLATYPUS, respectively. In this work, μ is referred to as the "slope parameter" and A,ν are the "strength parameters".

6.5 Coincidence Efficiency Determination

The final term in Eq. 6.12 that remains to be determined is the efficiency of detecting both breakup fragments in coincidence, ϵ_{BU}, which is called the "coincidence efficiency". The determination of the coincidence efficiency makes use of KOOKABURRA and M-PLATYPUS simulations to predict the total energy and angular distribution of breakup fragments, which are then filtered through the acceptance of BALiN. However, the total energy and angular distribution of the breakup fragments depends on the input breakup function, which must be determined from experiment. Therefore, the process of determining the coincidence efficiency and so the breakup functions is iterative. An initial estimate of the breakup function is used as the first input into KOOKABURRA or M-PLATYPUS, fragment detection efficiencies are extracted, and then a new breakup function determined. The new breakup function is then input into

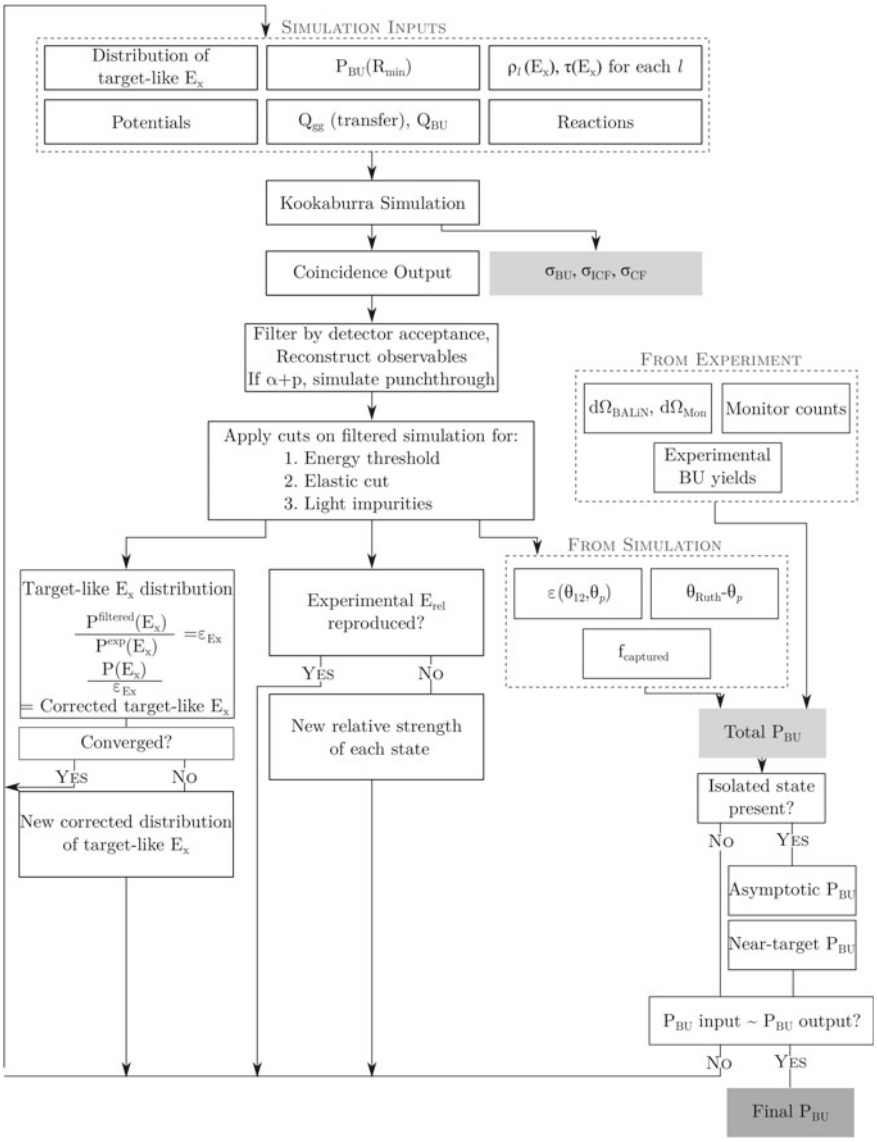

Fig. 6.6 Flow chart illustrating the process of extraction of breakup probabilities

KOOKABURRA or M-PLATYPUS and the process repeated until the breakup probabilities converge. This is shown schematically in Fig. 6.6. In addition to the experimentally determined breakup function, KOOKABURRA and M-PLATYPUS also take the distribution of target-like and projectile-like excitation energies as input. These

must also be found from experiment in an iterative fashion, and will be discussed in Sects. 6.7 and 6.6, respectively.

In previous work [5, 7, 8], coincidence efficiencies were determined as a function of breakup pseudoangle θ_p only. Since breakup cross-sections are determined as a function of θ_p, this is a not unreasonable approach. However, the coincidence efficiency of the detection of a breakup process in BALiN depends critically on the opening angle of the fragments. For example, due to the small θ_{12} of the fragments, the coincidence efficiency for detecting $\alpha + \alpha$ fragments from breakup of ^{8}Be in its 0^+ ground-state resonance will be large: if one fragment is detected, the other one is likely to be also. On the other hand, the coincidence efficiency for $\alpha + \alpha$ fragments arising from the 2^+ resonance of ^{8}Be will be smaller, due to the larger θ_{12} of the fragments – there is smaller probability of both fragments being within the acceptance of BALiN. Therefore, in this thesis, breakup yields are efficiency corrected two-dimensionally, on the basis of both θ_{12} and θ_p, giving an efficiency as a function of both θ_{12} and θ_p $\epsilon_{\mathrm{BU}}(\theta_{12}, \theta_p)$. The breakup yields are then efficiency corrected as a function of θ_{12} and θ_p

$$\frac{Y_{BU}(\theta_{12}, \theta_p)}{\epsilon_{BU}(\theta_{12}, \theta_p)}. \tag{6.21}$$

After efficiency correction, the yields are then projected into θ_p for evaluation of the differential breakup cross-section. The (θ_{12},θ_p) distribution for $\alpha + \alpha$ fragments measured the ^{7}Li + ^{27}Al$\rightarrow$^{8}Be + ^{26}Mg reaction at $E_{\mathrm{lab}} = 7.50$ MeV is shown in Fig. 6.7. The shape of this distribution depends on both θ_{12} and θ_p and arises from the underlying distribution of breakup fragments, filtered by the acceptance of BALiN. For example, breakup events with $\theta_p \lesssim 90°$ will be detected only if $\theta_{12} \lesssim 120°$, that is, if their opening angle is sufficiently small so that both fragments fall on DSSD A or B. If you assume that the efficiency of BALiN is constant as a function of θ_{12}, this fact will not be taken into account.

After adopting this two-dimensional approach, determining the coincidence efficiency is a two-step process. The first step is to calculate the coincidence efficiency of the BALiN array as a function of θ_{12} and breakup pseudoangle θ_p. If the angular acceptance of BALiN were the only relevant factor, any Monte-Carlo simulation could be used to obtain the coincidence efficiencies by simulating all θ_{12} at a given θ_p, and then determining what fraction register as a coincidence event in BALiN taking into account both the angular coverage and pixelization of BALiN. If breakup occurs isotropically in the rest frame of the projectile-like nucleus, these efficiencies are geometric and model-independent.

However, it is not only the angular acceptance that effects the coincidence efficiency. In Chap. 4 a number of cuts had to be placed on the measured yield of coincidence fragments to remove spurious coincidence events that were a result of elastic-X coincidences or cross-talk (Sect. 4.1). In addition, with lighter targets (^{27}Al, ^{28}Si, ^{58}Ni) breakup arising from interactions of the weakly bound nuclei with C, O and N target impurities was removed by reconstructing all breakup fragments as if the target were composed of the impurity in question, and removing those events

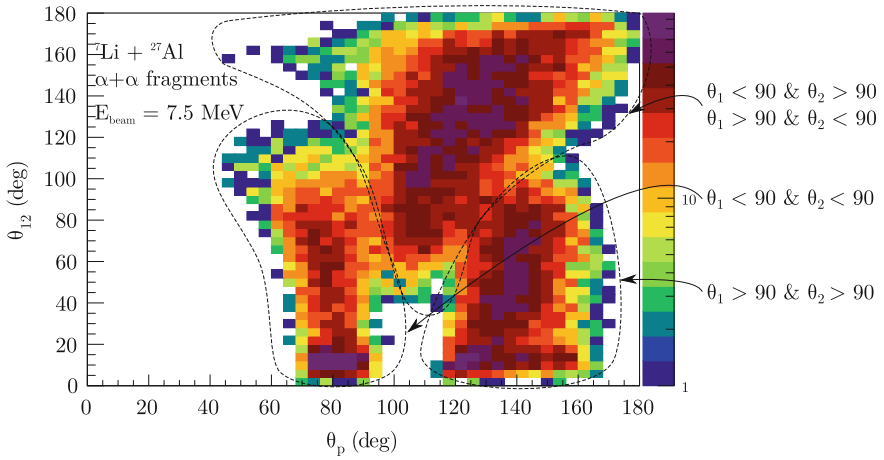

Fig. 6.7 Measured θ_{12} versus θ_p distribution of $\alpha + \alpha$ fragments produced in reactions of ^{7}Li with ^{27}Al at $E_{\text{beam}} = 7.5$ MeV with BALiN in the front-back configuration. This demonstrates the effects of the angular acceptance of BALiN on the measured distribution of coincidence breakup fragments. Events with $\theta_p \lesssim 90°$ and $\theta_{12} \lesssim 120°$ occur when both fragments are detected in the front DSSDs (A and B). Similarly, events with $\theta_p \gtrsim 110°$ and $\theta_{12} \lesssim 120°$ occur when both fragments are detected in the back DSSDs (C and D). When one fragment is incident on the front detector, and one on the back detector, the resulting θ_{12} extends from ∼50° to 180° for $60° \lesssim \theta_p \lesssim 180°$

that reconstructed to the expected Q, as described in Sect. 4.3. These cuts inevitably result in a removal of some valid breakup fragments, which must be accounted in the efficiency determination. Further, with light targets, the energy threshold of BALiN is relevant: breakup that produces a fragment with energy lower than the threshold will not be captured. Having to take into account these cuts is particular to light- to medium-mass systems.

A key advantage of simulating the coincidence efficiency using a Monte-Carlo model is that the cuts placed on the experimental data can be accounted for when evaluating the efficiency of the array for a given measurement. The required cuts are:

- **Energy thresholds**. The threshold placed on the amplifiers is ∼100 keV. However, this is the energy threshold for particles that have experienced energy loss through the target, PET foil, aluminium layer and detector deadlayer. The ∼100 keV threshold then corresponds to a ∼1.2 MeV effective threshold for breakup fragments prior to energy loss; fragments with energy $\lesssim$1.2 MeV will be below threshold after energy loss. The effective threshold depends on the breakup fragment identity, detector deadlayer, and the target thickness. Higher Z fragments will experience more energy loss and so have a higher effective threshold. A thicker target or detector deadlayer will result in greater energy loss through the target and also a higher effective threshold. Therefore, the effective energy threshold must be found for each fragment species and for every target in each DSSD. The appropriate effective thresholds were then also applied to the KOOKABURRA simulations.

- **Removal of elastic-X coincidences** In reactions of ^{9}Be and ^{7}Li with light- and medium-mass targets, the full-energy elastics detected in coincidence with another particle overlap with the energy of breakup particles. An example of this was shown in Fig. 4.1. The removal of the elastic-X coincidences by a narrow gate in E versus θ will remove the genuine breakup fragments which fall within the E versus θ cuts. To account for the decrease in efficiency due to removing these events, the same E versus θ cuts were placed on the KOOKABURRA simulations. The E versus θ cuts were placed on events that were energy-loss corrected as if they were the relevant breakup fragment in order to ensure that the E versus θ gate was compatible with both the experimental and KOOKABURRA data. Due to the fact that the energy loss correction was applied as if the particles were breakup fragments, rather than elastically scattered beam, the energy loss reconstruction of the beam particles was not complete. To account for this, the E versus θ cuts were placed on each DSSD separately due to their different deadlayers.
- **Removal of cross-talk**. In the experimental data, cross-talk events were identified and removed by examining those events that landed on adjacent pixels. This process also removed genuine some breakup events with small θ_{12}. The conditions were applied to the KOOKABURRA simulations.
- **Cuts due to light impurities**. In the experimental data, intense bands of breakup fragments due to interactions with light target impurities (^{12}C, ^{16}O and ^{14}N) were seen. Their presence was first identified by their characteristic curve in (Q, $E_{\rm rel}$) when breakup was reconstructed assuming their origin was a reaction with the heavy target nucleus of interest. These events were removed by reconstructing the breakup events as if they were due to interactions with the light impurity. Breakup that reconstructed to narrow straight bands in (Q, $E_{\rm rel}$) with the expected Q is then inferred to arise from interactions with that light impurity, and were removed via a narrow gate in (Q, θ_p). The Q and θ_p reconstructed assuming the target of interest will not be the same as that reconstructed assuming the target is a light impurity. Thus, a number of genuine breakup events from the target of interest will be removed in this process. To account for the loss of efficiency due to these cuts, the KOOKABURRA data, generated for a particular target, was reconstructed as if it were from ^{12}C, ^{16}O and ^{14}N, and exactly the same (Q, θ_p) cuts applied to the simulation as in the experimental data.

After placing the cuts on the simulated events, the coincidence efficiency is given by the ratio of simulated breakup events where both fragments would have landed in BALiN, subject to the cuts, to all simulated events at each θ_p and θ_{12}. As an example, the simulated (θ_p,θ_{12}) distribution of $\alpha+\alpha$ fragments produced in the $^{7}{\rm Li}+{}^{27}{\rm Al}\rightarrow\ {}^{8}{\rm Be}+{}^{26}{\rm Mg}$ reaction at $E_{\rm lab}$ =7.50 MeV is shown in Fig. 6.8a. Breakup has been simulated arising through the 0^+ and 2^+ resonances. The narrow band at all θ_p but with $\theta_{12}\lesssim 20^\circ$ corresponds to breakup through the narrow 0^+ ground-state resonance, while events arising through the 2^+ resonance have a very broad distribution in (θ_p,θ_{12}). The simulated events, subject to the angular acceptance of BALiN in the front-back configuration used in the RDUX run is shown in panel (b). Energy thresholds as well as the cuts that remove the elastic-X coincidences,

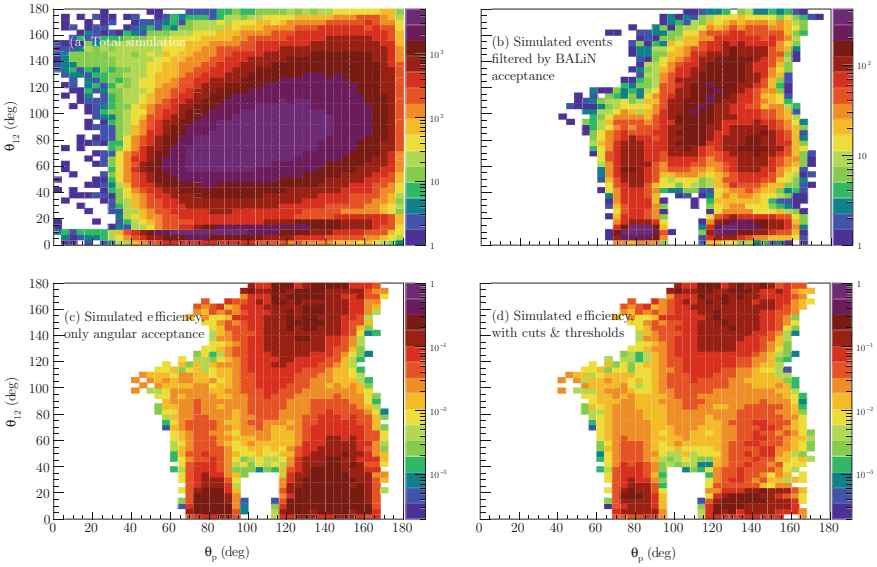

Fig. 6.8 **a** Simulated $\theta_{12} - \theta_p$ distribution for ^{7}Li + ^{27}Al $\rightarrow \alpha + \alpha + ^{26}$Mg at $E_{\text{lab}} = 7.48$ MeV. **b** The same events filtered by the acceptance of the BALiN array, with energy thresholds, and cuts applied as to the experimental data, seen in Fig. 6.7. **c** The associated coincidence efficiency of the BALiN array for as a function of θ_{12} and θ_p before the application of energy thresholds and cuts. **d** The coincidence efficiency after application of cuts and thresholds relevant to the experimental data

cross-talk, and light target impurities have been applied as described above. This simulation reproduces remarkably well the experimentally measured distribution of fragments for the same system, shown in Fig. 6.7. The coincidence efficiencies are generated by dividing the distribution shown in (b) by the parent distribution shown in (a). Panel (c) shows the efficiency matrix where the events have been filtered by the geometrical acceptance of BALiN but not had additional cuts placed on them. Panel (d) includes the complete set of cuts. The efficiency distributions are complex. Some major features are:

1. The efficiency peaks at small θ_{12} and at large θ_{12}. In the former case, the opening angle between the fragments is small enough that both will fall on the same DSSD.[1] In the latter, the opening angle is almost back-to-back in the laboratory frame. In this case, one fragment can fall on a front DSSD and one on a back DSSD, provided that θ_p is not to large or small.
2. The efficiency falls at $\theta_{12} \sim 90°$. Here, if one fragments hits a DSSD, the other fragment is often too far away to hit the same DSSD pair, but not far enough away to hit the other DSSD pair.

[1] However, if the opening angle is too small, both fragments will land in the same pixel, and be recorded as a coincidence event. Therefore, at the very smallest θ_{12}, the efficiency falls again.

3. The gap in efficiency for $95° \lesssim \theta_p \lesssim 115°$ and $0° < \theta_{12} \lesssim 40°$ is due to the gap in θ coverage between the forward hemisphere DSSDs and the backward hemisphere DSSDs. Breakup that has a reconstructed scattering angle in this region can only be detected if their opening angle is large enough so that one fragment is incident on the front pair, and one on the back pair.
4. In these efficiency distributions, the (θ_{12},θ_p) bins on the outside of the acceptance of BALiN have a very small number of counts after filtering. These bins have a large uncertainty in efficiency. The uncertainty in the efficiency calculation have been propagated into the final breakup probabilities.
5. Comparing panels (c) and (d), it can be seen that the cuts and thresholds significantly reduce the efficiency, particularly at backward θ_p. It is therefore essential that these cuts and thresholds are applied to the simulated efficiencies in light and medium mass targets.

These efficiencies are quite dependent on the reaction and configuration of BALiN. As a further example, the geometric coincidence efficiency matrix determined for $\alpha + \alpha$ fragments with $E_{\rm rel} > 0.3$ MeV produced in ^{9}Be + ^{208}Pb reactions at $E_{\rm lab} = 34.0$ MeV, taken in the lampshade configuration, is shown in Fig. 6.9c. These efficiencies were determined from the fraction of events within the acceptance of BALiN, Fig. 6.9b to the total number of events, Fig. 6.9a, in each (θ_p, θ_{12}). The experimentally determined (θ_p, θ_{12}) distribution for the same system is shown in Fig. 6.9d. In this system, the coincidence efficiency shows two triangular regions of high detector efficiency – at small $\theta_{12} \sim 10°$ with $\theta_p \sim 135°$ corresponding to the centre of the BALiN array, and at $\theta_{12} \sim 80°$ at backward $\theta_p \sim 180°$. The former is due to events with sufficiently small opening angle so that both fragments land on the same DSSD, while the latter is due to events that strike two different DSSDs. Compared to the ^{7}Li + ^{27}Al system, the total distribution shown in panel (a) is focused at smaller θ_{12} and larger θ_p, making the lampshade configuration the appropriate choice for this system.

6.5.1 *Events with Opening Angle Outside Detector Acceptance*

In both examples, there are values of θ_p within the acceptance[2] of BALiN where the efficiency is zero for some θ_{12}. The two-dimensional coincidence efficiencies described above do not account for the events that fall outside of the detector acceptance in (θ_p, θ_{12}). The second step in the efficiency determination is to use M-PLATYPUS or KOOKABURRA to simulate the total distribution of fragments in (θ_p, θ_{12}) and correct for those events with θ_{12} that fall outside the detector acceptance as a function of θ_p. This was done for each θ_p bin by taking the ratio of the number of

[2]Since differential cross-sections are determined as a function of θ_p, values of θ_p outside the acceptance of BALiN are not of interest.

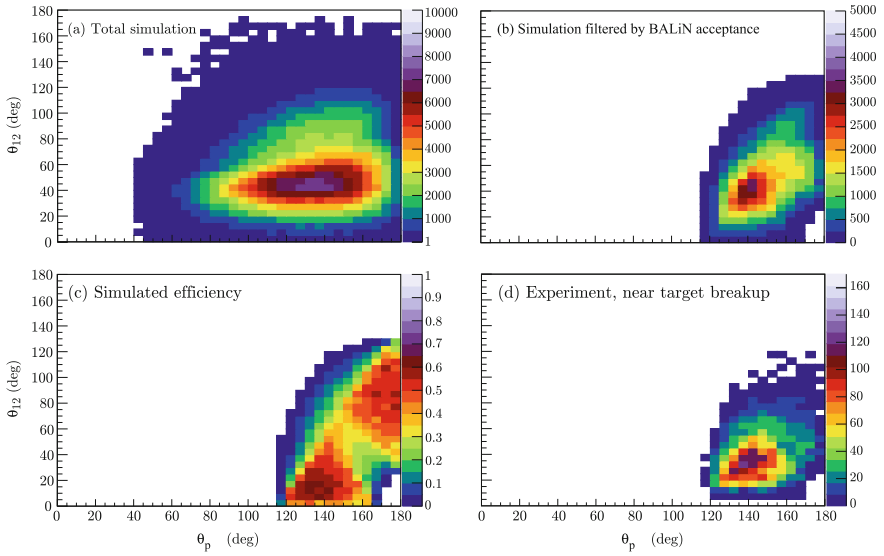

Fig. 6.9 **a** Simulated $\theta_{12} - \theta_p$ distribution using M-PLATYPUS for $^{8}Be^{2+}$ + $^{208}Pb \rightarrow \alpha + \alpha$ at $E_{^9Be} = 34.0$ MeV. **b** The same events filtered by the acceptance of the BALiN array. **c** The associated geometric coincidence efficiency of the BALiN array as a function of θ_{12} and θ_p. **d** Experimental $\theta_{12} - \theta_p$ distribution for near-target breakup events (region (ii) of Fig. 4.15) for $^{8}Be^{2+}$ + $^{208}Pb \rightarrow \alpha + \alpha$ at $E_{^9Be} = 34.0$ MeV

events produced outside the θ_{12} acceptance of BALiN N_{missed} and the total number of events N_{total} produced in that θ_p, such that

$$f_{\text{missed}}(\theta_p) = \frac{N_{\text{missed}}(\theta_p)}{N_{\text{total}}(\theta_p)}. \tag{6.22}$$

Then, the fraction of breakup fragments that could have been captured for each θ_p, $f_{\text{captured}}(\theta_p) = 1 - f_{\text{missed}}(\theta_p)$ constitutes a second efficiency correction. The efficiency term in Eq. 6.12 is the product of the first and second stage efficiency corrections. This factor depends on the full angular distribution of fragments as well as the known (θ_{12}, θ_p) acceptance of BALiN. Simulations with experimentally determined breakup functions $P(R_{\text{min}})$ show that the average correction is small in all instances seen in this thesis.

Two extremes of f_{missed} distributions can be seen in the ^{7}Li + ^{27}Al and ^{9}Be + ^{208}Pb cases, shown in Fig. 6.10a, b, respectively. The grey boxes indicate θ_p outside the acceptance of BALiN where breakup functions are not evaluated (i.e. where the efficiency is zero for all θ_{12}). In the ^{7}Li + ^{27}Al case, f_{missed} is zero for $116° < \theta_p < 156°$, where there is complete θ_{12} coverage, as can be seen in Fig. 6.8d. Between $\theta_p = 64°$ and 156°, f_{missed} is small. However, the correction becomes very large at the most backward and forward θ_p, where BALiN is sensitive to a very limited range

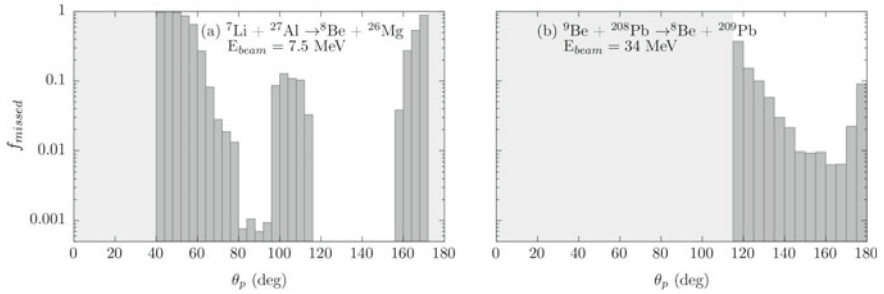

Fig. 6.10 Simulated f_{missed} for $\alpha + \alpha$ fragments produced in reactions of **a** ^{7}Li + ^{27}Al at $E_{\text{lab}} =$ 7.48 MeV in the front-back configuration and **b** ^{9}Be + ^{208}Pb at $E_{\text{lab}} = 34.0$ MeV in the lampshade configuration. θ_p outside the acceptance of BALiN are shown with the light grey shading. Away from the edge of the θ_p acceptance, the correction due to f_{missed} is small in both cases. In panel **a**, f_{missed} goes to zero for $116° < \theta_p < 156°$, where BALiN is sensitive to all θ_{12}

of θ_{12}. In the ^{9}Be + ^{208}Pb case, shown in panel (b), the θ_p coverage of BALiN is much more limited, but f_{missed} is small except for the first and last θ_p bins. θ_p bins where the correction due to f_{missed} is larger than 15% are not included in the final breakup functions. Therefore, while this second-step of the efficiency correction relies on an accurate simulation of breakup, its effects on the breakup functions are modest.

The coincidence efficiencies determined in this work for ^{9}Be + ^{144}Sm, ^{168}Er, ^{186}W, ^{196}Pt, ^{208}Pb and ^{209}Bi differ significantly from those found in the work by Rafiei et al. [5]. In the previous analysis, efficiencies were calculated as a function only of θ_p. However, as seen in Fig. 6.9c, for events with (θ_{12}, θ_p) distribution shown in Fig. 6.9a, the efficiency varies strongly as a function of θ_{12} for fixed θ_p. Efficiency correction as a function of θ_p alone results in an average over correction in the number of breakup pairs for each θ_p by a factor of ∼1.1 in the systems studied in this work (depending on θ_p, target mass and beam energy), compared to the new two-dimensional efficiency correction performed here. The efficiencies further change as the original version PLATYPUS used in Ref. [5] did not have a fully isotropic distribution of initial fragment directions over the breakup sphere: there was an over-abundance of events with similar scattering angles, $\theta_1 \sim \theta_2$, leading to an artificially high efficiency. This was corrected in 2011 [9], and the version of PLATYPUS that was modified for use in this work does distribute points uniformly across the breakup sphere. In addition, the modifications of PLATYPUS performed for this work resulted in a different angular distribution of fragments (and predictions for F_{ICF}) and so changed the model-dependent step of the efficiency corrections.

KOOKABURRA and M-PLATYPUS take the experimentally determined breakup functions as input. Therefore, the efficiency determination described here is iterative. Successive simulations were performed with breakup functions determined from the experimental data and KOOKABURRA and M-PLATYPUS simulations, until the breakup functions converged. In addition to the experimentally determined breakup function, the KOOKABURRA distributions depend on other input parameters that have

to be determined from experiment. Namely, the relative portion of different states in the projectile-like nucleus $\rho_\ell^{J^\pi}(E)$, and the distribution of target-like excitation. However, these quantities depend on the coincidence efficiency, which in turn depend on the simulated KOOKABURRA distributions. These quantities were also determined iteratively, and will be described below.

6.6 Excitation Energy of the Projectile-Like Nucleus

In this thesis, the excitation energy distribution of the projectile-like nucleus above its breakup threshold is modelled as a sum of contributions from different resonances. Using R-matrix theory, the excitation energy probability distributions $\rho_\ell^{J^\pi}(E)$ were shown in Sect. 2.5.2. The projectile-like excitation energy distribution $P_p(E)$ for a given unbound nucleus p is then a weighted sum of all contributing $\rho_\ell^{J^\pi}(E)$. In Chap. 5, comparisons between KOOKABURRA and experiment showed that satisfactory agreement was achieved by the following combinations of $\rho_\ell^{J^\pi}(E)$:

$$P_{^8Be}(E) = W_0\rho_0^{0^+}(E) + W_1\rho_2^{2^+}(E) \tag{6.23}$$

$$P_{^6Li}(E) = W_0\rho_2^{3^+}(E) + W_1\rho_0^{\text{continuum}}(E) \tag{6.24}$$

$$P_{^5Li}(E) = W_0\rho_1^{\frac{3}{2}^-}(E) + W_1\rho_1^{\frac{1}{2}^-}(E). \tag{6.25}$$

W_0 and W_1 are weighting factors such that $W_0 + W_1 = A$, where A is the strength parameter of Eq. 6.19.

This form makes the assumption that the slope μ of the breakup function is the same for different components of $P_p(E)$. In reactions that populate a nucleus with a narrow resonance, such as ^{8}Be and ^{6}Li, $P(R_{\text{min}})$ will be determined for the narrow resonance separately, giving breakup functions for each $\rho_\ell^{J^\pi}(E)$. Thus, no assumption about the slope needs to be made. We will see in Chap. 7 that indeed, the breakup function for these narrow resonances have a different slope to that of the near-target breakup.

However, in the case of reactions forming ^{5}Li, where no narrow resonance is populated, W_0 and W_1 must be determined by finding the values of W_0 and W_1 such that the simulation best matches the experiment. Due to its sensitivity to projectile-like excitation, the comparison between simulation and experiment has been done on the basis of E_{rel}. In Chap. 5, a comparison between experimental and simulated E_{rel} distributions of $\alpha + p$ fragments measured in reactions of ^{7}Li with ^{58}Ni at $E_{\text{beam}} = 11.70$ MeV were shown in Fig. 5.12f. In order to determine the weighting factors W_0 and W_1 of the $\frac{3}{2}^-$ and $\frac{1}{2}^-$ resonances, E_{rel} distributions for each resonance $F^{J^\pi}(E_{\text{rel}})$ were generated after filtering by the acceptance of BALiN and applying cuts and thresholds. Then, there exist some numbers R_0 and R_1 such that

$$F^{\text{combined}}(E_{\text{rel}}) = R_0F^{\frac{3}{2}^-}(E_{\text{rel}}) + R_1F^{\frac{1}{2}^-}(E_{\text{rel}}) \tag{6.26}$$

has the smallest χ^2 fit with respect to the experimentally determined $E_{\rm rel}$ distribution. The ROOT minimisation routine MINUIT was used to minimise χ^2 and find R_0 and R_1. R_0 and R_1 depends on the number of events in the simulated $F^{J^\pi}(E_{\rm rel})$ spectra $N^{J^\pi}_{\rm detected}$ and the efficiency of detecting breakup from that resonance.

The total number of events detected is related to the efficiency and the total number of events that were simulated by $N^{J^\pi}_{\rm total}\epsilon^{J^\pi} = N^{J^\pi}_{\rm detected}$. Making the approximation of a constant distribution of efficiency ϵ^{J^π} for a particular $E^{J^\pi}_{\rm rel}$, $R_{0,1}$ can be related to $W_{0,1}$ by

$$W_0 = \frac{R_0 N^{\frac{3}{2}^-}_{\rm total}}{R_0 N^{\frac{3}{2}^-}_{\rm total} + R_1 N^{\frac{1}{2}^-}_{\rm total}} A \tag{6.27}$$

$$W_1 = \frac{R_1 N^{\frac{1}{2}^-}_{\rm total}}{R_0 N^{\frac{3}{2}^-}_{\rm total} + R_1 N^{\frac{1}{2}^-}_{\rm total}} A. \tag{6.28}$$

As these quantities depend on the input breakup function as well as the coincidence efficiencies (which themselves depend on the input breakup function), the determination of the relative intensities of the different broad resonances contributing to the ^{5}Li excitation is an iterative process. The comparison between KOOKABURRA and experiment shown in Fig. 5.12f uses weighting factors determined using this method. The weighting factors for the states of ^{5}Li were determined in every system at each energy. The population of the higher energy $\frac{1}{2}^-$ state was found to increase with increasing $E_{\rm lab}$, as well as with increasing Z_T. For consistency when propagating to above-barrier energies, the weighting factors from the higher energy fit were adopted in every case.

6.7 Excitation Energy of the Target-Like Nucleus

The target-like recoil excitation energy $E^*_{\rm r}$ distributions used as input for KOOKABURRA and M-PLATYPUS were extracted from the experimental Q distributions, by subtracting the reconstructed Q from Q_{gg} such that,

$$E^*_{\rm r} = Q_{gg} - Q \tag{6.29}$$

The distributions were then binned into ∼200 keV bins,[3] and converted to probability distributions $P(E^*_{\rm r})$ for input into KOOKABURRA and M-PLATYPUS. In doing so, the

[3] In principle, the target-like excitation distribution is a series of (near) delta functions corresponding to levels in the target-like nucleus. However the choice to bin the experimental data was taken for two reasons: firstly, at high target-like excitations, the level density is too high to clearly identify states. Secondly, while the filtering process incorporates broadening due to the pixel size of BALiN, it does not consider the broadening due to energy loss of particles in the target and deadlayers of BALiN. If a single value of $E^*_{\rm r}$ is used, the simulated Q peak is narrower than experiment. To

extent and relative intensity of the excitation energies in the target-like nucleus is realistically modelled in KOOKABURRA and M-PLATYPUS. The measured E_r^* distribution is modified by the coincidence efficiency of BALiN, which is not constant as a function of E_r^*. As the energy carried by the target-like recoiling nucleus increases, the energies of the fragments decrease, and θ_p peaks at more backward angles. As was shown in Sect. 6.5, the efficiency of detecting the fragments depends strongly on θ_p. For example, the efficiency of $\alpha + \alpha$ pairs produced in reactions of ^{9}Be + ^{27}Al at $E_{lab} = 7.48$ MeV increases by a factor of three between $E_r^* = 0$ MeV and $E_r^* = 5$ MeV. Further, energy thresholds and the cuts placed on the simulations to match experiment remove different E_r^* preferentially.

To simulate the same distribution of E_r^* seen in experiment after filtering through the array, the experimentally determined $P^{exp}(E_r^*)$ distribution must be efficiency corrected to reflect the underlying distribution of E_r^*. This efficiency corrected distribution is then used as input into KOOKABURRA and M-PLATYPUS. To determine the input $P^{input}(E_r^*)$ distribution, the experimental distribution is compared to the simulated distribution after filtering (as described in Sect. 5.4.1) $P^{filtered}(E_r^*)$, and a 'E_r^* discrepancy function' $\epsilon_{E_r^*}$ is constructed:

$$\epsilon_{E_r^*} = \frac{P^{filtered}(E_r^*)}{P^{exp}(E_r^*)}. \tag{6.30}$$

This function is then applied as a correction factor to the input $P^{input}(E_r^*)$ distribution to give a new $P^{corrected}(E_r^*)$ distribution

$$P^{corrected}(E_r^*) = \frac{P^{input}(E_r^*)}{\epsilon_{E_r^*}}, \tag{6.31}$$

which is then used in the next iteration of the KOOKABURRA simulation. As the corrected distribution depends on the input distribution, this process is once again iterative, and is repeated until the filtered simulated E_r^* distribution corresponds to the experimental E_r^* distribution.

6.8 Punchthrough Correction

A final factor modifying the measured energy distribution of proton fragments compared to their true distribution is that of punchthrough. In BALiN, protons of energy greater than 7.5 MeV do not deposit their entire energy in the array before exiting the DSSD. As a result, the energy recorded for this particle is lower than reality. This in turn changes the reconstructed quantities such as E_{rel}, θ_p, β, and Q. However, the protons that do punch through are identified as protons by their ToF, so contribute

mock up the removal of events in KOOKABURRA due to the removal of light target impurities in experiment, a Q peak of width that better reproduces experiment is used.

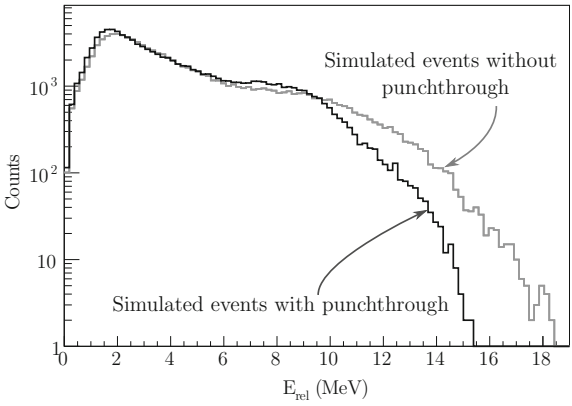

Fig. 6.11 Filtered simulated E_{rel} distribution before and after punchthrough correction for $\alpha + p$ fragments produced in reactions of ^{7}Li with ^{58}Ni at $E_{\mathrm{lab}} = 13.07$ MeV

to the total yield. Without a way to recover the energy of these protons event-by-event (such as with a ΔE telescope, used in Ref. [7]), the effect of punchthrough on the reconstructed kinematic quantities is estimated when filtering KOOKABURRA and M-PLATYPUS simulations.

The energy deposited ΔE by a proton of energy E in the DSSD is estimated by relating the range and energy of the protons, using the method of Ref. [10]. The thickness of the DSSD t is subtracted from the full range of the incident proton in Si (R_1), giving $R_2 = R_1 - t$. The resulting distance, R_2, corresponds to the range of the protons that have energy $E_2 = E - \Delta E$ exiting the DSSD. An energy-range table for protons in Si was generated in SRIM [11], and ΔE in the DSSD was mapped to the incident energy of the protons. The $E - \Delta E$ curve was then fit with a polynomial of order four, and implemented into the filtering of KOOKABURRA prior to the kinematic reconstruction of breakup observables. This method is approximate: all breakup fragments are assumed to enter the DSSDs at an angle normal to the surface (underestimating the energy loss experienced by the fragments), and it does not consider the energy loss of fragments through the inactive layers of BALiN (overestimating the energy loss experienced by the fragments). Nevertheless, as these factors will cancel each other out to some degree, it provides a good estimate of the behaviour of the kinematic observables due to punchthrough. The most important effect is seen in the reconstructed E_{rel} distributions. The filtered simulated E_{rel} distribution of $\alpha + p$ fragments produced in reactions of ^{7}Li with ^{58}Ni at $E_{\mathrm{lab}} = 13.07$ MeV before and after simulation of punchthrough is shown in Fig. 6.11. It is readily apparent that the high E_{rel} tail of the distribution is pushed to smaller E_{rel} when punchthrough is simulated. Including punchthrough effects improve the correspondence between simulation and experiment necessary for fitting the contribution of different resonances described in Sect. 6.6.

6.9 Mapping Breakup Pseudoangle to Rutherford Scattering Angle

The final task in extracting breakup functions is to determine the distance of closest approach R_{min}, which was defined in Eq. 6.2 assuming a Rutherford trajectory as a function of Z_P, Z_T, E_{CM} and Rutherford scattering angle θ_{Ruth}. θ_p and θ_{Ruth} will differ due to the presence of nuclear reactions as well as the fact that θ_p is a reconstructed quantity that will experience distortion from post-breakup acceleration of the fragments. It is therefore necessary to map the reconstructed scattering angle of the unbroken projectile θ_p to the Rutherford angle θ_{Ruth} of the incoming projectile $\theta_p \rightarrow \theta_{\text{Ruth}}$. This can be achieved with M-PLATYPUS and KOOKABURRA simulations. Shown in Fig. 6.12 are examples of the Rutherford scattering angle of the pseudoprojectile derived from the incident trajectory, θ_{Ruth}, plotted against the reconstructed breakup pseudoangle, for (a) M-PLATYPUS simulations of $^{8}\text{Be}(2^{+})$ + $^{207}\text{Pb} \rightarrow \alpha + \alpha + ^{207}\text{Pb}$ at $E_{\text{lab}} = 34$ MeV, (b) at the other extreme in target mass, for KOOKABURRA simulations of $^{7}\text{Li} + ^{27}\text{Al} \rightarrow \alpha + \alpha + ^{26}\text{Mg}$ at $E_{\text{lab}} = 7.48$ MeV and (c) KOOKABURRA simulations of $^{7}\text{Li} + ^{27}\text{Al} \rightarrow \alpha + p + ^{29}\text{Al}$ at $E_{\text{lab}} = 7.48$ MeV. A line of $\theta_p = \theta_{\text{Ruth}}$ has been drawn to guide the eye. The width of the distribution is much broader for the ^{27}Al target for both breakup modes, and the deviations from $\theta_p = \theta_{\text{Ruth}}$ are larger.

In the determination of the breakup functions, the deviations of θ_p from θ_{Ruth} were treated as a correction to θ_p. For each θ_p bin, the median value of the discrepancy between the Rutherford and reconstructed angles was added to θ_p. This correction was larger for breakup that occurs close to the target-like nucleus, and depended on Z_T, projectile and transfer mode. In reactions of ^{9}Be with ^{144}Sm, ^{168}Er, ^{186}W, ^{196}Pt, ^{208}Pb and ^{209}Bi producing $\alpha + \alpha$ pairs, the correction varied from -6° on average for Bi, to -2° for Sm. In reactions of ^{9}Be with ^{28}Si and ^{27}Al producing $\alpha + \alpha$ pairs, the average correction was 3° for ^{28}Si, and 0° for ^{27}Al. Reactions of ^{7}Li with ^{58}Ni, ^{28}Si and ^{27}Al producing $\alpha + \alpha$ pairs gave larger corrections than those for ^{9}Be, and had a stronger θ_p dependence, varying from $\sim 10^{\circ}$ at $\theta_p = 70^{\circ}$ to 1° at $\theta_p = 160^{\circ}$. In reactions with both ^{9}Be and ^{7}Li, the correction for reactions producing $\alpha + p$ pairs were larger and had a stronger θ_p dependence than reactions producing $\alpha + \alpha$ pairs, and ranged from up to 33° at $\theta_p = 70$–5° at $\theta_p = 160^{\circ}$. As a result, while the correction for $\alpha + \alpha$ breakup modes is relatively modest in all targets, the slope of the extracted $\alpha + p$ breakup distributions experience a larger shift. With these corrections determined, all quantities required for the extraction of breakup functions have been found. In the following chapter, the resulting breakup probability functions are presented, and the influence of breakup on above-barrier complete fusion suppression is explored.

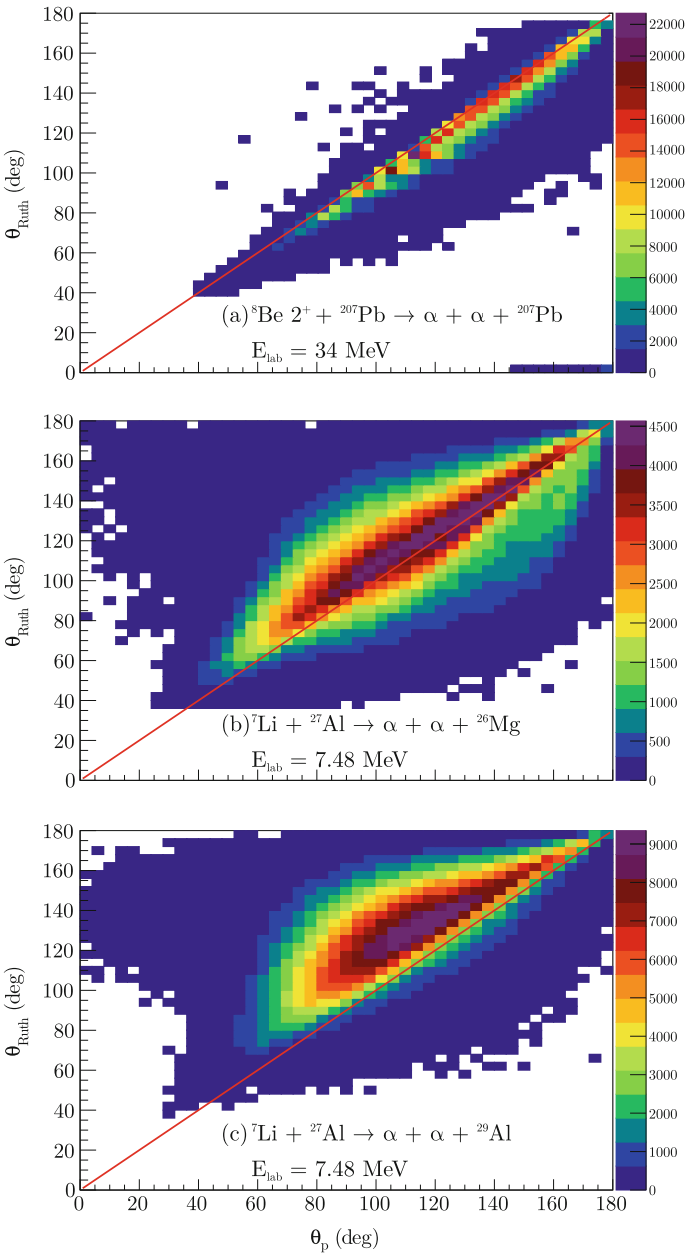

Fig. 6.12 (**a**) M-PLATYPUS simulation for ^{8}Be 2^{+} + ^{208}Pb → $\alpha + \alpha$ at $E_{\text{lab}} = 34$ MeV, demonstrating the relatively small difference between the Rutherford scattering angle of the ^{8}Be pseudo-projectile θ_{Ruth} and the angle θ_p that is reconstructed from the captured α particles. (**b**) At the other extreme in target mass, KOOKABURRA simulations of ^{7}Li + ^{27}Al → $\alpha + \alpha$+^{26}Mg at $E_{\text{lab}} = 7.48$ MeV and (**c**) KOOKABURRA simulations of ^{7}Li + ^{27}Al → $\alpha + p$+^{29}Al at $E_{\text{lab}} = 7.48$ MeV where the deviation of the distribution from $\theta_p = \theta_{\text{Ruth}}$ is larger. In these lighter targets, the distribution of θ_{Ruth} at a given θ_p is much larger. A line of $\theta_p = \theta_{\text{Ruth}}$ has been drawn to guide the eye

References

1. Signorini, C., Andrighetto, A., Guo, J.Y., Ruan, M., Stroe, L., Soramel, F., Löbner, K.E.G., Müller, L., Pierroutsakou, D., Romoli, M., Rudolph, K., Thompson, I., Trotta, M., Vitturi, A.: The potential of the loosely bound ^{9}Be from ^{209}Bi elastic scattering: unusual behaviour at near threshold energy. Nucl. Phys. A **701**, 23c (2002)
2. Parkar, V.V., Jha, V., Pandit, S.K., Santra, S., Kailas, S.: Exploring the breakup and transfer coupling effects in ^{9}Be elastic scattering. Phys. Rev. C **87**(3), 034602 (2013)
3. Yu, N., Zhang, H.Q., Jia, H.M., Zhang, S.T., Ruan, M., Yang, F., Wu, Z.D., Xu, X.X., Bai, C.L.: Unusual potential behaviour for the weakly bound nucleus ^{9}Be in elastic scattering from ^{208}Pb and ^{209}Bi near the threshold. J. Phys. G: Nucl. Part. Phys. **37**(7), 075108 (2010)
4. Zagrebaev, V.I., Denikin, A.S., Alekseev, A.P., Karpov, A.V., Samarin, V.V., Naumenko, M.A., Kozhin, A.Y.: OM Code. Nuclear Reactions Video Project. http://nrv.jinr.ru/nrv/
5. Rafiei, R., du Rietz, R., Luong, D.H., Hinde, D.J., Dasgupta, M., Evers, M., Diaz-torres, A.: Mechanisms and systematics of breakup in reactions of ^{9}Be at near-barrier energies. Phys. Rev. C **81**(2), 024601 (2010)
6. Satchler, G.R.: Introduction to Nuclear Reactions, 2nd edn. Macmillan Educaation, London (1990)
7. Luong, D.H.: Mechanisms and time-scales in breakup of ^{6,7}Li. Ph.D. thesis, Australian National University (2012)
8. Luong, D.H., Dasgupta, M., Hinde, D.J., du Rietz, R., Rafiei, R., Lin, C.J., Evers, M., Diaz-Torres, A.: Predominance of transfer in triggering breakup in sub-barrier reactions of ^{6,7}Li. Phys. Rev. C **88**(3), 34609 (2013)
9. Diaz-Torres, A.: PLATYPUS: A code for reaction dynamics of weakly-bound nuclei at near-barrier energies within a classical dynamical model. Comput. Phys. Commun. **182**(4), 1100 (2011)
10. Knoll, G.F.: Radiation Detection and Measurement, 4th edn. Wiley, New York (2010)
11. Ziegler, J.F.: Stopping Range of Ions in Matter (SRIM-2012). http://www.srim.org/ (2012)

Chapter 7
Mapping Below-Barrier Breakup Probabilities to Above-Barrier Complete Fusion Suppression

Science makes people reach selflessly for truth and objectivity; it teaches people to accept reality, with wonder and admiration, not to mention the deep awe and joy that the natural order of things brings to the true scientist

Lise Meitner 1878–1968

Breakup functions for below-barrier reactions of ^{9}Be with ^{27}Al, ^{28}Si, ^{144}Sm, ^{168}Er, ^{186}W, ^{196}Pt, ^{208}Pb and ^{209}Bi and ^{7}Li with ^{27}Al, ^{28}Si, and ^{58}Ni were extracted using the methods described in the previous chapter. Separate breakup functions for each transfer process in each beam-target combination will be presented and systematic trends will be investigated. These below-barrier breakup functions will be used as input to KOOKABURRA and M- PLATYPUS to predict the contribution of breakup to above-barrier complete fusion suppression. Breakup functions were not extracted for reactions with the ^{16}O, ^{12}C, and d targets, due to concerns about the reliability of the classical dynamical models in these light systems.

7.1 E_{rel} and Q Dependence of Breakup Functions

In Chap. 4, kinematic reconstruction of breakup modes demonstrated that a large range of target- and projectile-like excitations were populated in transfer-triggered breakup. The question is then: is the use of a single, "total" breakup slope for a given breakup mode appropriate, or does the slope vary with target- and projectile-like excitation energy? It may be expected that due to the different binding energies associated with different excitation energies, the transfer probability and therefore the breakup probability may vary. This question may be addressed by extracting breakup functions for individual target-like states in Q, and for different E_{rel} as a proxy for different projectile-like excitations. For long-lived resonances, it is clear that a gate on E_{rel} selects a distinct state in the projectile-like nucleus. For short-lived

K. J. Cook, *Zeptosecond Dynamics of Transfer-Triggered Breakup*,
Springer Theses, https://doi.org/10.1007/978-3-319-96017-3_7

states, by choosing a light target, the post-breakup acceleration is minimised, and $E_{\rm rel}$ remains closer to E_p^*. The extracted $P(R_{\rm min})$ breakup functions, with associated least-squares fits (to Eq. 6.19) are shown in Fig. 7.1a, for different Q bands of $\alpha+\alpha$ fragments with $E_{rel} > 0.4$ MeV measured in neutron-pickup triggered breakup in reactions of ^{9}Be with ^{27}Al at $E_{\rm beam} = 10$ and 8.9 MeV. The Q-$E_{\rm rel}$ spectra for these reactions are shown in Fig. 4.13 and in Appendix C.8. These data were collected with BALiN in the front-back configuration and binned into 9° bins in θ_p and θ_{12}. The breakup probabilities have been offset from each other for clarity, although they do not have the same overall "strength" due to the different population probabilities of the states. It is the slope parameter μ we wish to investigate; if the slope is constant, the breakup strengths can simply be summed. The resulting fitted slope parameters as a function of Q are shown in Fig. 7.1b. Except for the $5.9 < Q < 6.8$ MeV slice, corresponding to the ground-state of ^{28}Al, the slopes are identical within error. The interpretation of this result is not clear. It may be expected that breakup that populates different target-like states at different excitation energy will have different slopes. However, the fact that the breakup slopes are constant across 5 MeV of excitation energy suggests otherwise. This requires further investigation across a variety of targets. From this result, in this thesis, breakup functions are integrated across all excited states in the target-like nuclei.

To examine the effect of excitation energy in the projectile-like nuclei, Fig. 7.1c shows $P(R_{\rm min})$ extracted for different $E_{\rm rel}$ of $\alpha+\alpha$ pairs measured in reactions of ^{9}Be with ^{27}Al $3.4 < Q < 4.7$ MeV. The associated slope parameters are shown in panel (d). The number of counts is relatively low, but the slopes are consistent within error and are consistent with the slopes across all Q shown in panel (b), with the exception of $0 < E_{rel} < 0.5$ MeV, where the slope is significantly shallower. $\alpha+\alpha$ pairs with this $E_{\rm rel}$ correspond to asymptotic breakup through the long-lived 0^+ ground state of ^{8}Be. The higher $E_{\rm rel}$ events arise through the broad 2^+ resonance or the short-lived high excitation energy tail of the 0^+ state. Given this result, where narrow resonances exist (in the breakup of ^{8}Be and ^{6}Li), breakup functions will be extracted for asymptotic and near-target breakup separately.[1]

In the case of the ^{9}Be + ^{144}Sm, ^{168}Er, ^{186}W, ^{196}Pt, ^{208}Pb and ^{209}Bi data, breakup functions were extracted in a re-analysis of Ref. [1] with a view of using the new methods of efficiency correction alongside the essential physics modifications made in M- PLATYPUS to investigate the role of sub-zeptosecond lifetimes in the suppression of complete fusion compared to previous work. Therefore, to provide a valid comparison to Ref. [1], breakup functions were extracted for near-target breakup

[1] KOOKABURRA and M- PLATYPUS take breakup functions for different resonances $\rho_\ell(E_{\rm p}^*)$ (Eq. 2.18) as input. Breakup functions for particular resonances are not necessarily the same as those found by gating on particular narrow peaks. As seen in Fig. 2.5a, b, distributions containing narrow resonances have a "tail" of probability extending to high $E_{\rm p}^*$. By producing breakup functions based on a gate on a narrow resonance, and assigning it to the whole excitation distribution containing the narrow resonance, contributions from the high $E_{\rm p}^*$ tail of that resonance are assigned to the broad resonances. This results in a slightly lower breakup strength for the narrow resonance and a slightly higher breakup strength for the broad resonance. However, given that the high $E_{\rm p}^*$ tail of events is weakly populated compared to the peak this is a fair approximation.

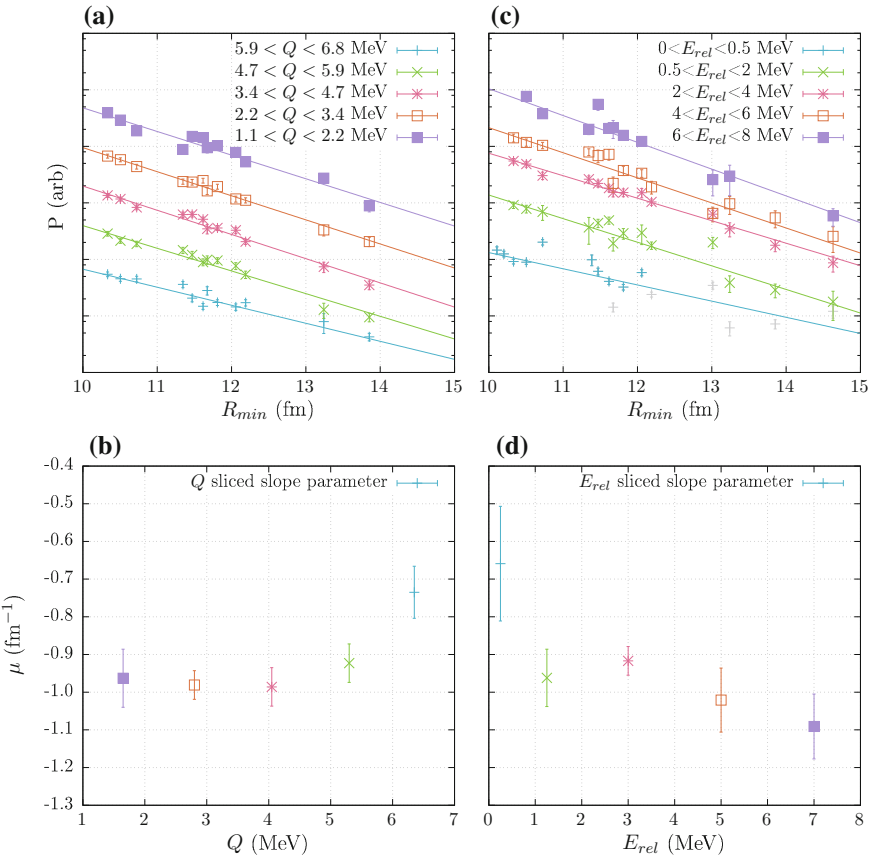

Fig. 7.1 Q (**a**) and E_{rel} (**c**) sliced $P(R_{\mathrm{min}})$ for $\alpha + \alpha$ fragments measured in neutron-pickup triggered breakup in reactions of ^{9}Be with ^{27}Al at $E_{\mathrm{beam}} = 10$ and 8.9 MeV. Grey points have been excluded from the fit, and are discussed in the text. The associated slope parameters are shown in panels **b** and **d**

only, excluding the ^{8}Be ground-state decay. In the ^{58}Ni, ^{28}Si and ^{27}Al systems, total breakup functions will be presented, as well as separate breakup functions for narrow resonances (asymptotic breakup) and broad resonances (near-target breakup).

7.2 ^{9}Be + ^{144}Sm, ^{168}Er, ^{186}W, ^{196}Pt, ^{208}Pb and ^{209}Bi

Near-target breakup probabilities for breakup triggered by neutron-stripping in reactions of ^{9}Be with ^{144}Sm, ^{168}Er, ^{186}W, ^{196}Pt, ^{208}Pb and ^{209}Bi are shown in Fig. 7.2a. The breakup functions have been offset in P from each other for clarity. Each group of points in R_{min} represent measurements with different E_{beam}, which

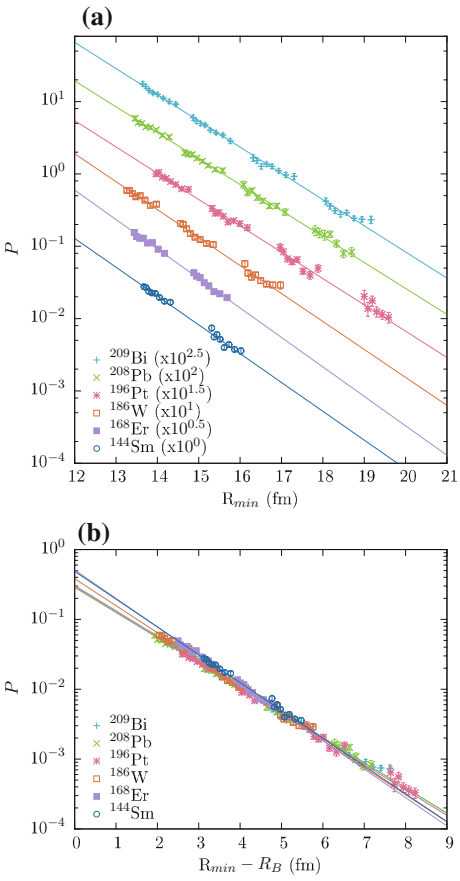

Fig. 7.2 Measured near-target [region (ii) of Fig. 4.15] breakup probabilities for the breakup of ^{8}Be formed following neutron transfer in reactions of ^{9}Be with ^{144}Sm, ^{168}Er, ^{186}W, ^{196}Pt, ^{208}Pb and ^{209}Bi at energies below the barrier **a** as a function of the separation of the centres of the nuclei, where values have been offset for clarity (indicated in the key), and **b** as a function of distance from the projectile-target barrier. Lines represent least-square fits with Eq. 2.58. Errors in P are statistical, and for the most part, are smaller than the symbol size

have been binned in 5° θ_p and θ_{12} bins. A least-squares fit using Eq. 6.20 to the experimental data was performed for each system, indicated by the solid lines in Fig. 7.2. These breakup functions enable comparison to Ref. [1] and are used as input to M- PLATYPUS. However, a perhaps more intuitive way to parameterise breakup probabilities is as a function of the distance of closest approach relative to the barrier radius R_{B}, such that

$$P(R_{\mathrm{min}}) = P(R_{\mathrm{B}})e^{\mu(R_{\mathrm{min}}-R_{\mathrm{B}})}, \tag{7.1}$$

where $P(R_{\mathrm{B}})$ is the probability of breakup along a trajectory that reaches R_{B}, and μ is the same slope parameter as in Eq. 6.20. Unlike the functional forms used as input in KOOKABURRA and PLATYPUS (Eqs. 6.19 and 6.20), this form gives clear physical meaning to the strength parameter $P(R_{\mathrm{B}})$. The barrier radii used here are the R_{B} of the calculated São Paulo potentials between the ^{8}Be pseudoprojectile and

the target-like nucleus.[2] The values of R_B for each system where breakup functions were extracted are listed in Appendix F. The resulting breakup probabilities when cast as a function of barrier separation are shown in Fig. 7.2b. From this, it is apparent that the dependence of breakup probability on the targets is small for reactions of ^{9}Be with ^{144}Sm, ^{168}Er, ^{186}W, ^{196}Pt, ^{208}Pb and ^{209}Bi. Instead, near-target ^{8}Be breakup triggered by neutron stripping is dominantly driven by how close the trajectory comes to $R_{\rm B}$. This agrees with what was found in Ref. [1] for surface separation. The fitted breakup function parameters using both parameterisations are given in Table 7.1. The reported uncertainties in the parameters come from each least-squares fit.

7.3 ^{9}Be + ^{27}Al and ^{28}Si

The breakup probabilities for reactions of ^{9}Be with ^{28}Si and ^{27}Al are shown in Fig. 7.3 as a function of $R_{\rm min}$ (bottom scale) and $R_{\rm min} - R_{\rm B}$ (top scale). The data were extracted from data taken at two energies in the RDUX experimental run, where the BALiN array was placed in the front-back configuration. Bins of width 9° in θ_p and θ_{12} were used. Due to the extended θ coverage of the array compared to the lampshade array, points from the two beam energies overlap and cover a larger range in $R_{\rm min}$ than seen in the ^{9}Be + ^{144}Sm, ^{168}Er, ^{186}W, ^{196}Pt, ^{208}Pb and ^{209}Bi data above. The errors in the breakup probabilities are statistical, with an additional 5% systematic error added, to account for additional uncertainty due to the normalisation process described in Chap. 6. Fits to the breakup probabilities using Eq. 6.19 are shown, and the associated slope and strength parameters are listed in Table 7.1. In some reactions, the breakup probabilities deviated significantly from a global exponential. In the total and near-target $\alpha + \alpha$ probabilities, the probability with the smallest $R_{\rm min}$ at each energy (shown in grey) jumps sharply – this may likely be attributed to an under estimation of the efficiency for events at the edge of the detector. The cause of this is not known – since it is not seen (to the same extent) for $\alpha + \alpha$ breakup (or in $\alpha + d$ breakup, as we will see) – it is likely due to the simulated distribution of fragments in M- PLATYPUS and KOOKABURRA, rather than an incorrect determination of the geometry of BALiN. These points have been excluded from the fit and are shown in grey in Fig. 7.3. Of more concern is the deviation of points from the exponential at large $R_{\rm min}$ seen in asymptotic $\alpha + \alpha$ breakup for ^{9}Be + ^{28}Si [panel (a)] and in $\alpha + p$ breakup for ^{9}Be + ^{27}Al [panel (d)]. The cause of this fall-off is not immediately clear, but they are associated with the most forward-angle events. It may be expected that breakup functions should not follow a global exponential curve, but instead level off at small $R_{\rm min}$, when competition between reaction modes increases. This flattening at small $R_{\rm min}$ has been previously observed, for example for ^{16,18}O,^{19}F + ^{208}Pb [2] and ^{32}S + ^{64}Ni and ^{28}Si + ^{68}Zn [3] transfer reactions. However, that this flattening

[2]For reactions of ^{9}Be with ^{144}Sm to ^{209}Bi targets, a useful parameterisation of $R_{\rm B}$ is $R_{\rm B} = 1.44(A_T^{1/3} + A_P^{1/3})$, which reproduces the SPP calculation of $R_{\rm B}$ to within 0.1 fm.

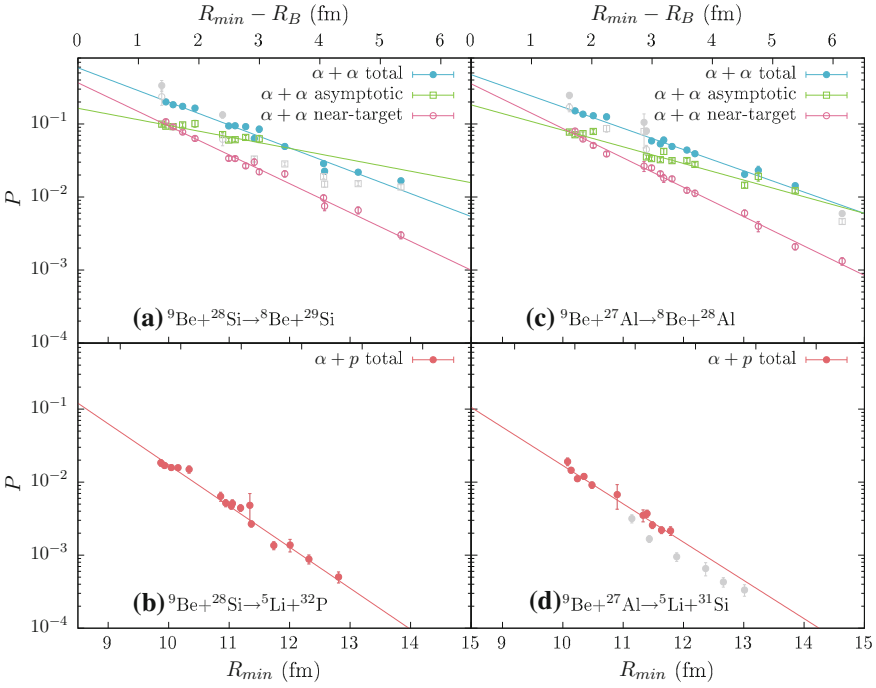

Fig. 7.3 Measured breakup probabilities for reactions induced in collisions of ^{9}Be with ^{28}Si at below-barrier energies of $E_{\text{beam}} = 11.0$ and 10.0 MeV. Probabilities are shown as a function of distance of closest approach (bottom scale) and distance from the projectile-target barrier ($R_{\text{B}} = 8.5$ fm and $R_{\text{B}} = 8.48$ fm for ^{28}Si and ^{27}Al, respectively) (top scale). Lines represent least-squares fit to the data with Eq. 6.19, and the fit parameters are given in Table 7.1. Errors in P are statistical with an additional estimated 5% systematic error, and for the most part, are smaller than the symbol size. Points that have been excluded from the fit are shown in grey. Their origin is discussed in the text. Neutron stripping forming ^{8}Be is shown in **a** and three-neutron one-proton stripping forming ^{5}Li in **b**. Breakup probabilities for collisions of ^{9}Be with ^{27}Al at energies of $E_{\text{beam}} = 10.0$ and 8.9 MeV for the same reaction modes are shown in panels **c** and **d**. In reactions forming ^{8}Be, the total breakup probability (filled circles) is shown, along with the probabilities for asymptotic breakup (open squares) and near-target breakup (open circles). In reactions forming ^{5}Li, all breakup occurs close to the target, and thus only the total breakup probability is shown

is not universally seen in these breakup functions casts doubt on the validity of this conclusion for these data, and an unknown factor influencing the efficiency cannot be excluded. As the probability at small R_{min} is the quantity of relevance to above-barrier complete fusion suppression, when the probabilities deviated from a global exponential, the fit was made to small R_{min}.

The near-target and asymptotic breakup probabilities for neutron stripping triggered breakup of ^{8}Be after reactions of ^{9}Be with ^{28}Si and with ^{27}Al, shown in Fig. 7.3a, c, respectively, are very similar. As noted in Chap. 4, the reconstructed Q for this mode are very similar in the two systems, due to the fact that the transferred neutron fills the same n levels in ^{29}Si and ^{28}Al. It was also observed in Chap. 4 that

the yield from asymptotic breakup from the 0^+ ground-state of ^{8}Be was much greater than that from near-target breakup. This is reflected in the breakup probabilities, but the slopes are very different. While asymptotic breakup has a fairly shallow fall-off with R_{min}, the fall-off of near-target breakup is much steeper, and the measured probabilities overlap at $R_{\text{min}} \approx 10$ fm. As a result, while asymptotic breakup is the most significant contribution to the total $\alpha + \alpha$ yield at below-barrier energies (large R_{min}), near-target breakup becomes the dominant breakup mode at above-barrier energies (small R_{min}). This highlights the importance of extracting quantitative measures of breakup probabilities: this cannot be seen in the below-barrier Q-E_{rel} spectra shown in Chap. 4.

The breakup probabilities for $\alpha + p$ pairs produced in reactions of ^{9}Be with ^{28}Si and ^{27}Al, shown in panels (b) and (d) of Fig. 7.3 are also fairly similar. This is not as easily explained as the $\alpha + \alpha$ case. While the three transferred neutrons fill the same levels, the transferred proton does not. In addition, the Q-values for these reactions are rather different, as are the density of states in the target-like nuclei at low excitation energies. These factors are reflected in the different Q spectra for these events, shown in Appendix D. While the probability for $\alpha + p$ production is weak compared to $\alpha + \alpha$ production, the breakup functions are very steep, and so will contribute to above-barrier ICF cross-sections.

7.4 ^{7}Li + ^{27}Al, ^{28}Si and ^{58}Ni

Breakup probabilities for reactions of ^{7}Li with ^{58}Ni at energies of $E_{\text{beam}} = 13.10$ MeV and 11.70 MeV are shown in Fig. 7.4 for (a) proton pickup forming ^{8}Be, (b) neutron stripping forming ^{6}Li and (c) two neutron stripping forming ^{5}Li. The extracted breakup functions for reactions of ^{7}Li with ^{28}Si and ^{27}Al are shown in Fig. 7.5 for (a) proton pickup forming ^{8}Be and (b) two neutron stripping forming ^{5}Li. Fits to the breakup probabilities using Eq. 6.19 are shown, and the slope and strength parameters listed in Table 7.1. In these measurements, the higher energy data set was taken in the 2014 LIAL run, and the lower energy in the 2015 RDUX run. The fact that these breakup probabilities fall on one exponential curve gives confidence in the different normalisation factors for these two experiments, described in Chap. 6.

Unlike the reactions with ^{9}Be, near-target breakup of ^{8}Be is by far the dominant mode of $\alpha + \alpha$ breakup for all R_{min} in ^{7}Li induced reactions. For both projectiles, and for all targets, we see that the asymptotic $\alpha + \alpha$ breakup functions are shallower than near-target $\alpha + \alpha$ breakup. This is also seen in $\alpha + d$ breakup induced by ^{7}Li + ^{58}Ni collisions, shown in Fig. 7.4, where breakup occurring through the long-lived 3^+ state of ^{6}Li has a shallower slope than the (weak) near-target component. As with reactions induced by ^{9}Be, the breakup function associated with $\alpha + p$ pairs is the steepest of all the breakup modes.

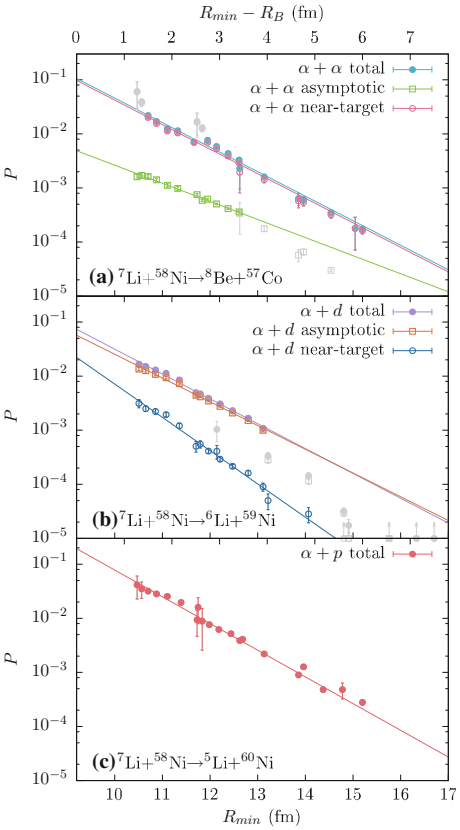

Fig. 7.4 Measured breakup probabilities for reactions induced in collisions of ^{7}Li and ^{58}Ni at below-barrier energies of $E_{\text{beam}} = 13.10$ and 11.70 MeV. Probabilities are shown as a function of distance of closest approach (bottom scale) and distance from the projectile-target barrier ($R_{\text{B}} = 9.2$ fm) (top scale). Where long-lived resonances are populated, such as in proton pickup forming ^{8}Be (**a**) or in neutron stripping forming ^{6}Li (**b**), breakup probabilities have been determined for the total yield (filled circles), the breakup populating the narrow resonance (open squares) and the near-target breakup (open circles). In two neutron stripping reactions forming ^{5}Li (**c**), no narrow resonances are populated, so the total breakup function is presented. Lines represent least-squares fit to the data with Eq. 6.19, and the fit parameters are shown in Table 7.1. Errors in P are statistical with an additional estimated 5% systematic error, and for the most part, are smaller than the symbol size. Points that have been excluded from the fit are shown in grey. Their origin is discussed in the text

The shallower slope of asymptotic breakup compared to prompt breakup may be explained in a classical picture by the lower excitation energy required to populate the long-lived ^{8}Be 0^+ and ^{6}Li 3^+ states compared to the short-lived states at higher excitation energies that result in near-target breakup. The lower excitation energy means that the state may be populated at larger projectile-target separations, resulting

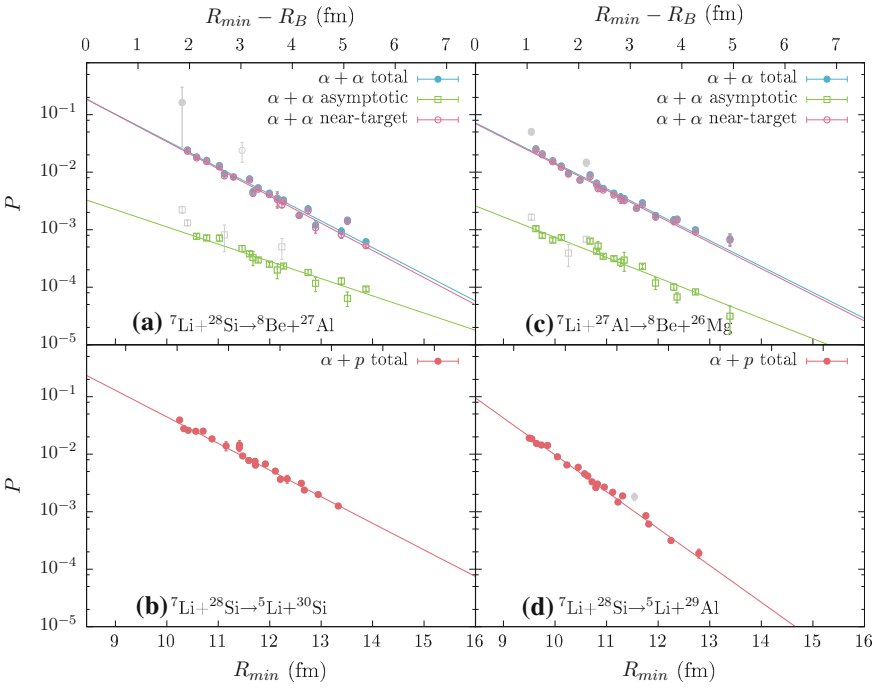

Fig. 7.5 Measured breakup probabilities for reactions induced in collisions of ^{7}Li with ^{28}Si at below-barrier energies of $E_{\text{beam}} = 7.50$ and 6.75 MeV for neutron stripping forming ^{8}Be (**a**) and three-neutron one-proton stripping forming ^{5}Li (**b**). Breakup probabilities for collisions of ^{9}Be with ^{27}Al at energies of $E_{\text{beam}} = 7.50$ and 6.75 MeV for the same reaction modes are shown in panels **c** and **d**. In reactions forming ^{8}Be, the total breakup probability (filled circles) is shown, along with the probabilities for asymptotic breakup (open squares) and near-target breakup (open circles). In reactions forming ^{5}Li, all breakup occurs close to the target, and thus the total breakup probability is shown. Probabilities are shown as a function of distance of closest approach (bottom scale) and distance from the projectile-target barrier ($R_{\text{B}} = 8.44$ fm and $R_{\text{B}} = 8.46$ fm for ^{28}Si and ^{27}Al, respectively) (top scale). Lines represent least-squares fit to the data with Eq. 6.19, and the fit parameters are shown in Table 7.1. Errors in P are statistical with an additional estimated 5% systematic error, and for the most part, are smaller than the symbol size. Points that have been excluded from the fit are shown in grey. Their origin is discussed in the text

in a shallower fall-off in breakup probability. In addition, effects of optimal Q-value and binding energies may be expected to influence the slope of the breakup function for different states of projectile-like nuclei, but the magnitude and direction of these effects will change with the transfer mode. It would be interesting to investigate the change in slope with excitation energy for a nucleus that is populated in multiple narrow resonances.

Table 7.1 Total, near-target and prompt breakup function parameters determined through least-squares fits to the experimental data shown in Figs. 7.2, 7.3, 7.4 and 7.5 for the systems studied in this work. For convenience, all breakup strength parameters, ν, A and $P(R_B)$ have been provided. Errors represent statistical uncertainty in each least-squares fit

				μ (fm^{-1})	ν	A	$P(R_B)$
^{9}Be	^{209}Bi	$\alpha+\alpha$	NT	-0.83 ± 0.01	8.4 ± 0.1	4600 ± 600	0.33 ± 0.01
	^{208}Pb	$\alpha+\alpha$	NT	-0.83 ± 0.01	8.3 ± 0.2	3900 ± 500	0.31 ± 0.01
	^{196}Pt	$\alpha+\alpha$	NT	-0.84 ± 0.01	8.3 ± 0.2	4000 ± 700	0.32 ± 0.02
	^{186}W	$\alpha+\alpha$	NT	-0.89 ± 0.01	9.0 ± 0.2	8300 ± 1600	0.42 ± 0.02
	^{168}Er	$\alpha+\alpha$	NT	-0.94 ± 0.02	9.6 ± 0.3	15000 ± 3400	0.56 ± 0.03
	^{144}Sm	$\alpha+\alpha$	NT	-0.92 ± 0.02	9.0 ± 0.3	7700 ± 2500	0.54 ± 0.05
	^{28}Si	$\alpha+\alpha$	T	-0.72 ± 0.03	5.6 ± 0.4	270 ± 90	0.59 ± 0.06
			NT	-0.91 ± 0.03	6.7 ± 0.3	800 ± 300	0.37 ± 0.03
			A	-0.36 ± 0.05	1.3 ± 0.5	4 ± 2	0.16 ± 0.01
		$\alpha+p$	T	-1.30 ± 0.05	8.9 ± 0.5	7000 ± 4000	0.12 ± 0.01
	^{27}Al	$\alpha+\alpha$	T	-0.67 ± 0.02	4.9 ± 0.2	140 ± 30	0.47 ± 0.03
			NT	-0.93 ± 0.02	6.8 ± 0.2	900 ± 200	0.35 ± 0.02
			A	-0.52 ± 0.03	2.7 ± 0.4	15.6 ± 0.5	0.18 ± 0.02
		$\alpha+p$	T	-1.21 ± 0.06	7.9 ± 0.6	3000 ± 2000	0.11 ± 0.01
^{7}Li	^{58}Ni	$\alpha+\alpha$	T	-1.04 ± 0.03	7.4 ± 0.4	1600 ± 600	0.10 ± 0.1
			NT	-1.05 ± 0.03	7.3 ± 0.4	1500 ± 600	0.097 ± 0.009
			A	-0.77 ± 0.03	1.8 ± 0.3	6 ± 2	0.0049 ± 0.0004
		$\alpha+d$	T	-1.06 ± 0.03	7.1 ± 0.3	1200 ± 400	0.073 ± 0.004
			NT	-1.42 ± 0.05	9.2 ± 0.6	10000 ± 6000	0.022 ± 0.003
			A	-1.01 ± 0.02	6.4 ± 0.2	600 ± 200	0.057 ± 0.003
		$\alpha+p$	T	-1.14 ± 0.02	8.8 ± 0.3	7000 ± 2000	0.19 ± 0.01
	^{28}Si	$\alpha+\alpha$	T	-1.07 ± 0.04	7.3 ± 0.5	1600 ± 700	0.19 ± 0.02
			NT	-1.09 ± 0.04	7.5 ± 0.4	1800 ± 800	0.18 ± 0.02
			A	-0.69 ± 0.04	0.1 ± 0.5	1.10 ± 0.70	0.003 ± 0.0005
		$\alpha+p$	T	-1.06 ± 0.03	7.5 ± 0.3	1800 ± 600	0.23 ± 0.02
	^{27}Al	$\alpha+\alpha$	T	-1.04 ± 0.03	6.2 ± 0.4	500 ± 200	0.072 ± 0.007
			NT	-1.05 ± 0.04	6.2 ± 0.4	500 ± 200	0.070 ± 0.006
			A	-0.81 ± 0.04	0.9 ± 0.5	2 ± 1	0.0026 ± 0.0003
		$\alpha+p$	T	-1.48 ± 0.03	10.1 ± 0.3	25000 ± 8000	0.095 ± 0.007

7.5 Trends of Below-Barrier Breakup

By examining the fitted probabilities of breakup at the barrier $P(R_B)$ and the breakup slope μ, trends in the breakup functions can be examined. The total probability of near-target breakup at the barrier for ^{9}Be reactions, shown in Fig 7.6a, shows no clear trend. In general, the prompt $\alpha + \alpha$ $P(R_B)$ is fairly constant, except for reactions with ^{168}Er and ^{144}Sm, where $P(R_B) \sim 0.55$ is very large. In reactions of ^{9}Be with ^{28}Si and ^{27}Al, ^{5}Li$\rightarrow \alpha + p$ breakup contributes significantly to the probability of prompt breakup at the barrier. As expected from the breakup functions, the near-target $P(R_B)$ for reactions of ^{9}Be with ^{27}Al and ^{28}Si are very similar. The prompt breakup probabilities for reactions of ^{7}Li with ^{58}Ni, ^{28}Si and ^{27}Al, shown in panel (b) of Fig. 7.6 vary significantly from target to target, and is very large for reactions with ^{28}Si.

It is not clear that in either the case of ^{9}Be or ^{7}Li that there should be any clear trend of $P(R_B)$ with Z_T. Since these breakup processes are triggered by transfer, they should be consistent with the probabilities of transfer, which will be complicated by factors such as the transfer Q, Q_{opt}, and the structure of both the projectile and target.

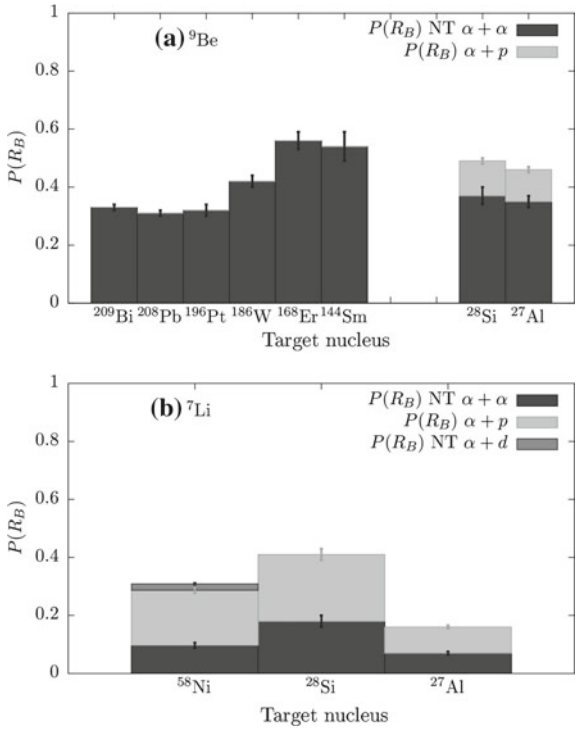

Fig. 7.6 Probabilities of near-target breakup at R_B determined using extrapolations of the exponential fits to the breakup probabilities tabulated in Table 7.1 for **a** reactions of ^{9}Be with ^{144}Sm to ^{209}Bi, ^{28}Si and ^{27}Al and for **b** reactions of ^{7}Li with ^{58}Ni, ^{28}Si and ^{27}Al. Uncertainties in $P(R_B)$ arise from the statistical uncertainty in the fitted breakup functions

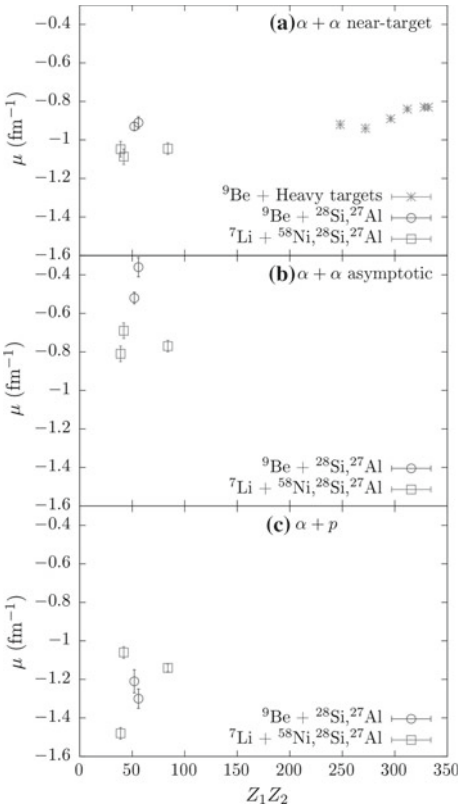

Fig. 7.7 Fitted slope parameters for near-target $\alpha+\alpha$ breakup (**a**), asymptotic $\alpha+\alpha$ breakup (**b**) and $\alpha+p$ breakup (**c**). Reactions of ^{9}Be with targets of ^{144}Sm to ^{209}Bi are shown by red asterisks, and reactions of ^{9}Be with ^{28}Si and ^{27}Al are shown with open blue circles. Reactions of ^{7}Li are shown with open green squares. Error bars represent the statistical uncertainty in the fit

Breakup probabilities for intermediate mass targets (and heavy targets in the case of ^{7}Li) will be useful to elucidate any trends due to Z_T or transfer Q-value present.

The slopes of the breakup functions as a function of $Z_P Z_T$ are shown in Fig. 7.7. In general, no clear trend with $Z_P Z_T$ is evident. Near-target $\alpha+\alpha$ breakup is shown in panel (a). In reactions with ^{9}Be, all slopes lie between -0.83 and $-0.94\,\text{fm}^{-1}$, and are fairly flat below $Z_T = 68$. In reactions of ^{9}Be with ^{144}Sm, ^{168}Er, ^{186}W, ^{196}Pt, ^{208}Pb and ^{209}Bi alone, there is a slight negative slope (line of best fit $\mu = 0.005 Z_T - 1.272$, shown in Fig. 7.8). It is evident that this trend does not continue to small $Z_P Z_T$. Once again, data for intermediate mass targets will prove useful. For reactions with ^{7}Li, once again there is no clear trend in $Z_P Z_T$ in the range of Z_T studied here. The asymptotic $\alpha+\alpha$ breakup slope parameters, shown in panel (b), are uniformly shallower than their near-target counterparts, as discussed above. The slopes for reactions with ^{9}Be are steeper than those with ^{7}Li and show more scatter. This may be partly due to the relatively large scatter in breakup probability seen for asymptotic $\alpha+\alpha$ breakup compared to other breakup modes. On the other hand,

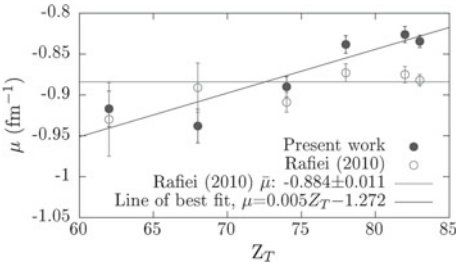

Fig. 7.8 Filled circles: Slope parameters μ (fm^{-1}) derived from least-squares fits to the experimental data shown in Fig. 7.2b, fit with $P(R_{\rm min}) = P(R_{\rm B})e^{\mu(R_{\rm min}-R_{\rm B})}$, There is a slight Z_T dependence on the slope, indicated by the line of best fit $\mu = 0.005Z_T - 1.272$. Open circles show results from Ref. [1], which have mean slope $\bar{\mu} = -0.884 \pm 0.011$ (red line). The reasons for the discrepancies between the present and previous work are discussed in the text

the slope parameters for $\alpha + p$ pairs produced in ^{7}Li or ^{9}Be induced reactions show no clear dependence on the projectile. This is perhaps unexpected, considering the rather different reactions that produce ^{5}Li in reactions with ^{7}Li compared to with ^{9}Be.

The breakup functions found for near-target $\alpha + \alpha$ breakup include a re-analysis of the work of Ref. [1], and so a brief comparison is appropriate. The parameters μ and $P(R_{\rm B})$ of the breakup functions are shown as a function of Z_T in Fig. 7.8. Unlike those found in Ref. [1], there is a fairly weak Z_T dependence on the fitted slope parameters – a line of best fit yields $\alpha = 0.005Z_T - 1.272$. However, as we have seen, this slope does not continue to lower Z_T.

While the breakup functions derived in this work are comparable to those found by Rafiei et al. [1], there is an average increase in the probability of breakup by a factor of 1.14 ± 0.09 at $R_{\rm min} - R_{\rm B} = 4$ fm. These differences result from the combined effects of several factors that have been discussed previously, but are summarised here: (i) the Rutherford scattering yield in the normalisation bin for every measurement is a factor of 0.921 ± 0.009 lower due to slight refinement in the actual position of the BALiN array, (ii) the coincidence efficiency of these $\alpha - \alpha$ pairs calculated using PLATYPUS with respect to θ_{12} is different to that deduced in the previous work, and has a different Z_T and $E_{\rm beam}$ dependence, and (iii) correcting for coincidence efficiency produces an efficiency corrected yield over all azimuthal angles, and the calculation of the Rutherford yield must reflect this, as discussed above. As seen in Fig. 7.8, the slope, μ, of the breakup function becomes shallower with increasing Z_T. The difference in average slope from the previous work is primarily driven by the two-dimensional coincidence efficiency correction used in this work.

Given these new breakup functions, the next step is then to determine the impact of breakup on complete and incomplete fusion cross-sections ($\sigma_{\rm CF}$ and $\sigma_{\rm ICF}$, respectively) with M- PLATYPUS and KOOKABURRA.

7.6 Characterising Fusion Suppression

There have been two major approaches towards characterising fusion suppression in collisions with weakly-bound nuclei. The first is through comparing measured above-barrier complete fusion cross-sections to coupled-channels predictions of fusion cross-sections $\sigma_{\mathrm{CF}}^{\mathrm{expt.}}/\sigma_{\mathrm{fus.}}^{\mathrm{calc.}}$ (e.g. [4–8]). This approach relies on accurate determination of the average barrier energy [5] and is somewhat model dependent [9]. The second approach equates fusion suppression to the ratio of incomplete fusion to total fusion $F_{\mathrm{ICF}} = \frac{\sigma_{\mathrm{ICF}}}{\sigma_{\mathrm{ICF}}+\sigma_{\mathrm{CF}}}$. Incomplete fusion is defined experimentally as capture of only part of the charge of the projectile. Measurements have found similar values for $(1\text{-}\sigma_{\mathrm{CF}}^{\mathrm{expt.}}/\sigma_{\mathrm{fus.}}^{\mathrm{calc.}})$ and F_{ICF} [4]. As such, F_{ICF} is thought to provide an indirect measure of fusion suppression that is model independent.

When trying to understand the role of breakup in the observed suppressions of complete fusion, it has been conjectured that σ_{ICF} (and thus F_{ICF}) is entirely due to breakup of the weakly-bound nucleus followed by capture of one of the fragments. However, it is very difficult to separate breakup followed by capture of one of the fragments from a transfer process forming the same nucleus. This is a particular problem for light projectiles, where it is far from clear that transfer and ICF are distinguishable at all. If transfer comprises a large fraction of σ_{ICF}, F_{ICF} cannot be attributed solely to breakup. Further, $\sigma_{\mathrm{ICF}}+\sigma_{\mathrm{CF}}$ can no longer be interpreted as the total fusion cross-section for these light projectiles. In the case of ^{7}Li + ^{165}Ho, exclusive measurements of γ-rays and charged fragments favour the interpretation that σ_{ICF} is predominantly due to breakup [10]. While the interpretation of σ_{ICF} is ambiguous experimentally, it is clear within a classical model. By using M- PLATYPUS or KOOKABURRA, the contribution of breakup to F_{ICF} can be estimated.

7.7 Calculating Above-Barrier Fusion Cross-Sections

M- PLATYPUS and KOOKABURRA are designed to provide predictions of σ_{CF} and σ_{ICF} at energies above the barrier, through the use of the experimentally determined breakup functions, applied at above-barrier energies. In the models, ICF is assumed to occur when a breakup fragment passes inside a critical radius, while CF occurs when either the unbroken projectile or both breakup fragments pass that same radius. In M- PLATYPUS, that radius is taken to be the barrier radius R_{B} [11], while in KOOKABURRA, fusion only occurs after nuclei pass $1.1r_0$, where r_0 is the radius parameter of the Woods-Saxon potential [12]. Calculations were performed using the near-target breakup functions determined from the least-squares fit to the below-barrier experimental data, which have parameters as shown in Table 7.1. Nuclear potentials were calculated using the São Paulo potential [13].

KOOKABURRA allows multiple breakup modes to be simulated simultaneously. This allowed "one-shot" simulations of breakup arising through both the 0^+ and 2^+ states of ^{8}Be as well as through the $\frac{1}{2}^-$ and $\frac{3}{2}^-$ states of ^{5}Li, and the 3^+ and continuum states of ^{6}Li, calculated in Sect. 2.5.2. In order to determine the relative strengths of the 0^+ and 2^+ states for ^{8}Be breakup, an approximation that the long-lived 0^+ peak comprises the entire strength of the 0^+ resonance was made. In fact, according to the calculations made in Sect. 2.5.2, it comprises ~85% of the total strength, making this assumption fairly reasonable. Likewise, the near-target yield was attributed to the 2^+ state in ^{8}Be. Similarly, in $\alpha + d$ breakup, the assumption was made that the long-lived 3^+ resonance comprised the entirety of the 3^+ contribution, and the short-lived tail was attributed to continuum breakup in other partial waves. The relative strengths of the $\frac{1}{2}^-$ and $\frac{3}{2}^-$ states in ^{5}Li were those found by the χ^2 fit to the $E_{\rm rel}$ distribution, described in Sect. 6.6 at the highest measured energy. In reactions of ^{9}Be + ^{28}Si, ^{27}Al and ^{7}Li + ^{58}Ni, ^{28}Si, ^{27}Al, KOOKABURRA was used to predict above-barrier ICF and CF. Simulations were performed for impact parameters up to $b = 18$ fm, with 2×10^6 breakup events simulated in total.

Calculations were made for ^{9}Be + ^{144}Sm, ^{168}Er, ^{186}W, ^{196}Pt, ^{208}Pb and ^{209}Bi reactions using M- PLATYPUS, and were performed for partial waves up to up to $100\hbar$, with 2×10^5 breakup events simulated in total. In these cases, the yield of near-target transfer-triggered breakup was attributed exclusively to breakup of the 2^+ resonance in ^{8}Be, and thus the modelled excitation energies and lifetimes of the ^{8}Be projectile were that of the 2^+ state, as shown in Fig. 2.5. Near-target breakup of ^{8}Be, in addition to arising from the 2^+ state, should have some contribution from the high excitation energy tail of the 0^+ state. Test calculations suggest that this contribution should be expected to *decrease* the overall suppression of complete fusion arising from near-target transfer-triggered breakup, as the average excitation energy of the high-energy tail of the 0^+ state is lower than that of the 2^+ state, and so the lifetimes longer, as can be seen in Fig. 2.5.

The reaction channels simulated in the KOOKABURRA and M- PLATYPUS simulations are shown in Table 7.2. To ensure that the two models give equivalent results, KOOKABURRA and M- PLATYPUS calculations were performed for reactions of ^{9}Be + ^{208}Pb under the same conditions. The resulting F_{ICF} differ by less than 0.4%.

Energies were chosen in $0.05V_B$ steps from $1.05-1.30V_B$, consistent with previous work [1]. Over the energy range of $1.05-1.30V_B$, F_{ICF} is energy dependent. The results from each energy step have been averaged to give an F_{ICF} value for each system, to compare to previous work, and to experimental measures. The energy dependence of F_{ICF} was not consistent across the systems studied in this thesis. The most extreme changes were seen in the ^{9}Be + ^{144}Sm, ^{168}Er, ^{186}W, ^{196}Pt, ^{208}Pb and ^{209}Bi systems, where F_{ICF} varies by a factor of two for each reaction, from $F_{ICF} = 0.16$ at $1.05V_B$ to 0.08 at $1.30V_B$ on average. Further study is required to understand these trends.

Table 7.2 List of reaction channels processed using M- PLATYPUS and KOOKABURRA, labelled by their reaction outcomes. CF indicates complete fusion, SCF indicates complete fusion following sequential capture of both breakup fragments, ICF indicates incomplete fusion, and NCBU indicates no capture breakup

Beam + Target	Primary reaction		Reaction Product(s)	Outcome
^{9}Be + ^{209}Bi§	^{8}Be + ^{210}Bi	→	^{218}Fr	CF
		→	^{218}Fr	SCF
		→	^{214}At + α	ICF
		→	^{210}Bi+ $\alpha + \alpha$	NCBU
^{9}Be + ^{208}Pb§	^{8}Be + ^{209}Pb	→	^{217}Rn	CF
		→	^{217}Rn	SCF
		→	^{213}Po + α	ICF
		→	^{209}Pb + $\alpha + \alpha$	NCBU
^{9}Be + ^{196}Pt§	^{8}Be + ^{197}Pt	→	^{205}Pb	CF
		→	^{205}Pb	SCF
		→	^{201}Hg + α	ICF
		→	^{197}Pt + $\alpha + \alpha$	NCBU
^{9}Be + ^{186}W§	^{8}Be + ^{187}W	→	^{195}Pt	CF
		→	^{195}Pt	SCF
		→	^{191}Os + α	ICF
		→	^{187}W + $\alpha + \alpha$	NCBU
^{9}Be + ^{168}Er§	^{8}Be + ^{169}Er	→	^{177}Hf	CF
		→	^{177}Hf	SCF
		→	^{173}Yb + α	ICF
^{9}Be + ^{144}Sm§	^{8}Be + ^{145}Sm	→	^{169}Er + $\alpha + \alpha$	NCBU
		→	^{153}Dy	CF
		→	^{153}Dy	SCF
		→	^{149}Gd + α	ICF
		→	^{145}Sm + $\alpha + \alpha$	NCBU
^{9}Be + ^{28}Si	Complete fusion		^{37}Ar	CF
	^{28}Si(^{9}Be,^{8}Be)^{29}Si	→	^{37}Ar	CF
		→	^{37}Ar	SCF
		→	^{33}S + α	ICF
		→	^{29}Si + $\alpha + \alpha$	NCBU
	^{28}Si(^{9}Be,^{5}Li)^{32}P	→	^{37}Ar	CF
		→	^{37}Ar	SCF
		→	^{33}S + α	ICF
		→	^{36}Cl + p	ICF
		→	^{32}P + $\alpha + p$	NCBU
^{9}Be + ^{27}Al	Complete fusion		^{36}Cl	CF
	^{27}Al(^{9}Be,^{8}Be)^{28}Al	→	^{36}Cl	CF
		→	^{36}Cl	SCF
		→	^{32}P + α	ICF
		→	^{28}Al + $\alpha + \alpha$	NCBU

Table 7.2 (continued)

Beam + Target	Transfer reaction		Final reaction	Outcome
	^{28}Si(^{9}Be,^{5}Li)^{31}Si	→	^{36}Cl	CF
		→	^{36}Cl	SCF
		→	^{32}P + α	ICF
		→	^{35}S + p	ICF
		→	^{31}S + $\alpha + p$	NCBU
^{7}Li + ^{58}Ni	Complete fusion		^{65}Ga	CF
	^{58}Ni(^{7}Li,^{8}Be)^{57}Co	→	^{65}Ga	CF
		→	^{65}Ga	SCF
		→	^{61}Cu + α	ICF
		→	^{57}Co + $\alpha + \alpha$	NCBU
	^{58}Ni(^{7}Li,^{6}Li)^{59}Ni	→	^{65}Ga	CF
		→	^{65}Ga	SCF
		→	^{61}Cu + α	ICF
		→	^{63}Zn + d	ICF
		→	^{59}Ni	NCBU
	^{58}Ni(^{7}Li,^{5}Li)^{60}Ni	→	^{65}Ga	CF
		→	^{65}Ga	SCF
		→	^{61}Cu + α	ICF
		→	^{64}Zn + p	ICF
		→	^{60}Ni + $\alpha + p$	NCBU
^{7}Li + ^{28}Si	Complete fusion		^{35}Cl	CF
	^{28}Si(^{7}Li,^{8}Be)^{27}Al	→	^{35}Cl	CF
		→	^{35}Cl	SCF
		→	^{31}P + α	ICF
		→	^{27}Al + $\alpha + \alpha$	NCBU
	^{28}Si(^{7}Li,^{5}Li)^{30}Si	→	^{35}Cl	CF
		→	^{35}Cl	SCF
		→	^{31}P + α	ICF
		→	^{34}S + p	ICF
		→	^{30}Si +$\alpha + p$	NCBU
^{7}Li + ^{27}Al	Complete fusion		^{34}P	CF
	^{27}Al(^{7}Li,^{8}Be)^{26}Mg	→	^{26}Mg(^{8}Be,γ)^{34}P	CF
		→	^{34}P	SCF
		→	^{30}Si + α	ICF
		→	^{26}Mg + $\alpha + \alpha$	NCBU
	^{28}Si(^{7}Li,^{5}Li)^{30}Si	→	^{34}P	CF
		→	^{34}P	SCF
		→	^{30}Si + α	ICF
		→	^{33}P + p	ICF
		→	^{30}Si + $\alpha + p$	NCBU

§As M- PLATYPUS does not simulate transfer, a pseudoprojectile of ^{8}Be is used
†Transfer-triggered breakup followed by capture of both fragments is indistinguishable from complete fusion

7.8 ICF and CF in ^{9}Be + ^{144}Sm, ^{168}Er, ^{186}W, ^{196}Pt, ^{208}Pb and ^{209}Bi

We begin with a discussion of the results of the M- PLATYPUS predictions for above-barrier $\sigma_{\rm CF}$ and $\sigma_{\rm ICF}$ in reactions of ^{9}Be with ^{144}Sm, ^{168}Er, ^{186}W, ^{196}Pt, ^{208}Pb and ^{209}Bi, before examining the results for lower Z_T. The reasons for this are twofold: firstly, the effect of the bug fixes to the model and key physics included in M- PLATYPUS, namely the effect of lifetime on $\sigma_{\rm CF}$ and $\sigma_{\rm ICF}$, can be compared to previous work [1] that did not include these effects. Secondly, it is in this region that $\sigma_{\rm CF}$ and $\sigma_{\rm ICF}$ can be independently measured without the use of statistical model codes because only neutrons are evaporated following fusion, making the distinction between ICF and CF unambiguous.

The predicted above-barrier $\sigma_{\rm CF}$ and $\sigma_{\rm ICF}$ are presented as $F_{\rm ICF}$ shown by the filled circles (blue) in Fig. 7.9. In contrast expectations from the empirical prediction of Ref. [14], these new predictions show no significant dependence on Z_T in the range studied in this work, and have a mean value of 0.11 ± 0.02, which is indicated by the solid line Fig. 7.9. For comparison, the $F_{\rm ICF}$ predictions from Ref. [1] are shown by open circles. These new values are significantly smaller than those of the previous work. Here the effect of the essential physics input to M- PLATYPUS can be seen. While several changes were made to the determination of coincidence efficiencies

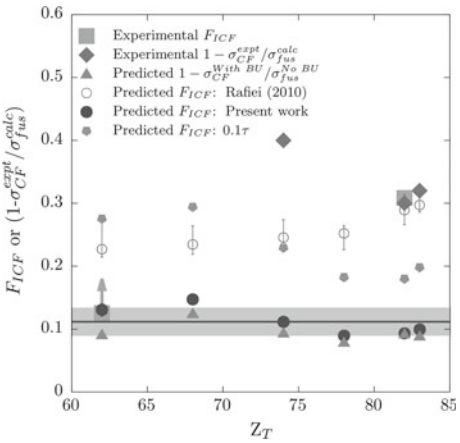

Fig. 7.9 Experimental values of $F_{\rm ICF}$ [6, 15] (filled squares), and $1 - \sigma_{\rm CF}^{\rm expt.}/\sigma_{\rm fus}^{\rm calc.}$ [5, 16] (filled diamonds), shown as a function of Z_T. Predictions of $F_{\rm ICF}$ (filled circles) and complete fusion suppression (filled triangles) using the new breakup functions and the modified version of platypus. Error bars (determined from the uncertainty in the least-squares fit) are smaller than the points. The $F_{\rm ICF}$ and complete fusion suppression predictions show no clear trend with Z_T. The $F_{\rm ICF}$ prediction has a mean value of 0.11 ± 0.02 shown as the solid line, and the shaded bar indicates $\pm 1\sigma$. The fusion suppression factor $1 - \sigma_{\rm CF}^{\rm With\ BU}/\sigma_{\rm fus}^{\rm No\ BU}$ has a mean value of 0.09 ± 0.02. $F_{\rm ICF}$ predictions made using the lifetime of the 2^+ state ten times smaller than expected are shown with pentagons. $F_{\rm ICF}$ predictions from Ref. [1] are shown with open circles

and extraction of breakup probabilities, as detailed in Chap. 6, the total change in the breakup functions used as input for calculations of above-barrier $F_{\rm ICF}$ was relatively modest, as already discussed. Therefore, the changes included in M- PLATYPUS to model breakup of ^{8}Be through the 2^{+} resonance are the major drivers towards the observed reduction of $F_{\rm ICF}$ by a factor of 2–3 relative to Ref. [1].

Experimentally, complete fusion suppression has been deduced, independently of $\sigma_{\rm ICF}$, through comparison with reactions forming the same compound nucleus involving only well bound nuclei [5, 17]. Within the classical dynamical model followed in M- PLATYPUS, $F_{\rm ICF}$ and complete fusion suppression are directly related, except for any trajectories that are either (a) outside the grazing trajectory and can only contribute to $\sigma_{\rm ICF}$ but not to $\sigma_{\rm CF}$ or (b) those that lead to no-capture breakup that would have otherwise undergone fusion had the projectile not undergone breakup, decreasing $\sigma_{\rm ICF}$ and $\sigma_{\rm CF}$.

To examine the role of such trajectories in these reactions, calculations with M- PLATYPUS switching off breakup were performed. The resulting fusion cross-section $\sigma_{\rm fus}^{\rm No\ BU}$ is compared with $\sigma_{\rm CF}^{\rm with\ BU}$ obtained with PLATYPUS. The quantity $(1 - \sigma_{\rm CF}^{\rm with\ BU}/\sigma_{\rm fus}^{\rm No\ BU})$, shown by purple triangles in Fig. 7.9, is very close to $F_{\rm ICF}$, with an average value of 0.09 ± 0.02. This demonstrates that contributions to $\sigma_{\rm ICF}$ from trajectories outside the grazing trajectory is small, and that fusion suppression due to no capture breakup is minimal in these reactions.

To understand the specific role of lifetime in $F_{\rm ICF}$ predictions, the lifetime of the 2^{+} state was changed to be a factor of ten smaller. The results are shown by the blue pentagons in Fig. 7.9, and are typically a factor of two larger than previously (blue circles). This result makes the importance of explicit handling of lifetimes very clear. Indeed, it was shown in Chap. 5 that the experimentally measured $\theta_{12} - \beta$ distributions compared to M- PLATYPUS and PLATYPUS simulations, shown in Fig. 5.10, indicates that at below-barrier energies, the explicit inclusion of lifetimes change the breakup observables.

Experimental measurements of $F_{\rm ICF}$ (which include any contributions from transfer) are shown in Fig. 7.9 as solid squares for ^{9}Be + ^{208}Pb [5] and ^{144}Sm [6]. For $F_{\rm ICF}$ measurements to be made, both CF and ICF cross-sections must be measured. However, in the case of ^{9}Be + ^{209}Bi [15] and ^{186}W [16], complete ICF cross-sections are unavailable, so fusion suppression factors $1 - \sigma_{\rm CF}^{\rm expt.}/\sigma_{\rm fus.}^{\rm calc.}$ are shown for as diamonds in Fig. 7.9. As both $F_{\rm ICF}$ and the fusion suppression factor are available for ^{9}Be + ^{208}Pb [5], both are shown, demonstrating the agreement between both measures in this system. The measured $F_{\rm ICF}$ and fusion suppressions for ^{9}Be + ^{209}Bi and ^{208}Pb are a factor of three times larger than the predicted contribution from neutron stripping triggered breakup, and the experimental fusion suppression determined for ^{9}Be + ^{186}W is a factor of four times larger. The $F_{\rm ICF}$ determined for ^{9}Be + ^{144}Sm is consistent with the prediction. However, the measured ICF cross-section in this experiment represents a lower limit, as cross-sections for ^{146}Gd and ^{148}Gd were not included [6]. As indicated in Fig. 7.9, even with lifetimes that are a factor of ten smaller than those estimated from the width of the 2^{+} resonance in ^{8}Be, the predicted $F_{\rm ICF}$ cannot be reconciled with experiment. As shown in Fig. 5.13, when the lifetimes used as input to KOOKABURRA are changed by a factor of ten, the predicted

$\theta_{12} - \beta$ distribution is also altered in such a way that it no longer well reproduces the experimentally measured distribution. A variation by a factor of ten can therefore be considered to be outside the uncertainty in the calculation of τ.

7.9 ICF and CF in ^{58}Ni, ^{28}Si and ^{27}Al

The predicted above-barrier σ_{CF} and σ_{ICF} for each system studied in this work are presented as $\mathrm{F_{ICF}}$ in Fig. 7.10a. The values of $\mathrm{F_{ICF}}$ for reactions with ^{58}Ni, ^{27}Al and ^{28}Si are significantly larger than those for reactions with heavy targets. Reactions of ^{9}Be with ^{28}Si and ^{27}Al show F_{ICF} of $0.27^{+0.01}_{-0.05}$ and $0.22^{+0.04}_{-0.03}$, respectively,[3] while reactions of ^{7}Li with ^{58}Ni, ^{28}Si and ^{27}Al have F_{ICF} that vary between $0.16^{+0.01}_{-0.03}$ for ^{58}Ni and $0.28^{+0.01}_{-0.03}$ for ^{28}Si. The fact that $\mathrm{F_{ICF}}$ does not decrease towards zero is contrary to what would be expected from direct breakup that depended on the gradient of Coulomb potential [14] and is therefore a consequence of the predominance of transfer-triggered breakup, which has been measured for the first time for these systems in this thesis. Although it is not immediately obvious why $\mathrm{F_{ICF}}$ should increase with decreasing Z_T, reasons that may explain this behaviour are discussed below.

Partially, $\mathrm{F_{ICF}}$ is driven by the strength and slope of the near-target breakup functions. In particular, the variation seen in $\mathrm{F_{ICF}}$ for reactions of ^{7}Li with ^{58}Ni, ^{28}Si and ^{27}Al (open green squares) correlates well with the variation in near-target $P(R_{\mathrm{B}})$ shown in Fig. 7.6b. On the other hand, even though the total near-target $P(R_{\mathrm{B}})$ for reactions of ^{9}Be with ^{168}Er, ^{144}Sm, ^{28}Si and ^{27}Al, shown in Fig. 7.6a are comparable, the resulting $\mathrm{F_{ICF}}$ are larger for ^{9}Be + ^{27}Al and ^{28}Si than they are for ^{168}Er and ^{144}Sm. Clearly, some other factors are at play. By scaling $\mathrm{F_{ICF}}$ by the total near-target $P(R_{\mathrm{B}})$, the effect of the total strength of the breakup function is removed. The scaled $F_{\mathrm{ICF}}/P(R_{\mathrm{B}})$ values, shown as a function of $Z_P Z_T$ in panel (b) of Fig. 7.10 show much less scatter than $\mathrm{F_{ICF}}$ alone, except for the ^{7}Li + ^{27}Al case, which lies far outside the systematics. Arguably, there is also some dependence of $F_{\mathrm{ICF}}/P(R_{\mathrm{B}})$ on $Z_P Z_T$ [panel (b)] and the average slope of near-target breakup, weighted by the probability of breakup at the barrier [panel (c)]. A possible explanation of the effect of $Z_P Z_T$ lies in the relevance of timescales to these processes. In systems with higher $Z_P Z_T$, the gradient of the Coulomb potential is higher for the same E/V_{B} as for systems with smaller $Z_P Z_T$. Therefore, in a classical trajectory model, the velocity of projectile-like nuclei are higher in heavier systems than for light systems. As a result, the time taken for projectile-like nuclei that were produced on the incoming trajectory to pass beyond the capture radius is smaller. The effect of this is that for the same τ, more

[3] The errors in F_{ICF} arise from the statistical error in the least squares fit to the breakup probabilities. The input breakup probability when calculating F_{ICF} was varied by ± 1 sigma in both slope parameter and strength parameter, and the resulting F_{ICF} calculated. The asymmetry in the error bars therefore arise from a nonlinear response of KOOKABURRA to variation in the breakup function. The model sensitivities of KOOKABURRA must be investigated further.

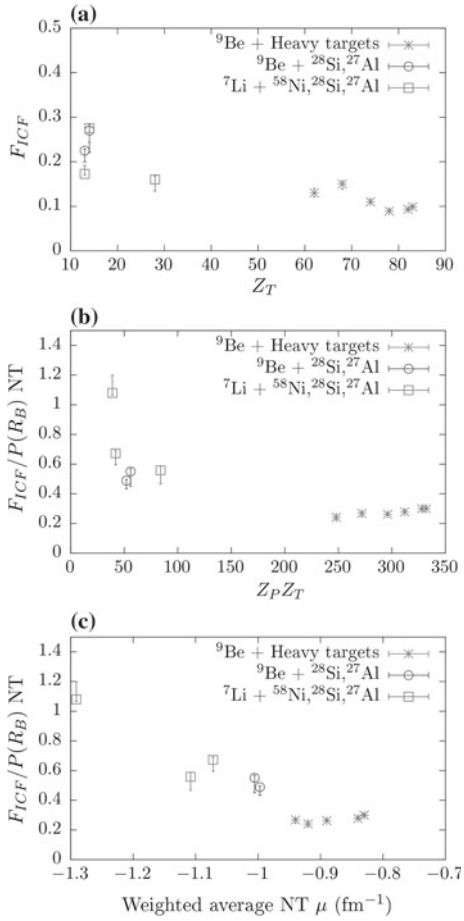

Fig. 7.10 M- PLATYPUS and KOOKABURRA predictions of F_{ICF} for the systems studied in this work (**a**). F_{ICF} divided by the total probability of near-target breakup as a function of $Z_P Z_T$ (**b**) and average near-target breakup slope parameter (**c**). Errors in F_{ICF} correspond to errors in the fit to the below-barrier breakup probabilities

breakup will occur on the incoming trajectory for light systems than for heavy systems. A more quantitative analysis will be possible with further understanding of the sensitivities of KOOKABURRA to $Z_P Z_T$ and to the slope parameter.

While F_{ICF} and fusion suppression factors $1 - \sigma_{CF}^{\text{With BU}}/\sigma_{\text{fus.}}^{\text{No BU}}$ were observed to correspond in reactions of ^{9}Be with ^{144}Sm, ^{168}Er, ^{186}W, ^{196}Pt, ^{208}Pb and ^{209}Bi, the same cannot be said of reactions with ^{58}Ni, ^{28}Si and ^{27}Al, as shown in Fig. 7.11a. In this figure, $1 - \sigma_{CF}^{\text{With BU}}/\sigma_{\text{fus.}}^{\text{No BU}}$ against F_{ICF} is shown for all of the systems studied in this work. As was shown in Fig. 7.9, $1 - \sigma_{CF}^{\text{With BU}}/\sigma_{\text{fus.}}^{\text{No BU}}$ and F_{ICF} are very similar for reactions of ^{9}Be + ^{144}Sm, ^{168}Er, ^{186}W, ^{196}Pt, ^{208}Pb and ^{209}Bi, though the fusion suppression is consistently lower than F_{ICF}. ^{9}Be + ^{208}Pb is the only system in which experimental values of both F_{ICF} and $1 - \sigma_{CF}^{\text{expt.}}/\sigma_{\text{fus.}}^{\text{calc.}}$ are available. Coincidentally, this is also the system in which the two quantities are the most similar in the calculations. In the reactions with ^{58}Ni, ^{28}Si and ^{27}Al, F_{ICF} is significantly lower than

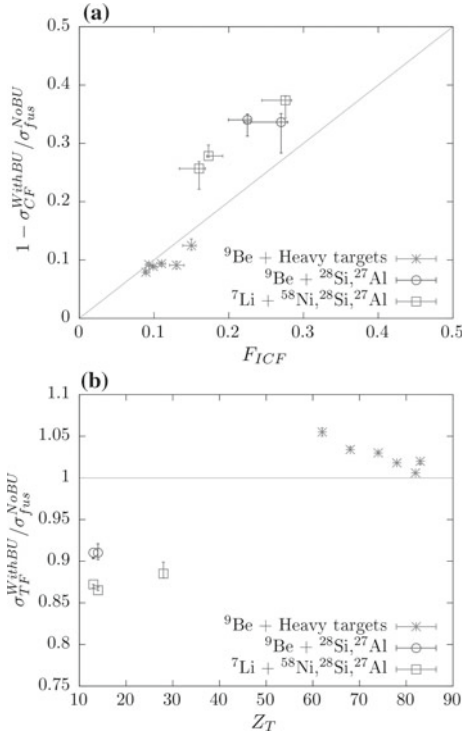

Fig. 7.11 **a** Comparison between F_{ICF} and fusion suppression factor $1-\sigma_{CF}/\sigma_{fus.}$ in the systems studied in this thesis. A line of $F_{ICF}= 1-\sigma_{CF}/\sigma_{fus.}$ has been drawn for reference. **b** Ratio of total fusion ($\sigma_{TF}=\sigma_{CF}+\sigma_{ICF}$) to the classical fusion cross-section σ_{fus}. A line of $\sigma_{TF}/\sigma_{fus}=1$ has been drawn for reference

$1-\sigma_{\mathrm{CF}}^{\mathrm{With\ BU}}/\sigma_{\mathrm{fus.}}^{\mathrm{no\ BU}}$. This is the opposite behaviour to what was seen for the heavy systems. This is an indication that there are trajectories that are leading to no-capture breakup that would have otherwise undergone fusion had the projectile not undergone breakup, decreasing σ_{CF} but not contributing to σ_{ICF}. It is not clear why these trajectories play a larger role in light systems than in heavy systems, although the geometrical size of the nuclei may play a role.

If there are a large number of trajectories that are leading to no-capture breakup, then one might expect that total fusion $\sigma_{\mathrm{TF}}=\sigma_{\mathrm{CF}}+\sigma_{\mathrm{ICF}}$ is suppressed relative to that with no breakup. Shown in Fig. 7.11b is the ratio of σ_{TF} to the classical fusion cross-section calculated using:

$$\sigma_{\mathrm{fus}}^{\mathrm{No\ BU}}=\pi R_{\mathrm{B}}^{2}\left(1-\frac{V_{\mathrm{B}}}{E_{\mathrm{CM}}}\right). \tag{7.2}$$

This expression reproduces the value of $\sigma_{\mathrm{fus}}^{\mathrm{No\ BU}}$ calculated using KOOKABURRA with breakup turned off to within 2%. The departure of F_{ICF} from $1-\sigma_{\mathrm{CF}}/\sigma_{\mathrm{fus.}}$ is seen in an effect on total fusion. *Total fusion* is (slightly) enhanced for reactions of ^{9}Be with ^{144}Sm, ^{168}Er, ^{186}W, ^{196}Pt, ^{208}Pb and ^{209}Bi, due to trajectories that contribute to σ_{ICF}

but could not contribute to σ_{CF}, even though in the same systems, *complete fusion* is hindered.

On the other hand, these calculations indicate that both *total fusion* and *complete fusion* should be hindered in reactions of ^{7}Li and ^{9}Be with ^{58}Ni, ^{28}Si and ^{27}Al. While complete fusion has not been measured in these systems, measurements of total fusion have been performed, but rely on statistical model calculations. It is not clear from experimental measurements whether or not above-barrier total fusion is hindered: Refs. [18–23] find a total fusion hindrance due to breakup by relating the fusion cross-section to the reaction cross-section, and comparing to well-bound nuclei. The measurements of [24–29] show agreement with BPM or coupled-channels calculations. However, it should be noted that the hindrance of total fusion that is predicted here is relatively modest, and within the uncertainty of many of the cross-sections reported in those works.

7.10 Summary

In this chapter, below-barrier transfer-triggered breakup functions for reactions of ^{9}Be + ^{27}Al, ^{28}Si, ^{144}Sm, ^{168}Er, ^{186}W, ^{196}Pt, ^{208}Pb, ^{209}Bi and ^{7}Li + ^{27}Al, ^{28}Si, ^{58}Ni were extracted from coincidence measurements of breakup fragments using an improved two-dimensional method of efficiency correction. In general, below-barrier breakup functions were found to be steeper for near-target breakup than for asymptotic breakup, though no clear trend with Z_T was identified. The below-barrier breakup functions were then used to predict the contribution of breakup to above-barrier suppression. In reactions of ^{9}Be + ^{144}Sm, ^{168}Er, ^{186}W, ^{196}Pt, ^{208}Pb and ^{209}Bi, the experimentally observed suppression of complete fusion is a factor of three larger than what can be explained by breakup. The predicted fusion cross-sections for reactions of ^{9}Be with ^{27}Al and ^{28}Si, and ^{7}Li with ^{27}Al, ^{28}Si and ^{58}Ni indicate that complete fusion should be suppressed by breakup to between 15 and 35% in these light systems. They further indicate that total fusion should be suppressed by approximately 15% in light systems. The implications of these results on our understanding of the mechanisms of above-barrier complete fusion suppression are discussed in Chap. 9.

It should be emphasised that this is the first use of KOOKABURRA for above-barrier predictions of σ_{CF} and σ_{ICF}. Further work is required to establish the sensitivities of the model. It would also be interesting to re-examine the breakup functions and above-barrier suppression predictions of the ^{6,7}Li + ^{207,208}Pb,^{209}Bi measurements of Ref. [30] with the improved methods of efficiency correction as well as improved classical trajectory calculations that include realistic resonant state excitation and lifetimes. Further measurements with intermediate mass targets will also be beneficial to understand the trends of breakup with decreasing Z_T.

References

1. Rafiei, R., du Rietz, R., Luong, D.H., Hinde, D.J., Dasgupta, M., Evers, M., Diaz-torres, A.: Mechanisms and systematics of breakup in reactions of ^{9}Be at near-barrier energies. Phys. Rev. C **81**(2), 024601 (2010)
2. Rafferty, D.C., Dasgupta, M., Hinde, D.J., Simenel, C., Simpson, E.C., Williams, E., Carter, I.P., Cook, K.J., Luong, D.H., McNeil, S.D., Ramachandran, K., Vo-Phuoc, K., Wakhle, A.: Multinucleon transfer in ^{16,18}O, ^{19}F+^{208}Pb reactions at energies near the fusion barrier. Phys. Rev. C **94**(2), 024607 (2016)
3. Saha, S., Agarwal, Y.K., Baba, C.V.K.: One- and two-proton transfer reactions in ^{32}S+ ^{64}Ni and ^{28}Si+ ^{68}Zn at near-barrier energies. Phys. Rev. C **49**(5), 2578 (1994)
4. Dasgupta, M., Hinde, D.J., Butt, R.D., Anjos, R.M., Berriman, A., Carlin, N., Gomes, P.R.S., Morton, C.R., Newton, J.O., Szanto de Toledo, A., Hagino, K.: Fusion versus breakup: observation of large fusion suppression for ^{9}Be+ ^{208}Pb. Phys. Rev. Lett. **82**(7), 1395 (1999)
5. Dasgupta, M., Gomes, P.R.S., Hinde, D.J., Moraes, S.B., Anjos, R.M., Berriman, A.C., Butt, R.D., Carlin, N., Lubian, J., Morton, C.R., Szanto de Toledo, A.: Effect of breakup on the fusion of ^{6}Li, ^{7}Li, and ^{9}Be with heavy nuclei. Phys. Rev. C **70**(2), 024606 (2004)
6. Gomes, P.R.S., Padron, I., Crema, E., Capurro, O.A., Fernández Niello, J.O., Arazi, A., Martí, G.V., Lubian, J., Trotta, M., Pacheco, A.J., Testoni, J.E., Rodríguez, M.D., Ortega, M.E., Chamon, L.C., Anjos, R.M., Veiga, R., Dasgupta, M., Hinde, D.J., Hagino, K.: Comprehensive study of reaction mechanisms for the ^{9}Be+^{144}Sm system at near- and sub-barrier energies. Phys. Rev. C **73**(6), 064606 (2006)
7. Palshetkar, C.S., Santra, S., Chatterjee, A., Ramachandran, K., Thakur, S., Pandit, S.K., Mahata, K., Shrivastava, A., Parkar, V.V., Nanal, V.: Fusion of the weakly bound projectile ^{9}Be with ^{89}Y. Phys. Rev. C **82**(4), 044608 (2010)
8. Parkar, V.V., Palit, R., Sharma, S.K., Naidu, B.S., Santra, S., Joshi, P.K., Rath, P.K., Mahata, K., Ramachandran, K., Trivedi, T., Raghav, A.: Fusion cross sections for the ^{9}Be+^{124}Sn reaction at energies near the Coulomb barrier. Phys. Rev. C **82**(5), 054601 (2010)
9. Gomes, P.R.S., Linares, R., Lubian, J., Lopes, C.C., Cardozo, E.N., Pereira, B.H.F., Padron, I.: Search for systematic behavior of incomplete-fusion probability and complete-fusion suppression induced by ^{9}Be on different targets. Phys. Rev. C **84**(1), 014615 (2011)
10. Tripathi, V., Navin, A., Nanal, V., Pillay, R.G., Mahata, K., Ramachandran, K., Shrivastava, A., Chatterjee, A., Kailas, S.: Experimental signatures for distinguishing breakup fusion and transfer in ^{7}Li+^{165}Ho. Phys. Rev. C **72**(1), 017601 (2005)
11. Diaz-Torres, A.: PLATYPUS: a code for reaction dynamics of weakly-bound nuclei at near-barrier energies within a classical dynamical model. Comput. Phys. Commun. **182**(4), 1100 (2011)
12. Dasgupta, M., Hinde, D., Hagino, K., Moraes, S.B., Gomes, P.R.S., Anjos, R.M., Butt, R.D., Berriman, A.C., Carlin, N., Morton, C.R., Newton, J.O., Szanto de Toledo, A.: Fusion and breakup in the reactions of ^{6}Li and ^{7}Li nuclei with ^{209}Bi. Phys. Rev. C **66**(4), 041602(R) (2002)
13. Chamon, L.C., Carlson, B.V., Gasques, L.R., Pereira, D., De Conti, C., Alvarez, M.A.G., Hussein, M.S., Cândido Ribeiro, M.A., Rossi, E.S., Silva, C.P.: Toward a global description of the nucleus-nucleus interaction. Phys. Rev. C **66**(1), 014610 (2002)
14. Hinde, D.J., Dasgupta, M., Fulton, B., Morton, C., Wooliscroft, R., Berriman, A., Hagino, K.: Fusion suppression and sub-barrier breakup of weakly bound nuclei. Phys. Rev. Lett. **89**(27), 7 (2002)
15. Dasgupta, M., Hinde, D.J., Sheehy, S.L., Bouriquet, B.: Suppression of fusion by breakup: resolving the discrepancy between the reactions of ^{9}Be with ^{208}Pb and ^{209}Bi. Phys. Rev. C **81**(2), 024608 (2010)
16. Fang, Y.D., Gomes, P.R.S., Lubian, J., Zhou, X.H., Zhang, Y.H., Han, J.L., Liu, M.L., Zheng, Y., Guo, S., Wang, J.G., Qiang, Y.H., Wang, Z.G., Wu, X.G., He, C.Y., Li, C.B., Hu, S.P., Yao, S.H.: Fusion and one-neutron stripping reactions in the ^{9}Be+^{186}W system above the Coulomb barrier. Phys. Rev. C **87**(2), 024604 (2013)

17. Rath, P.K., Santra, S., Singh, N.L., Tripathi, R., Parkar, V.V., Nayak, B.K., Mahata, K., Palit, R., Kumar, S., Mukherjee, S., Appannababu, S., Choudhury, R.K.: Suppression of complete fusion in the ^{6}Li + ^{144}Sm reaction. Phys. Rev. C **79**(5), 051601 (2009)
18. Figueira, M.C.S., Szanto, E.M., Anjos, R.M., Added, N., Carlin, N., Fante, J.R., Matheus, R., Szanto de Toledo, A.: Complete fusion of ^{9}Be+^{29}Si. Nucl. Phys. A **561**, 453 (1993)
19. Toledo, A.S.D., Added, N., Cardenas, W.H.Z., Carlin, N., Moura, M.M.D., Munhoz, M.G., Suaide, A.A.P., Szanto, E.M., Takahashi, J.: Fusion hindrance in light nuclear systems: binding energy and/or surface diffuseness effect? Nucl. Phys. A **679**, 175 (2000)
20. Signorini, C.: Interaction at the barrier with unstable/loosely bound projectiles. J. Phys. G: Nucl. Part. Phys. **23**, 1235 (1997)
21. Bodek, K., Hugi, M., Lang, J., Muller, R., Ungricht, E., Jankowski, K., Zipper, W., Jarczyk, L., Strzalkowski, A., Willim, G., Witala, H.: The energy dependence of fusion in the ^{9}Be + ^{28}Si system. Nucl. Phys. A **339**, 353 (1980)
22. Eck, J.S., Leigh, J.R., Ophel, T.R., Clark, P.D.: Total fusion cross-section for the ^{9}Be + ^{28}Si system. Phys. Rev. C **21**(6), 2352 (1980)
23. Hugi, M., Lang, J., Miller, R., Ungricht, E., Bodek, K., Jarczyk, L., Kamys, B., Magiera, A., Strzalkowski, A., Willim, G.: Fusion and direct reactions for strongly and weakly bound projectiles. Nucl. Phys. A **368**, 173 (1981)
24. Anjos, R.M., Muri, C., Lubian, J., Gomes, P.R.S., Padron, I., Alves, J.J.S., Martí, G.V., Fernández Niello, J.O., Pacheco, A.J., Capurro, O.A., Abriola, D., Testoni, J.E., Ramírez, M.: Liguori, Neto R., Added, N.: No evidence of break-up effects on the fusion of ^{9}Be with medium-light nuclei. Phys. Lett. B **534**, 45 (2002)
25. Pakou, A., Rusek, K., Alamanos, N., Aslanoglou, X., Kokkoris, M., Lagoyannis, A., Mertzimekis, T.J.: Total reaction and fusion cross sections at sub- and near-barrier energies for the system ^{7}Li + ^{28}Si. Eur. Phys. J. A **39**, 187 (2009)
26. Kalita, K., Verma, S., Singh, R., Das, J., Jhingan, A., Madhavan, N., Nath, S., Varughese, T., Sugathan, P., Parkar, V.V., Mahata, K., Ramachandran, K., Shrivastava, A., Chatterjee, A., Kailas, S., Barua, S., Basu, P., Majumdar, H., Sinha, M., Bhattacharya, R., Sinha, A.: Elastic scattering and fusion cross sections for ^{7}Be,^{7}Li+^{27}Al systems. Phys. Rev. C **73**(2), 024609 (2006)
27. Padron, I., Gomes, P.R.S., Anjos, R.M., Lubian, J., Muri, C., Alves, J.J.S., Martí, G.V., Ramírez, M., Pacheco, A.J., Capurro, O.A., Fernández Niello, J.O., Testoni, J.E., Abriola, D.: R. S.M., Abriola, D., Spinella, M.: Fusion of stable weakly bound nuclei with ^{27}Al and ^{64}Zn. Phys. Rev. C **66**(4), 044608 (2002)
28. Martí, G.V., Gomes, P.R.S., Rodríguez, M.D., Fernández Niello, J.O., Capurro, O.A., Pacheco, A.J., Testoni, J.E., Ramírez, M., Arazi, A., Padron, I., Anjos, R.M., Lubian, J., Crema, E.: Fusion, reaction, and breakup cross sections of ^{9}Be on a light mass target. Phys. Rev. C **71**(2), 027602 (2005)
29. Sinha, M., Majumdar, H., Bhattacharya, R., Basu, P., Roy, S., Biswas, M., Palit, R., Mazumdar, I., Joshi, P.K., Jain, H.C., Kailas, S.: Experimental investigation of ^{7}Li + ^{28}Si above the Coulomb barrier. Phys. Rev. C **76**(2), 027603 (2007)
30. Luong, D.H.: Mechanisms and time-scales in breakup of ^{6,7}Li. Ph.D. thesis, Australian National University (2012)

Chapter 8
Towards Measurements of ^{7}Be(d,p)^{8}Be

The nucleus is so small, and has so few parts, and still shows a tremendous variety of phenomena. What a marvellous invention! It is worth devoting a lifetime to it

Victor Weisskopf 1908–2002

The capability of the BALiN array for detection of charged particles in coincidence has been robustly demonstrated for a wide range of reactions. In this chapter, the feasibility of using this experimental capability to study the astrophysically relevant reaction ^{7}Be(d,p)^{8}Be is explored. There are two experimental considerations for measurements of ^{7}Be(d,p)^{8}Be that will be discussed in this chapter. The first centres around the need to understand the efficiency of BALiN for detection of coincidence fragments following reactions with light targets performed in inverse kinematics. To address this, test measurements with stable nuclei were performed, and are discussed in Sect. 8.1. The second task is to investigate the production of the ^{7}Be radioactive ion beam at the ANU with the ^{10}B (^{6}Li,^{7}Be)^{9}Be reaction. This will be discussed in Sects. 8.2 and 8.3.

8.1 Test Measurements with Stable Nuclei

A goal of this work is to investigate the feasibility of investigating the nuclear reaction relevant to Big Bang Nucleosynthesis (BBN), ^{7}Be(d,p)^{8}Be with the facilities at the ANU. As discussed in Chap. 1, this reaction may play an important role in the destruction of ^{7}Be during BBN. If the reaction rate is larger than previously estimated [1], it is capable of reducing the amount of ^{7}Li in the early universe, alleviating the cosmological lithium problem [2]. A previous measurement [3] found a smaller reaction rate than originally estimated, but was not sensitive to highly excited states in ^{8}Be, motivating a re-examination of the ^{7}Be(d,p)^{8}Be reaction rate.

K. J. Cook, *Zeptosecond Dynamics of Transfer-Triggered Breakup*,
Springer Theses, https://doi.org/10.1007/978-3-319-96017-3_8

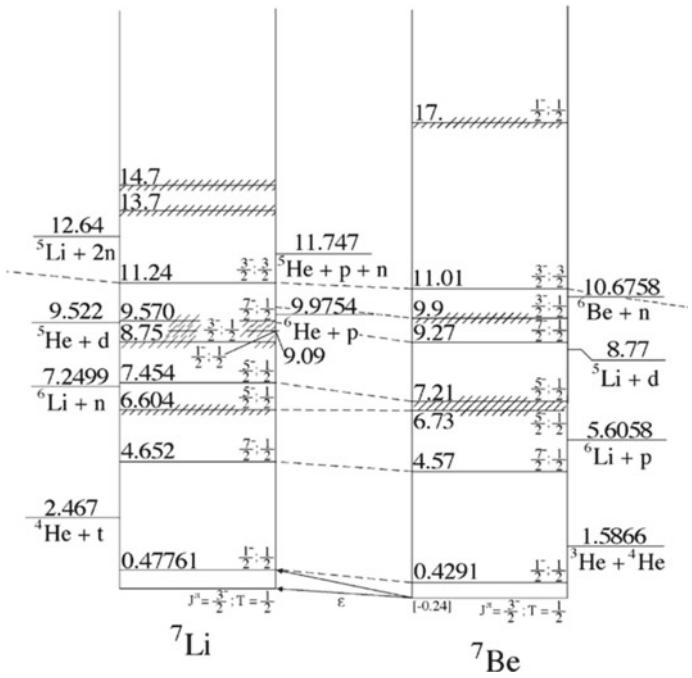

Fig. 8.1 Structure of ^{7}Li and ^{7}Be showing the charge independence of the nuclear force (see text). Reproduced from [4]

Since ^{7}Be is unstable ($t_{1/2} = 53.2$ days) producing a beam of ^{7}Be is challenging. To investigate the kinematics of the transfer and breakup process, and the suitability of BALiN to measurements of this system, it is useful to first perform a measurement with the mirror nucleus ^{7}Li. Mirror nuclei are pairs of nuclei with interchanged numbers of protons and neutrons $Z \leftrightarrow N$, that is, ${}^{7}_{3}\mathrm{Li}^{4} \leftrightarrow {}^{7}_{4}\mathrm{Be}^{3}$. Since the nuclear force is almost charge independent (see [5] and Refs. therein), the nuclear structure of ^{7}Li and ^{7}Be should only differ by the difference in the Coulomb potential due to the difference in the number of protons. Indeed, the low-lying structure of ^{7}Li and ^{7}Be presented in Fig. 8.1 show that the ordering and spacing of the levels in these nuclei are very similar. Further, the binding energies of the nuclei are close to each other, as reflected by the similarity of their mass excesses Δ, where $\Delta = 14.9070$ MeV for ^{7}Li and $\Delta = 15.7689$ MeV for ^{7}Be [6]. Because of this, the reactions ^{7}Li(d,n)^{8}Be$(\alpha + \alpha)$ and ^{7}Be(d,p)^{8}Be$(\alpha + \alpha)$ have very similar Q-values of 15.121 and 16.766 MeV, respectively. This makes the stable beam reaction ^{7}Li(d,n)^{8}Be$(\alpha + \alpha)$ an excellent test-bed for ^{7}Be(d,p)^{8}Be$(\alpha + \alpha)$ in terms of both reaction outcomes and reaction kinematics. As such, we begin by making measurements of d(^{7}Li,^{8}Be$(\alpha + \alpha)$)n; using inverse kinematics. However, this reaction results in a neutron in the final state whereas ^{7}Be(d,p)^{8}Be produces a proton. The difference is significant since BALiN is sensitive to protons, but not neutrons. One might expect to measure not

only $\alpha + \alpha$ pairs, but also coincidences with the proton. To understand this aspect of kinematic reconstruction, the reaction d(^{9}Be,^{8}Be)t, which produces three charged fragments in the final state, was also measured. Both of these measurements required the production of deuterium targets, which will be discussed in Sect. 8.3.1.

8.1.1 Measurements of d(^{7}Li,^{8}Be)n

Measurements of the d(^{7}Li,^{8}Be)n reaction were performed using a ^{7}Li beam of $E_{\text{beam}} = 2.80$ MeV. After traversing half the target thickness, the energy of the ^{7}Li was $E_{\text{lab}} = 2.51$ MeV, corresponding to a centre of mass energy of 0.558 MeV, which is 9% above the fusion barrier energy predicted by the SPP. This is the only above-barrier measurement performed in this thesis. A beam energy of 2.80 MeV required a terminal potential of 1.314 MV, the lowest potential used at the 14UD to deliver beam. As discussed in Chap. 1, the interest in the ^{7}Be(d,p)^{8}Be reaction is that it is a key candidate for the destruction of ^{7}Be during the Big Bang. BBN begins at an energy of approximately 0.1 MeV, after the photo-dissociation of deuterium ceases and stops when the temperature of the universe drops below 0.03 MeV [7]. Therefore, the centre of mass energy of 0.558 MeV for the measurements performed here is well above the energies of astrophysical interest. The production of lower energy beams at the ANU will require further experimental development.[1] The most recent measurement of ^{7}Be(d,p)^{8}Be described in Ref. [3] was at centre of mass energies between 0.13 and 0.38 MeV, and between 1.0 and 1.23 MeV, on either side of the present measurement. Therefore, we can relate the present measurements to those of Ref. [3]. In addition, the 15.121 MeV Q-value of the d(^{7}Li,^{8}Be)n reaction means that the difference in beam energy between this measurement and that of experimental interest will have little difference in the kinematic observables in this reaction. Further, the high Q-value (compared with E_{lab}) also means that this, rather than E_{lab}, will dictate the internal states of ^{8}Be that are likely to be populated. We can therefore expect that the inferences that can be drawn from a measurement of d(^{7}Li,^{8}Be)n at $E_{\text{beam}} = 2.80$ MeV will not change significantly at a lower energy. Since the $(^{nat}C_2D_4)_n$ target contains a significant amount of ^{12}C, it is pertinent to note that a ^{7}Be beam of 2.80 MeV is well below the barrier at $E_{CM}/V_b = 0.34$. As such, contributions to the coincidence yield from breakup in interactions of ^{7}Li with ^{12}C are expected to be low. To confirm this, an additional measurement was performed at $E_{\text{beam}} = 2.80$ MeV with a ^{12}C target to examine any contributions of ^{7}Li + ^{12}C reactions to the coincidence yield. No coincidence pairs were seen in this

[1] One way to achieve lower energies may be by removing the primary stripper, and instead using the secondary stripping foil, located one third of the way between the terminal and the bottom of the accelerator. The beam will decelerate between the terminal and the second stripper. Then, in this configuration, for a terminal potential of V_T, initial acceleration V_i and a post-stripping charge state q, the beam energy will be $E_{\text{beam}} = 2/3V_T(1+q) + V_i$, compared to the usual $E_{\text{beam}} = V_T(1+q) + V_i$ (Eq. 3.1).

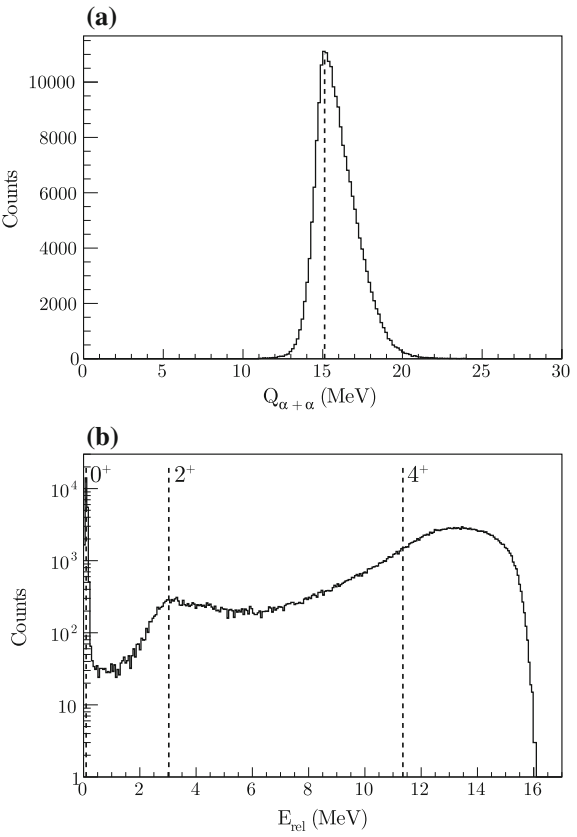

Fig. 8.2 Measured $Q_{\alpha+\alpha}$ (**a**) and E_{rel} (**b**) distributions of $\alpha + \alpha$ fragments detected in coincidence for the reaction of ^{7}Li with d at $E_{\text{beam}} = 2.8$ MeV. The line in panel **a** corresponds to the calculated Q-value for the ^{7}Li(d,n)^{8}Be reaction, while the lines in panel **b** indicate the expected E_{rel} due to on-resonance excitation of ^{8}Be in its first 0^+, 2^+ and 4^+ resonances

measurement, giving confidence that all $\alpha + \alpha$ pairs measured in reactions of ^{7}Li with $(^{nat}C_2D_4)_n$ at this energy correspond to reactions with deuterium.

The separation of valid coincidence pairs from spurious coincidences proceeded in the same manner as described in Chap. 4. Only one peak in $Q_{\alpha+\alpha}$ is produced, corresponding to the expected Q-value of 15.121 MeV, as can be seen in Fig. 8.2a. The large width of this peak (2.4 MeV FWHM) is attributable to the large fraction of energy that is carried by the recoiling neutron. Any error in BALiN location, pixelisation effect, or uncertainty in energy loss is much more significant in this measurement than in measurements seen earlier in this thesis with much heavier targets. The E_{rel} distribution is more interesting. Shown in Fig. 8.2b is the resulting E_{rel} distribution for the $\alpha + \alpha$ pairs measured in reactions of ^{7}Li with d at $E_{\text{beam}} = 2.8$ MeV. The sharp cut at 16 MeV is due to limit of the energy available to the fragments. The on-resonance excitation of ^{8}Be in its ground state 0^+ resonance, as well as its 2^+ and 4^+ resonances are indicated by the dashed lines in the figure. As with all measurements of $\alpha + \alpha$ fragments in this thesis, there is a peak in E_{rel} at 92 keV, associated with breakup from the ground-state resonance of ^{8}Be. In general, (as

discussed in Sect. 2.8.4 and shown in Eq. 2.40) the measured E_{rel} results from the sum of three components: the breakup Q-value of the transfer product, the excitation energy of the transfer product above its ground state, and the post-acceleration of the fragments due to the fragment-recoil Coulomb field. However, in this measurement, the recoiling nucleus is a neutron. Therefore, the breakup fragments experience essentially no post-breakup acceleration. The resulting relative energy distribution will therefore represent the distribution of the internal excitation energy of ^{8}Be, E_{p}^{*} filtered by the detector efficiency, so that

$$E_{\mathrm{rel}} = E_{\mathrm{p}}^{*} + Q_{\mathrm{BU}}. \tag{8.1}$$

As seen in Fig. 8.2b, there is a peak in E_{rel} corresponding to the ground-state and first 2^{+} state of ^{8}Be, as we would expect. However, the peak in high E_{rel} does not lie at the position of the 4^{+} peak at $E_{\mathrm{p}}^{*} = 11.35$ MeV. This is very likely due to a strong dependence on the opening angle θ_{12} of the coincidence efficiency of BALiN for each state, which was discussed in detail in Chap. 6. An additional factor affecting the efficiency of the array is the energy threshold of BALiN. In the measurements, the energy threshold of the amplifiers was set at approximately 900 keV. This corresponds to an energy of the α particles prior to energy loss through the target, PET foil, Al layer and Si deadlayer of approximately 2 MeV.

The effect of the energy threshold and coincidence efficiency of the BALiN array can be seen most starkly in a plot of $\theta_{12} - \beta$, shown in Fig. 8.3. The asymptotic expectations of the $\theta_{12} - \beta$ relationship for the on-resonance excitation of ^{8}Be in its ground and first two resonances are shown by the white-bordered black lines. Areas where *all* events have at least one particle below the detection threshold are shown (approximately) by the shaded regions, determined by KOOKABURRA simulations. As the recoiling nucleus is uncharged, all breakup should follow the asymptotic expec-

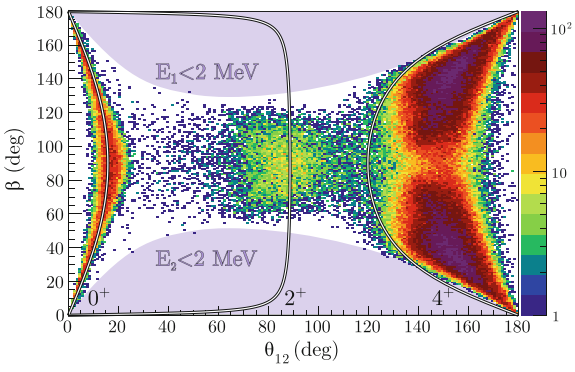

Fig. 8.3 Reconstructed $\theta_{12} - \beta$ distribution of $\alpha + \alpha$ fragments produced in the ^{7}Li(d,n)^{8}Be reaction at $E_{\mathrm{beam}} = 2.8$ MeV. Lines indicate the asymptotic $\theta_{12} - \beta$ relationship expected for breakup of ^{8}Be with on-resonance excitation energy of the (from left to right) 0^{+}, 2^{+} and 4^{+} states. Shaded areas indicate regions where every event is below the ~2 MeV energy threshold of BALiN

tations. The 0^+ band of events follow asymptotic expectations well. The opening angle between the fragments is smallest for these events. Therefore, if one fragment hits the array, the probability of measuring the other fragment is high. This results in a high efficiency for measuring breakup from the 0^+ state. As expected from the E_{rel} distribution, there is a group of events in $\theta_{12} - \beta$ that correspond to the 2^+ $E^*_{\mathrm{p}} = 3.03$ MeV state. The opening angle of the 2^+ events that are above the energy threshold is approximately 80°. This opening angle means that, on average, particles are too far apart to land on the same pair of detectors, but not far enough apart to have one fragment fall on the forward pair of detectors and one on the backward pair of detectors. This leads to a minimum of efficiency in intermediate opening angles ($40 \lesssim \theta_{12} \lesssim 130$). As a result, the probability of detecting events corresponding to the 2^+ resonance is small. As the opening angle of the particles increase, the likelihood of detecting one particle in the forward pair of detectors and the other in the backward increases, and the efficiency increases rapidly at the largest opening angles $\theta_{12} \gtrsim 130°$. This may explain the distribution of events associated with high E^*_{p}. The asymptotic expectation for the on-resonance excitation of the 4^+ resonance is shown in Fig. 8.3. The observed region of highest intensity in E_{rel} and $\theta_{12} - \beta$ occurs at higher values of E_{rel} and θ_{12} than would be expected. Since the efficiency rapidly increases for $\theta_{12} \gtrsim 130°$, the distribution will be skewed to higher E_{rel} and θ_{12}, as is observed.

The goal of this measurement was to understand the experimental conditions required for measuring coincidence fragments produced in the ^{7}Li(d,n)^{8}Be reaction, as guidance for the ^{7}Be(d,p)^{8}Be reaction. We have seen that the kinematic reconstruction techniques developed for studies of breakup remain useful in these measurements, and that it is possible to use the E_{rel} and $\theta_{12} - \beta$ distributions to identify the excitation energy of ^{8}Be prior to decay. As discussed in Chap. 1, a key issue in previous measurements of ^{7}Be(d,p)^{8}Be [3] was that by only measuring the recoiling protons, the measurements were insensitive to high excitations of ^{8}Be, as the energy of the protons were then below the measurement threshold at BBN energies. By measuring both α particles, high excitations of ^{8}Be can be measured. A key experimental goal of measurements of ^{7}Be(d,p)^{8}Be with BALiN would be to measure the full distribution of excitation energies in ^{8}Be, and therefore obtain a robust cross-section.

The efficiency of detecting pairs of particles in BALiN depends strongly on the opening angle, and therefore the E_{rel}, of the fragments. Due to this strong dependence of detector efficiency and energy threshold on the observed $E_{\mathrm{rel}} = Q_{\mathrm{BU}} + E^*_{\mathrm{p}}$ distribution, it is not possible to say anything quantitative about the relative population of the 0^+, 2^+ and 4^+ resonances without first characterising the efficiency of BALiN. This was done in detail for the measurements with heavier targets in Chap. 6. Here we simply give the results for efficiency calculations using KOOKABURRA. The population of different resonances of ^{8}Be can be estimated by matching the experimentally measured and the simulated (filtered through the acceptance of BALiN)

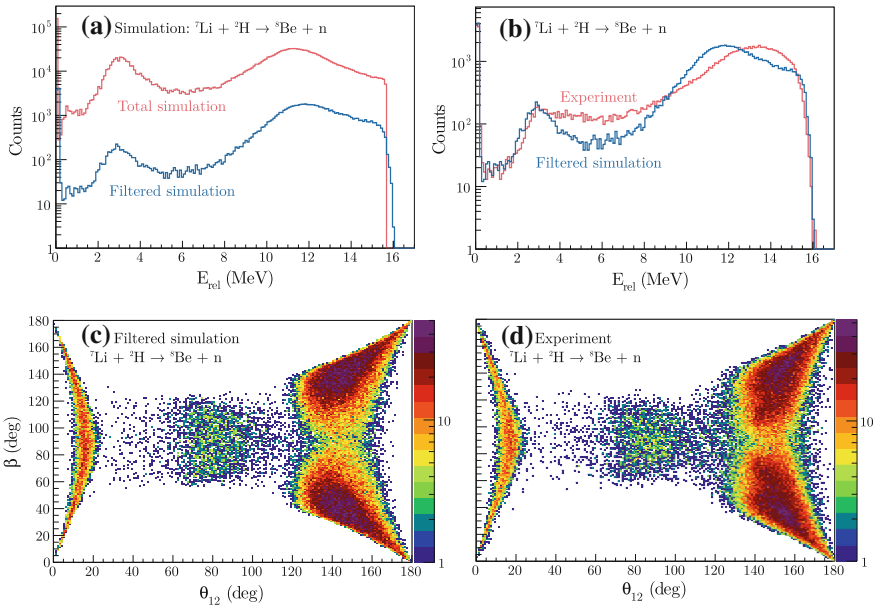

Fig. 8.4 **a** The total (red line) and filtered (blue line) E_{rel} distribution for a KOOKABURRA simulation of $\alpha + \alpha$ pairs produced in ^{7}Li(d,n)^{8}Be reactions at $E_{\mathrm{lab}} = 2.51$ MeV. The filtered simulation is compared to the experimental E_{rel} distribution (**b**) and shows remarkably good agreement of the shape of the E_{rel} spectrum. The simulated $\theta_{12} - \beta$ distribution (**c**) when compared to the experimental $\theta_{12} - \beta$ distribution **d** also shows good agreement. The total number of events in the simulation after filtering is the same as in the experimental distribution

distributions of events.[2] The caveats are that KOOKABURRA is a classical model, the slope of the transfer probability is not known, and that the angular distribution of events depends strongly on the input excitation energy probability distribution.

The total and filtered simulated E_{rel} distribution using KOOKABURRA for ^{7}Li(d,n)^{8}Be at $E_{\mathrm{lab}} = 2.51$ MeV, is shown in Fig. 8.4a. The energy of the ^{7}Li projectile corresponds to the energy of the beam in the experimental measurement after traversing half of the target thickness, and filtering has been done on the basis of the angular acceptance and energy threshold of the BALiN array. The filtered E_{rel} simulation compared to the experimental distribution (for the same total number of $\alpha + \alpha$ pairs) in Fig. 8.4b, and the simulated and experimental $\theta_{12} - \beta$ distributions

[2]Reference [3] discusses the excitation of ^{8}Be in terms of populations of the 0^{+}, 2^{+} and 4^{+} states. However, the 2^{+} and 4^{+} states are quite broad, and as can be seen in Fig. 2.5, different resonances can populate the same excitation energy. It is not clear how this issue was addressed in Ref. [3]. It is more natural to correct for the efficiency of BALiN on the basis of opening angle (and thus E_{rel}) and not assign a particular resonance to a particular excitation energy when the resonances are broad. This removes the sensitivity to the input resonance shape, the determination of which is especially problematic for broad resonances. However, to make a comparison with Ref. [3], the population of resonances will be estimated.

are shown in panels (c) and (d), respectively. The slope of the transfer function has been assumed to be the same for each resonance, and has been estimated as 1.2 fm^{-1}, as this value reproduces the data well, although varying the slope between 1 and 1.4 does not change the E_{rel} distribution in any significant way. The strength of each resonance has been chosen so to reproduce the relative fraction of events in $\theta_{12} < 30°$, $30° < \theta_{12} < 110°$ and $110° < \theta_{12} < 180°$, where the strength of the 0^+, 2^+ and 4^+ states, respectively, are strongest.

The simulated E_{rel} and $\theta_{12} - \beta$ distributions correspond fairly favourably with the experimental distributions. Thus, the total E_{rel} spectrum of the simulation (unfiltered by BALiN), shown in Fig. 8.4a is taken to represent the genuine distribution of fragments. In this total simulation, 9% of events arise through the 0^+ resonance, 22% of events arise through the 2^+ resonance, and 69% through the 4^+ resonance. The resonant structures of these states overlap. Experimentally only the relative energy is measured – an event with excitation of 8 MeV cannot be definitively assigned to either the 2^+ or the 4^+ resonance.[3] However, gating the simulation around the peak of each resonance in E_{rel} gives a close correspondence to the input to the simulation: 8% of events correspond to the 0^+ peak, 22% to the 2^+ peak, and 70% to the 4^+ peak. Regardless of the assignment of the resonance, it is clear that a large fraction of events are through highly excited ^{8}Be.

To the extent that ^{7}Li(d,n)^{8}Be is a good analogue for ^{7}Be(d,p)^{8}Be, this measurement indicates that ^{8}Be should be expected to be populated strongly in its 4^+ resonance in the ^{7}Be(d,p)^{8}Be reaction. Reference [3] puts an upper limit of 36% for the population of the 4^+ resonance in ^{7}Be(d,p)^{8}Be reactions at astrophysical energies. The result of 70% in the present measurement is in tension with that result, although for the mirror reaction. This experiment demonstrates the utility of measuring particles in coincidence with large solid angle detectors for reactions of astrophysical interest. More detailed information on the kinematics of the reaction is available, and there is a high sensitivity to the population of highly excited states of ^{8}Be, which were previously experimentally inaccessible and represent a significant fraction of the cross-section of this reaction. The cost of measuring particles in coincidence is that reliable efficiency determination becomes more challenging.

It is not immediately obvious how the population of ^{8}Be in its 0^+, $2^+$and 4^+ ground state band will change if it is populated by proton pickup with ^{7}Li or by neutron pickup with ^{7}Be. Measurements have not established the detail of the reaction mechanism for these reactions. ^{7}Be(d,p)^{8}Be and ^{7}Li(d,n)^{8}Be may proceed via a direct transfer of a nucleon or via fusion to form ^{9}B or ^{9}Be followed by emission of a proton or neutron. It is not clear that the mechanism will be identical in the two cases. As a result, the energy dependence of ^{7}Be(d,p)^{8}Be and ^{7}Li(d,n)^{8}Be may not be the same. In addition, the larger Q-value for ^{7}Be(d,p)^{8}Be of 16.67 MeV as opposed to 15.03 MeV in ^{7}Li(d,n)^{8}Be may result in population of the 16.626 MeV 2^+ state in ^{8}Be in the former reaction. However, this state has been interpreted as a single proton state, and so the population of this state via neutron pickup should be weak [8]. At slightly higher beam energies, but still in the astrophysically relevant region, the 16.922 MeV

[3] Indeed, there is a small probability that it arises through the tail of the 0^+ resonance.

state in ^{8}Be is likely to be strongly populated as it is known to be a single neutron state [8]. As demonstrated in this thesis, these aspects can be thoroughly investigated in the future through measurements of $\alpha + \alpha$ pairs in coincidence.

8.1.2 Measurements of d(^{9}Be,^{8}Be)t

A measurement of d(^{9}Be,^{8}Be)t was performed at $E_{\text{beam}} = 2.20$ MeV ($E_{\text{lab}} = 1.87$ MeV, $E/V_b = 0.50$) to investigate the experimental considerations required when there are three charged particles of similar mass and energy in the exit channel. In this measurement, 27881 coincidence level two events were measured, while there were 898 coincidence three events, representing just 3% of all events. Therefore, examining coincidence two events will prove more fruitful.

Time of flight information was not recorded in this measurement. However, kinematic considerations allow particles to be identified. The (θ_1, AE_1) distribution, after removal of spurious events, is shown in Fig. 8.5. The expected broad distribution of energy due to three body reactions can be seen, along with a relatively sharp band of events at $\theta_1 \sim 20°$ and $\theta_1 \sim 120°$ starting at $AE_1 \sim 5$ MeV. Like in the measurements with ^{12}C targets described in Chap. 4, these events are consistent with the two-body d(^{9}Be,^{7}Li)α reaction. After removing transfer reactions that result in two nuclei in the exit channel, the reconstructed coincidence events are shown in Fig. 8.6a assuming $\alpha + \alpha$ fragments and in Fig. 8.6b assuming $\alpha + t$ fragments. Under each assumption, a different subset of the data reconstructs to Q near the expected value of 4.68 MeV. By selecting those events that reconstruct as expected in each case, the identity of each particle identified in coincidence is assigned. Shown

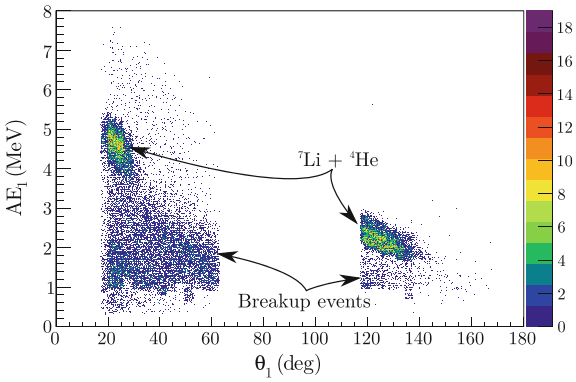

Fig. 8.5 (θ_1, AE_1) distribution for particles detected in coincidence in reactions of ^{9}Be with d at $E_{\text{beam}} = 2.20$ MeV. A broad distribution of events was measured, consistent with breakup leading to three particles in the exit channel, as well as a sharp distribution of events indicating a reaction producing two particles in the exit channel. The energy of these particles is consistent with the d(^{9}Be,^{7}Li)α reaction

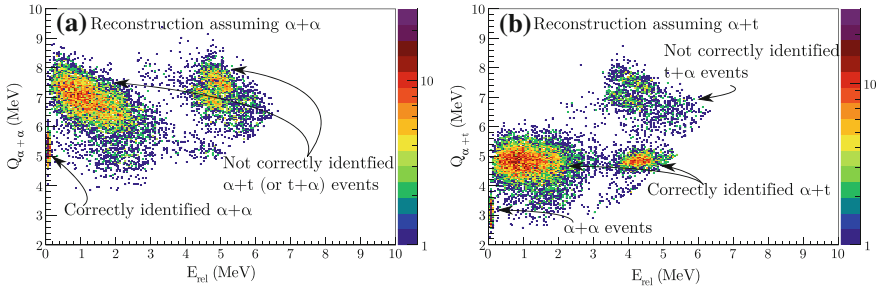

Fig. 8.6 Q-E_{rel} distribution of $\alpha + \alpha$ and $\alpha + t$ pairs measured in the reaction of ^{9}Be with d at $E_{\text{beam}} = 2.20$ MeV. **a** Q-E_{rel} distribution reconstructed assuming $\alpha + \alpha$ pairs were detected. An E_{rel}= 92 keV peak near the expected Q for this reaction indicates that these are $\alpha + \alpha$ events. At higher E_{rel} there are bands of events with strong slopes in $Q_{\alpha+\alpha}$, indicating that the assumption of $\alpha + \alpha$ for Q-E_{rel} reconstruction was incorrect. If Q-E_{rel} is reconstructed under the assumption that the events are $\alpha + t$ pairs, the distribution in **b** is seen. The straight bands of events near the expected Q indicate that they are indeed $\alpha + t$ pairs. The $\alpha + \alpha$ pairs that previously reconstructed to the correct Q are now at 3 MeV. An additional band of events with a strong band in $Q_{\alpha+t}$ corresponds to $\alpha + t$ pairs with reversed identity, that is, $t + \alpha$ pairs

in Fig. 8.7a is the E_{rel} distribution of the correctly identified fragments. This distribution is the combination of the E_{rel} for the $\alpha + \alpha$ pairs, and that for the $\alpha + t$ pairs. As expected, there is a sharp peak of events at 92 keV, corresponding to breakup through the ^{8}Be ground-state resonance. To understand the origin of the other peaks, KOOKABURRA simulations were performed, and the events were filtered through the geometry of BALiN. The broad peak centred around $E_{\text{rel}} \sim$ 1.5 MeV is likely to have two origins, a weak peak due to ^{8}Be breakup where both α fragments were detected from the ^{8}Be 2^{+} state (Fig. 8.7b), and a slightly lower E_{rel} peak due to $\alpha + t$ pairs produced after ^{8}Be was populated the same 2^{+} state, where one α fragment was detected in coincidence with the recoiling t (Fig. 8.7c). The peak at $E_{\text{rel}} \sim$ 4.5 MeV represents the relative energy between an α from the decay of ^{8}Be in its ground state and the recoiling t. This identification has been made assuming the particles have been produced in the d(^{9}Be,^{8}Be)t reaction. It is possible to produce $\alpha + \alpha$ and a triton in the exit channel via the d(^{9}Be,^{7}Li)α reaction, if ^{7}Li is populated above its direct breakup (^{7}Li$\rightarrow \alpha + t$) breakup threshold. As the same final state is produced, the Q for either reaction is identical, though the E_{rel} of the fragments should differ. KOOKABURRA simulations are consistent with reactions proceeding through d(^{9}Be,^{8}Be($\rightarrow \alpha + \alpha$))t, though simulations of d(^{9}Be,^{7}Li($\rightarrow \alpha + t$))α should also be performed.

The number of $\alpha + \alpha$ pairs detected in this d(^{9}Be,^{8}Be)t measurement is 1238, while the number of $\alpha + t$ pairs is 10 882. This suggests that the efficiency for detection of $\alpha + t$ pairs is much larger than $\alpha + \alpha$ pairs, which is supported by KOOKABURRA calculations. The fact that different pairs of events can be detected from the same reaction mechanism with very different efficiencies adds a level of complication to the data analysis for reactions such as d(^{9}Be,^{8}Be)t and ^{7}Be(d,p)^{8}Be.

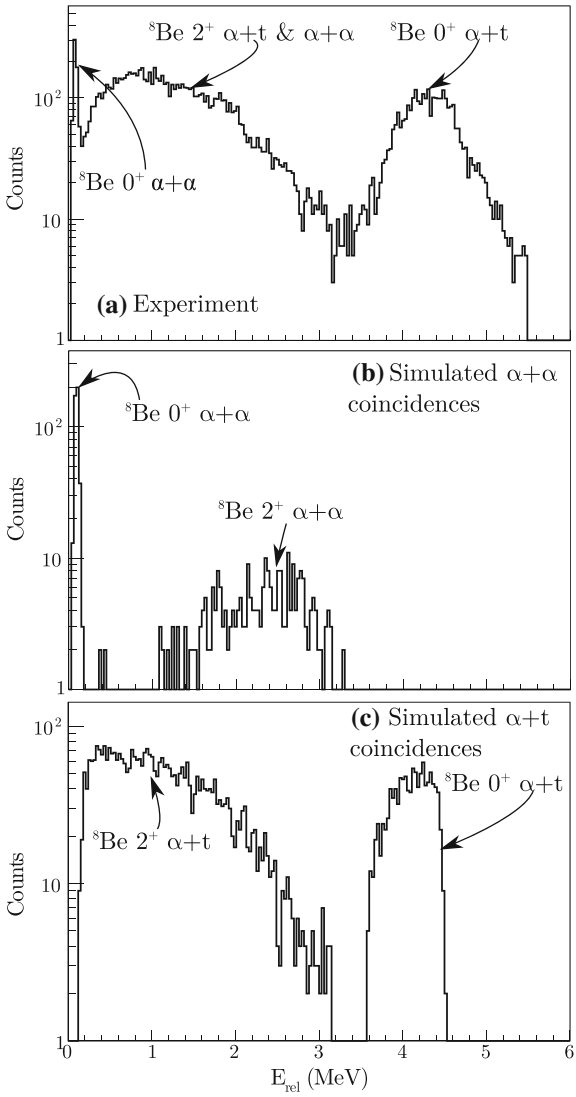

Fig. 8.7 Experimental E_{rel} distribution for reactions producing three particles in the reaction of ^{9}Be with d at $E_{beam} = 2.20$ MeV (**a**). Simulated filtered E_{rel} distribution of $\alpha + \alpha$ (**a**) and $\alpha + t$ (**b**) pairs within the acceptance of BALiN in the same reaction. By relating the simulated and experimental distributions, it is possible to identify the origins of the peaks in the experimental E_{rel} distribution. The sharp peak of events at 92 keV corresponds to the relative energy between $\alpha + \alpha$ pairs produced after the decay of ^{8}Be in its 0^+ ground state. The peak at ∼4.5 MeV corresponds to the relative energy between $\alpha + t$ pairs, where the α has been produced in the decay of ^{8}Be in its 0^+ ground state. The broad peak of events between 0.1 and 3 MeV corresponds to $\alpha + t$ and $\alpha + \alpha$ pairs produced through the population and decay of ^{8}Be in its first 2^+ resonance

However, the kinematic reconstruction of Q and E_{rel} provides a tool to distinguish these events, and further, simulations such as those done with KOOKABURRA can provide insight into the population of the projectile-like nucleus in this case.

8.2 ^{7}Be Beam Production Through ^{10}B(^{7}Li,^{7}Be)^{10}Be

After establishing the suitability of BALiN for measuring reactions such as ^{7}Be(d,p)^{8}Be, the second task is to produce the ^{7}Be beam. As has been mentioned, ^{7}Be is radioactive, with a half life of 53.2 days. As such, production of a ^{7}Be beam is not as straightforward as the production of the stable ^{7}Li and ^{9}Be beams used in the rest of this work.

For radioactive isotope with a fairly long half-life such as ^{7}Be, there are essentially two beam production techniques: on- and off-line. In off-line production, ^{7}Be is produced via the ^{7}Li(p,n)^{7}Be reaction using intense beams of protons incident on a ^{7}Li metallic target [9–11]. The resulting ^{7}Be is then chemically separated from ^{7}Li. This method enables relatively high intensity, high quality beams of ^{7}Be to be produced. However, there are some complications that make off-line production of ^{7}Be beams at the ANU impractical. Firstly, very high beam currents of protons ($\sim$20 μA) are required for a long period of time (two weeks). Secondly, the resulting sample has an activity of 20 GBq, and ANU lacks the appropriate radiochemistry facility. Thirdly, the use of a radioactive sample in the SNICS II ion source will contaminate it.

Therefore, ^{7}Be is better produced at the ANU using an online in-flight separation method, where beams of ^{7}Be are produced in a nuclear reaction, separated from other reaction products while in flight, then impinged on a secondary target. At other facilities, beams of ^{7}Be have been produced using this scheme, though the reaction mechanism differs. At high energies (800 MeV/nucleon), fragmentation of ^{11}B has been used to produce 99.9% pure ^{7}Be beams at Lawrence Berkeley Laboratory [12]. For lower energy beams, production via transfer reactions is preferable. At the Inter-University Accelerator Centre (IUAC), New Delhi, ^{7}Be beams were produced via the p(^{7}Li,^{7}Be)n inverse kinematics reaction, using a polypropylene foil target and ^{7}Li beam. The HIRA recoil mass separator was then used to separate the ^{7}Be beam from the ^{7}Li, resulting in beams of 10^{4} pps have been produced with 99% purity [13–15]. Similarly, at the Laboratori Nazionali di Legnaro (LNL, Italy), the EXOTIC facility has been used to produce 3×10^{5} pps beams of ^{7}Be via the p(^{7}Li,^{7}Be)n reaction, using a cryogenic H_2 gas target [16]. Also using a gas target, $10^{4} - 10^{5}$ pps ^{7}Be beams have been produced at the RIBRAS facility [17, 18] at the University of São Paulo with the ^{3}He(^{6}Li,^{7}Be)d reaction [19, 20]. At the University of Notre Dame, the Radioactive Nuclear Beam (RNB) facility[4] [23] was used to produce ^{7}Be beams through the ^{1}H(^{10}B,^{7}Be)^{4}He, ^{12}C(^{3}He,^{7}Be)^{8}Be and ^{10}B(^{6}Li,^{7}Be)^{9}Be reactions [24, 25], which had yields ranging between 3.3×10^{3} to 1.6×10^{4} pps.

At the ANU, the ^{10}B(^{6}Li,^{7}Be)^{9}Be reaction was chosen to be investigated initially. This is for several reasons: no cryogenic gas target is available at the ANU, which is needed for the p(^{7}Li,^{7}Be)n reaction. ^{3}He beams are not available at the ANU for use in the ^{12}C(^{3}He,^{7}Be)^{8}Be reaction. The experience using $(^{nat}C_2D_4)_n$ targets, which will be discussed below, and the resulting rapid thinning of the target with the use of a low ^{7}Li beam current led to reservations about using a polypropylene $(C_2H_6)_n$ target,

[4] A precursor to TwinSol, the current RIB facility at the University of Notre Dame [21, 22].

as used in Refs. [13–15] for the p(^{7}Li,^{7}Be)n reaction. Using a TiH_2 target was also ruled out as Ref. [25] reported migration of H_2 out of their TiH_2 target due to local target heating. On the other hand, ^{10}B is a much more robust target. Plentiful beams of ^{6}Li are available at the ANU HIAF, and so beam availability is not an issue in this reaction. Further, in Ref. [24], the authors propose that ^{10}B(^{6}Li,^{7}Be)^{9}Be should have the largest achievable beam currents out of those that they studied. Therefore, test measurements for the production of ^{7}Be through the ^{10}B(^{6}Li,^{7}Be)^{9}Be reaction were undertaken for this thesis work using the SOLEROO RIB facility at the ANU.

8.2.1 SOLEROO

SOLEROO (SOLenoidal Exotic Rare IsOtOpe separator) is a radioactive beam capability based on a 6.5 T superconducting solenoidal separator. SOLEROO is shown schematically in Fig. 8.8, and is described in detail in Refs. [26–28]. Radioactive ions of interest are produced through transfer reactions of an intense primary beam incident on a thick production target located near to the entry of the solenoid. Ions that have a scattering angle between 2° and 6° enter the solenoid, where they experience the strong axial magnetic field of the solenoid. The field is chosen such that the ions of interest are focused onto a secondary target located on-axis after the exit of the solenoid. The angular acceptance of the solenoid is restricted to 2–6° to reduce the secondary beam spot size and angular divergence to less than ±5°. An axial rod and adjustable blocking disks are used to block scattered particles with smaller magnetic rigidity than the beam of interest. With this single stage solenoidal separator, purities of up to 40% can be achieved [28]. This is not sufficient for reaction studies. At the RIBRAS and TwinSol facilities, an additional superconducting solenoid is used for further purification. At the ANU, beam identification and tagging is performed offline using a pair of Parallel Plate Avalanche Counters (PPACs) placed after the

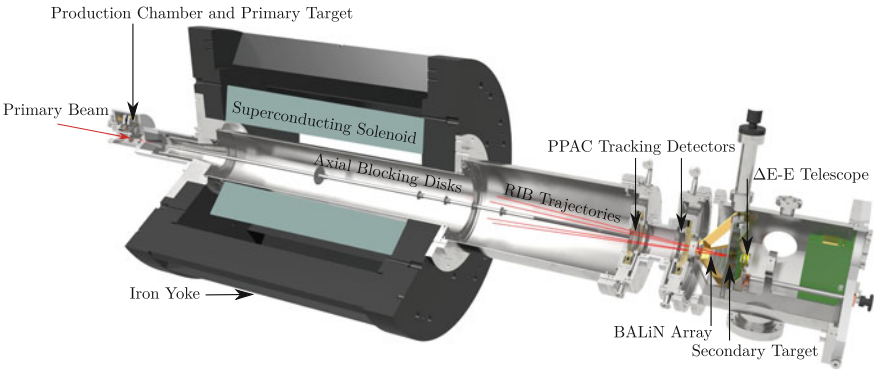

Fig. 8.8 Cross-sectional view of the SOLEROO RIB facility, described in text. Adapted from [27]

exit of the solenoid, with 150 mm spacing. The PPACs were developed by I.P. Carter in his PhD work [29]. Particles exiting the solenoid deposit energy in each PPAC that is proportional to $\frac{mZ^2}{E}$, and the ToF between each PPAC is $ToF = d\sqrt{\frac{m}{2E}}$. Increased separation by ToF can be achieved, if required, by the use of a pulsed beam from the 14UD. In this scheme, the ToF of each ion is measured between the target and one PPAC, increasing the flight path d to 1700 mm, and so the separation in ToF. However, this is at the expense of a lower primary beam intensity.

The combination of deposited energy and ToF allows the species of each ion to be identified in offline analysis. Further, the PPACs are position sensitive in both the x and y planes, with position resolution of $\leq$1 mm FWHM. Measuring the position of every ion in each PPAC enables the trajectory of each ion to be reconstructed, which is crucial for reaction studies, where the angle between the beam and scattered particle is relevant. We will also see that the position spectra can be used for further beam purification. The PPACs can operate at rates of $\sim 10^6$ Hz, allowing measurements with virtually pure RIBs of good intensity to be made. The SOLEROO facility has been used for the production of ^{6}He and ^{8}Li beams of intensity 7.38×10^4 cts/s/mg/cm^2/μeA and 5.14×10^5 cts/s/mg/cm^2/μeA respectively. The purity of the electronically identified ^{6}He and ^{8}Li beams is >95%. The BALiN array has been placed around the secondary target, and the first measurements of elastic scattering and breakup of ^{8}Li at the facility were performed as a part of I.P. Carter's PhD project [29].

For beam diagnostics, a $\Delta E - E$ telescope of ion implanted silicon detectors can be moved to just behind the secondary target position. The thickness of the ΔE and the E detector are 59.6 and 300 μm thick, respectively. This telescope, along with the PPACs, was used to examine the rate and purity of ^{7}Be beams produced through the ^{10}B(^{6}Li,^{7}Be)^{9}Be reaction at SOLEROO in a series of experiments in April and May of 2015.

In these experiments, a beam of 45 MeV ^{6}Li was delivered by the 14UD and impinged on a 145 μg/cm^2 production target of ^{10}B that was available from a different experiment. The thickness of the target is lower than what is required for useful RIB intensities, but it does allow for a study of the production of ^{7}Be. The beam intensity was lowered to 10 nA to prevent excessive rate in the $\Delta E - E$ telescope. The experimental considerations for production of a thick ^{10}B target that is required for a RIB measurement will be discussed at the end of this chapter. A test of the ^{6}Li beam showed that intensities of greater than 1 μA could be achieved on the production target. The beam energy of 45 MeV was chosen to ensure that particles were not stopped in the ΔE detector.

A sample $\Delta E - E$ spectrum is shown in Fig. 8.9 for a field strength of 2.7 T. The ^{7}Be ions are seen at a well defined peak in $\Delta E - E$, as indicated in the figure. A large amount of energy degraded elastically scattered ^{6}Li is seen, along with some ^{7}Li, presumably formed in the ^{10}B(^{6}Li,^{7}Li)^{9}B neutron stripping reaction. In addition, a large number of low energy α particles are transmitted through the solenoid. ^{7}Be represents 1% of the $\Delta E - E$ spectrum. The energy degraded elastic particles are not a problem in the production of the ^{6}He and ^{8}Li beams. This is because, unlike

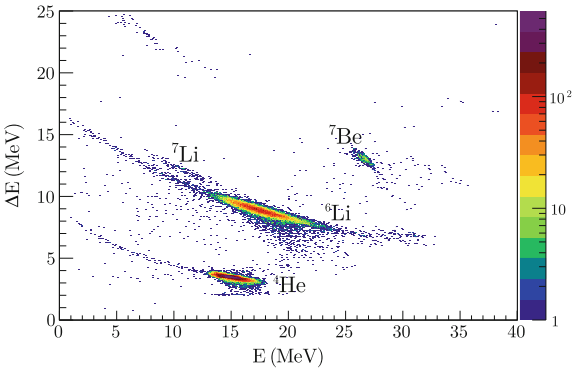

Fig. 8.9 $\Delta E - E$ spectrum for particles transmitted through the solenoid and focussed on the secondary target position for the ^{10}B(^{6}Li,^{7}Be)^{9}Be at a magnetic field of 2.7 T. The unique $\Delta E - E$ relationship for each species allows identification of each ion. A tightly grouped peak of ^{7}Be particles are focused on the detector, along with a large amount of elastically scattered ^{6}Li, ^{7}Li produced via neutron pickup, and ^{4}He produced in various reactions with the primary target. The amplifier threshold for the ΔE detector was set above the ΔE for p, d, t, and so none are seen in this spectrum

the ^{6}He and ^{8}Li secondary beams, the elastically scattered ^{6}Li has a larger magnetic rigidity than the ^{7}Be beam, and upstream scattering of ^{6}Li poses a more significant issue.

A field scan from 2.0 to 2.9 T was performed to determine the optimal magnetic field in the solenoid. ^{7}Be was identified in the $\Delta E - E$ spectrum, and successive measurements were made for a fixed integrated charge of 10^{-6} Coulombs. The resulting rate curve is shown in Fig. 8.10, where the ^{7}Be rate is normalised for the beam current and target thickness to units of cts/s/mg/cm^{-2}/μeA. The shape of this curve is due to the fact that the ^{9}Be is populated in discrete states. The total rate is larger than the sum of the rates for individual states at low magnetic fields. At these low fields, a low energy tail of ^{7}Be ions are transmitted through the solenoid that did not belong to an easily identifiable state. These ions contribute to the total ^{7}Be rate, but not to the rate curve of a specific state. A field of 2.7 T was chosen as the optimum field as only one state is transmitted through SOLEROO, allowing for good energy definition of the beam. However, since the field can be chosen to best transmit any of the states, this allows multiple secondary beam energies to be selected. A field of 2.3 T transmits ^{7}Be at an energy 10 MeV lower than the ^{7}Be beam at 2.7 T, a property that may become useful for the low energy beams required for astrophysical interest. The data were taken during the first ^{7}Be test run, where the Hevimet collimator that limits the angular acceptance of the solenoid to $2° \leq \theta \leq 6°$ [26] was displaced from its nominal location, reducing the angular acceptance of the solenoid and so reducing the beam intensity. This was rectified before the second ^{7}Be test run, increasing the beam intensities by a factor of 4.6 at 2.7 T. The rate curve has been normalised to the latter measurement, correcting for the effect of the Hevimet collimator.

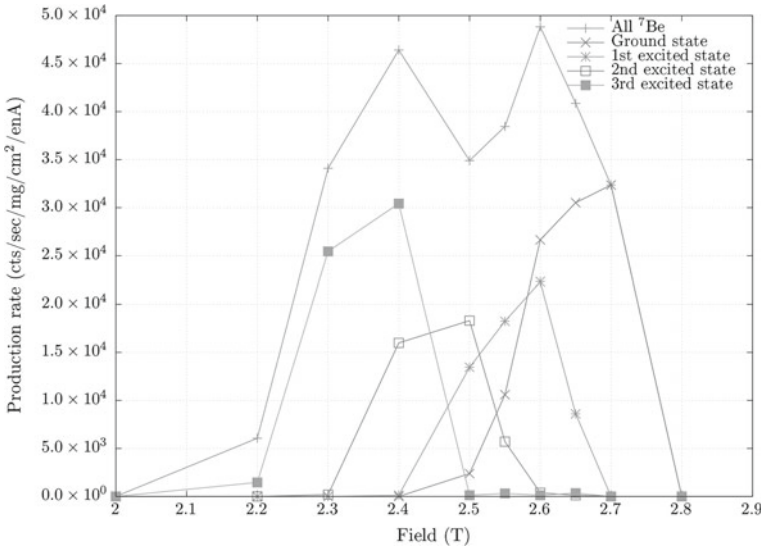

Fig. 8.10 Normalised production rate for ^{7}Be ions measured in the $\Delta E - E$ telescope for solenoid magnetic fields varying from 2 to 2.9 T, shown by the points. The lines guide the eye. The total ^{7}Be production rate is shown, along with the rates for the distinct groups of ^{7}Be ions seen in $\Delta E - E$

Of course, in a real measurement, beams cannot be purified with the $\Delta E - E$ telescope. The typical approach for beam purification is to gate on the energy deposited in one PPAC against the ToF between the PPACs. This spectrum is shown in Fig. 8.11a, for all events, and Fig. 8.11b for ^{7}Be identified in the $\Delta E - E$. An ellipse is shown in the same location on each spectrum to guide the eye. It is clear that a gate on Fig. 8.11a will not allow clear beam identification to be made – approximately 7% of the events in the ellipse can be identified as ^{7}Be in $\Delta E - E$. Plotting the energy deposited in one PPAC against the ToF between the PPAC and the primary target when a pulsed beam was used yields the spectrum shown in Fig. 8.11c. The ^{7}Be ions are indicated in the figure and shown in Fig. 8.11d. The increased flight path improves the separation, giving a beam purity of ∼84%. The remaining impurities are due to energy degraded ^{6}Li particles. It may be possible to improve the suppression of ^{6}Li by considering sources of scattering of ^{6}Li upstream from the solenoid, as well as any scattering inside the solenoid, from the warm bore, for example.

The beam purity can be further improved by using the position spectra of the PPAC closest to the secondary target. This can be done by first selecting ions with ToF less than 207 ns in the spectrum shown in Fig. 8.11c. This removes the bulk of the ^{4}He and ^{6}Li. The position spectrum for these ions is shown in Fig. 8.12. The central peak of events corresponds to ^{7}Be being focussed on the secondary target, and the less focussed events correspond to energy degraded ^{6}Li. The fact these events are so

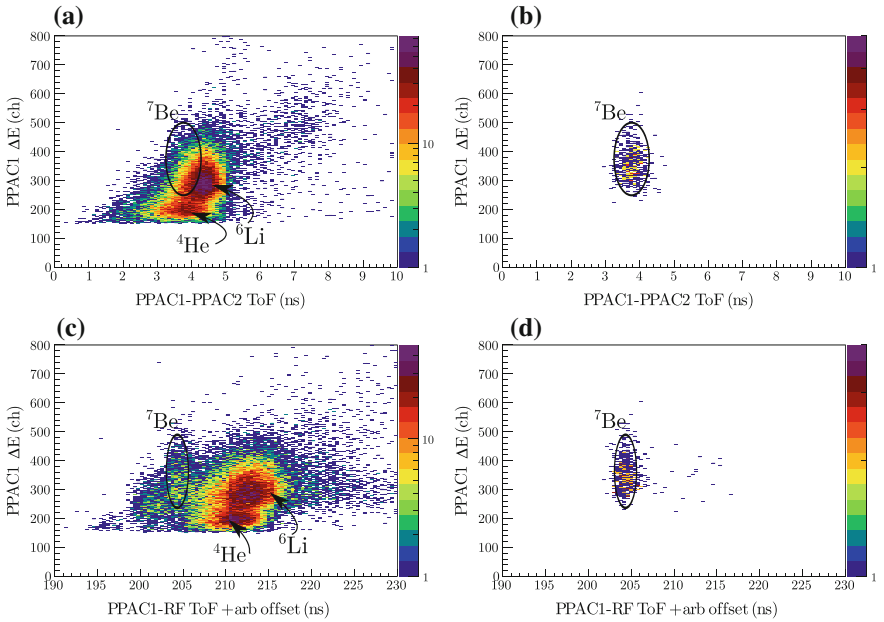

Fig. 8.11 For beam purification in an RIB experiment, the energy deposited in the PPACs and the ToF of particles is used. Shown in **a** is the energy deposited in the PPAC closest to the solenoid against the time of flight of each ion between the two PPACs. The position of the ^{7}Be ions, elastically scattered ^{6}Li and the ^{4}He ions produced in reactions are indicated. In **b**, the same quantities with a gate on the $\Delta E - E$ telescope shows the ^{7}Be ions cleanly. It is readily apparent that a gate on **a** will not cleanly identify the ^{7}Be ions. Shown in **c** is the energy deposited the PPAC closest to the solenoid against the time of flight of the ions between the target and the PPAC. **b** shows the same quantities, with a gate on $\Delta E - E$. The increased flight path improves the separation

distinctly grouped allows the PPAC position spectra to be used not only for trajectory reconstruction, but also for beam purification. Further, no tight gate is required in the ToF - PPAC ΔE spectrum shown in Fig. 8.11c. Gating on these events gives a beam purity of ∼96%, consistent with the beam purities found for ^{6}He and ^{8}Li beams, and a total ^{7}Be production rate of 3.22×10^{4} cts/s/mg/cm^{2}/μeA at a field of 2.7 T. Such production rates are reasonable for a measurement to be made using a bunched primary beam of sufficient energy and a sufficiently thick target. However, this production rate is for a 45 MeV ^{6}Li beam, which gives ^{7}Be at an energy that is far too high for measurements at BBN energies. Further work is required to investigate the production rate at lower energies.

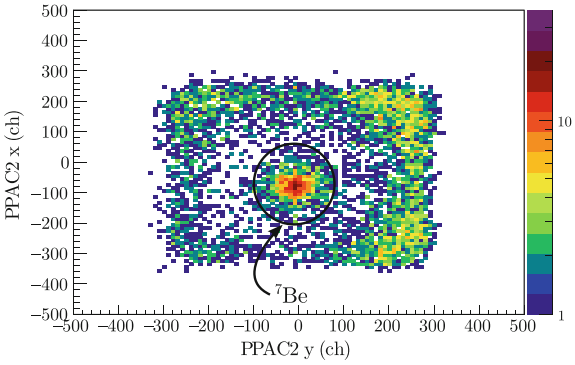

Fig. 8.12 Position spectrum in the PPAC closest to the secondary target of the events that have a measured ToF between PPAC1 and the target, shown in Fig. 8.11c of less than 207 ns. The central tight group of events corresponds to ^{7}Be. A gate on this spectrum allows for additional beam purification, and does not require the restrictive gate shown in Fig. 8.11c to be applied

8.3 Target Considerations

8.3.1 Deuterium Targets

In order to make measurements of ^{7}Li and ^{9}Be interactions with deuterium it was necessary to produce deuterium targets. As ANU does not currently have a gas target capability, the next best option was a thin deuterated polyethylene target $(C_2D_4)^n$. As reactions were performed near to or below the fusion barriers of ^{7}Li, ^{9}Be + d and thus far below the barrier for ^{7}Li, ^{9}Be + ^{12}C, reactions with carbon are not expected to contaminate the results. While polyethylene targets are not uncommon in nuclear physics experiments, no sufficiently thin commercial film was available. Literature exists concerning the production of thin film deuterated polyethylene targets [30, 31], but it was not possible to produce satisfactory films using the methods outlined without some modification.

Methods were initially tested using non-enriched high-density polyethylene $(C_2H_4)^n$. However it was found that it was not a good analogue to the behaviour of the deuterated polyethylene. To produce the deuterium targets, 20 mg of $(C_2D_4)^n$ pellets[5] were mixed with 5 g of Xylene in a small Erlenmeyer flask, and heated using a hot plate until all of the polyethylene was dissolved. The solution was mixed by swirling the flask occasionally during this time. The solution was then heated for a further thirty minutes. The flask was removed from the heat, and left to sit for ninety seconds. The solution was then poured on to room temperature new glass slides, and left to evaporate for twenty-four hours, leaving a film of polyethylene. Whilst the consistency of the films varied, there were sufficient areas of continuous film from which to produce targets. The film was then scored with a small scalpel blade, and

[5]Produced by Oak Ridge National Lab, 98.3% enriched.

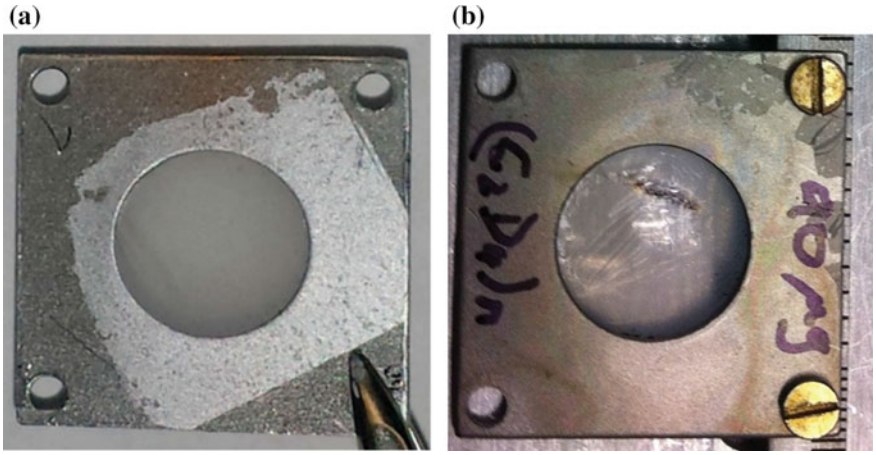

Fig. 8.13 Deuterated polyethylene targets. **a** Target before use. **b** Target after irradiation with 1 enA ^{9}Be beam for four hours, thinning and scorch marks are evident

floated off the glass substrate in distilled water. The films were then placed onto target frames with diameter 1/4" or 3/8". This method produced films between 80 and 200 μg/cm^2, the thicknesses of which were determined by measuring energy loss with the mixed α source described in Chap. 3. An example of a $(C_2D_4)^n$ target produced for the BELICK run is shown in Fig. 8.13a.

A key concern during measurements on polyethylene targets was the robustness of the targets under heavy ion irradiation, due to the low thermal and electrical conductivity of polyethylene. The degradation of the targets over the course of the run was monitored using the data acquisition system event rate as a proxy. The targets did degrade over time, and it was necessary to use multiple targets over the course of the experiment. Shown in Fig. 8.13b is a target after irradiation with a ^{9}Be beam of $\sim$1 enA for approximately four hours. As can be seen, the target has visibly thinned, and has a scorch mark. Over the course of the experiment, it was seen that targets placed on target frames with 1/4" diameter holes showed a slower rate of thinning compared to those on larger target frames, suggesting that the target frame acts as a heat-sink for the target, increasing the longevity.

8.3.2 Target Heating

Due to the large current required to be incident on the primary target for an acceptable production rate of ^{7}Be, the risk of damage to the primary ^{10}B target due to melting or oxidation was investigated. Boron has a very high melting point of 2349 K, whilst

oxides[6] begin to form at 600 K, peaking at 1000 K, though the reactivity is low [32]. The possible degradation of the target due to oxidation with any remaining air in the production chamber was of concern. Whilst SOLEROO has a rotating target capability in order to minimise local target heating [33], it was useful to first examine whether it will be required in this case. It would be advantageous if use of the rotating target wheel could be avoided, as the primary target could be made much smaller if it could be kept stationary.

To estimate the degree of target heating, consider a 1 eμA 23 MeV $^{6}Li^{3+}$ beam incident on a 2 mg/cm^2 ^{10}B target. According to SRIM [34] calculations, the energy loss of the beam through the target is 1.49 MeV. This corresponds to an incident power of 0.498 W. With a typical beam spot of radius $r = 0.5$ mm, the flux is 0.63 W/mm^2. If heat dissipates only via radiation, one can simply derive the equilibrium temperature of the target, as described by the Stefan–Boltzmann equation:

$$P = 2A\epsilon\sigma_b(T^4 - T_0^4), \tag{8.2}$$

where P is the incident power, A is the area of the beam-spot (here, we take the radius of the beam spot $r_{bs} = 0.5$ mm), ϵ the emissivity of boron ($\epsilon = 0.6$), σ_b is the Stefan–Boltzmann constant, T the target temperature, and T_0 room temperature. The factor of two accounts for radiation from both sides of the target. Solving for T, one obtains an equilibrium temperature of 1747 K. Certainly low enough that melting of the target due to heating by the beam is not of concern, but well above the temperature at which boron begins to oxidise.

It is not sufficient to only consider heat loss due to radiation. Due to the good thermal conductivity of boron, conduction of the heat from the beam-spot to the rest of the target and into the target frame will be a significant fraction of the heat loss. The equilibrium temperature in this case can be found in the solution to the time-dependent heat equation [35]

$$P = mC_v\frac{dT}{dt} + \lambda\frac{A}{d}(T(t) - T_o) + 2\epsilon\sigma_b A(T(t)^4 - T_0^4). \tag{8.3}$$

The left hand side represents heat brought into the target by the beam – the beam power P, while the right hand side represents the dissipation of energy. This equation is a consequence of energy conservation. The first term on the right hand side gives heat dissipation away from the beam-spot into the mass of the target, where $C_v = 1030$ J Kg^{-1}K^{-1} is the heat capacity, and m the mass of the target. It is this term that dictates how quickly the target temperature equilibrates. The second term is the conduction term, and is simply Fourier's law, where T_0 is the temperature of the heat-sink, λ the thermal conductivity of boron (27.4 W m^{-1}k^{-1}), A the area of the beam-spot (1 mm in diameter) and d the distance from the beam-spot to the heat-sink. Here, the target frame is in thermal contact with the environment, so we take a conservative beam-target frame distance of 1 cm as the distance to the heat

[6]The burning reaction is $4B + 3O_2 \rightarrow 2B_2O_3$.

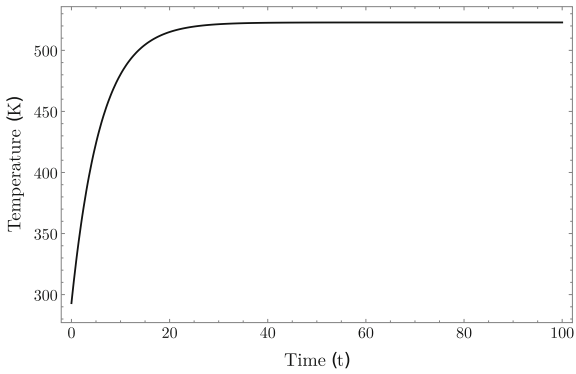

Fig. 8.14 Solution to Eq. 8.3. Calculated temperature of a 2 mg/cm^{-2} boron target as a function of time after the beam is incident. The temperature of the target at the beam spot equilibrates after ∼40 s at a temperature of 522 K

sink. The third term is the Stefan–Boltzmann law for radiative cooling, as shown in Eq. 8.2. Solving this expression for $T(t)$ gives the temperature of the boron target at the beam-spot as a function of time, and is shown in Fig. 8.14. Including cooling via conduction results in a lower equilibrium temperature that is on the order of 522 K, which is much lower than the melting point of boron. It is approaching the point at which boron begins to oxidise, but the rate is very low at this temperature [32]. This means that a rotating target is not required allowing smaller, simpler to produce, targets to be fabricated

In addition, this predominance of the effects of heat loss through conduction rather than radiation furthers the hypothesis in Sect. 8.3.1 that the size of the target frame had an impact on target longevity – the proximity of the heat-sink to the beam spot decreased the equilibrium temperature of the deuterated target.

8.3.3 Proposed Methods for the Production of Thick ^{10}B and $(^{nat}C_2D_4)_n$ Targets

In RIB measurements, the secondary beam is much less intense and much larger in diameter than a stable beam. As a result, the secondary target must be thicker and larger than would be used for a corresponding stable beam experiment. In addition, to obtain the best beam intensity, the ^{10}B production target must be thick. Before measuring the ^{7}Be(d,p)^{8}Be reaction with SOLEROO and BALiN using the ^{10}B (^{6}Li,^{7}Be)^{9}Be production reaction, thick targets of ^{10}B and $(^{nat}C_2D_4)_n$ will have to be made. Here proposed methods for the production of both will be discussed briefly.

8.3.3.1 ^{10}B

A production ^{10}B target should have an areal density on the order of 1 mg/cm^{-1}. Boron is a metalloid, and therefore isn't sufficiently ductile for a target produced

by rolling. Electron beam vapour deposition is appropriate for thin targets, but is very slow for the thick targets required for this work. The high melting point of boron, discussed above, makes target production via evaporation challenging, as very high temperatures are required. Thin boron targets have been previously made via evaporation [36–38]. In Refs. [36, 38], the boron was heated in a carbon "boat" with molybdenum auxiliary components that ensure low resistance except for in the centre of the boat. It has been argued that carbon boats are superior to other boats made of high melting point materials such as tungsten (used in Ref. [37]), as reactions with boron form a thin film of boron carbide around the boat, which has a higher melting point than elemental boron, protecting the boat. This method may be used for the production of thick boron targets at the ANU.

8.3.3.2 $(^{nat}C_2D_4)_n$

The method for $(^{nat}C_2D_4)_n$ target production, described at the beginning of this section, was optimised for the production of targets with areal density between 90 and 200 μg/cm^2. The surface tension between the xylene and $(^{nat}C_2D_4)_n$ solution and the glass microscope slide limits the amount of solution poured on the slide, resulting in the desired thin films. For thicker targets, on the order of 1 mg/cm^{-1}, a slightly different method will have to be used. The method of Ref. [39] seems promising. A level mould, in the desired shape and size of the final target, with a tantalum substrate is placed in a heated oil bath at 120°. A xylene and $(^{nat}C_2D_4)_n$ solution, prepared as discussed above, is poured into the mould and the xylene allowed to evaporate. The mould enables a thick target to be produced, and the oil bath results in target uniformity by preventing the polyethylene from dropping out of solution too quickly.

References

1. Parker, P.D.: Comments on the destruction of ^{7}Be in the solar interior. Astrophys. J. **175**, 261 (1972)
2. Coc, A., Vangioni-Flam, E., Descouvemont, P., Adahchour, A., Angulo, C.: Updated big bang nucleosynthesis compared with known Wilkinson microwave anisotropy probe observations and the abundance of light elements. Astrophys. J. **600**, 544 (2004)
3. Angulo, C., Casarejos, E., Couder, M., Demaret, P., Leleux, P., Vanderbist, F., Coc, A., Kiener, J., Tatischeff, V., Davinson, T., Murphy, A., Achouri, N., Orr, N., Cortina-Gil, D., Figuerra, P., Fulton, B., Mukha, I., Vangioni, E.: The ^{7}Be(d, p)2α cross section at Big Bang energies and the primordial ^{7}Li abundance. Astrophys. J. Lett. **630**(2), 105 (2005)
4. Tilley, D., Cheves, C., Godwin, J., Hale, G., Hofmann, H., Kelley, J., Sheu, C., Weller, H.: Energy levels of light nuclei A = 5,6,7. Nucl. Phys. A **708**, 3 (2002)
5. Machleidt, R., Slaus, I.: The Nucleon-Nucleon Interaction. J. Phys. G: Nucl. Part. Phys. **27**, R69 (2001)
6. Audi, G., Kondev, F., Wang, M., Pfeiffer, B., Sun, X., Blachot, J., MacCormick, M.: The Nubase 2012 evaluation of nuclear properties. Chin. Phys. C. **36**(12), 1157 (2012)
7. Steigman G. *Big bang nucleosynthesis: probing the first 20 minutes*. Carnegie Observatories Astrophysics Series, Vol. 2: Measuring and Modeling the Universe, **2**, 169 (2004)

8. Marion, J.B., Wilson, M.: The ^{7}Li(p,γ)^{8}Be reaction and single-particle levels in ^{8}Be. Nucl. Phys. **77**, 129 (1966)
9. Gialanella, L., Greife, U., Cesare, N.D., Dõonofrio, A., Romano, M., Campajola, L., Formicola, A., Fulop, Z., Gyurky, G., Imbriani, G., Lubritto, C., Ordine, A., Roca, V., Rogalla, D., Rolfs, C., Russo, M., Sabbarese, C., Somorjai, E., Strieder, F., Terrasi, F., Trautvetter, H.P.: Off-line production of a ^{7}Be radioactive ion beam. Nucl. Instrum. Methods Phys. Res. B **197**, 150 (2002)
10. Limata, B.N., Gialanella, L., Leva, A.D., Cesare, N.D., D'Onofrio, A., Gyurky, G., Rolfs, C., Romano, M., Rogalla, D., Rossi, C., Russo, M., Somorjai, E., Terrasi, F.: ^{7}Be radioactive beam production at CIRCE and its utilization in basic and applied physics. Nucl. Instrum. Methods Phys. Res. B **266**(10), 2117 (2008)
11. Gialanella, L., Strieder, F., Campajola, L., D'Onofrio, A., Greife, U., Gyurky, G., Imbriani, G., Oliviero, G., Ordine, A., Roca, V., Rolfs, C., Romano, M., Rogalla, D., Sabbarese, C., Somorjai, E., Terrasi, F., Trautvetter, H.: Absolute cross section of p(^{7}Be,γ)^{8}B using a novel approach. Eur. Phys. J. A **7**(3), 303 (2000)
12. Tanihata, I., Hamagaki, H., Hashimoto, O., Shida, Y., Yoshikawa, N., Sugimoto, K., Yamakawa, O., Kobayashi, T., Takahashi, N.: Measurements of interaction cross sections and nuclear radii in the light p-shell region. Phys. Rev. Lett. **55**(24), 2676 (1985)
13. Barua, S., Das, J., Jhingan, A., Varughese, T., Madhavan, N., Sugathan, P., Verma, S., Kalita, K., Bhattacharjee, B., Datta, S., Boruah, K.: Study of elastic scattering of mirror nuclei ^{7}Be + ^{7}Li. Nucl. Phys. A **746**, 467 (2004)
14. Verma, S., Das, J.J., Jhingan, A., Kalita, K., Barua, S., Golda, K.S., Madhavan, N., Sugathan, P., Nath, S., Varughese, T., Gehlot, J., Mandal, S., Sahu, P.K., John, B., Nayak, B.K., Jha, V., Saxena, A., Datta, S.K., Singh, R.: Interaction of loosely bound radioactive 7Be and stable 7Li with 9Be. Eur. Phys. J. A **44**(3), 385 (2010)
15. Kalita, K., Verma, S., Singh, R., Das, J., Jhingan, A., Madhavan, N., Nath, S., Varughese, T., Sugathan, P., Parkar, V.V., Mahata, K., Ramachandran, K., Shrivastava, A., Chatterjee, A., Kailas, S., Barua, S., Basu, P., Majumdar, H., Sinha, M., Bhattacharya, R., Sinha, A.: Elastic scattering and fusion cross sections for ^{7}Be,^{7}Li+^{27}Al systems. Phys. Rev. C **73**(2), 024609 (2006)
16. Mazzocco, M., Torresi, D., Fierro, N., Acosta, L., Boiano, A., Boiano, C., Glodariu, T., Guglielmetti, A., Commara, M.L., Martel, I., Mazzocchi, C., Molini, P., Pakou, A., Parascandolo, C., Parkar, V.V., Patronis, N., Pierroutsakou, D., Romoli, M., Sanchez-Benitez, A.M., Sandoli, M., Signorini, C., Silvestri, R., Soramel, F., Stiliaris, E., Strano, E., Stroe, L., Zerva, K.: Scattering process for the system ^{7}Be + ^{58}Ni at 23.2 MeV beam energy. J. Phys.: Conf. Ser. **420**, 012077 (2013)
17. Lépine-Szily, A., Lichtenthäler, R., Guimarães, V., Arazi, A., Barioni, A., Benjamim, E.A., de Faria, P.N., Descouvemont, P., Gasques, L.R., Mendes, D.R., Morais, M.C., Morcelle, V., Moro, A.M., Condori, R.P., Pires, K.C.C., Rodriguez-Gallardo, M., Scarduelli, V., Shorto, J.M.B., Zamora, J.C.: Recent results on reactions with radioactive beams at RIBRAS (Radioactive Ion Beams in Brazil). J. Phys.: Conf. Ser. **590**(1), 012012 (2015)
18. Lichtenthäler, R., Lépine-Szily, A., Guimar, Aes V., Perego, C., Placco, V., Camargo, O., Denke, R., De Faria, P.N., Benjamim, E.A., Added, N., Lima, G.F., Hussein, M.S., Kolata, J., Arazi, A.: Radioactive ion beams in Brazil (RIBRAS). Eur. Phys. Journal. A **25**(s01), 733 (2005)
19. Morcelle, V., Lichtenthäler, R., Linares, R., Morais, M.C., Guimarães, V., Lépine-Szily, A., Gomes, P.R.S., Lubian, J., Mendes Junior, D.R., De Faria, P.N., Barioni, A., Gasques, L.R., Shorto, J.M.B., Pires, K.C.C., Zamora, J.C., Condori, R.P., Scarduelli, V., Kolata, J.J., Amro, H., Becchetti, F.D., Jiang, H., Aguilera, E.F., Lizcano, D., Martinez-Quiroz, E., Garcia, H.: Elastic scattering and total reaction cross section for the ^{7}Be+^{27}Al system at near-barrier energies. Phys. Rev. C **89**(4), 044611 (2014)
20. Lichtenthäler, R., Alvarez, M.A.G., Lépine-Szily, A., Appannababu, S., Pires, K.C.C., da Silva, U.U., Scarduelli, V., Condori, R.P., Deshmukh, N.: RIBRAS: the facility for exotic nuclei in Brazil. Few-Body Syst. **57**(3), 157 (2016)

21. Lee, M.Y., Becchetti, F.D., O'Donnell, T.W., Roberts, D.A., Zimmerman, J.A., Guimarães, V., Kolata, J.J., Peterson, D., Santi, P., DeYoung, P.A., Peaslee, G.F., Hinnefeld, J.D.: Study of nuclear reactions with intense, high-purity, low-energy radioactive ion beams using a versatile multi-configuration dual superconducting-solenoid system. Nucl. Instrum. Methods Phys. Res. A **422**(1–3), 536 (1999)
22. Becchetti, F.D., Lee, M.Y., O'Donnell, T.W., Roberts, D.A., Kolata, J.J., Lamm, L.O., Rogachev, G., Guimarães, V., DeYoung, P.A., Vincent, S.: The TwinSol low-energy radioactive nuclear beam apparatus: status and recent results. Nucl. Instrum. Methods Phys. Res. A **505**, 377 (2003)
23. Kolata, J.J., Morsad, A., Kong, X.J., Warner, R.E., Becchetti, F.D., Liu, W.Z., Roberts, D.A., Jänecke, J.W.: A radioactive beam facility using a large superconducting solenoid. Nucl. Instrum. Methods Phys. Res. B **40–41**, 503 (1989)
24. Becchetti, F.D., Brown, J.A., Ashktorab, K., Jänecke, J.W., Liu, W.Z., Roberts, D.A., Smith, R.J., Kolata, J.J., Lamkin, K., Morsad, A., Warner, R.E.: Production and use of ^{6}He, ^{7}Be, ^{7}Li, ^{12}B and metastable nuclear beams. Nucl. Instrum. Methods Phys. Res. B **56**, 554 (1991)
25. Smith, R.J., Kolata, J.J., Lamkin, K., Morsad, A., Ashktorab, K., Becchetti, F.D., Brown, J., Janecke, J., Liu, W., Roberts, D.: Production and use of radioactive ^{7}Be beams. Nucl. Instrum. Methods Phys. Res. A **294**, 26 (1990)
26. Rafiei, R., Hinde, D.J., Dasgupta, M., Weisser, D.C., Muirhead, A.G., Harding, A.B., Cooper, A.K., Wallace, H.J., Lobanov, N.R., Wakhle, A., Brown, M.L., Lin, C.J., Horsley, A.J., Du Rietz, R., Luong, D.H., Evers, M.: SOLEROO: a solenoidal exotic rare isotope separator at the Australian National University. Nucl. Instrum. Methods Phys. Res. A **631**(1), 12 (2011)
27. Carter, I.P., Ramachandran, K., Dasgupta, M., Hinde, D.J., Rafiei, R., Luong, D.H., Williams, E., Cook, K.J., McNeil, S., Rafferty, D.C., Harding, A.B., Muirhead, A.G., Tunningley, T.: An ion beam tracking system based on a parallel plate avalanche counter. EPJ Web of Conf. **63**, 02022 (2013)
28. Carter, I.P., Dasgupta, M., Hinde, D.J., Luong, D.H., Williams, E., Ramachandran, K., Cook, K.J., Muirhead, A.G., Marshall, S., Tunningley, T.: Recent developments of SOLEROO: Australia's first high energy radioactive Ion Beam capability. EPJ Web Conf. **91**, 00001 (2015)
29. Carter, I.P. Developing techniques for high fidelity studies of reactions with light weakly bound nuclei. Ph.D. Thesis, The Australian National University (2016)
30. Tripard, G.E.: Preparation of thin film deuterated polyethylene targets. Rev. Sci. Instrum. **38**(3), 435 (1967)
31. Matsuki, S., Yasue, M., Yamashita, S.: A method for preparing thin films of deuterated polyethylene. Nucl. Instrum. Methods **94**, 387 (1971)
32. Wang, Y., Fan, J., Trenary, M.: Surface chemistry of boron oxidation. 1. Reactions of oxygen and water with boron films grown on Ta(ll0). Chem. Mater. **5**, 192 (1993)
33. Rafiei, R.: Dynamics of Breakup and Quasifission - Mechanisms Inhibiting Fusion. Ph.D. thesis, The Australian National University (2010)
34. Ziegler, J.F.: Stopping Range of Ions in Matter (SRIM-2012) (2012). http://www.srim.org/
35. Greene, J.P., Gabor, R., Heinz, A.: Calculations of damage to rotating targets under intense beams for super-heavy element production. In: Application of Accelerators in Research and Industry: 17th International Conference, pp. 775–780 (2003)
36. Safford, G.J.: Improved technique for the evaporation of boron. Rev. Sci. Instrum. **27**(1956), 972 (1956)
37. McElligott, P.E., Roberts, R.W.: Preparation and characterization of evaporated boron films. J. Appl. Phys. **37**(5), 1992 (1966)
38. Hill, H.A.: Evaporation of boron. Rev. Sci. Instrum. **27**(1956), 1086 (1956)
39. Katz, J., Connell, K.O., Fletcher, K., Geneseo, S., Frenje, J., Casey, D.: Preparation of deuterated polymer films for the omega magnetic recoil spectrometer. In: 49th Annual Meeting of the APS Division of Plasma Physics (2007)

Chapter 9
Conclusions and Outlook

Coming back to where you started is not the same as never leaving

Sir Terry Pratchett 1948–2015

The work in this thesis was centred around four key aims: (1) to identify the modes of breakup seen in interactions of ^{7}Li and ^{9}Be with light targets of $6 \leq Z \leq 28$; (2) to investigate the kinematic signatures of breakup through short-lived resonant states; (3) to quantitatively predict the effect of breakup from short-lived resonant states on incomplete fusion at above-barrier energies; and (4) to explore the use of coincidence measurement and reconstruction techniques developed for the study of breakup to measure the astrophysically relevant ^{7}Be(d, p)^{8}Be reaction. Progress towards addressing these goals is summarised here, and future directions discussed.

9.1 Suppression of Complete Fusion by Breakup

9.1.1 Breakup Mechanisms

To interrogate the mechanisms and timescales of breakup in reactions of ^{9}Be and ^{7}Li, coincidence measurements of charged particles produced in reactions of ^{9}Be and ^{7}Li with low ($6 \leq Z \leq 28$) Z targets were performed at below-barrier energies. The measurements were performed with the large solid angle, highly pixelated BALiN array allowing key kinematic quantities to be reconstructed. Time-of-flight analysis techniques were implemented for the first time using the BALiN array, allowing clear of separation breakup modes that are not kinematically distinct, which is important in reactions with some medium mass targets.

Furthering the work of Refs. [1–4], it was shown that transfer-triggered breakup dominates over direct breakup over all Z_T from ^{2}H to ^{209}Bi. Indeed, while direct

K. J. Cook, *Zeptosecond Dynamics of Transfer-Triggered Breakup*,
Springer Theses, https://doi.org/10.1007/978-3-319-96017-3_9

breakup (^{9}Be$\rightarrow \alpha + \alpha + n$, ^{7}Li$\rightarrow \alpha + t$) has been observed in below-barrier reactions of ^{9}Be and ^{7}Li with high Z targets [1–4], it vanishes in reactions with $1 \leq Z \leq 28$ targets.

Consistent with the breakup modes observed in reactions of ^{9}Be with nuclei from ^{144}Sm to ^{209}Bi, the dominant breakup mode in reactions of ^{9}Be with ^{12}C, ^{27}Al and ^{28}Si is neutron stripping (^{8}Be $\rightarrow \alpha + \alpha$). In addition, in reactions with ^{27}Al and ^{28}Si, small yields of $\alpha + p$ pairs were measured, populating distinct peaks in ^{31}S and ^{32}P. The transfer Q-value for the production of $\alpha + p$ pairs is highly positive in these reactions, unlike for reactions with ^{12}C and ^{144}Sm, ^{168}Er, ^{186}W, ^{196}Pt, ^{208}Pb and ^{209}Bi, where the Q-values are highly negative. The presence of $\alpha + p$ pairs, even though a large number of nucleons must be transferred is a demonstration that highly positive transfer Q-values drive transfer triggered breakup probabilities.

In reactions of ^{7}Li with ^{58}Ni, the dominant breakup mode is two neutron stripping forming unbound ^{5}Li$\rightarrow \alpha + p$, followed by proton pickup (^{8}Be $\rightarrow \alpha + \alpha$) and neutron stripping forming ^{6}Li above its breakup threshold (^{6}Li $\rightarrow \alpha + d$). On the other hand, for reactions of ^{7}Li with ^{28}Si two neutron stripping and proton pickup are found in almost equal amounts, while in reactions of ^{7}Li with ^{27}Al, proton pickup dominates by a factor of two over two neutron stripping. The only breakup mode observed for reactions of ^{7}Li with ^{16}O was proton pickup forming $\alpha + \alpha$ pairs. Strong $\alpha + p$ breakup was seen in reactions of ^{7}Li with ^{12}C, followed by a smaller yield of $\alpha + \alpha$ pairs. The variation between these results is again indicative of the key role of target structure and transfer Q-value in breakup mechanisms.

It would be interesting to examine the trends of breakup in intermediate Z targets to "fill in the gaps" between the previous work on high Z targets and the present work. In particular, direct breakup was seen to be present in reactions with high Z targets, it is not seen with low Z targets. Further, transfer-triggered breakup probabilities depend on the transfer Q-value, as well as the structure of the target and projectile nuclei. In addition to intermediate Z targets, a re-analysis of the work of Refs. [1–3] where breakup was studied in reactions of ^{6,7}Li with ^{144}Sm, ^{207,208}Pb and ^{209}Bi, with the improved efficiency correction method described in this work may provide insight into the role of transfer Q-value and target structure in the dominant mode of transfer-triggered breakup.

9.1.2 Prompt and Asymptotic Breakup

To determine the effect of breakup on complete and incomplete fusion it is not sufficient to simply know the probability of any given breakup mode: the lifetime of the state populated in breakup is also important. It has been well established that transfer populating (long-lived) narrow resonances cannot suppress complete fusion. It was shown in this thesis that attention must also be given to the (sub-zeptosecond) lifetime of broad resonances. At below-barrier energies, these timescales are experimentally accessible by comparison of experimental $\theta_{12} - \beta$ distributions with model calculations. Explicit inclusion of excitation energies and lifetimes of unbound resonances

are crucial to model breakup and fusion. In the absence of a quantum mechanical model of transfer-triggered breakup, they have been included by modifying the classical dynamical code PLATYPUS (resulting in M- PLATYPUS), and by the creation of a new model KOOKABURRA which simulates the transfer step. Explicit inclusion of resonant state lifetimes in M- PLATYPUS and KOOKABURRA resulted in a significant improvement over PLATYPUS in the correspondence of simulated energy and angular correlations to those from experiment. Further, it was also shown that variation of the lifetime of the 2^+ state of ^{8}Be by as little as a factor of two was apparent in the simulated $\theta_{12} - \beta$ simulations. While comparison of KOOKABURRA and M- PLATYPUS simulations with experiment were generally favourable, there is scope for improvement via the inclusion of additional physical effects. For example, the role of the target nucleus in inducing a preferential orientation in the projectile-like nucleus may be investigated through the reconstructed azimuthal orientation of breakup fragments with respect to the reaction plane γ. In addition the role of the target in modifying the mean lifetime of resonant states should be examined.

9.1.3 Breakup Functions and ICF

Using these new models that explicitly include the lifetime and excitation energies of unbound states, together with an improved (and intricate) coincidence efficiency correction procedure, below-barrier breakup probability functions were extracted for reactions of ^{9}Be with ^{27}Al, ^{28}Si, ^{144}Sm, ^{168}Er, ^{186}W, ^{196}Pt, ^{208}Pb, ^{209}Bi and ^{7}Li with ^{27}Al, ^{28}Si, and ^{58}Ni. It was shown that near-target breakup probability functions have a steeper slope than asymptotic breakup associated with the long-lived states of ^{8}Be and ^{6}Li. To make quantitative predictions of complete fusion suppression at above-barrier energies, the breakup functions were used as input into M- PLATYPUS and KOOKABURRA.

Above the barrier, the inclusion of sub-zeptosecond lifetimes significantly reduce the predicted above-barrier complete fusion suppression. This occurs because a larger fraction of nuclei remain intact until reaching the barrier. As a result, predicted complete fusion cross-sections are not suppressed to the extent expected from earlier calculations that do not explicitly include lifetimes. This result is expected to apply to weakly-bound nuclei in general.

In reactions of ^{9}Be with ^{144}Sm, ^{168}Er, ^{186}W, ^{196}Pt, ^{208}Pb and ^{209}Bi, calculations with M- PLATYPUS that explicitly include sub-zeptosecond lifetimes resulted in incomplete fusion to total fusion fractions $F_{\mathrm{ICF}} = \sigma_{\mathrm{ICF}}/(\sigma_{\mathrm{CF}} + \sigma_{\mathrm{ICF}})$ of $\sim$11% at above-barrier energies. The related complete fusion suppression of $\sim$9% is much less than the experimentally measured F_{ICF} and complete fusion suppressions of 30−40% [5–7]. In reactions of both ^{7}Li and ^{9}Be with light mass targets, the predicted F_{ICF} were much higher, varying from 16% for reactions of ^{7}Li + ^{58}Ni to 28% for reactions of ^{7}Li + ^{28}Si. As no experimental measures of F_{ICF} exist for these systems, it is difficult to evaluate these results in the context of the role of breakup in complete fusion suppression. These results may indicate another role of lifetime:

the reaction timescale may be significantly longer for, say, ^{9}Be + ^{27}Al as compared to ^{9}Be + ^{209}Bi due to the weaker gradient of the interaction potential. As a result, unbound states with the same mean life will have greater opportunity to break up prior to capture for ^{9}Be + ^{27}Al reactions than for ^{9}Be + ^{209}Bi reactions.

The above-barrier fusion cross-sections for reactions with light target nuclei also bring into question the use of F_{ICF} as an empirical measure of complete fusion suppression. It was seen that F_{ICF} was reduced compared to $1 - \sigma_{CF}^{\text{With BU}}/\sigma_{fus}^{\text{No BU}}$ in reactions with ^{27}Al, ^{28}Si and ^{58}Ni, with an associated reduction of total fusion. This contrasts to what was seen in reactions of ^{9}Be with ^{144}Sm to ^{209}Bi, where F_{ICF} was very similar to $1 - \sigma_{CF}^{\text{With BU}}/\sigma_{fus}^{\text{No BU}}$. This "uncoupling" of F_{ICF} and $1 - \sigma_{CF}^{\text{With BU}}/\sigma_{fus}^{\text{No BU}}$ in light systems is likely due to trajectories that lead to no capture breakup that would have otherwise fused, and is consistent with the observed increase of the reaction cross-section observed in reactions of ^{9}Be with ^{27}Al [8], although no clear suppression of total fusion has been observed. This is the first use of KOOKABURRA for above-barrier fusion cross-sections for reactions with light targets, and the role of model sensitivities in ICF and CF should be investigated.

The key consequence of the inclusion of the lifetime of broad resonant states is a reduction of the predicted F_{ICF} and reduced suppression of complete fusion due to breakup to a level that is well below that observed in experiment wherever experimental results are available. Three key conclusions are drawn from this result:

(1) As the calculated F_{ICF} is much less than measured, the cross-sections that are attributed experimentally to ICF may include a significant contribution from transfer directly producing the same heavy nucleus.

(2) If σ_{ICF} contains contributions from both ICF and transfer, it is not clear that defining an empirical complete fusion suppression F_{ICF} in terms of σ_{ICF} is valid.

(3) The observed reduction of complete fusion at above-barrier energies has been measured independently of σ_{ICF} in several reactions through direct comparison with reactions of well bound nuclei [6, 9]. Since the results from this study shows that breakup cannot explain this, then other processes must contribute. Experimental values of F_{ICF} and $1 - \sigma_{CF}^{\text{expt.}}/\sigma_{fus.}^{\text{calc.}}$ have been found to be similar [6] in reactions of ^{9}Be with ^{208}Pb, thus it is reasonable to suspect that the two quantities are linked. If transfer is shown to make a large contribution to products previously attributed to ICF, then a mechanism by which transfer may suppress complete fusion needs to be considered. In a classical picture, if transfer removes energy from the relative motion, it will reduce fusion. However in a coupled-channels approach, it is not clear whether above-barrier fusion can be suppressed by transfer. These questions require further investigation.

9.2 Towards Measurements of ^{7}Be(d, p)^{8}Be

The experimental groundwork was laid for making a measurement of the astrophysically relevant ^{7}Be(d, p)^{8}Be reaction at the ANU. Deuterium targets were produced, and the efficacy of using a large solid angle coverage array and kinematic reconstruc-

tion techniques for measuring pairs of α particles produced in the mirror reaction ^{7}Li(d,n)^{8}Be was demonstrated. In the ^{7}Li(d,n)^{8}Be reaction, a high population of the broad 4^{+} resonance was observed, totalling 87% of all observed $\alpha + \alpha$ pairs. Using KOOKABURRA to relate the measured angular distribution of the observed $\alpha + \alpha$ pairs to the total distribution yielded a population of 69% in the 4^{+} state. This result indicates that high population of this resonance should also be expected in the ^{7}Be(d, p)^{8}Be reaction.

A reliable determination of the coincidence efficiency of the BALiN array in the ^{7}Be(d, p)^{8}Be and ^{7}Li(d,n)^{8}Be reactions will be crucial for extraction of cross-sections. Regardless of the target mass, the coincidence efficiency relies on a good determination of the angular distribution of the fragments. In this thesis, the angular distribution of fragments has been simulated with KOOKABURRA and M- PLATYPUS. In very light systems, the applicability of these classical simulations is questionable. Since there is little [in the case of ^{7}Be(d, p)^{8}Be] or no [in the case of ^{7}Li(d,n)^{8}Be] post-breakup acceleration of the fragments, it may be more reliable to use DWBA to predict the angular distribution of the transfer product, and perform a Monte-Carlo simulation of fragment opening angles θ_{12} at each projectile-like nucleus scattering angle.

The ^{7}Li(d,n)^{8}Be reaction has larger relevance to this thesis work beyond its astrophysical interest. A major theme of this work was the role of post-breakup acceleration in influencing the energy and angular distribution of breakup fragments. The lack of this influence in the ^{7}Li(d,n)^{8}Be reaction can be used as a test for our interpretation of quantities such as E_{rel} and $\theta_{12} - \beta$. The fact that peaks in the data corresponding to asymptotic expectations of E_{rel} and $\theta_{12} - \beta$ were seen quite clearly in the experimental results indicates that our interpretation of E_{rel} and $\theta_{12} - \beta$ as indications of the projectile-like excitation is essentially correct. However, KOOKABURRA simulations do not quite reproduce experimental E_{rel} and $\theta_{12} - \beta$ distributions totally satisfactorily. A culprit may be the input excitation energy probability distribution for each resonance. It may be possible to use the measured E_{rel} distributions in ^{7}Li(d,n)^{8}Be to infer information on the underlying resonance structure of ^{8}Be populated after neutron pickup with ^{7}Li, and so improve the input distributions for KOOKABURRA calculations.

Given the success of using the BALiN array for measurements of the ^{7}Li(d,n)^{8}Be reaction, investigations were made into producing a ^{7}Be beam at the ANU. Test measurements of ^{7}Be production via the ^{10}B(^{6}Li,^{7}Be)^{9}Be reaction were made using the SOLEROO RIB capability. Normalised secondary beam intensities above 10^{4} cts/s/mg/cm^{2}/μeA were achieved with beam purity of $\sim$96%, and good energy resolution of the beam at a magnetic field of 2.7 T. This beam purity was achieved by pulsing the primary ^{6}Li beam at the cost of reducing the primary beam intensity by a factor of two, and by gating on the position spectra in the PPAC. The most significant beam impurity is energy degraded ^{6}Li beam particles. Higher beam intensities can be extracted at lower fields, at the cost of increasing the variation of energy of the ^{7}Be secondary beam. The fact that the kinematic reconstruction of reactions depends on

the mass of the projectile and target nuclei, as well as the number of nuclei in the exit channel, will enable the separation of $\alpha + \alpha$ pairs produced with ^{7}Be and with ^{6}Li beam impurities. The encouraging production rate and purity motivated investigation into the methods for the production of thick ^{10}B and $(^{nat}C_2D_4)_n$ targets. Future work will involve the fabrication of these targets, and measurements with a ^{7}Be beam.

9.3 Outlook

Transfer-triggered breakup is the dominant process by which near-target breakup occurs across the nuclear chart for reactions of ^{7}Li and ^{9}Be. If breakup is the mechanism that suppresses above-barrier complete fusion, it must be through transfer-triggered breakup.

It may be interesting in the context of the study of the fusion of neutron rich RIBs to investigate the role of neutron richness along a chain of weakly bound Li isotopes (i.e. ^{6}Li, ^{7}Li, ^{8}Li) in terms of their breakup modes and the probability of breakup. In addition, extending the study of transfer-triggered breakup to above-barrier energies will be useful. While such measurements will be complicated by the presence of absorption, the evolution of breakup mechanisms at above-barrier energies may shed light on the role of breakup in complete fusion suppression. In addition, detailed comparisons of coincidence and singles breakup fragment distributions in reactions at above-barrier energies will help to validate classical trajectory models.

While the detailed measurements of this thesis provide unprecedented insight into the dynamics of breakup, a complete understanding of the impact of breakup on ICF is yet to emerge. Classical trajectory models show that when sub-zeptosecond lifetimes are taken into account, sufficient breakup does not occur in reactions of ^{9}Be with high Z targets to explain the observed suppression of complete fusion. There is a need to understand the magnitude of the contribution from transfer directly producing the same heavy nucleus as breakup followed by capture. If transfer proves to be a large portion of σ_{ICF}, the mechanism by which transfer can suppress complete fusion should be investigated. It is not clear whether the two processes can be distinguished. There may be scope to do so by examining the kinematics of the remaining projectile-like fragment after ICF in using coincidences with decay α from ICF products with sub-microsecond lifetimes. Clearly, there is a need for a fully quantum mechanical model of transfer-triggered breakup to accurately model these processes.

Classical trajectory models have enabled a detailed examination of breakup. However, a systematic understanding of the sensitivities of the models in regards to above-barrier complete and incomplete fusion cross-sections is warranted.

References

1. Luong, D.H., Dasgupta, M., Hinde, D.J., Du Rietz, R., Rafiei, R., Lin, C.J., Evers, M., Diaz-torres, A.: Insights into the mechanisms and time-scales of breakup of ^{6,7}Li. Phys. Lett. B **695**, 105 (2011)
2. Luong, D.H., Dasgupta, M., Hinde, D.J., du Rietz, R., Rafiei, R., Lin, C.J., Evers, M., Diaz-Torres, A.: Predominance of transfer in triggering breakup in sub-barrier reactions of ^{6,7}Li. Phys. Rev. C **88**(3), 34609 (2013)
3. Luong, D.H.: Mechanisms and time-scales in breakup of ^{6,7}Li. Ph.D. thesis, Australian National University (2012)
4. Rafiei, R., du Rietz, R., Luong, D.H., Hinde, D.J., Dasgupta, M., Evers, M., Diaz-torres, A.: Mechanisms and systematics of breakup in reactions of ^{9}Be at near-barrier energies. Phys. Rev. C **81**(2), 024601 (2010)
5. Fang, Y.D., Gomes, P.R.S., Lubian, J., Zhou, X.H., Zhang, Y.H., Han, J.L., Liu, M.L., Zheng, Y., Guo, S., Wang, J.G., Qiang, Y.H., Wang, Z.G., Wu, X.G., He, C.Y., Li, C.B., Hu, S.P., Yao, S.H.: Fusion and one-neutron stripping reactions in the ^{9}Be+^{186}W system above the Coulomb barrier. Phys. Rev. C **87**(2), 024604 (2013)
6. Dasgupta, M., Gomes, P.R.S., Hinde, D.J., Moraes, S.B., Anjos, R.M., Berriman, A.C., Butt, R.D., Carlin, N., Lubian, J., Morton, C.R., Szanto de Toledo, A.: Effect of breakup on the fusion of ^{6}Li,^{7}Li, and ^{9}Be with heavy nuclei. Phys. Rev. C **70**(2), 024606 (2004)
7. Dasgupta, M., Hinde, D.J., Sheehy, S.L., Bouriquet, B.: Suppression of fusion by breakup: resolving the discrepancy between the reactions of ^{9}Be with ^{208}Pb and ^{209}Bi. Phys. Rev. C **81**(2), 024608 (2010)
8. Martí, G.V., Gomes, P.R.S., Rodríguez, M.D., Fernández Niello, J.O., Capurro, O.A., Pacheco, A.J., Testoni, J.E., Ramírez, M., Arazi, A., Padron, I., Anjos, R.M., Lubian, J., Crema, E.: Fusion, reaction, and breakup cross sections of ^{9}Be on a light mass target. Phys. Rev. C **71**(2), 027602 (2005)
9. Rath, P.K., Santra, S., Singh, N.L., Tripathi, R., Parkar, V.V., Nayak, B.K., Mahata, K., Palit, R., Kumar, S., Mukherjee, S., Appannababu, S., Choudhury, R.K.: Suppression of complete fusion in the ^{6}Li + ^{144}Sm reaction. Phys. Rev. C **79**(5), 051601 (2009)

Appendix A
Si Detector Deadlayer Measurement

The deadlayers of the DSSDs were determined using two methods. In the first, by varying the distance between the detector and the hub, the angle of incidence β of a mixed (^{239}Pu, ^{241}Am, ^{244}Cm) α was varied. As outlined in Refs. [1, 2], energy loss through the deadlayer for particles with energy E_0 at a given incidence angle is given by

$$\Delta E(\beta) = \frac{dE_0}{dx} t \frac{1}{\cos\beta}. \tag{A.1}$$

Thus, the measured difference between the energies of α particles at different incidence angles is

$$\begin{aligned} E(\beta_1) - E(\beta_2) &= (E_0 - \Delta E(\beta_1)) - (E_0 - \Delta E(\beta_2)) \\ &= \frac{dE_0}{dx} t \left(\frac{1}{\cos\beta_2} - \frac{1}{\cos\beta_1} \right). \end{aligned} \tag{A.2}$$

Therefore by plotting the difference of pulse heights at different β as a function of $\left(\frac{1}{\cos\beta_2} - \frac{1}{\cos\beta_1}\right)$, the slope gives $\frac{dE_0}{dx} t$. As the coverage of BALiN is large, β changes across the array. Since any α particle must pass through first the PET and aluminium layers, E_0 also depends on β, and Eq. A.2 becomes:

$$E(\beta_1) - E(\beta_2) = (E_0(\beta_1) - \Delta E(\beta_1)) - (E_0(\beta_2) - \Delta E(\beta_2)). \tag{A.3}$$

Since $\frac{dE_0}{dx}$ is slowly varying for ~5 MeV α particles, we can write

$$(E(\beta_1) - E(\beta_2)) - (E_0(\beta_1) - E_0(\beta_2)) = \frac{dE_0}{dx} t \left(\frac{1}{\cos\beta_2} - \frac{1}{\cos\beta_1} \right). \tag{A.4}$$

Plotting $(E(\beta_1) - E(\beta_2)) - (E_0(\beta_1) - E_0(\beta_2))$ as a function of $(\frac{1}{\cos\beta_2} - \frac{1}{\cos\beta_1})$ still yields the deadlayers, however this method relies heavily on the energy calibration of the array, which in turn relies on the correct determination of the deadlayers. As such, this method becomes iterative.

K. J. Cook, *Zeptosecond Dynamics of Transfer-Triggered Breakup*,
Springer Theses, https://doi.org/10.1007/978-3-319-96017-3

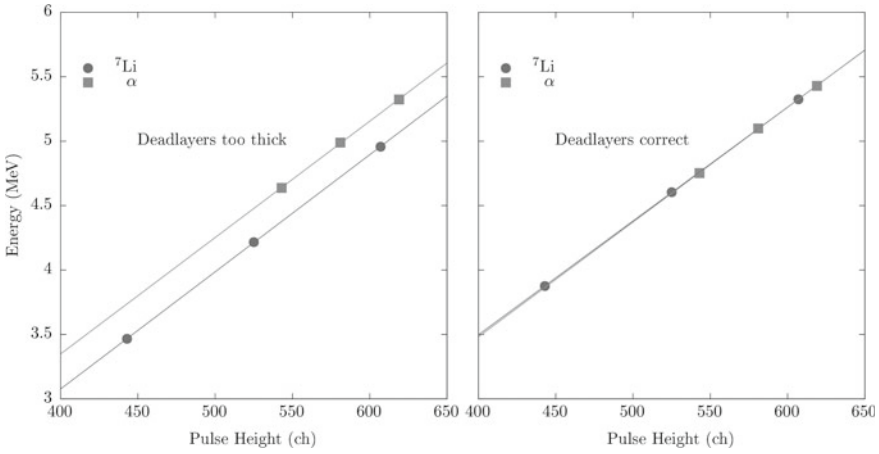

Fig. A.1 Relationship between pulse height and calculated incident energy of α particles and elastically scattered ^{7}Li. Shown

However, this dependence of the energy calibration on the deadlayers allows us to skip a step, and use the energy calibration to determine the deadlayers. This is still iterative, but somewhat more sensitive approach was developed to make use of the z_i dependence of the Bethe-Bloch equation (Eq. 3.3). Assuming that the pulse height response of the detector is independent of Z for the light nuclei relevant here, the relationship between the energy loss of an incident particle and pulse height (in channels) should not differentiate between α particles from a mixed α source and from elastically scattered ^{7}Li. As the incident energy of particles on the active area of the DSSD follows energy loss through the deadlayer, Al and PET layers, it is only when the deadlayers are determined correctly (and so the incident energy determined correctly) that the relationship between energy and pulse height does not depend on Z.

Therefore the pulse height as a function of expected incident energy for the aforementioned mixed α source and for elastically scattered ^{7}Li from ^{196}Pt at 6, 6.75 and 7.5 MeV were compared. The thickness of the Si deadlayers were varied for each detector until the relationship between energy and pulse height for the α particles and the elastically scattered ^{7}Li converged, indicating that the deadlayers were correctly determined. Shown in Fig. A.1 are the pulse height against energy relationships after using the angle method (left) and after using the z_i dependence of the Bethe-Bloch equation (right). If the deadlayers are overestimated, as in the left hand side of Fig. A.1, the total energy loss of ^{7}Li is overestimated to a greater extent than that of the α particles. This process was performed on every arc of each DSSD, and the final deadlayers, together with the thicknesses of the PET and Al layers are shown in Table A.1, providing a summary of the layers of BALiN where particles experience energy loss.

Table A.1 Summary of the thicknesses of the deadlayers for each detector, along with the thicknesses of the PET foils and Al layers through which particles must pass

DSSD	Deadlayer manufacturer specification (μm)	Deadlayer (μm) (remeasured)	Al layer (μm)	PET foil (μm)
A	0.5	2.00	0.2	0.7
B	0.5	2.05	0.2	0.7
C	0.5	0.95	0.2	0.7
D	0.5	2.10	0.2	0.7

In the BEX run, the array was not fully biased, so the depletion region of each DSSD was smaller, and the corresponding deadlayer larger. In the re-analysis of the BEX run, the deadlayers found in [3] were used.

References

1. Knoll, G.F.: Radiation Detection and Measurement, 4th edn. Wiley, New York (2010)
2. Elad, E., Inskeep, C.N., Sareen, R.A., Nestor, P.: Dead layers in charged-particle detectors. IEEE Trans. Nucl. Sci. **20**(1), 534 (1973)
3. Luong, D.H.: Mechanisms and time-scales in breakup of ^{6,7}Li. Ph.D. thesis, Australian National University (2012)

Appendix B
Characterising ToF Spectra

The ToF spectra shown in Fig. 3.14 have restricted y-axes, to show only those ToF that are valid for time calibration. Shown in Fig. B.1 is the full ToF spectrum for ^{7}Li + ^{58}Ni at 11.7 MeV, for the RDUX run. Data are shown from the RDUX run, as the RF subtraction was performed offline, as discussed in Sect. 3.4.6. As such interpretation of ToF spectra in this instance is more easily performed. The offset is different to that of the LIBEX run, described above. Here, valid ToFs fall at ∼100 ns. There are groups of events ∼107 and ∼214 ns below the valid ToFs – these are events arising from different beam bunches which are separated by 106.6 ns.

There are a large number of events above 480 ns. These correspond to events where the energy of the particle was recorded, but not the ToF. In taking the difference between the RF reference and the measured ToF, shown in Eq. 3.26, 4550 channels (445.9 ns) were added to ensure ToFs were positive. When the timing signal is missing Eq. 3.26 becomes $ToF_{measured} = RF + 4550$, pushing these events up by 445.9 ns. The offset of this group from 445.9 ns is due to the recorded time of the RF signal of ∼20 ns. The width of this group is 25 ns - the jitter from the 40 MHz clock in the TDC. There is a further group at ∼450 ns: these events correspond to energy signals in the first arc of detector D. Timing signals from this arc were sacrificed to record the RF reference signal. Therefore, Eq. 3.26 becomes $ToF_{measured} = RF - RF + 4550$, putting the events at ∼450 ns.

When particles are detected in coincidence, *two* valid ToFs as well as the presence of the RF reference signal are required. Shown in Fig. B.2 are the ToFs for two particles detected in coincidence, for the same measurement shown in Fig. B.1. There are a number of possible combinations of whether or not a timing signal was recorded, whether or not both particles are in the same beam bunch, and whether or not the RF reference was recorded. These are enumerated in Table B.1, and labelled in Fig. B.2. We will revisit this spectrum when finding the deadtime of the array due to the TDC.

K. J. Cook, *Zeptosecond Dynamics of Transfer-Triggered Breakup*,
Springer Theses, https://doi.org/10.1007/978-3-319-96017-3

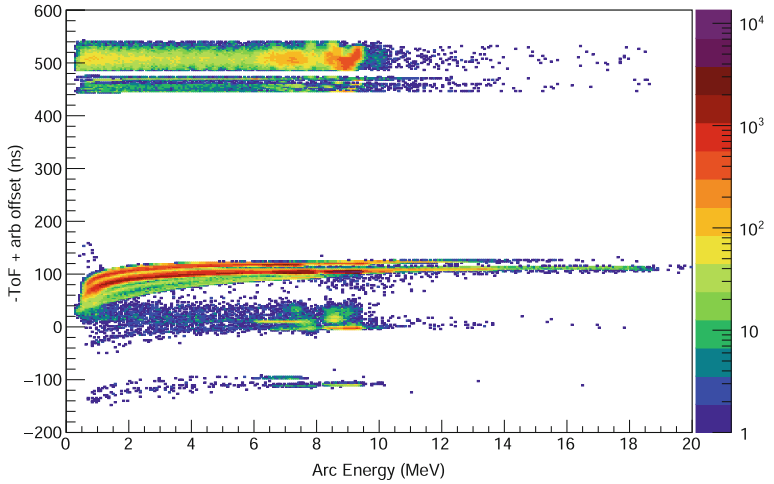

Fig. B.1 Full Arc Energy versus ToF spectrum for ^{7}Li + ^{58}Ni at 11.7 MeV in the RDUX run. Valid ToFs fall around ∼100 ns. The cause of invalid ToFs is discussed in text

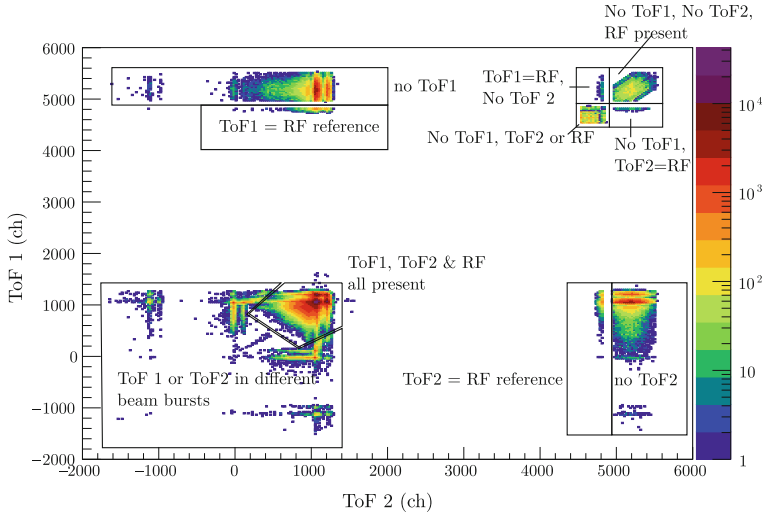

Fig. B.2 ToF$_1$ versus ToF$_2$ spectrum for ^{7}Li + ^{58}Ni at E_{beam} = 11.7 MeV, labelled with the reason behind the particular ToF$_1$ versus ToF$_2$ location of each group of events, based on enumeration of possible signal and zero-signal combinations, shown in Table B.1

Table B.1 Enumeration of possible combinations of present and missing time signals and RF references for coincidence events. Combinations identical under reversal of the Time 1 and Time 2 labels have been omitted

Time 1	Time 2	RF	ToF1 (ch)	ToF2 (ch)
✗	✓	✓	5050	500
✗	✗	✓	5050	5050
✗	✗	✗	4550	4550
✓	✓	✗	0	0
✓	✓	✓	500	500
= RF	✓	✓	4550	500
= RF	✗	✓	4550	5050

Appendix C
Breakup at Additional Energies

In Chap. 4, results were shown for each beam-target combination at one energy and detector configuration. Here, for completeness, the Q-E_{rel} Q, and E_{rel} spectra for measurements of the same systems at different energies and detector configurations are shown (Figs. C.1, C.2, C.3, C.4, C.5, C.6, C.7, C.8 and C.9).

K. J. Cook, *Zeptosecond Dynamics of Transfer-Triggered Breakup*,
Springer Theses, https://doi.org/10.1007/978-3-319-96017-3

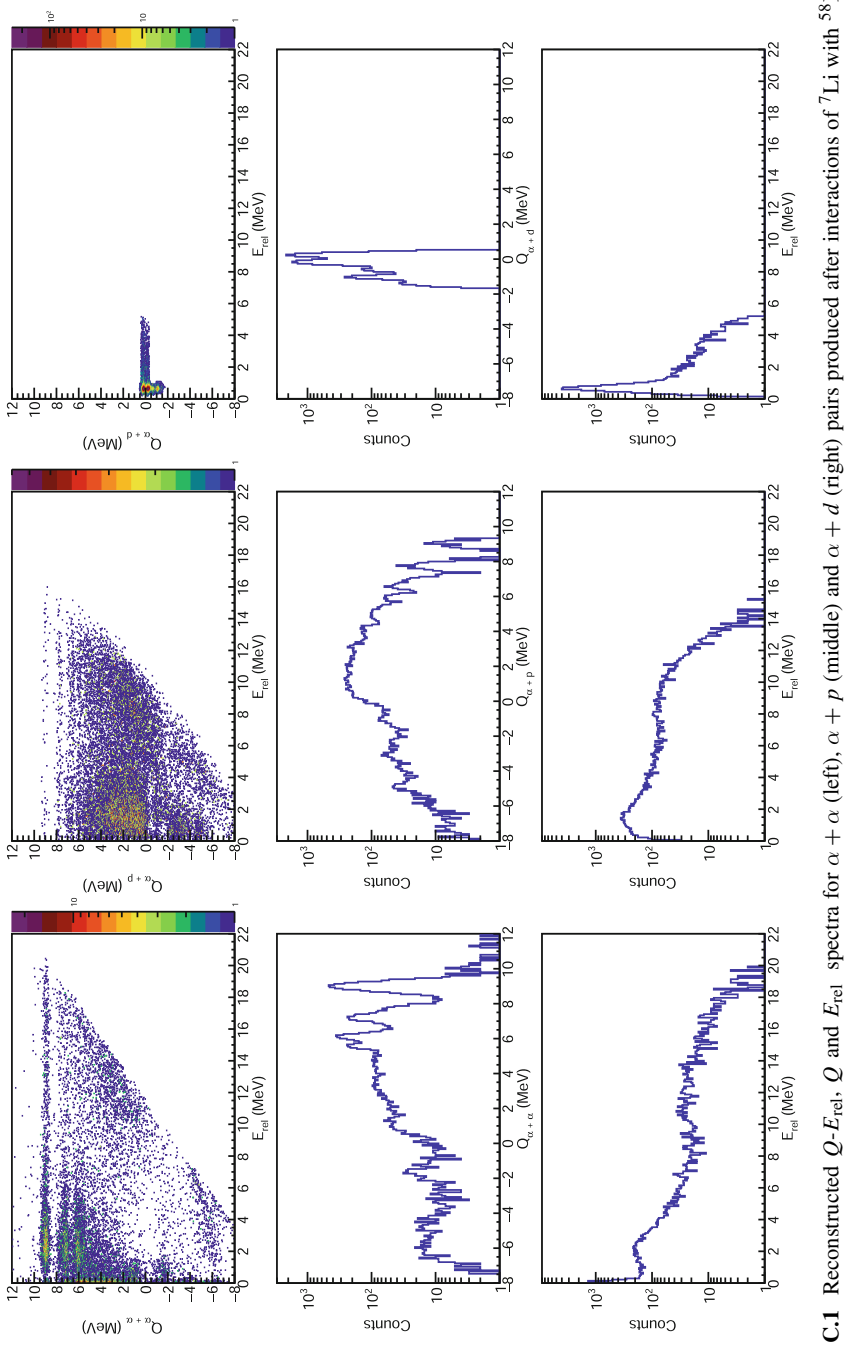

Fig. C.1 Reconstructed Q-E_{rel}, Q and E_{rel} spectra for $\alpha + \alpha$ (left), $\alpha + p$ (middle) and $\alpha + d$ (right) pairs produced after interactions of ^{7}Li with ^{58}Ni at $E_{beam} = 13.10$ MeV

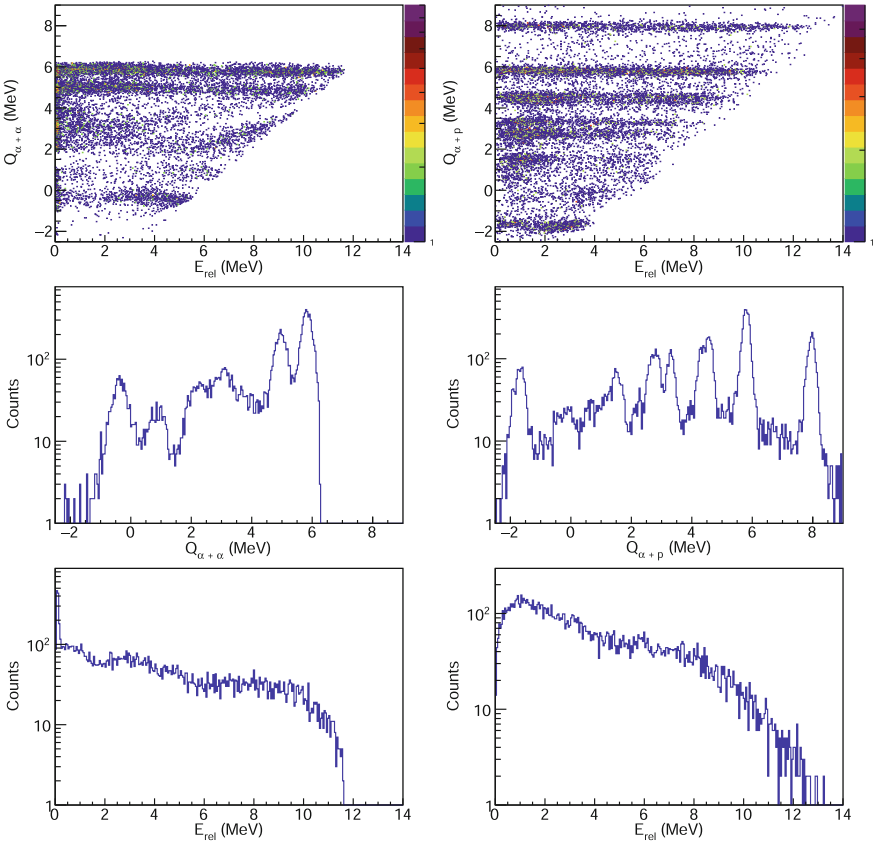

Fig. C.2 Reconstructed Q-E_{rel}, Q and E_{rel} spectra for $\alpha + \alpha$ (left) and $\alpha + p$ (right) pairs produced after interactions of ^{7}Li with ^{28}Si at $E_{beam} = 7.50$ MeV

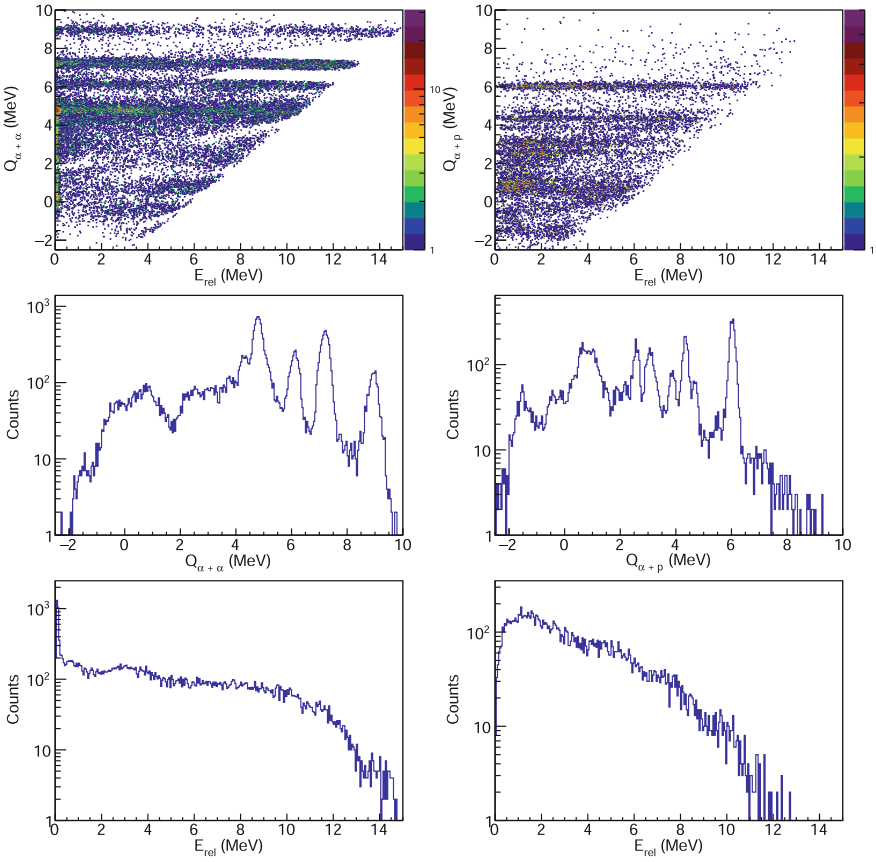

Fig. C.3 Reconstructed Q-E_{rel}, Q and E_{rel} spectra for $\alpha + \alpha$ (left) and $\alpha + p$ (right) pairs produced after interactions of ^{7}Li with ^{27}Al at $E_{beam} = 7.50$ MeV

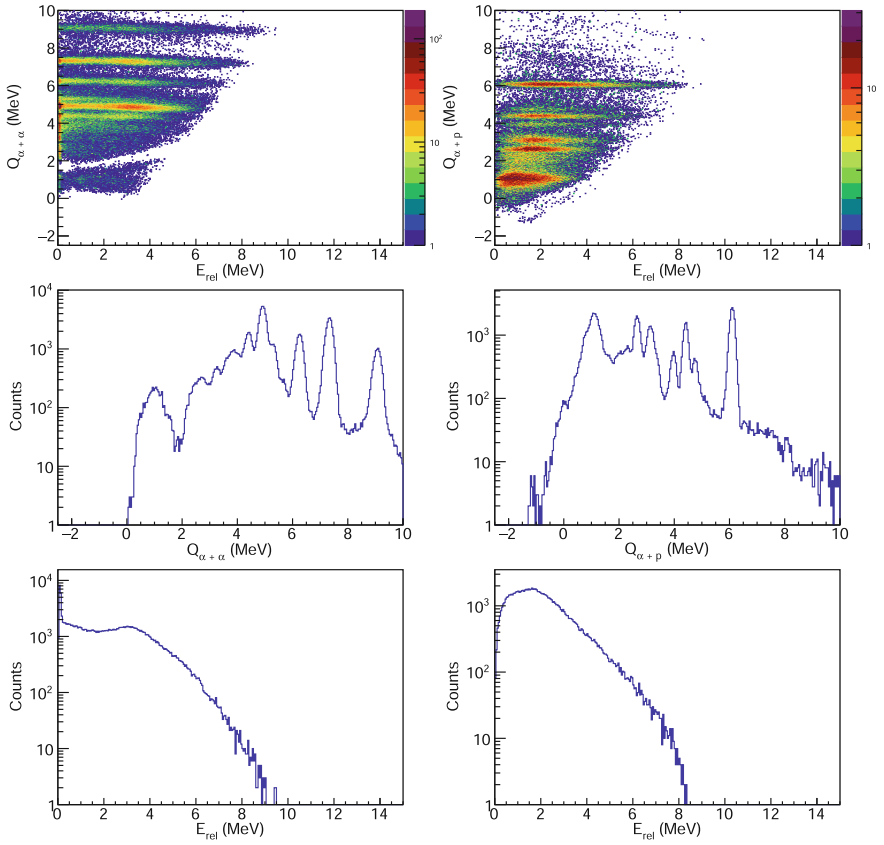

Fig. C.4 Reconstructed Q-E_{rel}, Q and E_{rel} spectra for $\alpha+\alpha$ (left) and $\alpha+p$ (right) pairs produced after interactions of ^{7}Li with ^{27}Al at $E_{beam} = 7.50$ MeV, with the BALiN array in the lampshade configuration

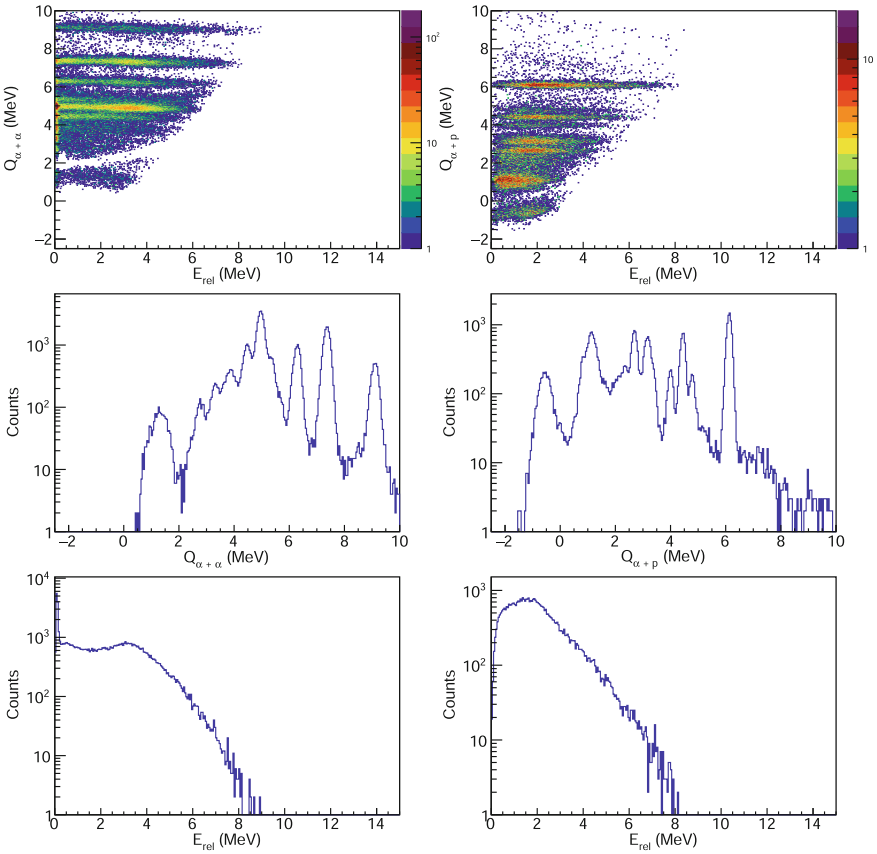

Fig. C.5 Reconstructed Q-E_{rel}, Q and E_{rel} spectra for $\alpha + \alpha$ (left) and $\alpha + p$ (right) pairs produced after interactions of ^{7}Li with ^{27}Al at $E_{beam} = 6.75$ MeV, with the BALiN array in the lampshade configuration

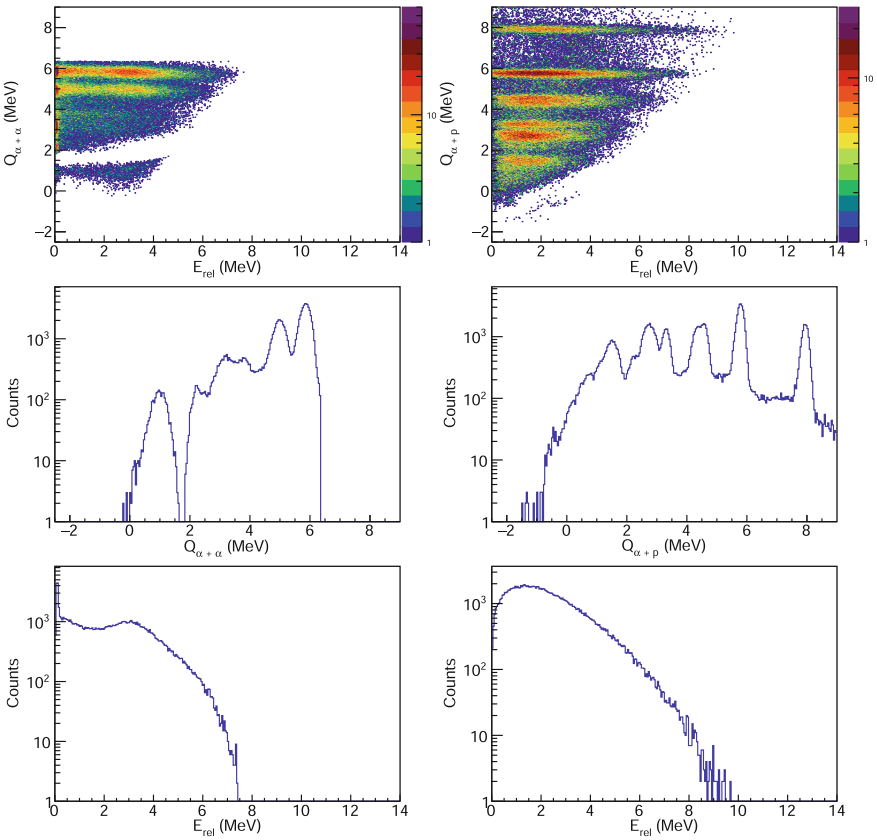

Fig. C.6 Reconstructed Q-E_{rel}, Q and E_{rel} spectra for $\alpha + \alpha$ (left) and $\alpha + p$ (right) pairs produced after interactions of ^{7}Li with ^{28}Si at $E_{beam} = 7.50$ MeV, with the BALiN array in the lampshade configuration

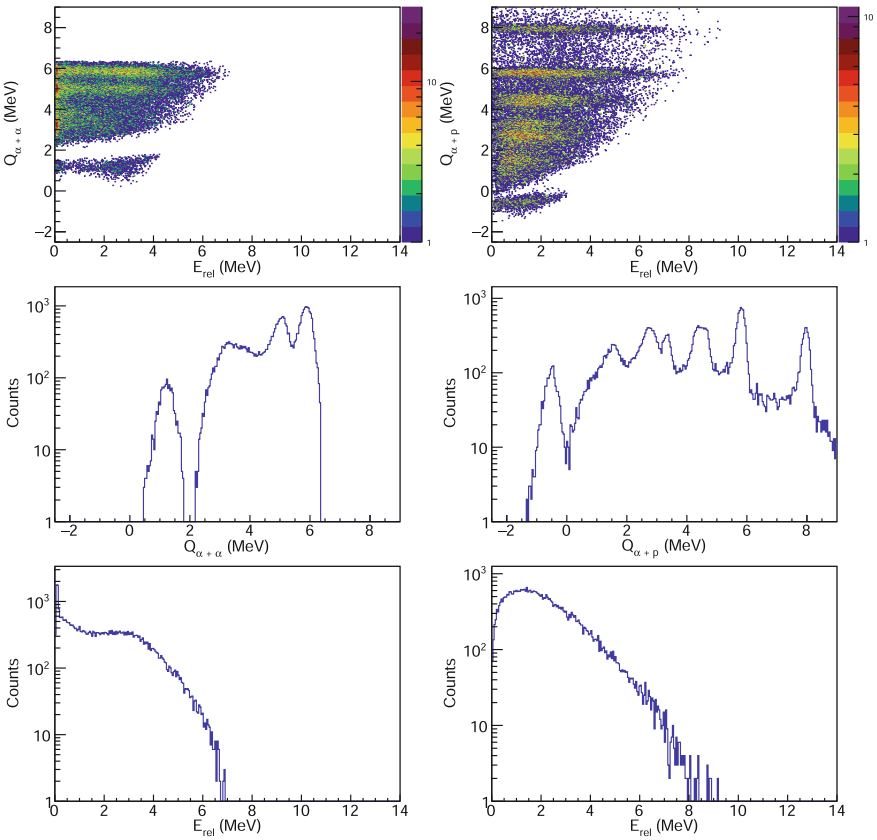

Fig. C.7 Reconstructed Q-E_{rel}, Q and E_{rel} spectra for $\alpha + \alpha$ (left) and $\alpha + p$ (right) pairs produced after interactions of ^{7}Li with ^{28}Si at $E_{beam} = 6.75$ MeV, with the BALiN array in the lampshade configuration

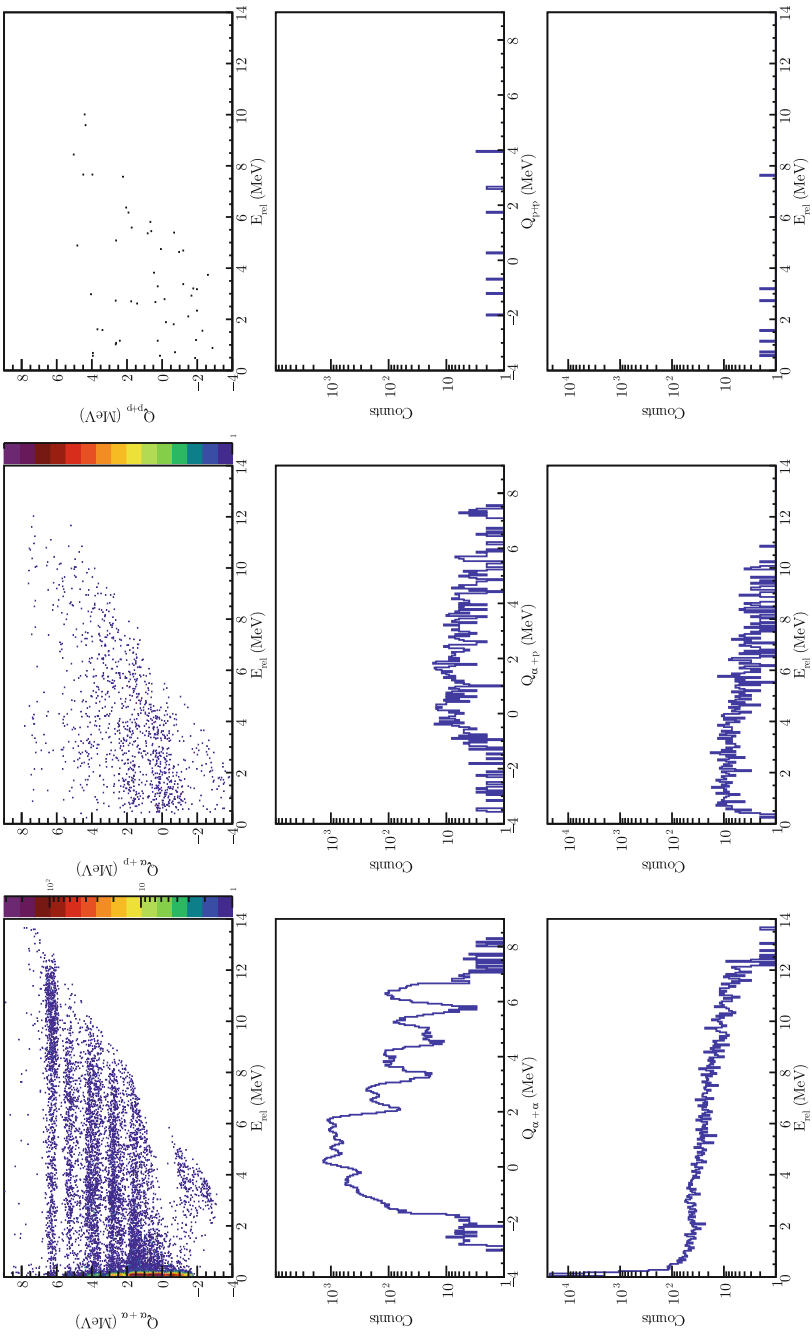

Fig. C.8 Reconstructed Q-E_{rel}, Q and E_{rel} spectra for $\alpha + \alpha$ (left), $\alpha + p$ (middle), and $p + p$ (right) pairs produced after interactions of ^{9}Be with ^{27}Al at $E_{beam} = 8.90$ MeV

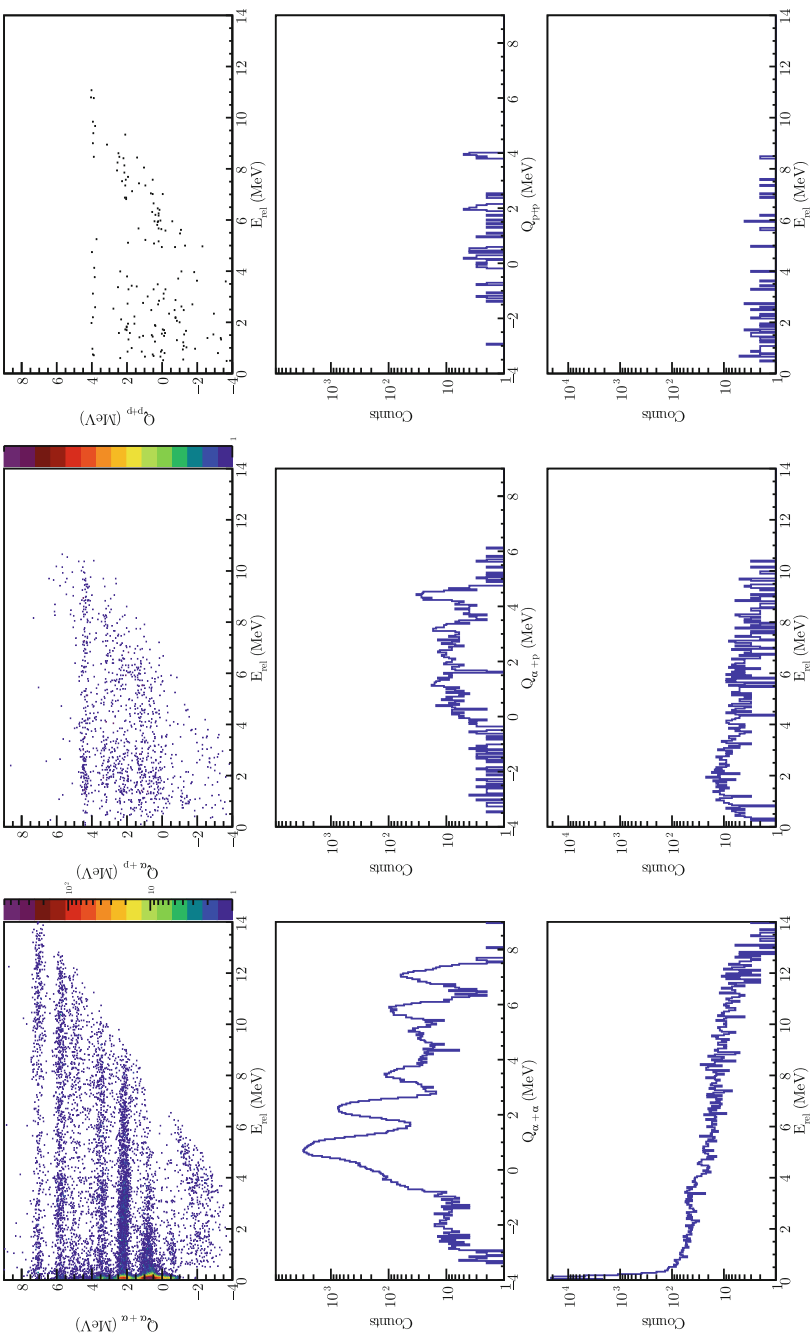

Fig. C.9 Reconstructed Q-E_{rel}, Q and E_{rel} spectra for $\alpha + \alpha$ (left), $\alpha + p$ (middle), and $p + p$ (right) pairs produced after interactions of ^{9}Be with ^{28}Si at $E_{beam} = 10.0$ MeV

Appendix D
Rare Breakup Modes in Reactions with ^{9}Be

As with the study of breakup after interactions of ^{7}Li with ^{58}Ni, ^{28}Si and ^{27}Al, ToF identification can be used to find rare coincidence two reaction modes in interactions of ^{9}Be with ^{28}Si and ^{27}Al. In reactions with heavy targets, the only positive or small negative Q breakup modes are those that produce two α particles: either triggered by neutron stripping or direct breakup. However, in reactions of ^{9}Be with ^{28}Si and ^{27}Al, the Q-value for producing an $\alpha + p$ pair is large and positive: 4.447 and 7.386 MeV, respectively. Therefore, it may be expected that $\alpha + p$ pairs will be produced in these reactions.

By gating on $\alpha + p$ pairs in ToF, it is readily apparent that this is the case. Shown in Fig. D.1 are the Q-E_{rel}, Q and E_{rel} spectra for ToF identified $\alpha + p$ pairs detected in reactions of ^{9}Be with (a), (c), (e) ^{28}Si and (b), (d), (f) ^{27}Al. Clear bands of events are produced at the ground-state Q and at lower Q, corresponding to excitation of the target-like recoiling nuclei ^{32}P and ^{31}Si, respectively.

Due to the peaks in Q that correspond to the excited states of ^{32}P and ^{31}Si, shown in Fig. D.1c, d, it is clear that the $\alpha + p$ pairs detected in BALiN do arise from reactions with the target and are not spurious coincidences. However, the reaction mechanism producing these pairs is not clear – for transfer to be responsible, three neutrons and one proton must be transferred; one step cluster transfer of "^{4}H" doesn't seem likely. However, the E_{rel} distribution of these fragments, shown in Fig. D.1e, f bears resemblance to the E_{rel} distribution of $\alpha + p$ fragments detected in reactions of ^{7}Li with ^{27}Al and ^{28}Si, shown in Figs. 4.9f and 4.11f. In the case of ^{7}Li, it seems clear that $\alpha + p$ pairs must be produced through two-neutron transfer populating ^{5}Li which subsequently decays into $\alpha + p$ pairs. To the extent that the E_{rel} distribution can be used to examine the structure of very[1] short lived nuclei such as ^{5}Li, the correspondence of the E_{rel} spectra of $\alpha + p$ pairs produced with a ^{7}Li or ^{9}Be projectile suggests a common origin.

As might be expected from the extreme amount of mass transfer necessary for $\alpha + p$ pairs to be produced with a ^{9}Be projectile, $\alpha + p$ pairs represent a small fraction of the (un-efficiency corrected) total genuine coincidence yield: $3.7 \pm 0.06\%$

[1] $\tau \sim 10^{-22}$s.

K. J. Cook, *Zeptosecond Dynamics of Transfer-Triggered Breakup*,
Springer Theses, https://doi.org/10.1007/978-3-319-96017-3

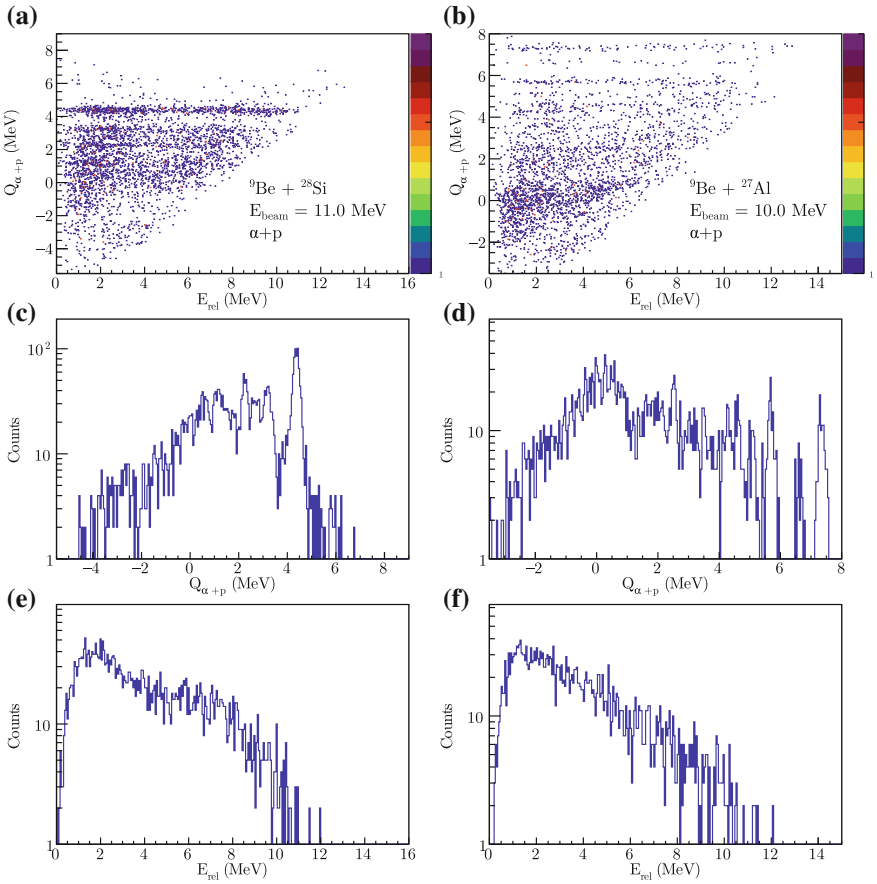

Fig. D.1 Reconstructed Q-E_{rel}, Q and erel spectra for $\alpha + p$ pairs produced after interactions of ^{9}Be with ^{27}Al and ^{28}Si. In **a**, **c** and **e** the spectra for ^{9}Be + ^{28}Si at $E_{beam} = 11.0$ MeV is shown, and in **b**, **d** and **f** the spectra for ^{9}Be + ^{27}Al at $E_{beam} = 10.0$ MeV is shown

for the measurement with ^{28}Si shown here at $E_{beam} = 11.0$ MeV and $2.65 \pm 0.05\%$ for the measurement with ^{27}Al. The fact that this reaction mode appears in the data at all is a demonstration of the way that large positive Q-values [4.447 MeV (^{28}Si) and 7.386 MeV (^{27}Al)] drive transfer probabilities in these measurements.

It is of course also possible to examine the possibility of $p + p$ pairs being produced in this reaction. The ground-state Q-value for ^{9}Be + ^{28}Si $\rightarrow$ $p + p$+^{35}S is $Q_{gg} = 4.123$ MeV, and for ^{9}Be + ^{27}Al $\rightarrow$ $p + p$+^{34}P it is $Q_{gg} = 4.122$ MeV. The large, positive Q-value would suggest that these reactions should be expected to be seen, though as with $p + p$ produced in reactions of ^{7}Li, the reaction mechanism producing these coincident protons is not immediately clear. The ToF gated Q_{p+p} shown in Fig. D.2a is the ToF gated Q_{p+p} spectrum for $p + p$ pairs produced in reactions of ^{9}Be with ^{28}Si at $E_{beam} = 11$ MeV. The $p + p$ pairs identified in this

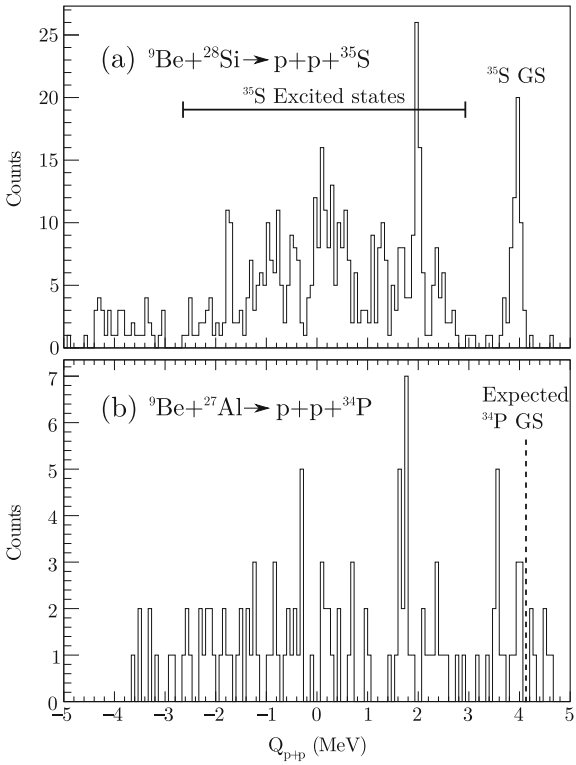

Fig. D.2 **a** Reconstructed Q_{p+p} for pairs of protons identified using ToF gating in reactions of ^{9}Be with ^{28}Si. Peaks in the reconstructed Q_{p+p} spectrum are easily seen in **a**, and their spacing corresponds to excited states in ^{35}S. **b** Reconstructed Q_{p+p} for pairs of protons identified using ToF gating in reactions of ^{9}Be with ^{27}Al. 131 events are present in this spectrum, and the presence of any peaks is somewhat dubious

reaction comprised $0.56 \pm 0.02\%$ of the total valid coincidence yield. Clear peaks are present in this spectrum, indicating transfer populating ^{35}S in its ground and excited states.

The reconstructed Q_{p+p} spectrum for $p + p$ pairs produced in reactions of ^{9}Be with ^{27}Al at $E_{beam} = 10$ MeV is shown in Fig. D.2b. Only 131 $p + p$ pairs were identified here, comprising $0.12 \pm 0.01\%$ of the total valid coincidence yield. Given the small number of counts, there is no obvious peak structure in this spectrum, barring perhaps one at $Q_{p+p} = 1.78$ MeV, which may correspond with the 2.3 MeV doublet of $(3^{(-)},4^{(-)})$ states arising from the $\pi s_{1/2}\nu f_{7/2}$ configuration in ^{34}P [1]. The existing nuclear structure data for ^{34}P is somewhat sparse. With greater statistics, it may be possible to use this reaction mode producing $p + p$ pairs after 2 proton 5 neutron transfer to examine the excited states and structure of neutron-rich isotopes.

Reference

1. Nica, N., Singh, B.: Data for ^{34}P. Nucl. Data Sheets **113**, 1563 (2012)

Appendix E
BALiN Solid Angle $\Delta\Omega_{\mathrm{BALiN}}(\theta_{\mathrm{bin}})$

Since the geometry of BALiN is well known, Eq. 6.11 enables the evaluation of the solid angle coverage of the monitor, but relies on knowledge of the solid angle coverage of BALiN.

The solid angle coverage of BALiN within a bin of width $\Delta\theta_{\mathrm{bin}}$ located at θ_{bin} is given by

$$\Delta\Omega_{\mathrm{BALiN}}(\theta_{\mathrm{bin}}) = \iint_{\mathrm{BALiN}} \sin\theta_{\mathrm{bin}} d\theta d\phi. \tag{E.1}$$

The coverage of BALiN in both θ and ϕ change with θ_{bin}, and depend on the exact location of BALiN in space. Rather than calculate these quantities analytically, we can instead use a Monte Carlo simulation that distributes events evenly on the surface of a sphere, and filter these events through the existing event filtering methods. Briefly, simulated coincidence events are tagged as either being within the acceptance of BALiN or outside it, then these events are randomised in (θ, ϕ) to match the pixelization of BALiN, then the simulated data are kinematically reconstructed as if it were experimental data. This program allows us to identify which events will have hit the detectors, and which will not. The events were simulated in (θ, ϕ) by choosing random variables A and B in the range $(0 - 1)$, then

$$\begin{aligned} \theta &= \cos^{-1}(2A - 1) \\ \phi &= 2\pi B. \end{aligned} \tag{E.2}$$

This produces a set of events isotropically distributed over the surface of a sphere [1]. This distribution is shown in Fig. E.1a. The uniform distribution in $d\Omega$ results in a $\sin\theta$ distribution in (θ, ϕ). The events are then filtered by the detector acceptance, as shown in Fig. E.1b. The grey dotted lines indicate 4° bins, and the grey rectangles indicate the "edge bins" of the detector, where the solid angle coverage of BALiN changes rapidly. Determining $\Delta\Omega_{\mathrm{BALiN}}$ with this method is especially advantageous for these bins. The ratio of the events that fall within the detector acceptance N_{BALiN} to the total number of events N_{bin} in each bin of width $\Delta\theta_{\mathrm{bin}}$ gives the ratio of the solid angle of the detector to the total solid angle of the bin, and solving for $\Delta\Omega_{\mathrm{BALiN}}$

K. J. Cook, *Zeptosecond Dynamics of Transfer-Triggered Breakup*,
Springer Theses, https://doi.org/10.1007/978-3-319-96017-3

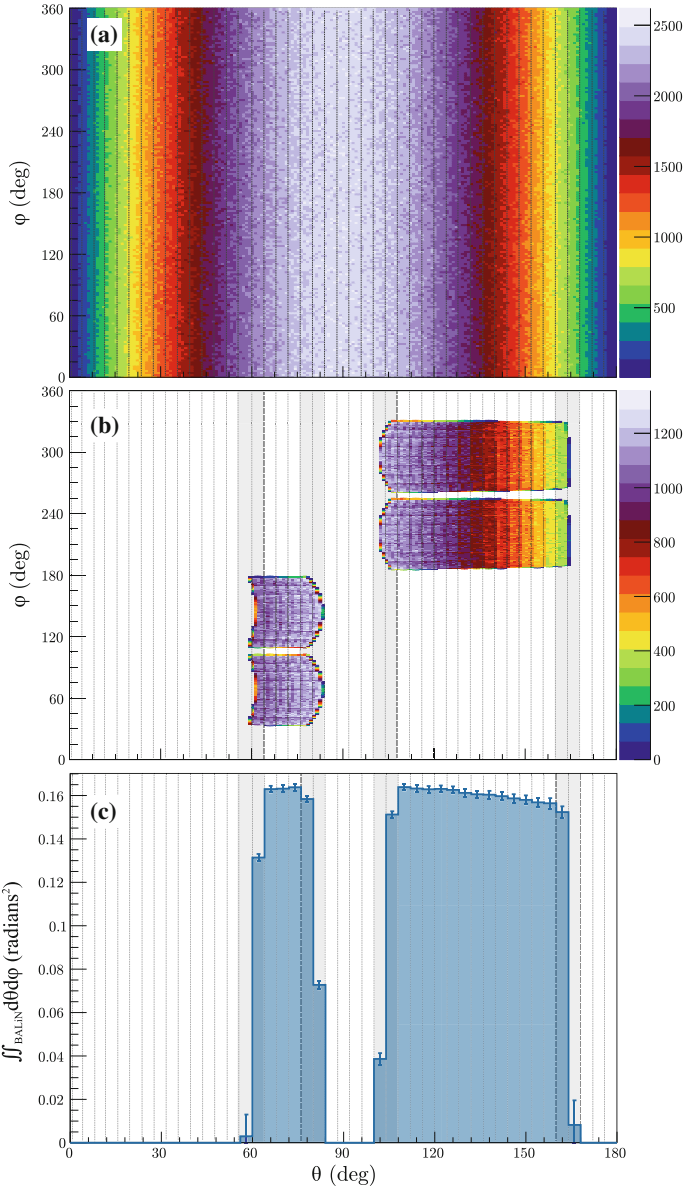

Fig. E.1 In order to determine the solid angle coverage of the BALiN array, a Monte Carlo simulation with points evenly distributed on a sphere is performed. Shown in **a** is the simulated distribution of events in (θ, ϕ), which is then filtered through the detector acceptance, shown in **b**. Here, the acceptance of the array for the RDUX run is shown. The resulting $\iint_{\mathrm{BALiN}} d\theta d\phi$ of each bin is shown in **c**. When multiplied by sin θ, this gives the detector solid angle $\Delta\Omega_{\mathrm{BALiN}}$. The grey dotted lines indicate 4° bins. Grey rectangles show the edge bins where the solid angle changes rapidly

$$\Delta\Omega_{\mathrm{BALiN}}(\theta_{\mathrm{bin}}) = \frac{N_{\mathrm{BALiN}}}{N_{\mathrm{bin}}}\Delta\Omega_{\mathrm{bin}} \tag{E.3}$$

$$\iint_{\mathrm{BALiN}} \sin\theta_{\mathrm{bin}} d\theta d\phi = \frac{N_{\mathrm{BALiN}}}{N_{\mathrm{bin}}} \iint_{\mathrm{bin}} \sin\theta_{\mathrm{bin}} d\theta d\phi. \tag{E.4}$$

Assuming that $\sin\theta$ varies slowly across the bin width, we can take out the $\sin\theta_{\mathrm{bin}}$ term which is the same on both sides,

$$\iint_{\mathrm{BALiN}} d\theta d\phi = \frac{N_{\mathrm{BALiN}}}{N_{\mathrm{bin}}} \iint_{\mathrm{bin}} d\theta d\phi \tag{E.5}$$

$$= \frac{N_{\mathrm{BALiN}}}{N_{\mathrm{bin}}} 2\pi\Delta\theta_{\mathrm{bin}}. \tag{E.6}$$

This is shown in Fig. E.1c. When the $\sin\theta$ term is removed, the slow change in $d\phi$ with scattering angle due to the offset of the BALiN detector from the beam axis as discussed in Sect. 3.4.2 is apparent. The solid angle of BALiN determined in Eq. E.4 is then used in Eq. 6.11.

Reference

1. Weisstein, E.W.: Sphere point picking. From MathWorld – A Wolfram Web Resource. http://mathworld.wolfram.com/SpherePointPicking.html

Appendix F
Adopted Barrier Radius Parameters

The adopted barrier radii R_B found from Woods-Saxon fits to SPP calculations are shown in Table F.1.

Table F.1 Barrier radii R_B found from Woods-Saxon fits to SPP calculations for each system where breakup probabilities were extracted

Beam + Target	R_B (fm)
^{9}Be + ^{209}Bi	11.54
^{9}Be + ^{208}Pb	11.53
^{9}Be + ^{196}Pt	11.36
^{9}Be + ^{186}W	11.22
^{9}Be + ^{168}Er	10.94
^{9}Be + ^{144}Sm	10.54
^{9}Be + ^{28}Si	8.50
^{9}Be + ^{27}Al	8.48
^{7}Li + ^{58}Ni	9.20
^{7}Li + ^{28}Si	8.44
^{7}Li + ^{27}Al	8.46

K. J. Cook, *Zeptosecond Dynamics of Transfer-Triggered Breakup*,
Springer Theses, https://doi.org/10.1007/978-3-319-96017-3